ULTRASOUND TISSUE CHARACTERIZATION USING SPECKLE STATISTICS

Anca Cristea

Numéro d'ordre : 329 - 2015 Année : 2015

THÈSE

ULTRASOUND TISSUE CHARACTERIZATION USING SPECKLE STATISTICS

Délivrée par
L'UNIVERSITÉ LYON 1
Spécialité: Traitement du Signal et de l'Image

Pour obtenir le
DIPLÔME DE DOCTORAT

ÉCOLE DOCTORALE: ELECTRONIQUE, ELECTROTECHNIQUE, AUTOMATIQUE

Soutenue publiquement le 9 décembre 2015 par
Anca CRISTEA

Jury

Simone Balloco	Professor Agregat, Universitat de Barcelona	Rapporteur
Ayache Bouakaz	Directeur de Recherche INSERM	Rapporteur
Emilie Franceschini	Chargé de Recherche CNRS, HDR	Examinateur
Olivier Basset	Professeur des Universités, Lyon 1	Directeur de thèse
Christian Cachard	Professeur des Universités, Lyon 1	Co-directeur de thèse

UNIVERSITE CLAUDE BERNARD - LYON 1

Président de l'Université	**M. François-Noël GILLY**
Vice-président du Conseil d'Administration	M. le Professeur Hamda BEN HADID
Vice-président du Conseil des Etudes et de la Vie Universitaire	M. le Professeur Philippe LALLE
Vice-président du Conseil Scientifique	M. le Professeur Germain GILLET
Directeur Général des Services	M. Alain HELLEU

COMPOSANTES SANTE

Faculté de Médecine Lyon Est – Claude Bernard	Directeur : M. le Professeur J. ETIENNE
Faculté de Médecine et de Maïeutique Lyon Sud – Charles Mérieux	Directeur : Mme la Professeure C. BURILLON
Faculté d'Odontologie	Directeur : M. le Professeur D. BOURGEOIS
Institut des Sciences Pharmaceutiques et Biologiques	Directeur : Mme la Professeure C. VINCIGUERRA
Institut des Sciences et Techniques de la Réadaptation	Directeur : M. le Professeur Y. MATILLON
Département de formation et Centre de Recherche en Biologie Humaine	Directeur : Mme. la Professeure A-M. SCHOTT

COMPOSANTES ET DEPARTEMENTS DE SCIENCES ET TECHNOLOGIE

Faculté des Sciences et Technologies	Directeur : M. F. DE MARCHI
Département Biologie	Directeur : M. le Professeur F. FLEURY
Département Chimie Biochimie	Directeur : Mme Caroline FELIX
Département GEP	Directeur : M. Hassan HAMMOURI
Département Informatique	Directeur : M. le Professeur S. AKKOUCHE
Département Mathématiques	Directeur : M. le Professeur Georges TOMANOV
Département Mécanique	Directeur : M. le Professeur H. BEN HADID
Département Physique	Directeur : M. Jean-Claude PLENET
UFR Sciences et Techniques des Activités Physiques et Sportives	Directeur : M. Y.VANPOULLE
Observatoire des Sciences de l'Univers de Lyon	Directeur : M. B. GUIDERDONI
Polytech Lyon	Directeur : M. P. FOURNIER
Ecole Supérieure de Chimie Physique Electronique	Directeur : M. G. PIGNAULT
Institut Universitaire de Technologie de Lyon 1	Directeur : M. le Professeur C. VITON
Ecole Supérieure du Professorat et de l'Education	Directeur : M. le Professeur A. MOUGNIOTTE
Institut de Science Financière et d'Assurances	Directeur : M. N. LEBOISNE

Abstract

The purpose of ultrasound tissue characterization or Quantitative Ultrasound (QUS) is to differentiate between tissue pathologies by associating model parameters to physical tissue features. The exclusive use of ultrasound for diagnosis would guarantee that the patient does not undergo a procedure that is invasive (e.g. a biopsy), using ionizing radiation (e.g. tomography) or simply uncomfortable and expensive (e.g. MRI). QUS methods extract information on the tissue microstructure from the temporal or spectral content of the acquired ultrasound signals. The temporal radiofrequency (RF) signal and its envelope are of interest because of the speckle patterns created by wave interference, which can be modeled by statistical distributions.

The present work proposes to explore the possibility of obtaining reliable QUS estimates by using statistical distributions as models for ultrasound speckle. The estimates consist in the parameters of the respective distributions and are indicators of the scatterer density in the medium. The evaluation is conducted on simulated images, particle phantoms and biophantoms.

In the first part, the Generalized Gaussian distribution is used to model the RF signal, and the Nakagami distribution is used to model its envelope. The two distributions show limitations in discriminating media with high scatterer densities, as the values of their shape parameters saturate in the fully developed speckle regime. Therefore, since the formation of fully developed speckle depends on the resolution of the imaging system, characterization can be done only at very high resolutions, corresponding to high frequencies that are not common in clinical ultrasound. An application of the Nakagami model on the second harmonic image shows the potential of the Nakagami shape parameter as a measure of the nonlinearity of the medium.

In the second part, the echo envelope was modeled using the Homodyned-K distribution. The scatterer clustering parameter α allows the discrimination of dense media up to a concentration that is higher than the one that limits the Nakagami distribution. However, this limit is difficult to estimate precisely, because the values of α that are characteristic for fully developed speckle suffer from large estimation bias and variance. The bias and the variance can be improved by performing the estimation on a very large amount of data.

In the final part, a deconvolution technique designed specifically for ultrasound tissue characterization has been analyzed. Extensive testing has shown it to not be sufficiently robust for clinical applications, since the deconvolved images are not reliable in terms of fidelity to the original reflectivity of the medium.

Résumé

L'objectif de la caractérisation des tissus par ultrasons ou ‘Quantitative Ultrasound (QUS)’ est de différencier les tissus pathologiques en associant les paramètres d’un modèle aux caractéristiques physiques du tissu. L'usage exclusif des ultrasons pour obtenir un diagnostic peut garantir que le patient ne subira pas une procédure invasive (e.g. une biopsie), utilisant des rayonnements ionisants (e.g. la tomographie) ou même inconfortable et coûteuse (e.g. IRM). Les méthodes de QUS extraient des informations sur la microstructure du tissu à partir du contenu spectral ou temporel des signaux ultrasonores. Le signal temporel radiofréquence (RF) et son enveloppe sont d'intérêt à cause du speckle crée par l’interférence des ondes, qui peut être modélisé par des distributions statistiques.

Ce travail propose d'explorer la possibilité d'obtenir des estimations QUS fiables en utilisant des distributions statistiques comme modèles pour le speckle ultrasonore. Les estimations sont constituées des paramètres des distributions respectives et dépendent de la densité de diffuseurs dans le milieu. L’évaluation s’effectue sur des images simulées, des fantômes de particules et des biofantômes.

Dans la première partie, la distribution Gaussienne Généralisée est utilisée pour modéliser le signal RF, et la distribution de Nakagami est utilisée pour modéliser son enveloppe. Les deux distributions sont limitées à discriminer les milieux avec une faible densité de diffuseurs, parce que les valeurs de leurs paramètres de forme saturent pour un speckle pleinement développé. Par conséquent, puisque la formation du speckle pleinement développé dépend de la résolution du système d'imagerie, la caractérisation peut se faire seulement à de très hautes résolutions, correspondant à des hautes fréquences qui ne sont pas communes en échographie clinique. Une application du modèle de Nakagami sur l’image crée par la seconde harmonique montre le potentiel du paramètre de forme de Nakagami en tant que mesure de la nonlinéarité du milieu.

Dans la deuxième partie, l'enveloppe a été modélisée en utilisant la distribution K-Homodyne. Le paramètre de regroupement des diffuseurs α permet de discriminer entre les milieux denses jusqu’à une limite supérieure à celle du paramètre de Nakagami. Pourtant, cette limite est difficile à estimer avec précision, parce que les valeurs caractéristiques pour le speckle pleinement développé sont affectées par un biais et une variance élevés. Le biais et la variance peuvent être améliorés en augmentant la quantité de données utilisée pour l’estimation.

Dans la dernière partie, une technique de déconvolution spécialement conçue pour la caractérisation des tissus a été évaluée. Des essais exhaustifs ont montré qu’elle n’est pas suffisamment robuste pour une application clinique, puisque les images déconvoluées ne sont pas fidèles à la réflectivité originale du milieu.

CONTENTS

1 INTRODUCTION

A specific category of pathologies, mainly benign and malignant tumors, produce histological changes in the underlying structure of the affected tissue: specifically the size, concentration and arrangement of the cells. At a cytological level, modifications of inner cell structures are also encountered. Typically, the diagnostic of such lesions is performed with the help of needle, excisional, endoscopic, laparoscopic or even laparotomic biopsies – here listed in increasing order of invasiveness. The extracted tissue sample is then analyzed by pathologists in order to deliver an exact result, as the structure of most such pathological tissues is well known.

Obviously, patients who are suffering from these pathologies would benefit from a non-invasive diagnostic technique that can offer similar reliability. Ultrasonic imaging allows the exploration of the human body without the risk on ionizing effects. However, relatively poor resolution (when performing an examination on structures located as a significant depth) and the low signal-to-noise ratio due to the effect of speckle noise are non-negligible drawbacks. Mitigation of these effects is also a subject for research. Tumor growths can be detected in the majority of cases during a classical ultrasound examination, but the nature of the tumor is usually impossible to determine. Therefore, different other techniques are used with the purpose of obtaining a more precise description of the pathology. These methods are grouped under the name of ultrasound tissue characterization (also called Quantitative Ultrasound - QUS). QUS is in development since the 1980's and uses spectral analysis and statistical analysis applied on the non-compressed RF ultrasound echo or echo envelope in order to estimate model parameters which can be associated to physical properties of the tissues (scatterer size, concentration, properties of the surrounding medium such as impedance contrast). A review of these techniques is included in the following chapter.

QUS estimates are often system-dependent. It is preferable to perform the analysis at high frequencies, because of the gain in bandwidth and resolution. Because of the small size of the reflectors (the smallest cells measure only a few microns), low frequencies do not offer the desired level of detail. Even at sub-resolution scale, the theory connects the reflector size to wavelength size and imposes certain limitations. The choice of the frequency range depends on the application, because of the depth-resolution compromise of ultrasound imaging. An interesting option for increased bandwidth at relatively low frequencies is offered by CMUTs (Capacitive Micromachined Ultrasound Transducers), a relatively new technology by comparison to the piezoelectric transducers used in clinical ultrasound (common name: PZT, short for lead zirconium titanate, the material used to fabricate them).

A schematic of the main building blocks of ultrasound tissue characterization, with emphasis on the elements tackled in this thesis, is presented in Figure 1.1. The research conducted here is focused on the speckle statistics. Based on the random walk theory, ultrasound speckle amplitudes can be modeled by a number of statistical distributions. The parameters that define

these distributions depend on the number of scatterers in the medium and on the backscattered energy. The quality of the estimates depends on the model, estimation methods, and available amount of data. In order to evaluate this, testing must be conducted on media with different scatterer densities. Deconvolution can be applied to the RF image prior to the statistical analysis,

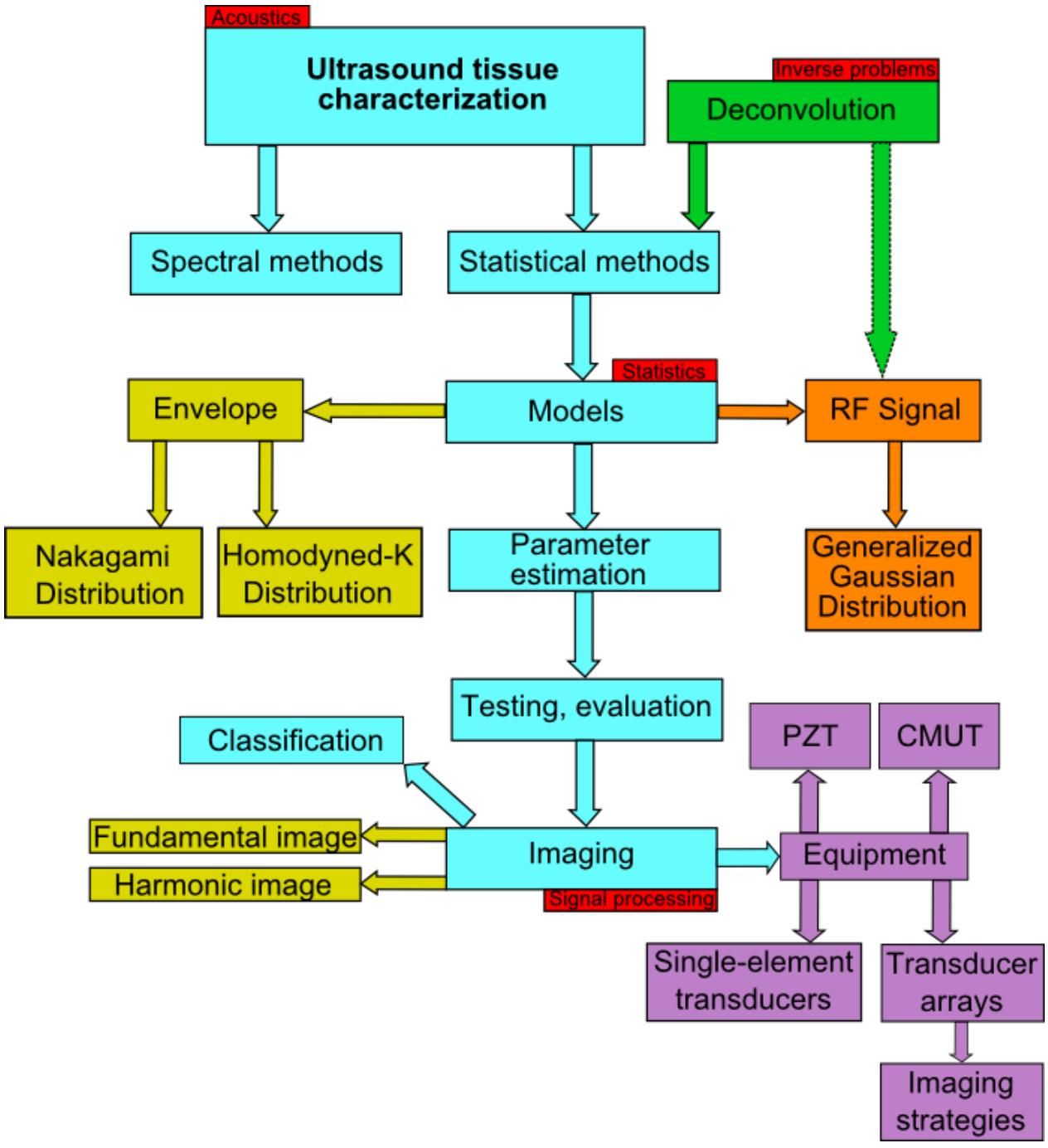

Figure 1.1 Schematic overview of the topics approached in this thesis

in an attempt to recover the original scatterer distribution (reflectivity) of the tissue. The statistical estimates can be computed on the fundamental or harmonic image. Upon concluding on the reliability of the estimates, they can be used as features for classification. Statistics can be applied on images obtained with different imaging modalities and equipment, depending on the necessities.

The work described in this thesis is dedicated to the further exploitation of speckle statistics, in order to assess the applicability and discriminant power of different statistical models for the radiofrequency (RF) signal and its envelope (with emphasis on the Nakagami and Homodyned-K distributions) when dealing with homogenous monodisperse media. In medical applications, this corresponds to focusing on a homogenous portion of an organ in order to assess the density of the scatterers that compose it. A change in scatter density, often together with a change in scatterer size, can be an indicator of the presence and/or progress of certain pathologies (for example liver fibrosis). Statistical models are often delicate to work with, particularly when attempting to characterize very dense media where the speckle structure (named fully developed speckle) shows very small differences between the different concentrations. Some models are limited to partially developed speckle conditions (referring mainly to the Nakagami distribution), while others can still discriminate fully developed speckle in certain conditions (the Homodyned-K distribution).

This introduction is followed by a chapter which summarizes the history and state-of-the-art methods for tissue characterization, as well as a description of the statistical models used for this purpose throughout the years. The third chapter focuses on the analysis using the Generalized Gaussian and Nakagami distributions, with emphasis on the effects of the imaging parameters, on both the fundamental and harmonic image. The fourth chapter comprises a study that assesses the conditions in which the Homodyned-K distribution delivers reliable estimates. The fifth chapter resumes results obtained when applying a deconvolution technique as a pre-processing step prior to the statistical analysis.

2 STATE OF THE ART IN ULTRASOUND TISSUE CHARACTERIZATION

Ultrasound soft tissue characterization has been developing for several decades. From the oldest concepts dating from the 1970's to the current clinical applications, a multitude of qualitative and quantitative methods have been developed with the purpose of extracting information on tissue microstructure (the ensemble of sub-wavelength scattering structures termed simply as scatterers or reflectors) from the ultrasound signal. Some of these exploit the frequency spectrum of the backscattered signal, while the others focus on the spatial structure and statistical properties of the ultrasound speckle generated by scattering within the tissue. This section presents a brief history of ultrasound tissue characterization and a review of the main concepts used into this field.

It is worth noting that the scatterers who are the focus of ultrasound tissue characterization are not precisely identified. Considering the basics of ultrasound physics, reflexion occurs at the boundary of two areas with a strong impedance contrast, so we generally assume that the scatterers are those structures whose acoustic impedance is different from that of the surrounding medium. Although initially hypothesized that these would be the cell nuclei, some studies on biophantoms (Franceschini et al. 2014) and blood (Franceschini, Yu, and Cloutier 2008b) concluded that the scatterers are most probably the whole cells. Of course, in a complex tissue containing different cells with different acoustic properties, large specular reflectors, or aggregates such as in the case of blood, the problem becomes more complicated.

2.1 SPECTRAL ANALYSIS

Chronologically, the first methods are the ones who exploit the frequency spectrum. Holasek, Purnell and Sokollu (Holasek et al. 1975) published their ideas on the possibility of analyzing the tissue response to ultrasound excitations in different frequency bandwidths, terming the method Spectra-Color Ultrasonography. Even if the extracted information was almost impossible to quantify with the then-available technology, their work inspired other researchers to follow into their steps as technology progressed.

In the same decade, Fred Lizzi, one of the pioneers of the field, was working on ultrasound therapy in collaboration with an ophthalmologist named D. Jackson Coleman. After establishing the safe ultrasound doses which can be applied for both therapy and diagnostic, they proceeded to the validation of spectral measurements on ocular tissue for the purpose of differentiating ocular tumors. Some of their results have been published in (Coleman and Lizzi 1983) and (Coleman et

al. 1985). In 1983, F. Lizzi publishes a comprehensive framework for the spectral analysis of ultrasound echo (Lizzi et al. 1983), followed by (Lizzi et al. 1987), describing the theoretical procedure and experimental measures used for spectral tissue characterization. The importance of using calibrated power spectra is underlined, as it mitigates the effects of the imaging system on the acquired data. Furthermore, the acquired spectrum depends on the tissue microstructure, beam directivity, and the local gating function. At an analytical level, each influence translates into a spatial autocorrelation function: of the relative impedance between scatterers and the surrounding medium, of the beam directivity function and of the gating function, respectively. For the tissue microstructure, a number of three scattering models (each characterized by a spatial autocorrelation function) are described and applied for comparison: the sphere model, the Gaussian model and the exponential model. In order to associate tissue features to measured ultrasound characteristics, spectral features such as the spectral slope, intercept and mid-band fit are computed for each case. Having delivered numerical results characteristic for tissue features instead of simple measurements, the method constituted the basis for quantitative ultrasound (QUS).

A more comprehensive theoretical description of ultrasound scattering by sub-wavelength structures is presented in (Insana et al. 1989). Additionally, test results on the application of three scattering models (fluid sphere, Gaussian and Faran) show a good agreement with the theory in the case of ka values inferior to 1 (where k is the wavenumber and a is the average scatterer diameter, as the medium is assumed to be monodisperse). If the propagation medium supports shear wave propagation, the Faran model is adequate because shear waves are taken into account. This is an important aspect because according to current knowledge on the scattering properties of biological tissues, collagen is responsible for most of the scattering and generates significant amounts of shear waves.

Another notable application of linear regression parameters (spectral slope, intercept and mid-band fit) is an in-vitro high-frequency characterization of cell apoptosis. This is interesting because of its potential to track the progress of cytostatic treatments. The phenomenon has been explored in (Czarnota et al. 1999), (Kolios et al. 2002), (Banihashemi et al. 2008), (Sannachi et al. 2014). The conclusions were that the spectral slope and mid-band fit (the value of the regression line at central frequency) tend to increase as scatterer size decreases during apoptosis. More recently, a follow-up of these studies assessed the same properties in-vivo and showed a clear differentiation between the estimates in the case of patients who are responsive versus those who are nonresponsive to cytostatic cancer treatments (Sannachi et al. 2014).

The progress of QUS using spectral estimates is conditioned by multiple issues, the main one being the measurement and model fitting of the backscatter coefficient (BSC). The BSC is defined as the time-averaged scattered intensity in the backward direction per unit solid angle per unit volume, normalized by time-averaged incident intensity ($cm^{-1}Sr^{-1}$) (Ghoshal et al. 2013) and is a fundamental property of tissue microstructure. It depends essentially on frequency and a form factor describing variations in the scattering properties of the medium as a function of frequency

and scatterer properties. The form factor was otherwise defined as the ratio of the scattering cross-section for a finite-sized scatterer to that for a point scatterer (Chen et al. 1998).

The reference method for measuring the backscatter coefficient is described in (Insana and Hall 1990): a broadband substitution technique using a weakly-focused transducer when the gated sample volume is placed near the radius of curvature of the transducer. The measured spectrum is compared to that of a reference medium, and attenuation coefficient measurements are included. Estimates of the scatterer properties are obtained by comparing the measured and theoretical backscattering coefficients. An in-vivo validation of the backscatter techniques on rat mammary tumors is presented in (Topp, Zachary, and O'Brien 2001), with measurements of the backscattering slope. In (Oelze, Zachary, and O'Brien 2002) and (Oelze, Zachary, and O'Brien 2002b), it is shown that scatterer diameter estimates successfully discriminate between tumors and surrounding tissue in parametric images, and in (Oelze et al. 2004), (Oelze and O'Brien 2006) and (Oelze and Zachary 2006) scatterer diameter and concentration discriminate between fibroadenomas and carcinomas. (Kanzler and Oelze 2008) proposed a coded excitation and pulse compression technique to improve the eSNR (echo signal to noise ratio) and subsequently the bias of the scatterer size estimates. More recently, the analysis of the actual scatterer size distribution in studies such as (Lavarello and Oelze 2010) highlights the need to include the assumption of polydispersity in the scattering models.

A phenomenon that has a strong effect in ultrasound imaging is attenuation. Just like speckle, can be seen both as a negative effect that needs to be compensated for, and as a useful physical property which offers information on the medium. Attenuation compensation is always applied, mainly because of its non-negligible effect at the typical high frequencies used in tissue characterization. The attenuation compensation functions used for this purpose need to take into account the exponential decrease in amplitude as a function of propagation distance and the linear dependency of the attenuation coefficient on frequency. The simplest form is called point attenuation (Oelze and O'Brien 2002). Other attenuation-compensation functions have been proposed, which also take into account the gate length (O'Donnel and Miller 1981), the value of the attenuation coefficient and the gate length (Oelze and O'Brien 2002), and even the window function and beam pattern (Bigelow and O'Brien 2004). On the other hand, attenuation imaging (Jirijk, Taxt, and Jan 2004) is a form of parametric imaging which can highlight additional features compared to classical B-mode images. Measurement have also been performed in-vivo (Oosterveld et al. 1991).

Regarding the various form factors, other studies have been conducted on rat tumors (Hafez et al. 2009) and blood: (Franceschini, Yu, and Cloutier 2008a) , (Franceschini, Yu, and Cloutier 2008b). In (Franceschini, Yu, and Cloutier 2008a) and (Franceschini, Yu, and Cloutier 2008b), a simultaneous estimation of the scatterer diameter and attenuation is proposed. These works also mark the beginning of the implementation of the structure factor model (SFM) (Yu and Cloutier 2007) for ultrasound spectral tissue characterization. Further validations of the SFM have been made in (Saha, Franceschini, and Cloutier 2011), (Franceschini, Metzger, and Cloutier 2011). The structure factor model and its low-frequency limit approximation, the packing factor, can

best describe the decrease in backscattered power with the increase in spatial correlation among particles with increasing particle crowding. The packing factor can be seen as a correction factor that accounts for increasing destructive phase interference (coherent field) introduced by the increase in correlation between particles at high concentrations. Additionally, in comparison with the Gauss, Faran and Particle models, it allows a better estimation of scatterer size and concentration (Franceschini and Guillermin 2012). A compound SFM for polydisperse media is validated in (Franceschini et al. 2014) and (Han et al. 2015).

Scatterer size imaging was also implemented for ultrasound tomography by (Lavarello et al. 2009). (Teisseire et al. 2010) have introduced the concentric sphere scattering model into QUS, together with a cell pellet biophantoms technique. A good agreement between theory and measurements showed that both tools can be practical in the study of backscattered spectra.

Regarding other types of methods, the Urbana team (Oelze, Zachary, and O'Brien) also attempted tissue characterization with the help of acoustic impedance maps, in (Mamou, Oelze, and Zachary 2005) and (Mamou et al. 2008). The impedance map of a tissue phantom is built with the help of a light microscope. This is a complicated process, but the scatterer size estimates are accurate and consistent with the histological data.

2.2 STATISTICAL ANALYSIS OF ULTRASOUND SPECKLE

The second category of methods exploits the speckle pattern generated by the spatial distribution of the reflectors within the insonified medium. Speckle is the result of the interference between waves having the same frequency but different amplitudes and phases, so that its amplitudes and phases of the result vary randomly. Therefore, it can be modeled as a random walk. This assumption constitutes the basis for the development of statistical models for ultrasound speckle.

Speckle formation and some interesting properties are described in (Goodman 1976). Speckle is characteristic to all types of coherent imagery: radar astronomy, synthetic-aperture radar, acoustical imagery. Moreover, analogous statistical phenomena appear in radio-wave propagation, temporal statistics of incoherent light, the theory of narrowband electrical noise, and the general theory of spectral analysis of random processes. A notable observation is that, in any speckle pattern, large-scale size fluctuations are the most populous, and no scale sizes are present beyond a certain small-size cutoff. The distribution of scale sizes in between these limits depends on the autocorrelation function of the object radiance distribution, and on the autocorrelation function of the point spread function of the imaging system. The statistical nature of speckle is also discussed, together with the basic assumptions that are applied when deriving statistical models. It is necessary to mention that the statistical models (or distributions) presented here are used to model the statistics of the echo envelope. The phase information contained in the

radiofrequency (RF) signal is generally considered as not of interest, since the phase is uniformly distributed.

Statistical modelling for ultrasound speckle has relied for a long time on the Rayleigh distribution (Burckhardt 1978), (Wagner et al. 1983). This is a valid model for the case where the insonified resolution cell contains a large number of sub-resolvable scatterers. This "large" number has been subject to some research (for example in (Tuthill, Sperry, and Parker 1988)) before convening to approximately 10 (Rao, Mehra, and Zhu 1990), (Thijssen 2003). A speckle pattern with a Rayleigh distribution is equivalent to fully developed speckle. A speckle pattern produced by a number of scatterers per resolution cell which is inferior to 10 is called partially developed or having pre-Rayleigh statistics. An interesting study based on Rayleigh statistics (Dantas, Costa, and Leeman 2005) showed how equivalent images with equivalent speckle patterns can be produced by using a large number of randomly placed scatterers or a small number of periodic scatterers.

In (Tuthill, Sperry, and Parker 1988), we also encounter the first mention of the Rice distribution in this context. The Rice distribution takes into consideration the presence of a coherent component in the backscattered echo, stemming from specular reflections or echoes produced by periodic scatterers. The resulting speckle is termed post-Rayleigh.

It has been suggested by Jakeman in (Jakeman and Pusey 1976), (Jakeman 1980) that the number of steps in the random walk model can itself be modeled as a random variable following a negative binomial law. This can account for scatterer number fluctuations in the random walk model, especially when then resolution cell contains a low number of scatterers (Shankar 1995). Under this assumption, the K-distribution has been introduced for use in low-density media (Dutt and Greenleaf 1995), (Shankar 1995).

The Nakagami distribution has been used extensively, after being introduced into the field by P.M. Shankar, in (Shankar 2000). It was shown to be useful in the classification of breast masses in (Shankar et al. 2001),(Shankar et al. 2003) (Tsui et al. 2008) and liver fibrosis in (Ho et al. 2012). The simplicity of the model and estimation of its parameters was perhaps what attracted a lot of research teams. The Nakagami parameters have been also used in elastography (Tsui et al. 2013), fetal imaging (Namburete, Rahmatullah, and Noble 2013), segmentation (Destrempes et al. 2009) and 3D ultrasound imaging (Tsui et al. 2010). Studies have been conducted for the assessment of the effects of transducer characteristics (Tsui and Wang 2004), noise (Tsui, Yes, and Yang 2008), logarithmic compression (Tsui, Huang, and Wang 2006) and statistical estimators (Tsui et al. 2015) on Nakagami imaging. In this period, the number of publications on tissue characterization using statistics started occupying a greater proportion of the tissue characterization literature, after a long period when spectral analysis took the most part.

The model that is considered to be the most complete and comprehensive for ultrasound speckle is represented by the Homodyned-K distribution. Its first mention into tissue characterization literature is in (Dutt and Greenleaf 1994), based on the theory presented in (Jakeman and Tough 1987). Multiparameter classification has showed the applicability of the

Homodyned-K distribution model into the characterization of lymph nodes ex-vivo (Mamou et al. 2011), and breast tumors in-vivo (Oelze, O'Brien, and Zachary 2007), (Trop et al. 2014).

Developing estimators for the parameters of complex distributions is often a nontrivial task. When the classical methods of moments or maximum likelihood deliver estimates with high biases, or have no closed form expressions, the estimate is frequently found by means of optimization techniques. For example, a reliable estimation technique for the Nakagami parameter is integrating the maximum likelihood estimates into an iterative method. Concerning the Homodyned-K distribution, two state-of-the art estimators exist: one is based on the SNR, skewness and kurtosis, presented in (Hruska and Oelze 2009), and the more recent "XU" estimator (Destrempes, Porée, and Cloutier 2013) is based on the mean intensity and two log-moments of the distribution.

Other models have been proposed in order to account for different factors, for example the general Nakagami model for the tails of the distributions, in (Shankar 2001), or the inverse Rician distribution to make it possible to implement speckle filters, by (Eltoft 2006). A comprehensive model that would theoretically take into consideration the effect of multiple scattering, the compound Nakagami distribution, is proposed in (Shankar et al. 2005). The results of a study exploring multiple statistical models for the purpose of detecting metastases in dissected human lymph nodes (mostly obeying pre-Rayleigh conditions), are published in (Bui et al. 2014).

In conclusion, statistical analysis seems to offer the best performances when combined with spectral QUS in multiparameter approaches. Therefore, it can be seen as a complementary method. The greatest difficulties are encountered when analyzing dense media that generates post-Rayleigh speckle, a problem that has been more or less successfully tackled using the Nakagami and the Homodyned-K distributions (Fang and Tsui 2015), (Mamou et al. 2011).

2.3 STATISTICAL MODELING OF THE ULTRASOUND SPECKLE. THE RANDOM WALK

Ultrasound images are characterized by the presence of speckle, a granular texture resulting from the constructive and destructive interference of waves scattered by structures of sizes smaller than the ultrasound wavelength, and contained within one resolution cell of the ultrasound system. An interesting characteristic of ultrasound speckle is its deterministic nature, as it can be exactly reproduced if the scan is repeated. Moreover, its structure varies from tissue to tissue and is usually specific for each tissue, when a certain scanner is used. This allows the retrieval of more than visual information from an ultrasound scan. The uncompressed RF echo carries information that can be exploited by statistical modeling. Since the phase of the RF signal

is uniformly distributed between $-\pi$ and π, it does not offer additional information and can be discarded, leaving only the envelope.

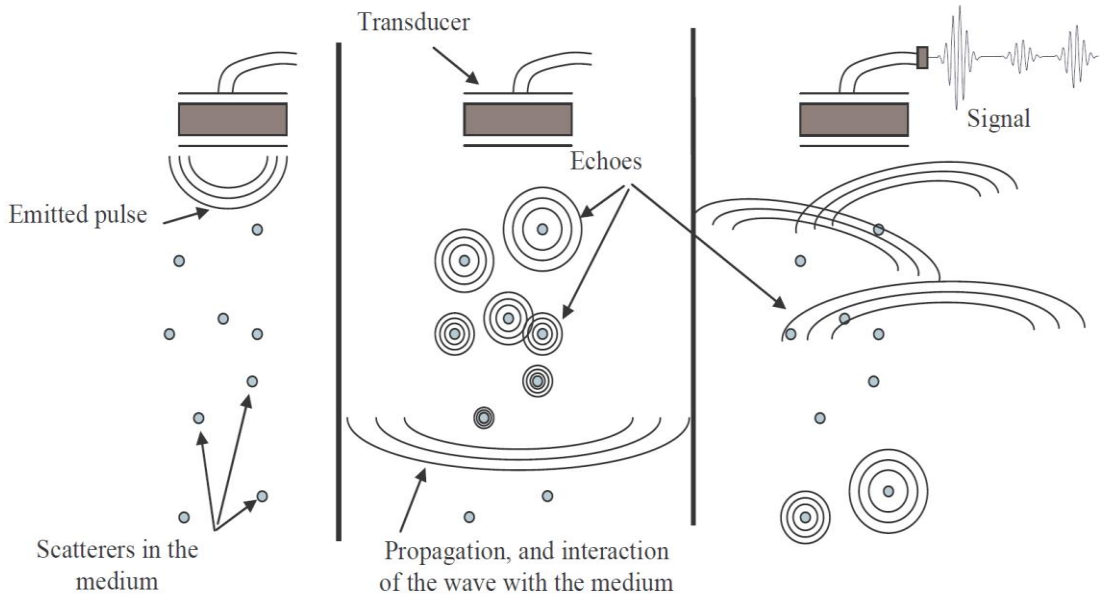

Figure 2.1A schematic of ultrasound imaging and speckle formation: the emitted pulse propagates through the medium, interacting with all the scatterers which in turn produce echoes that interfere during backpropagation (image from (Liebgott 2005)**)**

As the ultrasound RF echo is the result of individual contributions from all the (supposedly randomly placed) reflectors in the insonified medium (Figure 2.1), it can be modeled as a random walk equivalent to a sum of phasors (Burckhardt 1978),(Wagner et al. 1983) due to the random phase variations (from random locations of the scatterers) and random amplitude variations (from random backscatter coefficients of each individual scatterer). The resulting signal is a phasor sum of random amplitude phasors rotating at angular frequency ω_0, with amplitudes x_k and phase shifts θ_k:

$$X = Xe^{jq} = \sum_{i=0}^{N-1} x_i e^{j\theta_i} \qquad (2.1)$$

The phase shifts are uniformly distributed over the interval$[-\pi, \pi]$, and the amplitudes x_k are statistically independent, such that the real and imaginary components of the phasor sum X have zero mean and varianceσ^2.

2.3.1 Statistical models for the radiofrequency signal

The Gaussian model

The simplest model for the ultrasound echo amplitudes is the Gaussian model. Under the assumption that the medium contains a sufficiently large number of reflectors (generating what is known as fully developed speckle), the RF signal can be modeled as a gaussian distribution of zero mean and standard deviation σ, $p_{X_r}(x) \sim \mathrm{N}(0, \sigma^2)$:

$$p_{X_r}(X) = \frac{1}{\sqrt{2\pi\sigma^2}} e^{-\frac{X^2}{2\sigma^2}} \qquad (2.2)$$

Parameter estimation is usually conducted using the maximum likelihood method, which leads back to the classical expression for the variance, over n samples:

$$\sigma^2 = \frac{1}{n}\sum_{i=1}^{n}(X - \overline{X})^2 \qquad (2.3)$$

The K_{RF} model

The K_{RF} model can be derived from the K model for the echo envelope, as the RF signal is the real part of the analytic signal. It can be applied in the same conditions in which the K distribution is applied for the envelope: reduced number of reflectors, meaning partially developed speckle. By integrating the probability density of the analytic signal with respect to its imaginary part ((Bernard, D'hooge, and Friboulet 2006), (Bernard et al. 2007)) we obtain:

$$p_{X_r}(\mathrm{X}) = \frac{2b}{\sqrt{\pi}\Gamma(\gamma)}\left(\frac{b|X|}{2}\right)^{\gamma-0.5} K_{\gamma-0.5}(b|X|) \qquad (2.4)$$

where γ is a shape parameter, b is a scale parameter, and $K_{\gamma-0.5}(\cdot)$ is the modified Bessel function of the second kind. The most precise estimator is considered to be the Blacknell estimator (Blacknell and Tough 2001), according to which the expression for finding the shape parameter is:

$$\frac{E(\mathrm{X}^2\log(|\mathrm{X}|))}{E(|\mathrm{X}|^2)} - E(\log(|\mathrm{X}|)) = 1 + \frac{1}{2\gamma} \qquad (2.5)$$

After the estimation of the shape parameter, the scale parameter can be computed as:

$$b = \sqrt{\frac{2\gamma}{E(X^2)}} \qquad (2.6)$$

According to (Bernard et al. 2007), the measured values of the K-distribution parameter γ in-vivo ranged from 0.2 to 1.3 in the area of the myocardium, and were at least equal to 10 for the fully-developed speckle generated by blood. Different shapes of the pdf are presented in Figure 2.2.

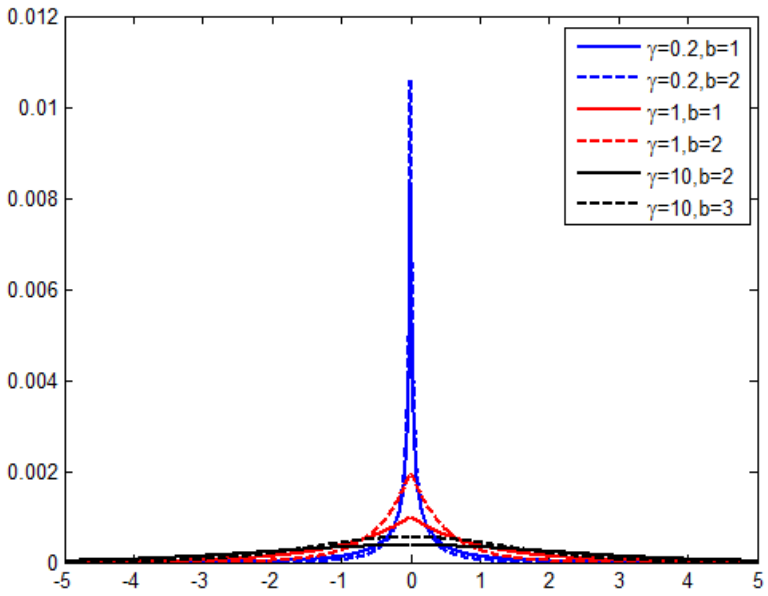

Figure 2.2 K_{rf} probability density functions for different pairs of parameters

The Generalized Gaussian model

The Generalized Gaussian distribution is an approximation of the K_{RF} distribution and has the advantage of a simpler expression, as well as closed form parameter estimates. Its expression is:

$$g_X(X) = \frac{\xi}{2b\Gamma\left(\frac{1}{\xi}\right)} e^{-\left(\frac{|X|}{b}\right)^{\xi}} \qquad (2.7)$$

where $\Gamma(\cdot)$ is the Gamma function, b is the scale parameter and ξ is the shape parameter. This model has already been employed for noise modeling in optical image analysis (Bouman and Sauer 1993),(Moulin and Liu 1998), wavelet coefficient statistical modeling (Mallat 1989) and radar domain(Moser, Zerubia, and Serpico 2006). This noise model is commonly used in

statistical studies since it captures the heavy tailed behavior that is often exhibited by real noise distributions. In ultrasound imaging, the Generalized Gaussian distribution appears as a good candidate to characterize the statistics of the RF signal for both fully and partially developed speckle situations. It is equivalent to the K_{RF} in two situations: when the shape parameter ξ =1, which corresponds to a K_{RF} with shape parameter ν=1 (also to the Laplace distribution), and when ξ =2, which corresponds to a K_{RF} with shape parameter $\nu \to \infty$. For biological tissues, the measured shape parameter is often comprised between the two, so that the quantification of intermediary situations is possible. For example, the shape parameters measured in (Bernard et al. 2007) in the myocardium ranged from 0.6 to 1.2, and in the blood from 1.5 to 1.9. The shape parameter can be calculated by integrating its maximum likelihood expression:

$$g(\xi_i) = 1 + \frac{\Psi\left(\frac{1}{\xi_{i-1}}\right)}{\xi_{i-1}} - \frac{\sum_{j=1}^{N}\left(\left|x_j-\mu\right|^{\xi_{i-1}} log\left|x_j-\mu\right|\right)}{\sum_{j=1}^{N}\left|x_j-\mu\right|^{\xi_{i-1}}} + \frac{\log\left(\frac{\xi_{i-1}}{N}\sum_{i=1}^{N}\left|x_i-\mu\right|^{\xi_{i-1}}\right)}{\xi_{i-1}} \qquad (2.8)$$

where ξ_i is the shape parameter estimated at each iteration, μ is the mean value of the samples x_i, N is the sample number and $\Psi(\cdot)$ is the digamma function, in a Newton-Rhapson iterative scheme. The scale parameter is then estimated as:

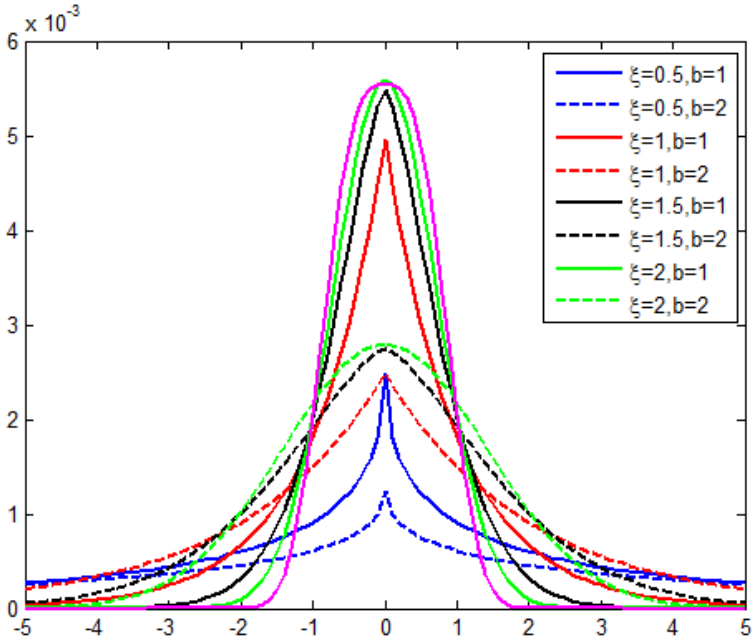

Figure 2.3 Generalized Gaussian probability density functions for different parameter pairs

$$\alpha = \left(\frac{\xi}{N} \sum_{i=1}^{N} \left| x_i - \mu \right|^{\xi} \right)^{\frac{1}{\xi}} \qquad (2.9)$$

Different speckle structures are defined by the shape parameter. The effect of the scale parameter is to distribute the values over a greater range, as can be seen in Figure 2.3.

2.3.2 Statistical models for the echo envelope

The Rayleigh model

Under the same assumptions made for the Gaussian-distributed RF echo, the corresponding signal envelope can be computed as the amplitude of the complex phasor X, whose real and imaginary parts X_r and X_i follow a gaussian distribution with the same parameters$\sim N(0, \sigma^2)$, so that their joint probability distribution is:

$$p_{X_r, X_i}(x) = \frac{1}{\sqrt{2\pi\sigma^2}} e^{-\frac{X_r^2 + X_i^2}{2\sigma^2}} \qquad (2.10)$$

A change of coordinates from rectilinear to polar, $X = \sqrt{X_r^2 + X_i^2}$ and $\phi = tan^{-1} \frac{X_r}{X_i}$ will result in the density function in polar coordinates as:

$$p_{X\phi}(X, \phi) = \frac{X}{2\pi\sigma^2} e^{-\frac{X^2}{2\sigma^2}}, X \geq 0 \qquad (2.11)$$

The probability distribution of the amplitudes is the marginal density:

$$p_X(X) = \int_{-\pi}^{\pi} p_{X\phi}(X, \phi) d\phi \qquad (2.12)$$

which evaluates to

$$p_X(X) = \frac{X}{\sigma^2} e^{-\frac{X^2}{2\sigma^2}} \qquad (2.13)$$

respectively $p_X(X) \sim Rayleigh(\sigma)$. Examples of Rayleigh pdfs with different standard deviations σ are shown in Figure 2.4. The maximum likelihood estimate for the variance is:

$$\sigma^2 = \frac{1}{2n}\sum_{i=1}^{n} y_i^2 \qquad (2.14)$$

The Rice model

If a coherent component s (of constant amplitude, a result of reflections from periodically unresolved scatterers or specular reflection) is included in our random walk model, the revisited phasor sum will have the following expression:

$$X = s + \sum_{i=0}^{N\text{-}1} x_i e^{j\theta_i} \qquad (2.15)$$

The addition of a randomly phased but constant amplitude step s is called homodyning (Jakeman 1980), and it is also applied in the derivation of the Homodyned-K distribution. Therefore the joint density function of the real and imaginary parts of X will be:

$$p_{X_r,X_i}(x) = \frac{1}{\sqrt{2\pi\sigma^2}} e^{-\frac{(X_r+s)^2+X_i^2}{2\sigma^2}} \qquad (2.16)$$

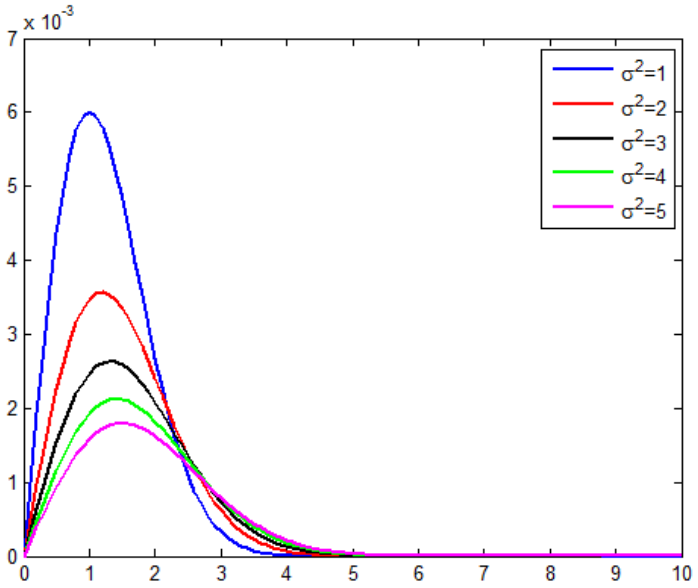

Figure 2.4 Rayleigh probability density functions for different values of the variance

Here, in the case of speckle that obeys gaussian statistics, the envelope (the amplitude X) follows the Rice distribution, whose probability density function is given by:

$$p_X(X) = \frac{X}{\sigma^2} e^{-\frac{X^2+s^2}{2\sigma^2}} I_0\left(\frac{sX}{\sigma^2}\right) \qquad (2.17)$$

where I_0 is the modified Bessel function of the first kind of order zero. This was the first model used for media with a high density of scatterers which produce coherent reflections due to the presence of a specular reflection or periodically spaced scatterers. Parameter estimation is done using the method of moments:

$$s^2 = \sqrt{2E^2[A^2] - E[A^4]}$$
$$\sigma^2 = E[A^2] - \hat{s}^2 \qquad (2.18)$$

Different pdfs corresponding to different values of the variance and coherent component are represented in Figure 2.5.

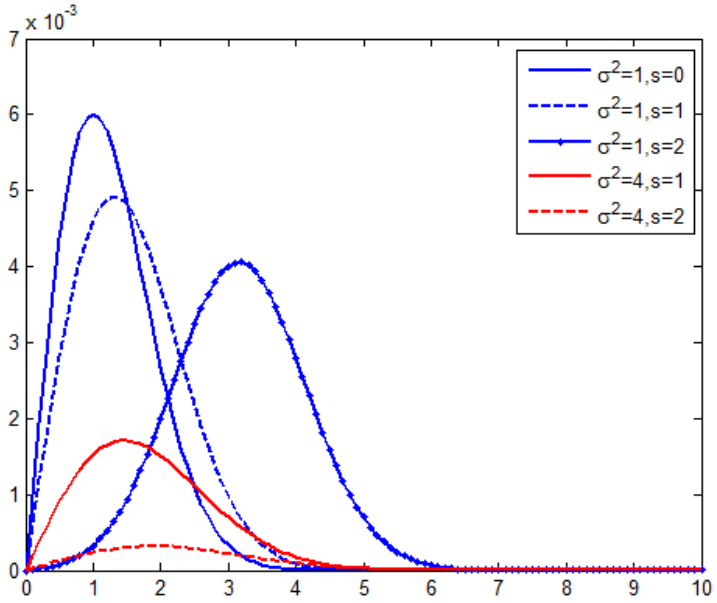

Figure 2.5 Rice probability density functions for different pairs of parameters

The K model

The K-distribution was introduced in medical ultrasound in (Shankar et al. 1993). The model is appropriate for media with a low number of scatterers, case in which the central limit theorem does not apply (as opposed to the Rayleigh and rice models). The number of steps in the random walk is considered finite and variable, and it follows a negative binomial distribution $N \sim NegBin(\alpha, 1/(1+\bar{N}/\alpha))$, with $\bar{N}$ the mean number of steps and α the effective number of

steps, equivalent to the effective number of scatterers in the medium. The probability density of the K distribution is, according to (Shankar et al. 2003):

$$p_A(X) = \frac{2b}{\Gamma(\gamma)}\left(\frac{bX}{2}\right)^{\gamma} K_{\gamma-1}(bX) \qquad (2.19)$$

where $\Gamma(\cdot)$ is the Gamma function, $K_{\gamma-1}(\cdot)$ is the modified Bessel function of the second kind, γ is a shape parameter and b is a scale parameter. As in the case of the K_{RF} model, the best estimator is considered to be the Blacknell estimator:

$$\frac{E(\mathrm{Xlog(X)})}{E(\mathrm{X})} - E(\mathrm{log(X)}) = \frac{1}{2}\left(1+\frac{1}{\gamma}\right) \qquad (2.20)$$

$$b = \sqrt{\frac{2\gamma}{E(\mathrm{X}^2)}} \qquad (2.21)$$

The model's effectiveness decreases as the number of scatterers increases, making it useful only for media which qualify as pre-Rayleigh. Figure 2.6 shows how the parameters influence the shape of the pdf.

The Homodyned-K model

The Homodyned-K is considered to be the most complete and complex distribution in ultrasound speckle modeling. It takes into consideration the presence of the coherent component, as well as the negative binomial distribution of the number of steps in the random walk. Its probability density function is:

$$p_A(\mathrm{A}) = \mathrm{A}\int_0^{\infty} xJ_0(\varepsilon x)J_0(\mathrm{A}x)\left(1+\frac{x^2\sigma^2}{2}\right)^{-\alpha} dx \qquad (2.22)$$

with α the scatterer clustering parameter, ε^2 the mean power of the coherent component, and $2\alpha\sigma^2$ the mean power of the diffuse component. The pdf can also be written in compound form, as a Rice distribution with the diffuse signal component modulated by a Gamma distribution:

$$p_A(\mathrm{A}) = \int_0^{\infty} p_{Ri}(\mathrm{A}\,|\,\varepsilon,\sigma^2\,\mathrm{w})\,\mathrm{G}(w\,|\,\alpha,1)dw \qquad (2.23)$$

Parameter estimation for the Homodyned-K is not trivial, with a number of methods published in the last decade (Hruska and Oelze 2009),(Destrempes, Porée, and Cloutier 2013) , out of which the most recent one will be also used in this work.

Figure 2.7 presents different pdf shapes. A shape parameter greater than 10 does not have a big influence on the shape of the pdf. This normally designates the fully developed speckle regime.

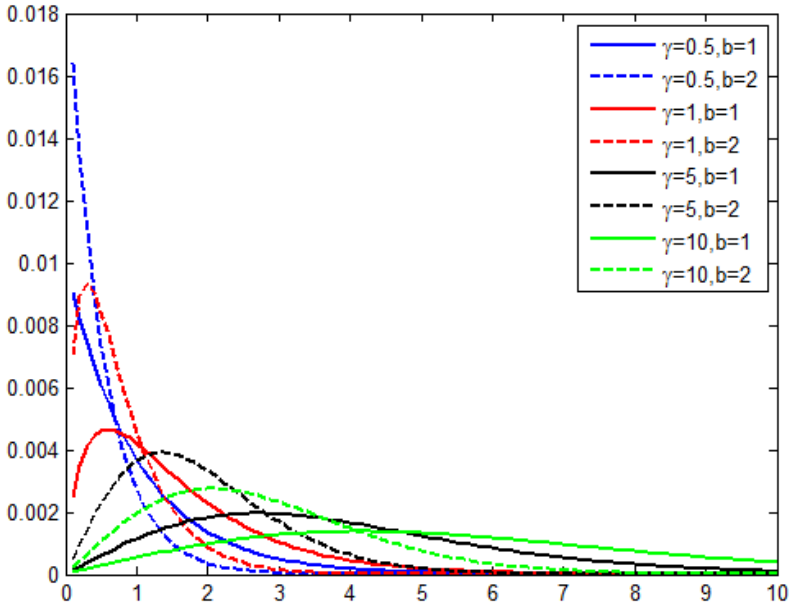

Figure 2.6 K probability density functions for different pairs of parameters

The Nakagami model

An approximation of the Homodyned-K distribution, the Nakagami has the following probability density function:

$$p_X(\mathrm{X}) = \frac{2m^m}{\Gamma(m)\Omega^m} x^{2m-1} \exp\left(-\frac{m}{\Omega}x^2\right) \qquad (2.24)$$

with m (alternative notation: μ) being the shape parameter and Ω the scale parameter. The parameters can be estimated by the method of moments, with the disadvantage of a high bias for small values of the parameter m. The shape parameter estimate using the method of moments is:

$$m = \frac{E^2(X^2)}{Var(X^2)} \qquad (2.25)$$

Alternatively, and in the present work, estimation can be made by an iterative maximum likelihood, similar to the estimation method for the Generalized Gaussian parameters. The expression to be iterated for the parameter m is:

$$g_i(\mathrm{m}) = \ln(\mathrm{m}) + \ln(\Omega) - \frac{1}{N}\sum_{j=1}^{N}\ln(\mathrm{x}_j^2) + \Psi(\mathrm{m}) \qquad (2.26)$$

The maximum likelihood and the method of moments lead to the same results for the scale parameter Ω, namely the mean value of the square of the samples, equivalent to the signal intensity.

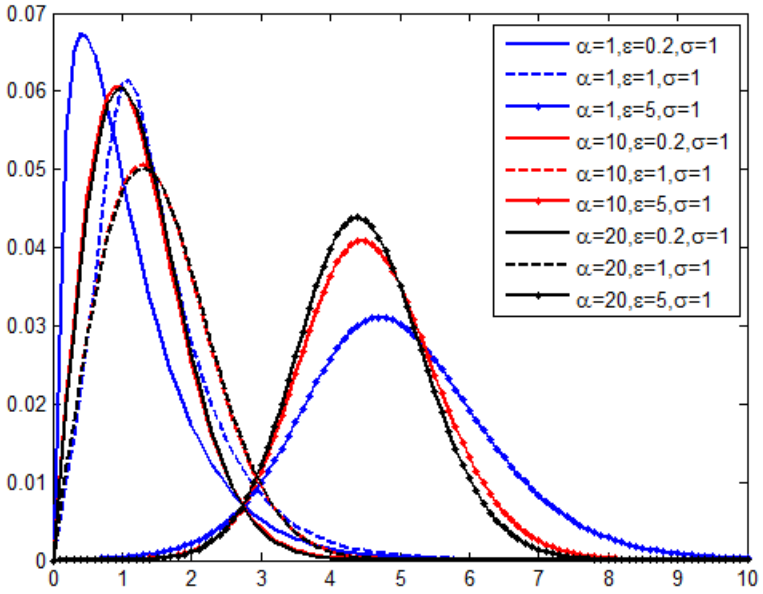

Figure 2.7 Homodyned-K probability density functions for different sets of parameters

2.3.3 Conclusions

Ultrasound speckle can be modeled by a number of statistical distributions, depending on the scatterer density per resolution cell. Certain distributions can be applied for all types of speckle (pre-Rayleigh, Rayleigh, post-Rayleigh), namely the Generalized Gaussian for the RF signal and the Nakagami and Homodyned-K for the RF signal envelope. These models will be evaluated during this work, in different conditions and on various data, in order to assess the advantages and disadvantages of each one.

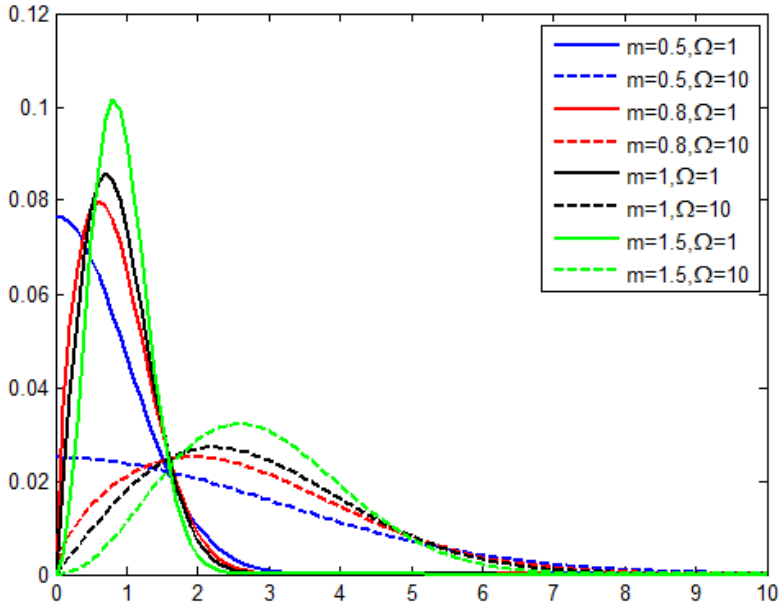

Figure 2.8 Nakagami probability density functions for different pairs of parameters

3 STATISTICS OF THE BACKSCATTERED ECHO USING THE GENERALIZED GAUSSIAN AND NAKAGAMI DISTRIBUTIONS

Although the statistical modeling of ultrasound is focused on the echo envelope, there are certain advantages to modelling the RF signal, the main one being that it allows for the development of image restoration filters. Some models allow for a better fitting of the ultrasound speckle. By using the General Gaussian distribution (GGD), studies have showed that it can provide excellent fits for ultrasound speckle acquired on heart tissue (Bernard et al. 2007), (Bernard, D'hooge, and Friboulet 2006).

Concerning the envelope, The Nakagami distribution for the echo envelope has been used extensively in the past two decades for parametric imaging to help highlight tissue structures that are not visible in B-mode images, and tissue characterization: (Shankar 2000), (P.M. Shankar et al. 2001), (Tsui et al. 2008) (Liao et al. 2012), (Namburete, Rahmatullah, and Noble 2013).

In this chapter, the GGD and the Nakagami distribution are used to fit the speckle amplitudes (RF signal and envelope), in order to assess the scatterer density of a medium in tissue characterization applications.

3.1 DATA PROCESSING PROTOCOL

Selection of the region of interest: The theory on which speckle statistical modelling is based assumes that a certain number of scatterers are present in the insonified resolution cell. Hence, in order to respect this assumption and obtain statistical estimates that can be interpreted as measures of the scatterer concentration, the size of the resolution cell within the analyzed region of interest (ROI) should have a constant size. Ideally, the size should also be minimal. This is valid in the focal zone of the ultrasound transducer. Since we are dealing with statistics, it is advantageous to select the maximum number of samples available in these conditions, in order to obtain non-biased estimates. 2D ROIs defined in the ultrasound scan plane are used.

Signal processing: For each experiment, the statistical analysis is performed on equally sized ROIs selected from the ultrasound echo. The analysis concerns mainly the fundamental image, which offers the best Signal-to-Noise Ratio (SNR), so any harmonics or noise are filtered out. The acquisition system is usually set up such as there are no saturated signals (RF lines), but this is verified post-acquisitions and any saturated signals are removed. The resulting RF image is simply fitted to the Generalized Gaussian distribution. Its envelope is calculated as the absolute

value of the Hilbert Transform of the RF image and then fitted to the Nakagami distribution.

Fitting: Fitting essentially means parameter estimation. Here, this is done by integrating the maximum likelihood expressions into Newton-Rhapson iterations. This is the classical method for the Generalized Gaussian Distribution, according to (Bernard et al. 2007), and it offers minimum bias for the Nakagami distribution. Additionally, the goodness-of-fit is assessed using the Kullback-Leibler Divergence (KLD) between two distributions (here P and Q):

$$D_{KL}(P||Q) = \sum_i P(i) ln \frac{P(i)}{Q(i)} \qquad (3.1)$$

Figures 3.1 and 3.2 show examples of statistical fits for partially and fully developed speckle obtained from data acquired from cell pellet biophantoms (Chapter 4). Typical speckle histograms will show a better fit of the Generalized Gaussian distribution over the RF signal than of the Nakagami distribution over the envelopes. Also, models tend to better fit fully-developed speckle. Using the same data set from Chapter 4, obtained from diluted media as well as concentrated media, we calculated the mean KLD for concentrations ranging from 1% to 30% in volume, equivalent to approximately 3 to 150 in scatterers/resolution cell (Figure 3.3). This set of results is presented in order to show the applicability of the models on data produced by ultrasound acquisitions.

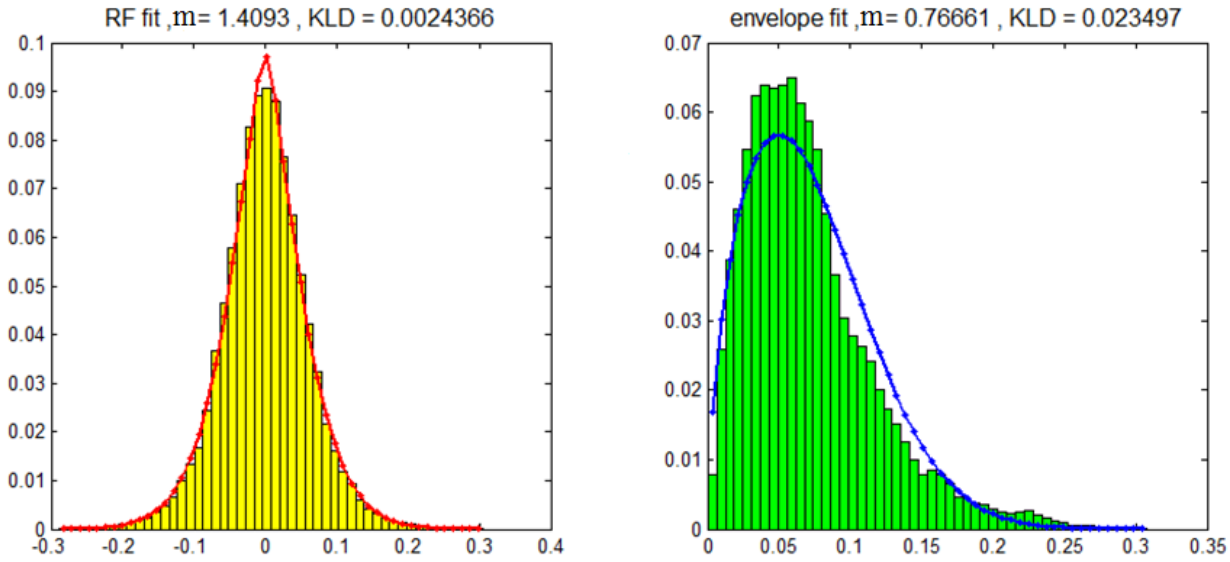

Figure 3.1 Example of histogram fit of partially developed speckle. Acquisition from cell pellet biophantoms: (left) RF image using the Generalized Gaussian distribution (right) envelope using the Nakagami distribution

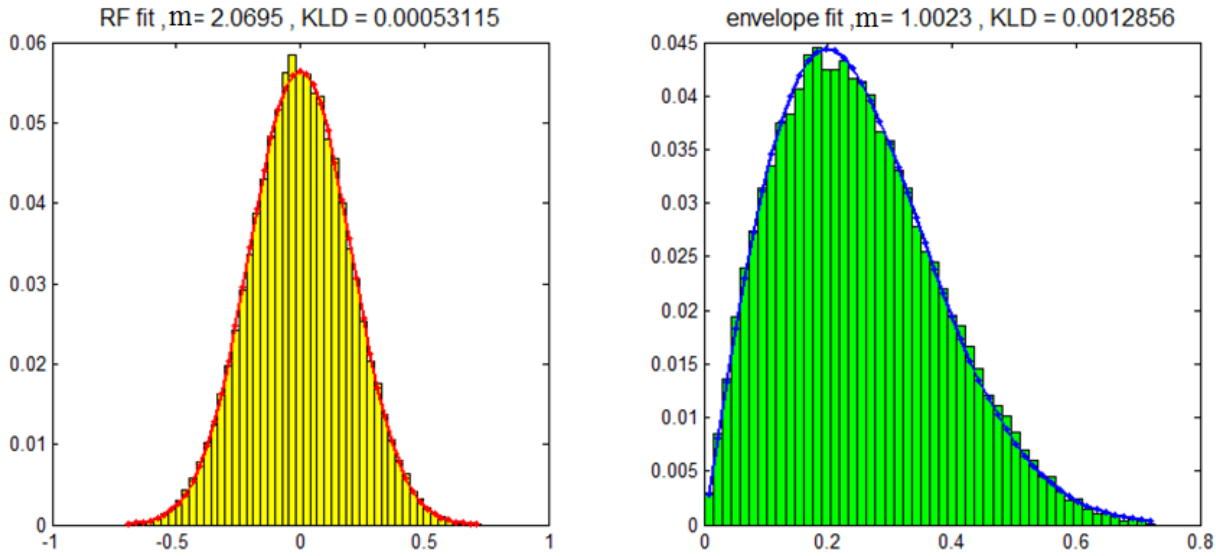

Figure 3.2 Example of histogram fit of fully developed speckle. Acquisition from cell pellet biophantoms: (left) RF image using the Generalized Gaussian distribution (right) envelope using the Nakagami distribution

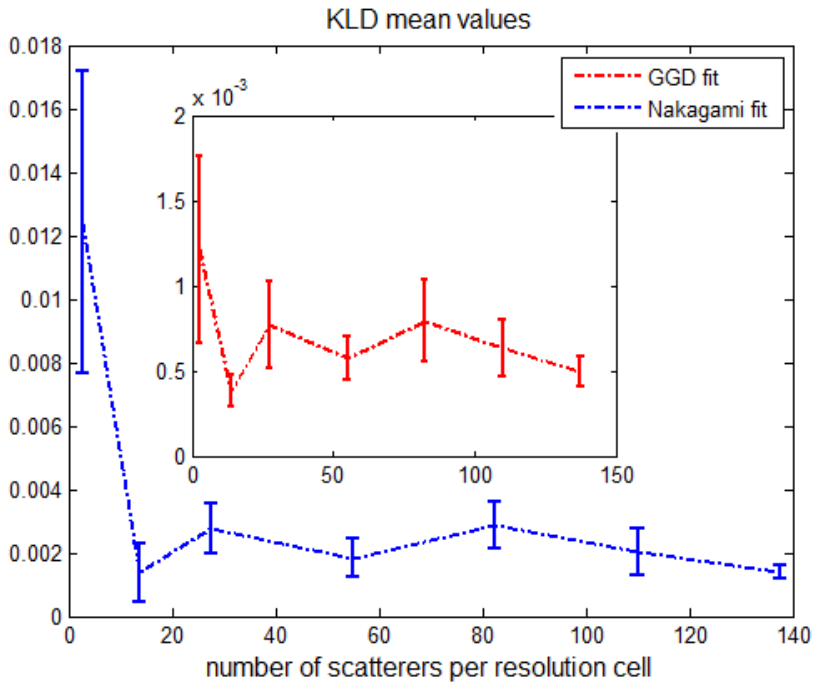

Figure 3.3 Mean values of the Kullback-Leibler divergence between data acquired from cell pellet biophantoms and the respective fits by the Generalized Gaussian Distribution and the Nakagami distribution

3.2 SIMULATION OF ULTRASOUND IMAGES

Simulations were conducted using the ultrasound simulation software CREANUIS (Varray et al. 2013). For this application, the main advantage of CREANUIS over the more classical Field II (Jensen et al. 1996) is the computation speed. As in can be seen in Figures 3.5 and 3.6, the two simulators generate very similar images when given a certain distribution of (point) scatterers. Differences in the computation of the acoustic field lead to a difference in the lateral size of the PSF (Figure 3.4), which in turn influences the speckle pattern. This is more visible for the partially developed speckle (Figure 3.5). The distributions were composed of 400 respectively 4000 scatterers/mm^2, corresponding to 2.4, respectively 24 scatterers/resolution cell with a measured size of the resolution cell of approx. 0.006 mm^2.

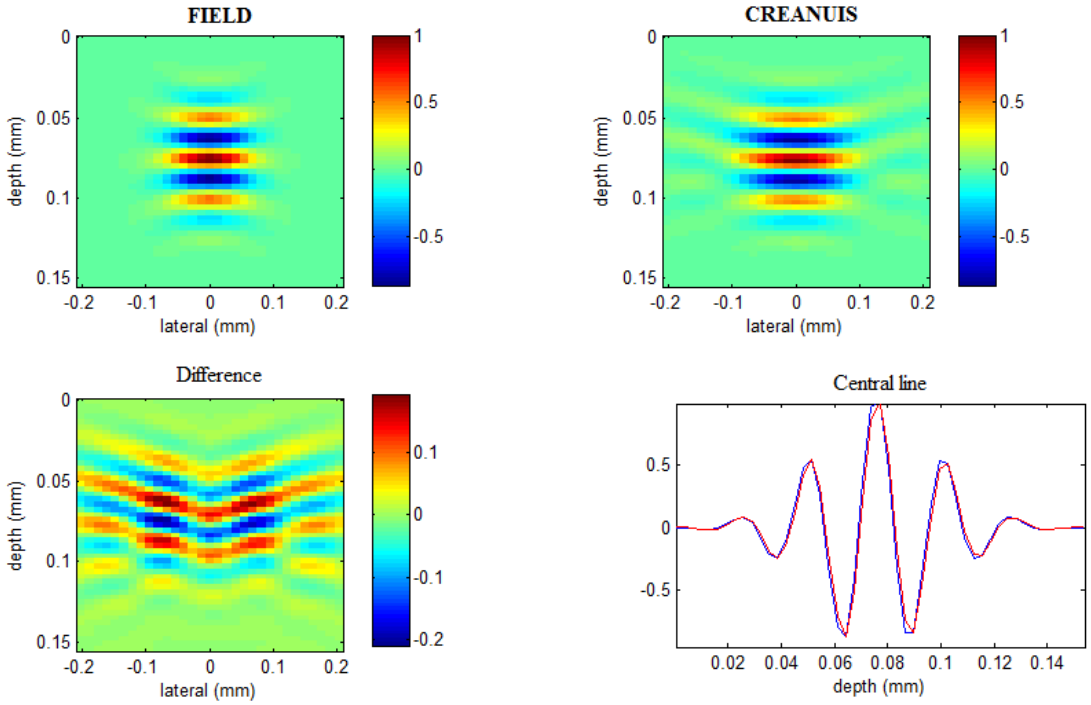

Figure 3.4 Point Spread Functions obtained by taking the image of a point scatterer using FIELD II and CREANUIS. The configuration was identical: ultrasound probe using 64 active elements, transmission frequency: 30 MHz with a 60% bandwidth, element pitch = 0.068 mm, kerf = 0.004 mm, height = 0.62 mm, focus at 6 mm, Hanning apodization window both in emission and in reception

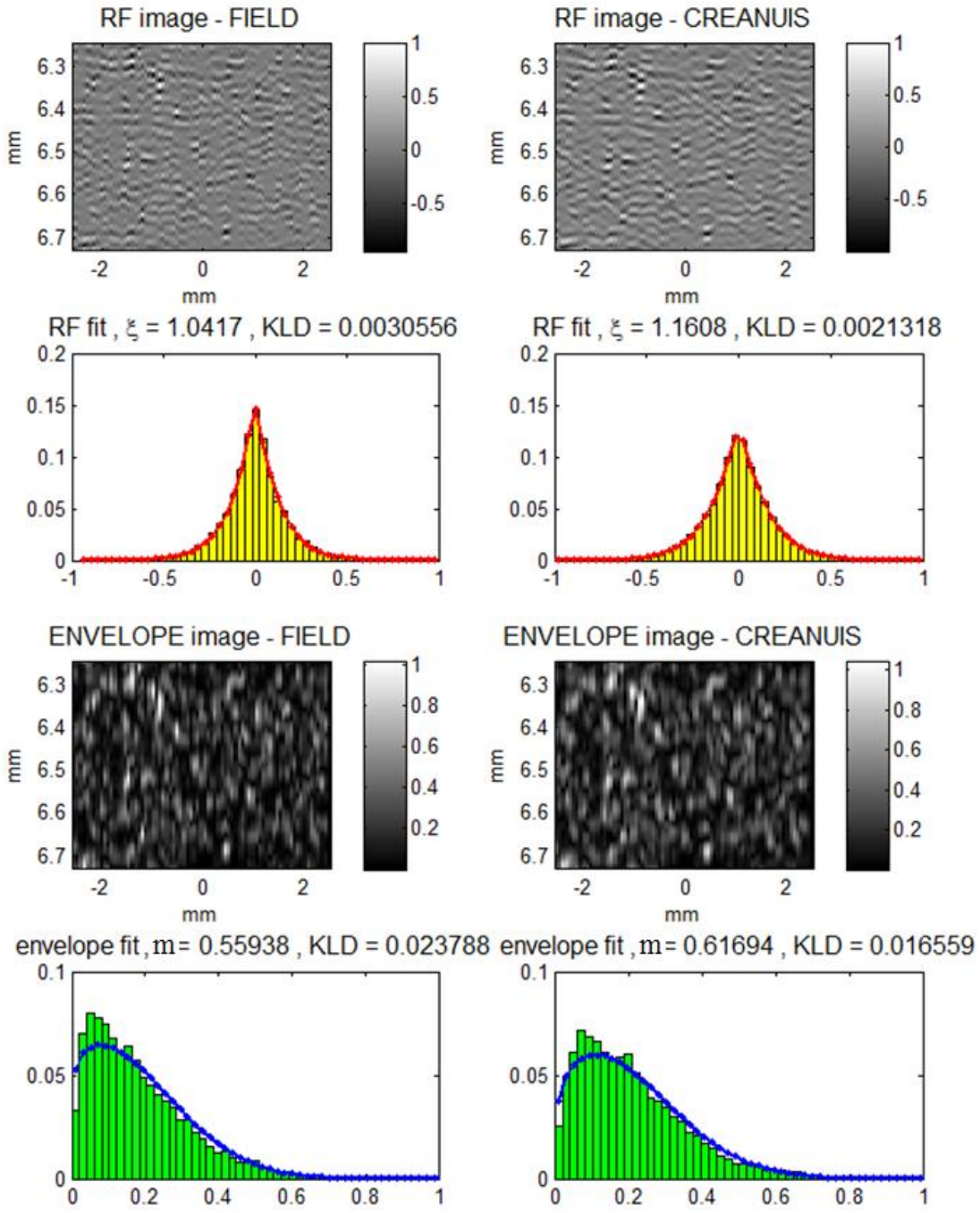

Figure 3.5 Simulated images and their respective statistical fits for a 2D sparse distribution of scatterers (400/mm^2), generating partially developed speckle, using FIELD (left column) and CREANUIS (right column), with ξ - the GGD shape parameter and m – the Nakagami shape parameter

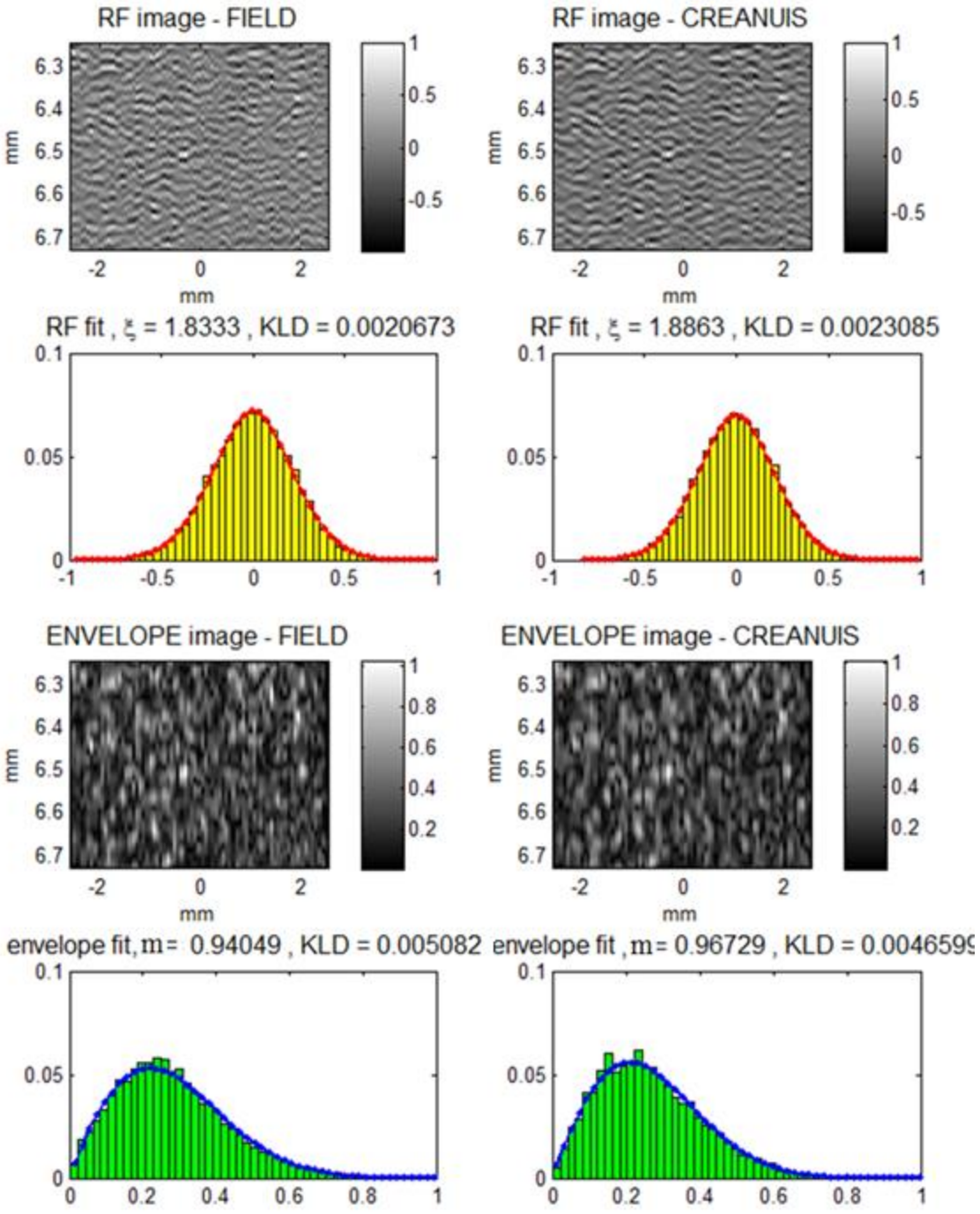

Figure 3.6 Simulated images and their respective statistical fits for a 2D dense distribution of scatterers (4000/mm^2), generating fully developed speckle, using FIELD (left column) and CREANUIS (right column), with ξ - the GGD shape parameter and m – the Nakagami shape parameter

3.3 STATISTICS AS A FUNCTION OF THE SYSTEM RESOLUTION. RESULTS FROM SIMULATIONS AND ACQUISITIONS USING ULTRASOUND PROBES

The purpose of this section is to present the influence of different factors on the system resolution and subsequently on the statistical parameters of ultrasonic speckle.

The simulations were conducted using CREANUIS, the same as in the previous section.

Experiments were conducted using four imaging systems:

- Vevo 770 + RMV 704 transducer (VisualSonics), F_c = 30 MHz
- Ula-Op + LA533 linear PZT probe (MsD Lab, Florence, Italy), F_c= 8 MHz
- Sonix MDP + L14-5W/60 linear PZT probe (Ultrasonix), F_c = 7 MHz
- Sonix MDP + linear CMUT probe (Vermon, Tours, France), F_c = 4 MHz

The insonified media consisted of tissue-mimicking phantoms. The phantoms were prepared by mixing a specific concentration of Orgasol (ultrafine polyamide particles having a density of 1030 kg/m3, produced by Arkema Inc., Colombes, France) with distilled water and 1% w/w ICI Synperonic NP 10 surfactant (Fluka, Sigma-Aldrich Chimie S.a.r.l., St. Quentin Fallavier, France) to minimize the surface tension at the particle-liquid interface and thus minimize particle aggregation and improve the homogeneity of the suspension.

3.3.1 Definition of the Resolution Cell

The resolution cell is the minimum volume that can be resolved by the imaging system. The resolution of an ultrasound system is usually considered as the Full Width at Half-Maximum (FWHM) of its Point-Spread Function in the three dimensions: axial, lateral (azimuthal) and elevation (Van Wijk and Thijssen 2002). Axial resolution is conditioned by the length of the emitted pulse, which in turn depends directly on its bandwidth:

$$r_{ax} = \frac{c}{2 * BW} \qquad (3.2)$$

where c is the sound velocity in human tissue, and BW is the signal bandwidth measured at -6 dB. Lateral resolution and elevation resolution are equivalent to the beam diameters in the specific direction and depend on the central frequency and geometry of the ultrasound beam:

$$r_{lat} = \lambda \frac{D_f}{D_{ap}} \qquad (3.3)$$

where λ is the wavelength corresponding to the central frequency, D_f is the focal distance and D_{ap} is the aperture diameter. For a single-element probe, the aperture is approximately equivalent to the element diameter; whereas in the case of a multi-element probe it is necessary to take into account all of the emitters. Here, a relatively rough approximation has been used for the resolution cell. We considered it as a cube with the dimensions equal to each resolution (given in the previous equations).

3.3.2 Statistics of the Backscattered Echo as a Function of the Exploration Frequency

The frequency is the main factor that influences the size of the resolution cell. Short wavelengths (high frequencies) make it possible to distinguish small structures inside the insonified medium, but also carry less energy and lose more energy than long wavelengths (low frequencies). Therefore, as frequency increases, the maximum attainable exploration depth will decrease accordingly. Also, what is essential and intuitive is the fact that the size of the resolution cell decreases with frequency, which means that the number of scatterers per resolution cell also decreases, which in its turn will influence the speckle statistics. This section sets on proving this fact experimentally.

2D simulations of five media with different scatterer concentrations (between 10 and 1000 per mm^2) were conducted. The ultrasound propagation speed was set to 1540 m/s. Six linear ultrasound probes were simulated for the exploration (Table 3-1). The size of the resolution cell and the equivalent density of scatterers per resolution cell were calculated accordingly (Table 3-2). The shape of the scatterers is not taken into account, they are considered as point scatterers. The ROI size was selected as a function of the wavelength, comprising 10 wavelengths in the axial (depth) dimension and 20 wavelengths in the lateral dimension.

Fc (MHz)	λ (µm)	Pitch (µm)	Kerf (µm)	Height (mm)	Focus (mm)
5	308	428	25.00	4.00	17.5
10	154	214	12.5	2.00	15.5
15	102	141	8.33	1.33	12.5
20	77	107	6.35	1.00	10.0
25	61	85	5.00	0.72	8.0
30	51	68	4.00	0.62	6.0

Table 3-1 Characteristics of the simulated probes

The shape and scale parameters of both GGD and Nakagami distributions were calculated for 50 images corresponding to each configuration, and the results agreed with the initial assumption. The value of the shape parameter (Figure 3.7) increases as a function of scatterer concentration, until it reaches saturation, which corresponds to a fully developed speckle. Higher values

correspond to larger resolution cells, respectively larger numbers of scatterers per resolution cell. The interval of possible values is smaller at low frequencies and higher at high frequencies. Therefore, high frequency transducers do not only provide a better resolution, but also allow distinguishing higher concentrations using statistical analysis. Therefore, they are preferred for tissue characterization. The scale parameters (Figure 3.7), on the other hand, essentially measure the reflected mean power, which increases with an increasing number of scatterers and also with decreasing frequency, since ultrasound of low frequencies conveys more energy.

Fitting the RF signal by using the Generalized Gaussian distribution or its corresponding envelope to the Nakagami distribution leads to very similar results. Therefore, combining them would seem redundant.

Fc (MHz) / Scatterer density (nb part/mm^2)	10	50	100	500	1000	Resolution cell size (mm^2)
5	1.800	9.00	18.00	90.00	180.0	0.1800
10	0.450	2.25	4.50	22.50	45.0	0.0450
15	0.200	1.00	2.00	10.00	20.0	0.0200
20	0.110	0.55	1.10	5.50	11.0	0.0110
25	0.075	0.37	0.75	3.75	7.5	0.0075
30	0.050	0.25	0.50	2.50	5.0	0.0050

Table 3-2 Number of scatterers per resolution cell

3.3.3 Statistics of the Backscattered Echo as a Function of Probe Bandwidth

Signal bandwidth influences axial resolution. The bandwidth of the emitted signal and the bandwidth of the probe must both be considered. In simulation, the bandwidth of the resulting PSF can be controlled (Figure 3.8). In experiments, the emitted signal can be controlled, and its spectrum can be measured, as well as the spectrum of the backscattered echo. Figure 3.9 shows how the change in bandwidth affects the echo statistics, in simulated images.

The CMUT probe that was used has a resonance frequency of 4 MHz, and emissions at different frequencies will not significantly shift the power maximum (an emission was composed of one pulse, in order to minimize its length), but will increase the transmitter power over a larger bandwidth, which will in turn reduce the size of the resolution cell (Eq.3.2). If the second harmonic is filtered out, the resolution cell size will be less significant (Figure 3.10).

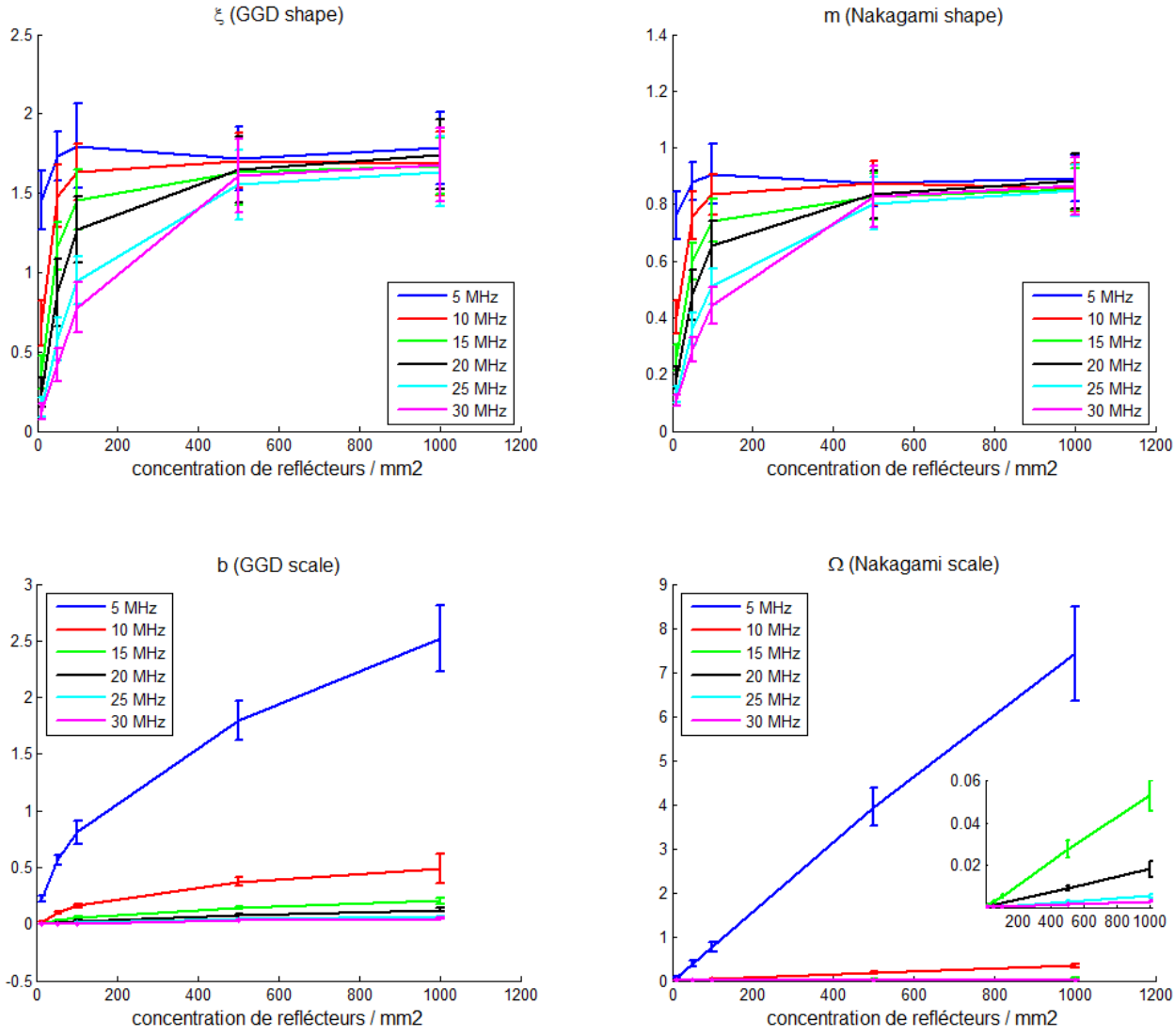

Figure 3.7 Shape and size parameters of the Nakagami distribution as a function of the exploration frequency and scatterer density per mm^2. Results obtained from simulated images.

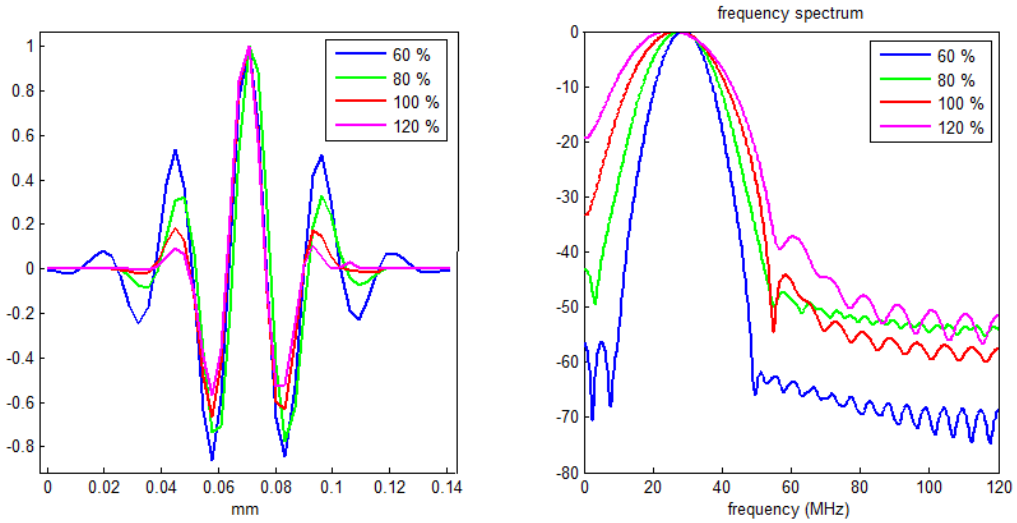

Figure 3.8 The 1D Point Spread Functions used in the simulations and their respective spectra. As the bandwidth increases, the PSFs have fewer oscillations and decreasing effective length, determining better resolution

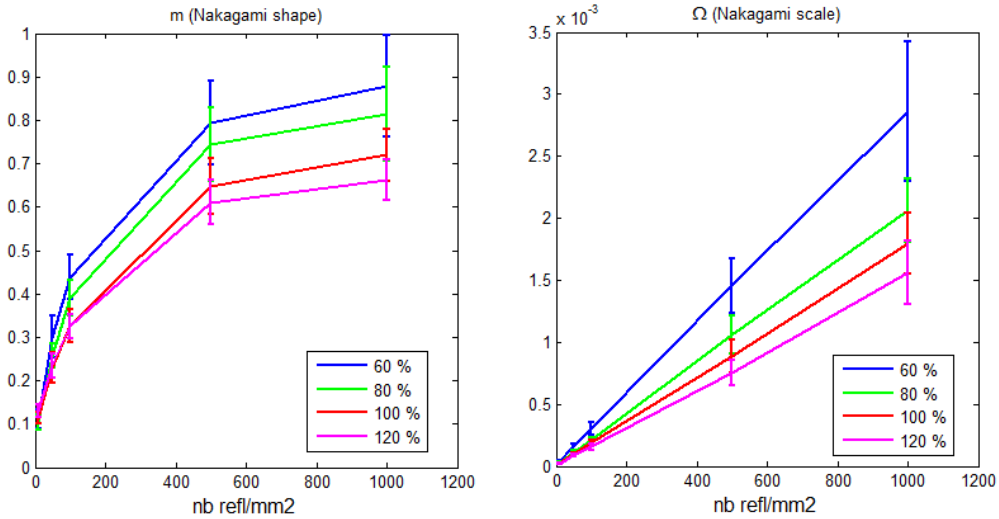

Figure 3.9 Shape and size parameters of the Nakagami distribution as a function of the probe bandwidth (expressed in % of the central frequency). Results obtained from on simulated images.

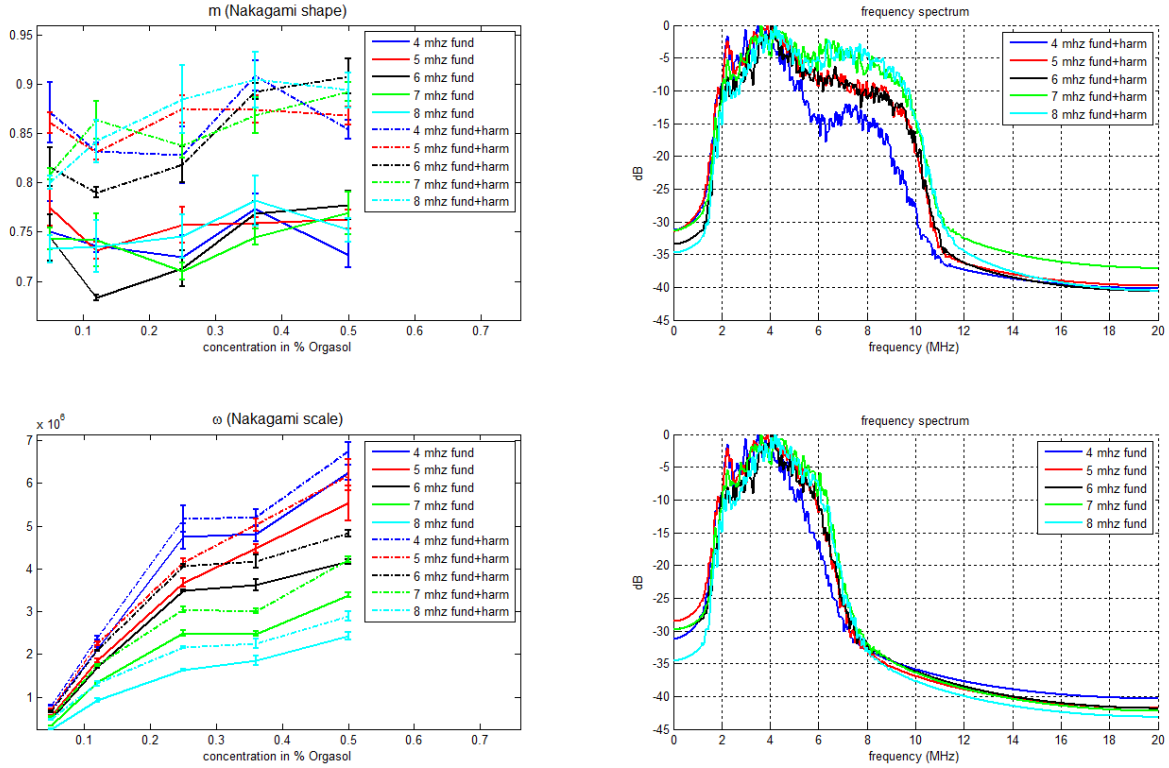

Figure 3.10 Nakagami parameters obtained on data acquired from Orgasol phantoms with low densities of particles (between 0.01% and 0.5%), and backscattered frequency spectrums received the CMUT probe used for the acquisition. Results obtained on the entire image and on the filtered fundamental image

3.3.4 Statistics of the Backscattered Echo as a Function of the Exploration Depth

Lastly, the exploration depth plays an essential role in the size of the resolution cell. The main factor intervening here is the width of the ultrasound beam, or the lateral resolution. For high frequencies, attenuation will also have an effect on the axial resolution at higher exploration depths. In order to observe the isolated effects of each factor by a statistical approach, simulations can be run with a zero-attenuation medium, respectively a plane wave. The effect of the exploration depth is studied here. Results for the no-attenuation case are presented in Figures 3.11 (in simulation) and 3.12 (on particle phantoms). This proves to be an interesting method of observing the evolution of the beam width, respectively focalization. In the focal zone, the shape parameter is at a minimum, considering that the number of reflectors per resolution cell is minimal. On the other hand, the scale parameter is at a maximum because that is where the beam power is concentrated.

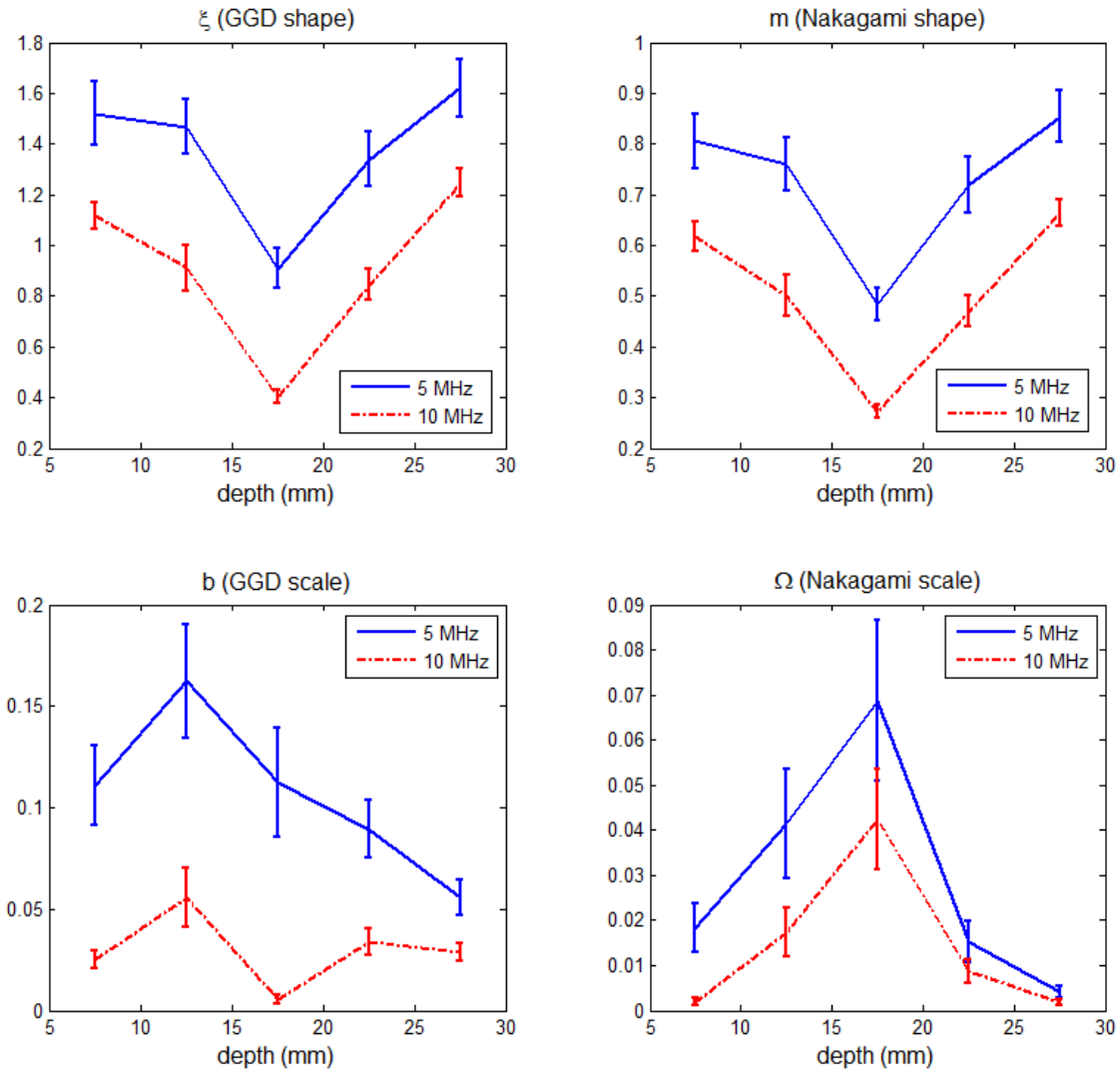

Figure 3.11 Shape (top) and scale (bottom) GGD and Nakagami parameters as a function of the exploration depth. Simulation of the same medium imaged with two probes emitting at 5, respectively 10 MHz.

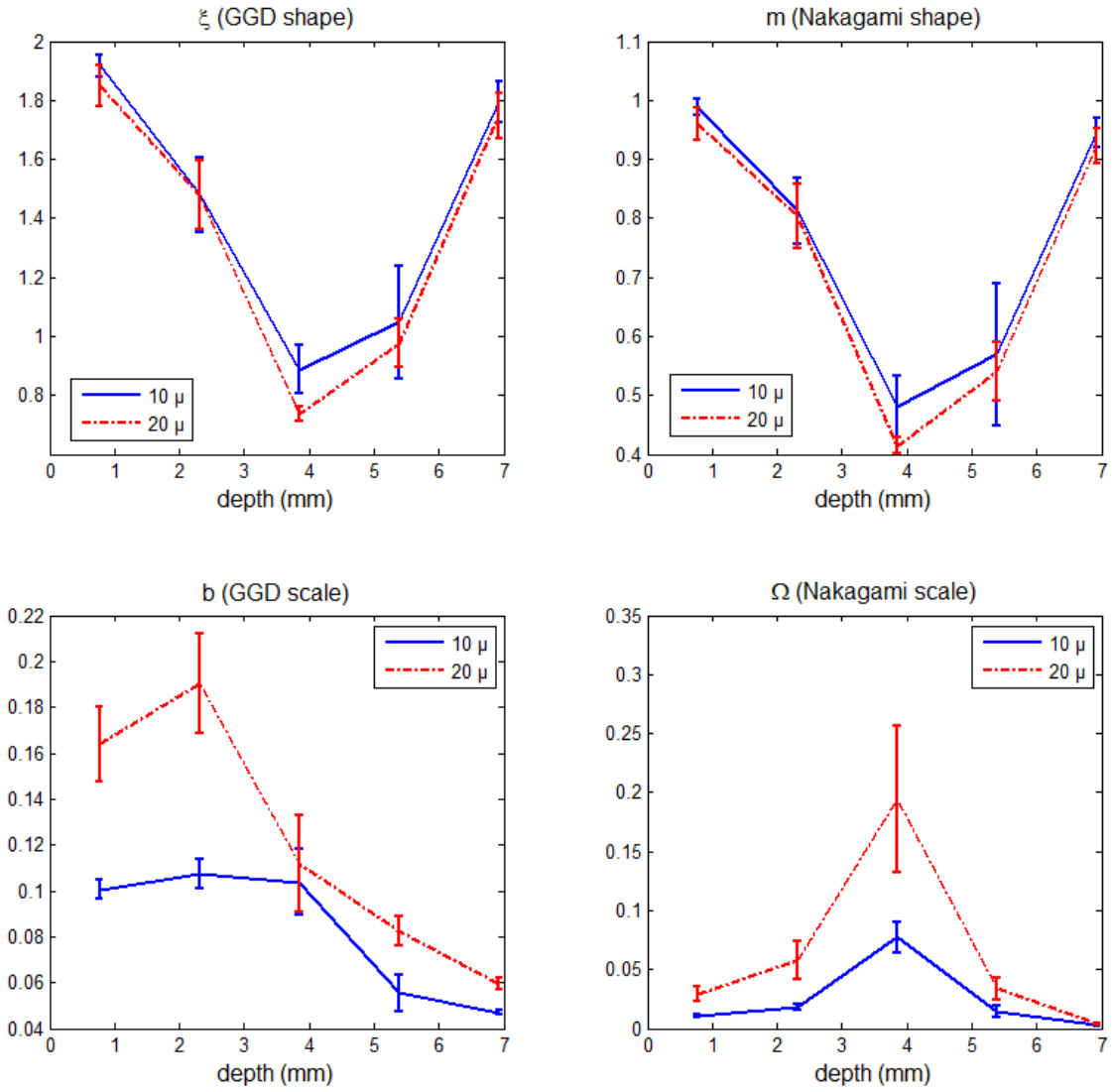

Figure 3.12 Shape (top) and scale (bottom) Nakagami parameters as a function of the exploration depth. Experiments with Orgasol particles of 10μ respectively 20μ in diameter, imaged at 30 MHz.

3.3.5 Dependence of the Shape Parameters on the Number of Reflectors per Resolution Cell

The dependence of the statistical shape parameters on the system resolution is proven, what's left to determine is if their relationship is invariable from one resolution system to another. We have managed to establish a relationship between the shape parameters and the number of reflectors per resolution cell. This relationship can be described analytically by:

$$f(x) = a_1(1 - a_2 e^{(-a_3 x)}) \qquad (3.4)$$

where x is the number of particles per resolution cell, and f (x) is the shape parameter of the Generalized Gaussian or Nakagami distribution. Since the evolutions are very similar (Figure 3.13), we will focus on the Nakagami parameter.

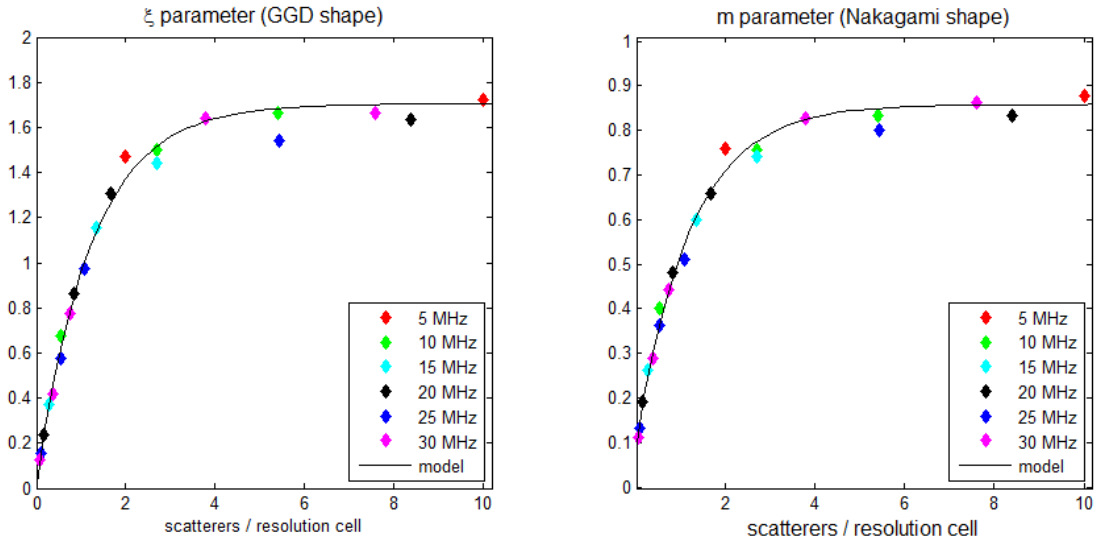

Figure 3.13 Evolution of the shape parameters of the Generalized Gaussian and Nakagami distributions as a function of particle concentration per resolution cell. Same simulated data from Section 3.3.2. Parameters of the model curve: (left) a_1=0.98, a2=0.81, a_3=1.70; (right) a_1=0.90 ,a_2=0.82, a_3=0.85.

Fitting the Nakagami parameter to the exponential model has given very different results for the experimental data (Figure 3.14), showing that the saturation of the parameter occurs at a limit much lower than 10 scatterers/resolution cell. The desired purpose of the model would be to use it for conducting inversions, but we encounter difficulties associating a value of the *m* parameter to a specific number of scatterers per resolution cell. Measurements from experimental data tend to produce very different curves for reasons that are not precisely understood. They can stem from but are not limited to: an inaccurate measurement of the resolution, a large variability of the scatterer size distribution, an insufficient amount of data for a reliable fit, the presence of reflexions of different origins that influence the statistics. Indeed, we always assume that the scatterers have constant size, and that our phantoms are perfectly clear of other structures that can

produce a diffuse background. The nature of the scatterers and their acoustical properties may also play a role. Also, the inversion would be clearly limited to partially developed speckle.

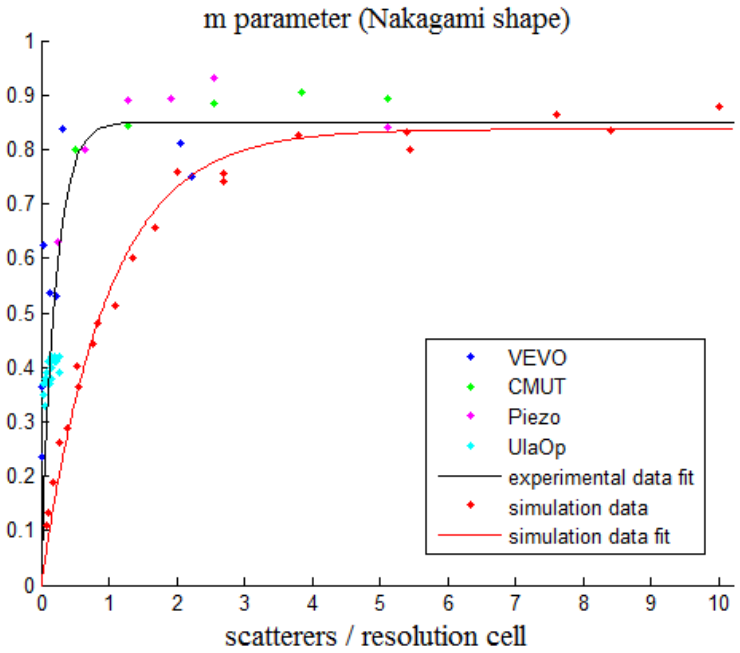

Figure 3.14 Evolution of the shape parameters of the Nakagami distribution as a function of particle concentration per resolution cell, for both simulated and experimental data. Parameters of the model curve: a1=0.87, a2=0.55, a3=2.57

3.4 INFLUENCE OF GAUSSIAN WHITE NOISE

During the ultrasound data acquisition process, electric noise can be present. Depending on the imaging system, this can be more or less intense. This type of noise is usually additive white gaussian noise (AWGN) Considering a gaussian distribution of the noise amplitudes and a number of six scenarios where the signal is corrupted by different levels of noise, the evolution of the shape of the speckle histogram was studied for a speckle that is initially not fully developed (Figure 3.15) and one that is fully developed (Figure 3.16). For the two cases, the quality of the Generalized Gaussian fit remains just as good, as there are no major differences in the Kullback-Leibler divergence between the data histogram and the fitted pdf. Nonetheless, the shape does change and it evolves to that of a more fully developed speckle, which can be seen in the increasing values of the shape parameter. This is more obvious for the first case. The scale parameter also increases but the values are not given here because this fact is trivial, since the noise power adds to the signal power.

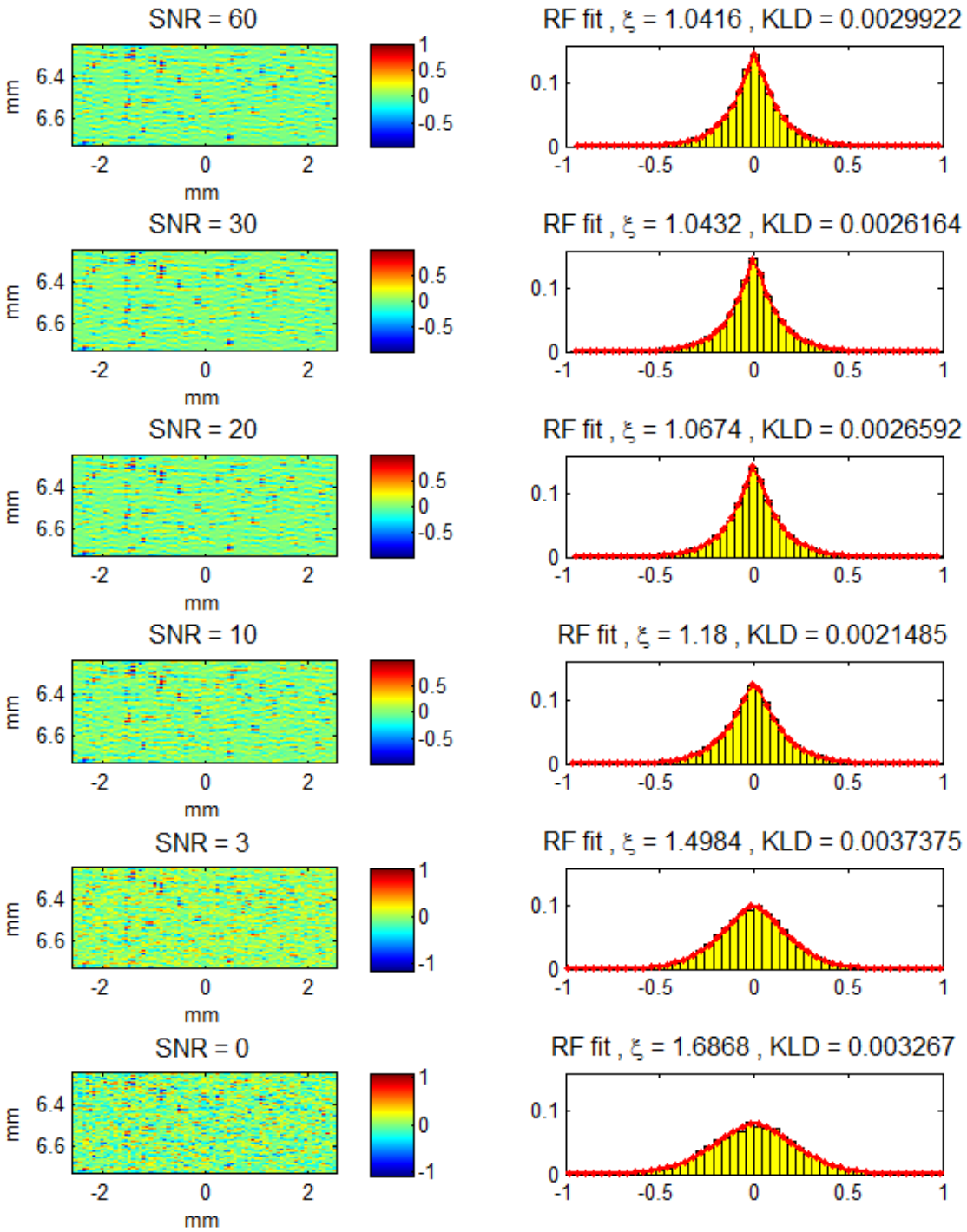

Figure 3.15 Simulated RF images and their respective statistical fits for a 2D sparse distribution of scatterers (400/mm^2) affected by different levels of noise

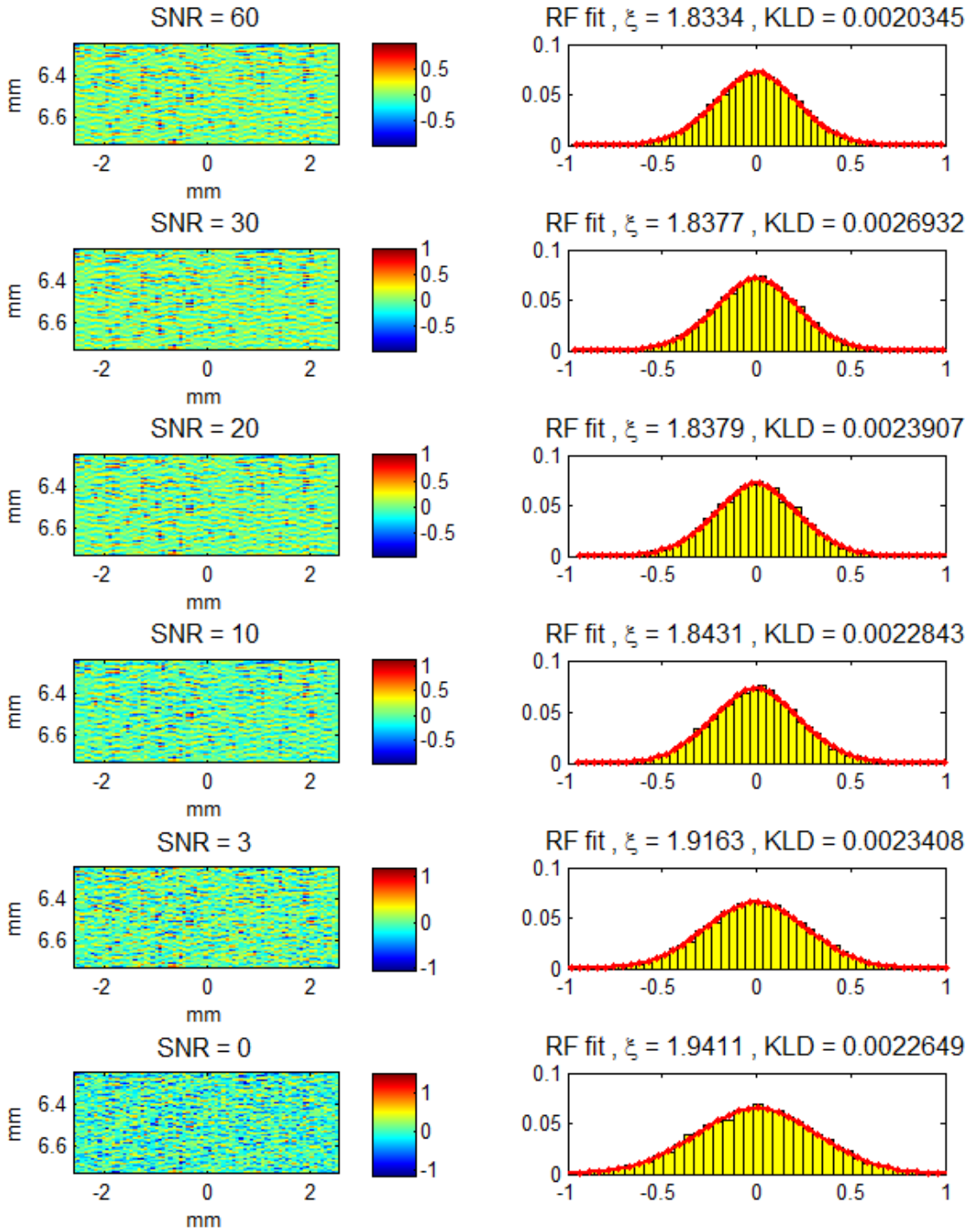

Figure 3.16 Simulated RF images and their respective statistical fits for a 2D dense distribution of scatterers (4000/mm^2) affected by different levels of noise

3.5 STATISTICS OF HARMONIC SIGNALS USING THE NAKAGAMI DISTRIBUTION

Speckle statistics are normally studied on the global RF signal received from the insonified medium. Associating parameter estimates to a tissue (or another medium) with a specific density of scatterers is a Quantitative Ultrasound (QUS) technique. The QUS estimates can be obtained from the envelope statistics. To our knowledge, previous studies analyze the entire backscattered signals and do not extend their scope to the eventual harmonic components. However, harmonic imaging is of interest for medical applications because different tissues have different nonlinearity coefficients which can be used in tissue characterization. The literature on nonlinear coefficient estimation methods does not comprise statistical estimations; therefore we wish to test if the harmonic images of media with different nonlinearities produce different statistics, and if they can be discriminated by the characteristic statistical parameters. The Nakagami model is used for fitting the harmonic envelopes of simulated media with different nonlinearity coefficients and different scatterer concentrations. Results show that the estimates computed from the harmonic image in the same region as the fundamental image do differentiate media with different concentrations, similarly to those computed on the fundamental. In addition, the parameters are also related to the nonlinear property of the medium.

3.5.1 Nonlinear Propagation

Nonlinear propagation effects in medical ultrasound have been demonstrated in (Muir and Carstensen 1980), thus proving the need to be taken into consideration when analyzing wave propagation and providing a reliable approximation for the phenomenon. Previously, ultrasound wave propagation inside the tissue was approximated as a linear process. While the approximation deriving from this assumption may be satisfying for certain applications, the amplitude of the harmonic components of the signal becomes non-negligible in certain tissues, especially fatty tissues (Table 3-3).

Ultrasound wave propagation is inherently nonlinear, due to the existence of a positive pressure phase and a negative pressure phase. The immediate consequence of an increase in local pressure is an increase of the temperature and subsequently of the propagation speed. Therefore, the propagation of the positive pressure front is faster than that of the negative pressure front, which leads to a distortion of the waveform (Figure 3.17). Notably in the case of modern echographs that emit high pressure waves (of the order of MPa), the acoustic pressure within the tissue will be far greater than the pressure in the stationary tissue, thereby generating a highly nonlinear acoustic wave. From a spectral point of view, the phenomenon generates harmonics.

In the propagation of ultrasound waves, the compression of the medium is considered adiabatic and reversible, therefore isentropic. The pressure is considered as a function of density

$P = f(\rho)$ and developed in a Taylor series around ρ_0 in order to choose an appropriate approximation:

$$P = \sum_{k=0}^{\infty} \frac{1}{k!} \left(\frac{\partial^k p}{\partial \rho^k} \right)_s \left(\rho - \rho_0 \right)^k \tag{3.5}$$

The accuracy of the series development depends on the number of terms used for the approximation. If the linear and quadratic terms are kept, a relationship between the pressure and density variations can be derived. It is useful to define the parameters A and B as:

$$A = \rho_0 \left(\frac{\partial P}{\partial \rho} \right)_s = \rho_0 c_0^2 \tag{3.6}$$

$$B = \rho_0^{\,2} \left(\frac{\partial^2 P}{\partial \rho^2} \right)_s \tag{3.7}$$

Where s denotes the entropy at which calculations are made. If the desired approximation is linear, then only the first term is used. Then by definition the wave propagation speed (calculated at entropy s) is:

$$c^2 = \left(\frac{\partial p}{\partial \rho} \right)_s \tag{3.8}$$

When the second term (corresponding to the second harmonic) is taken into consideration, then the ratio of the two previously defined parameters is called the nonlinearity parameter, and is equal to:

$$\frac{B}{A} = \frac{\rho_0}{c_0^2} \left(\frac{\partial^2 P}{\partial \rho^2} \right)_s \tag{3.9}$$

The nonlinearity parameter intervenes in the speed of the wave:

$$c = c_0 \left(1 + \frac{B}{2A} \frac{u}{c_0} \right)^{\frac{2A}{B}+1} \tag{3.10}$$

where u is the particle (or medium) velocity. If the ratio u / c_0 is small, the velocity is usually simplified to:

$$c = c_0 + \left(1 + \frac{B}{2A}\right)u \tag{3.11}$$

The nonlinearity of the medium can also be described by using the term appearing in the parenthesis, the nonlinearity coefficient:

$$\beta = 1 + \frac{B}{2A} \tag{3.12}$$

By introducing the parameter β and the expression of the particle velocity in equation (3.11), then the maximum and minimum wave celerities c^+ and c^- which correspond to the positive pressure and negative pressure wave, respectively, are:

$$c^{\pm} = c_0 \pm \beta \frac{p}{\rho_0 c_0} \tag{3.13}$$

In the case of a single plane wave propagating in an inviscid and lossless medium, the propagation of the wave as a function of distance can be described by the lossless Burgers equation:

$$\frac{\partial P}{\partial z} = \frac{\beta P}{p_0 c_0^3}\frac{\partial P}{\partial \tau} \tag{3.14}$$

The solutions to the Burgers equation show how the amplitude of the harmonic waves increases as a function of the propagation distance z :

$$P(\mathrm{z},\tau) = \mathrm{p}_0 \sum_{n=1}^{\infty} \frac{2}{nz / z_{sh}} J_n(nz / z_{sh}) \sin(\mathrm{n}\,\omega_0 \tau) \tag{3.15}$$

where n is the harmonic number, J_n is the Bessel function of the first kind, and z_{sh} is the shock distance length. The distortion of a non-attenuated wave is bound to increase up to the point where the wave has a sawtooth shape. The distance to this point is the shock distance:

$$z_{sh} = \frac{\rho_0 c_0^3}{\omega_0 \beta P_0} \tag{3.16}$$

In practice, in medical ultrasound, the amplification of the harmonic waves is limited by the attenuation effect.

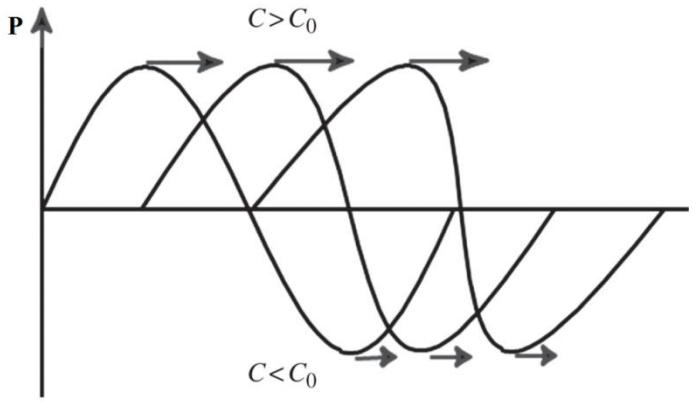

Figure 3.17. Tissue harmonic generation: as the wave propagates, the higher pressure portion travels faster owing to the higher density of the medium and the lower pressure travels slower, leading to wave distortion and harmonic generation (Powers and Kremkau 2011).

Regarding the nonlinearity parameter estimation methods, two major families are present in the literature: thermodynamic methods and finite amplitude methods. Thermodynamic methods are more accurate than the finite amplitude ones (Law, Frizzell, and Dunn 1985), but cannot be easily used for in vivo exams because of the complicated experimental setup that is necessary for the measurements. They are mostly used by chemists for the study of different properties of liquid mixtures. The principle is to determine the values of the nonlinearity parameter by measuring the change of sound velocity with pressure and temperature. Finite amplitude methods use direct measurements of the pressure of the second harmonic generated in the medium, by a single frequency or composite transmission. The pressure of the second harmonic is measured at various transmitter-receiver distances, with a single measurement or a double measurement - one for the medium of interest and one for a reference medium (the insertion-substitution method). In the following, we will test the applicability of statistical parameters as measures of the medium nonlinearity.

Medium	Celerity	B/A
Blood	1570	6.1
Brain	1540	6.6
Fat	1450	10.0
Liver	1550	6.8
Muscle	1590	7.4
Water	1480	5.2

Table 3-3 Mean propagation speed and nonlinearity coefficients for tissues and water (taken from (Wells 1999))

3.5.2 Measurements of Statistical Parameters on Simulated Ultrasound Images

Simulations of ultrasound images with different nonlinearities were conducted using CREANUIS. The simulated probe transmits at a frequency of 10MHz, is focalized at 20 mm, and has the following dimensions: a pitch of 214 μm, kerf of 12.5 μm, and a height of 2 mm. respectively. The region of interest (ROI) has a depth of 4.3 mm centered at the focal depth. The RF lines are sampled at 80 MHz and spaced at a distance equal to the probe pitch. There is no interpolation in the lateral direction; this is why the visual quality of the images is poor. In the simulation setup, the ROI and the surrounding medium have different nonlinearity coefficients β (from 3.5 to 50). Scatterers with variable densities (2-30 scatterers/ resolution cell) are placed only in the ROI (Figure 3.18). For each concentration and each nonlinear coefficient, 50 images with randomly distributed scatterers were simulated. Each simulated image was filtered around the fundamental band or second-harmonic band, using a 3-order Butterworth filter. These filtered image envelopes were used to estimate the Nakagami shape parameter m and scale parameterω, using the iterative maximum-likelihood estimator (subsection 2.3.2), same as in the other experiments described in this chapter.

The statistical parameters were computed for both the fundamental and the harmonic images, for comparison. As seen previously, the amplitudes of the non-filtered images in the focal zone are homogenous, because the power is focalized equally and the resolution cell is also of constant size. If the fundamental and the second harmonic images are considered separately in the same zone, the fundamental is very similar to the whole image in terms of the resolution cell size, because most of the energy is contained in the fundamental component. In the harmonic image, the central frequency is doubled, meaning that both the axial and lateral resolutions are improved by a factor of 2 (eq. 3.2, 3.3). Therefore, computing the statistics of the second harmonic would be equivalent to considering a number of scatterers per resolution cell that is 4 times smaller than that in the fundamental image. However, because the amplitude of the harmonic wave increases with propagation depth, the amplitudes in the ROI are longer homogenous. Because of the gradual shift in the spectrum and central frequency of the propagating wave, the resolution changes accordingly. Of course, for a small enough depth, the resolution cell can be considered constant and the computed Nakagami shape parameter is effectively a measure of the local scatterer concentration. Our interest, however, is to measure the heterogeneity of the harmonic image in order to obtain more discriminant shape parameters. This is why the same ROI is considered for the fundamental and for the harmonic image.

A simple visual inspection of the images corresponding to media with very different nonlinearity parameters (and constant scatterer density) shows the differences in the amplitude level and in the increase rate of the respective amplitudes. The envelope fits back up the observations (Figures 3.19 and 3.21). For the less homogenous image (β=50), the accumulation of low-level amplitudes of the harmonic at low depth give the histogram an aspect corresponding to a low density of scatterers. In the image corresponding to β=3.5, the amplitudes are globally lower since a smaller proportion of the energy is conveyed by the harmonic, but the histogram

resembles that of a more fully developed speckle. The shape parameters decrease globally for the same concentration, as a function of the medium nonlinearity, and the distinction between the evolutions corresponding to each density is also clearly visible (Figure 3.21).

Differences are visible also in the images of media with a constant nonlinearity parameter but different scatterer concentrations, in the classical sense (Figure 3.20). The image and histogram of the more concentrated medium illustrate the more fully developed speckle. Also, because attenuation was not considered, the reflected energy also increases with concentration.

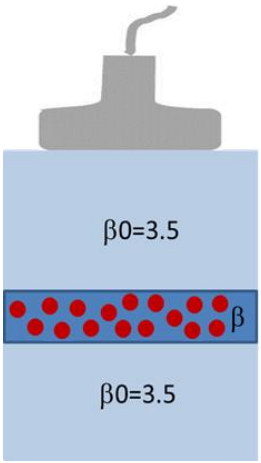

Figure 3.18 Schematic representation of the simulation of nonlinear media: the ultrasound probe scans a phantom with an inclusion with a variable scatterer density and nonlinear coefficient.

The observations are backed up by the global estimation results (Figure 3.23). For the nonfiltered images and fundamental images, the estimated values are almost identical, and the curves corresponding to each nonlinearity coefficient overlap. For the harmonic images, however, the values are different and there is a clear separation of the curves corresponding to the chosen nonlinearity coefficients.

3.5.3 Conclusion on the Statistics of Harmonic Signals

We have been able to show in simulations that Nakagami statistical parameters can be used as a measure of the medium nonlinearity, if they are computed on the harmonic image. Of course, some of the chosen values of the nonlinear coefficient are very high by comparison with the typical ones encountered in tissues. The study evaluates the theoretical discriminant capacity of the statistical estimates. If an actual application is desired for tissues, a more complete study on a larger amount of data would be necessary in order to assess accuracy. Not having a method to build phantoms with a specific nonlinearity coefficient could be an impediment. Using the statistical estimates as a complementary characterization method could prove as interesting, and could provide support for a better classification if the estimates are considered as features of the respective media.

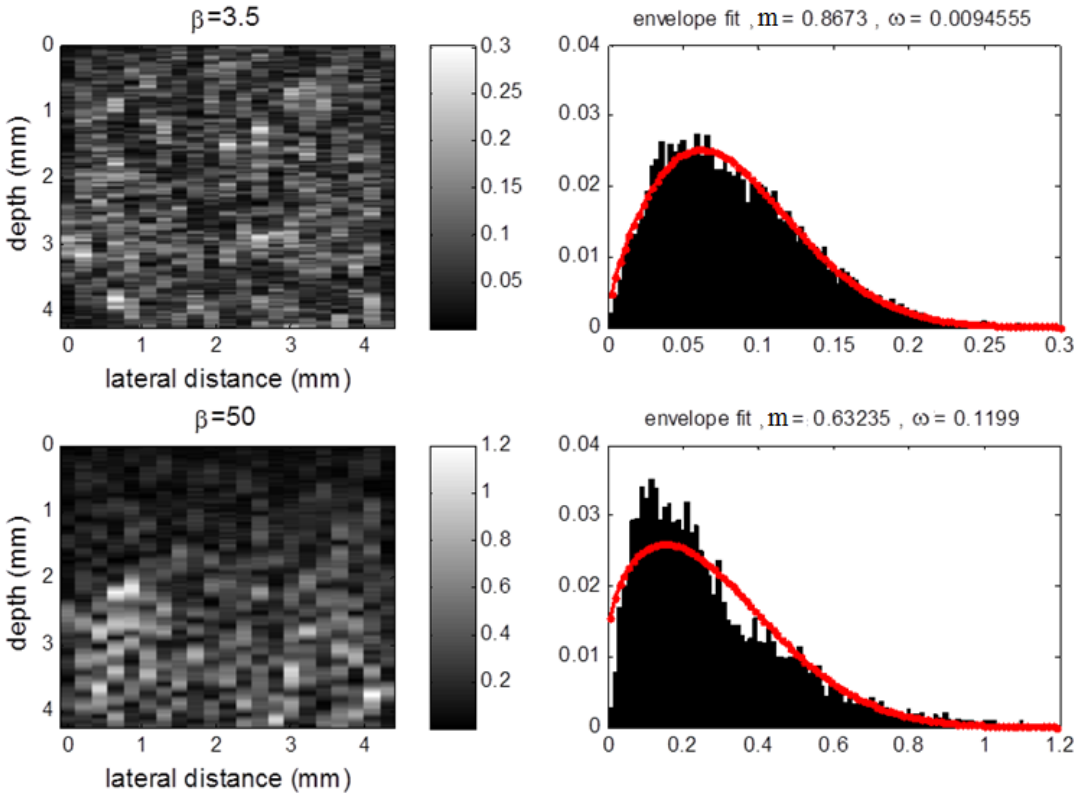

Figure 3.19 Examples of two simulated harmonic envelopes and their corresponding Nakagami fits, for media with 14 scatterers/resolution cell, and β parameters equal to 3.5 (top) and 50 (bottom)

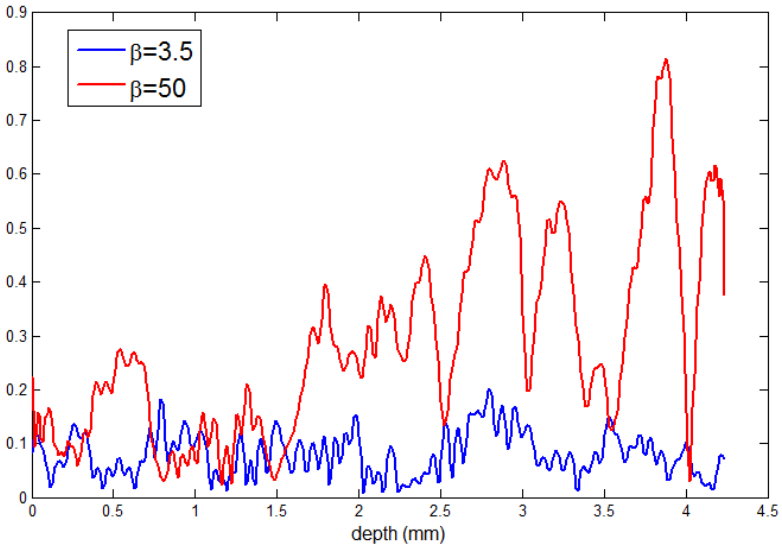

Figure 3.20 1D lines extracted from the envelopes shown in Figure 3.19, showing the harmonic wave amplitude increase for two nonlinearity parameters.

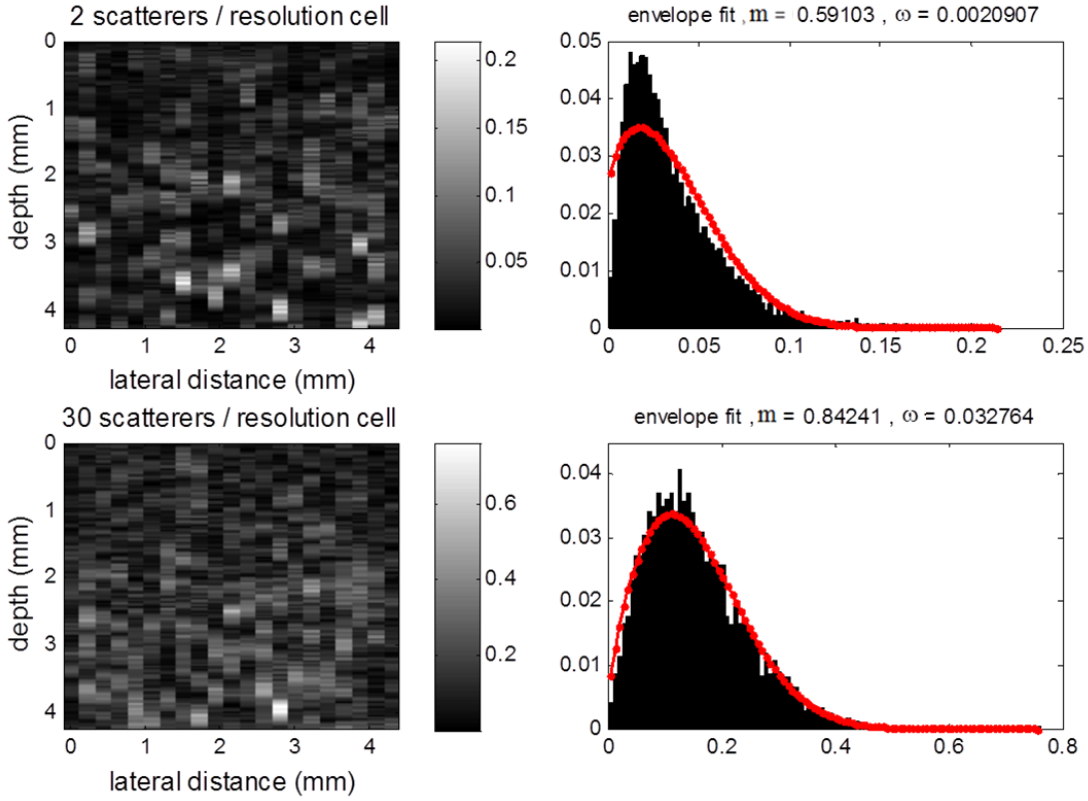

Figure 3.21 Examples of two simulated harmonic envelops and their corresponding Nakagami fits, for media with a β parameter equal to 10, and a density of 2 scatterers/resolution cell (top) and 30 scatterers/resolution cell (bottom)

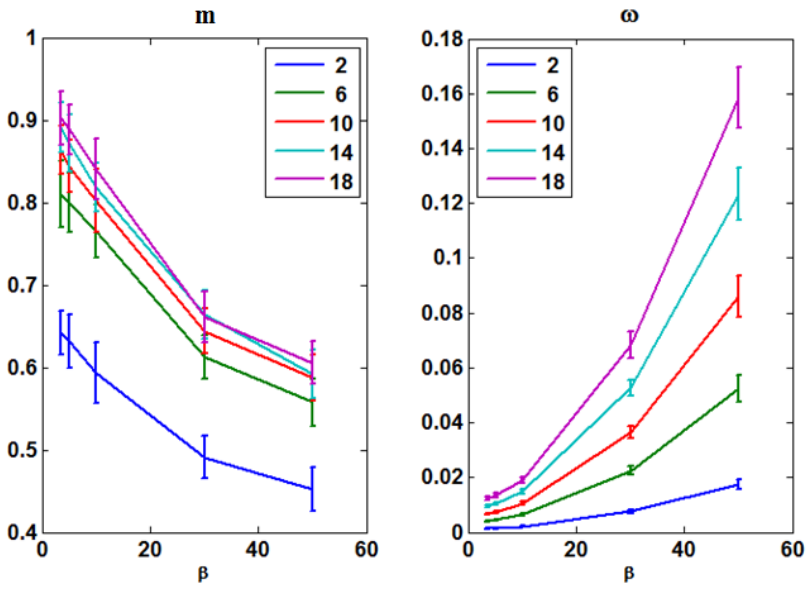

Figure 3.22 Estimates of the shape (m) and scale (ω) Nakagami parameters for the harmonic images as a function of β. Legend: number of scatterers per resolution cell.

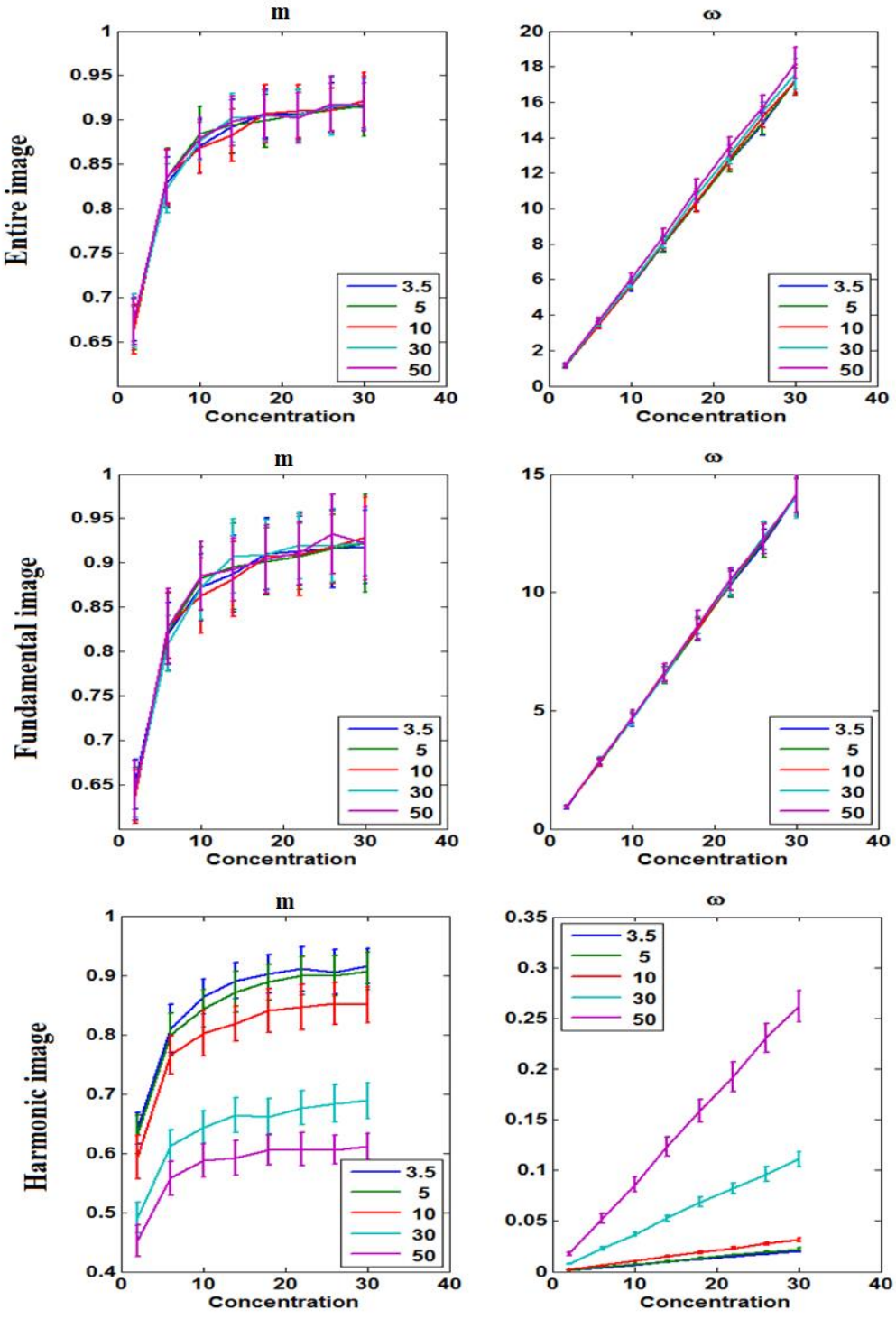

Figure 3.23 Estimates of the shape (m) and scale (ω) Nakagami parameters for the entire (nonfiltered) images, fundamental images and harmonic images as a function of the number of scatterers per resolution cell. The values of the β coefficient are given in the legend.

3.6 CONCLUSION

The purpose of the studies described in this chapter was to assess the possibility of characterizing media with different scatterer concentrations by using statistical parameters as measures. According to the random walk model, the speckle structure depends on the number of scatterers in the resolution cell, therefore on the system resolution. Tests were conducted using simulations and phantoms composed of Orgasol particles, in order to observe this phenomenon and validate the assumptions.

The Generalized Gaussian distribution and the Nakagami distribution were used to model the RF echo and its envelope, respectively. As it is also the case of other distributions used for this purpose, each of the two are described by a shape and a scale parameter, of which the shape depends on the scatterer density per resolution cell, and the scale depends on the backscattered energy. The scale parameter, especially in the case of the Nakagami distribution, provides information on the amount of backscattered echo, and it is therefore quite redundant. The shape parameter, on the other hand, does indeed reflect fluctuations in the scatterer density as the resolution cell size changes, for instance when the frequency and bandwidth of the emitted pulse change, or as the beam width changes as with depth. Nevertheless, at high scatterer densities, the speckle is fully developed and it becomes impossible to distinguish between different densities. The Generalized Gaussian shape parameter saturates at a value of 2, and the Nakagami shape parameter saturates at a value of 1.

The variance of the parameters can be due to changes in the concentration within the resolution cell, variations of the resolution cell size (increases rapidly with increasing attenuation and beam defocusing), or possibly the approximation used for the resolution cell. Solutions for variance reduction have been proposed and are being studied: deconvolution (Alessandrini et al. 2011), or the use of CMUT probes which in general offer a bandwidth superior to that of PZT probes.

The use of the statistical estimates is not restricted to the fundamental image. Simulations have shown that media with different nonlinearities can be distinguished by using statistical measures on the second harmonic images, but the study was not very extended and a practical implementation will require additional work.

4 STATISTICS OF THE BACKSCATTERED ECHO USING THE HOMODYNED-K DISTRIBUTION

As described in Chapter 2, the Homodyned-K is the most complete and versatile statistical distribution currently used to model the statistics of ultrasound speckle. It can be used to model scattering from both low density media (under 10 scatterers/resolution cell, pre-Rayleigh speckle) and high density media (over 10 scatterers/resolution cell, Rayleigh and post-Rayleigh speckle), while taking into consideration the presence of a constant-amplitude coherent component. The Homodyned-K belongs to the family of K distributions, which are compound distributions and can therefore be expressed in compound form, thus facilitating the simulation of independent, identically distributed random samples.

The Homodyned-K relates to other distributions. In the K distribution model, the number of steps in the random walk is also modeled by a negative binomial distribution. Moreover, the K distribution is a special case of the Homodyned-K, where the coherent component of the amplitude is vanishing. The Rice distribution corresponds to the limiting case where the scatterer clustering parameter implicit in the negative binomial distribution is infinite. The Rayleigh distribution corresponds to the Rice distribution with a vanishing coherent component. Both the Rice and the Rayleigh distributions correspond to a Gaussian random walk, unlike the Homodyned K-distribution or the K-distribution.

4.1 CHARACTERIZATION OF THE DISTRIBUTION

The Homodyned K-distribution is defined using three parameters: α, σ and ε:

$$p_A(\mathrm{A}) = \mathrm{A}\int_0^\infty x J_0(\varepsilon x) J_0(\mathrm{A}\,x)\left(1+\frac{x^2\sigma^2}{2}\right)^{-\alpha} dx \qquad (4.1)$$

The integral expression can be approximated to a summation that facilitates its numerical implementation:

$$p_A(A) = \sum_{n=0}^{\infty} \frac{\frac{2\alpha A}{\sigma^2}}{\Gamma(\alpha)(\mathrm{n}!)^2}\left(\frac{\alpha\varepsilon A}{2\sigma^2}\right)^2 \left(\frac{1}{\sigma}\sqrt{\frac{\alpha(\varepsilon^2+\mathrm{A}^2)}{2}}\right)^{\alpha-1-2n} K_{2n+1-\alpha}\left(\frac{1}{\sigma}\sqrt{2\alpha(\varepsilon^2+\mathrm{A}^2)}\right) \qquad (4.2)$$

In practice, it is sufficient to take into consideration the first 10 terms for accurately reconstructing the Homodyned-K pdf, for a large range of parameters. The first term has an overwhelming weight and it alone assures that the pdf will fit the data histogram reasonably well for many cases (Figure 4.1).

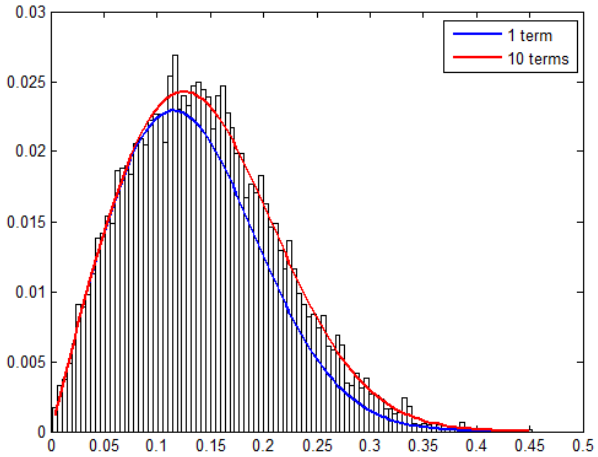

Figure 4.1 Example of data histogram and Homodyned-K fits using 1 term and 10 terms of the series described in eq 2 (parameters: α=80, ε=0.1, σ=0.01)

However, according to (Destrempes, Porée, and Cloutier 2013), the three parameters that carry a physical meaning are: the mean intensity μ, the scatterer clustering parameter α (which is also the clustering parameter in the negative binomial distribution) and the structure parameter κ (the ratio of the coherent signal power ε^2 to the diffuse signal power $2\sigma^2\alpha$):

$$\kappa = \frac{\varepsilon^2}{2\sigma^2\alpha} \tag{4.3}$$

Given a sample of the received amplitude, one is then interested in estimating those three parameters or related parameters, such as the signal-to-noise ratio (SNR) and the ratio of coherent signal to diffuse signal, k:

$$k = \frac{\varepsilon}{\sigma\sqrt{\alpha}} = \sqrt{2\kappa} \tag{4.4}$$

Concerning parameter estimation, due to the absence of a closed-form expression, it would be very difficult to develop an analytical form for the maximum-likelihood function. Moments on the other hand have closed-form expressions, so that moment-based strategies have become popular. In (Dutt and Greenleaf 1994), an estimator based on the first three moments of the intensity (i.e. the squared amplitude) E[I], E[I^2] and E[I^3] was proposed. The more recent and widely used estimator developed in (Hruska and Oelze 2009) is based on the SNR, skewness (the

third standardized moment) and kurtosis (a shifted version of the fourth standardized moment) of fractional orders of the amplitude. In this work, the parameters of interest are α and k (eq 4.4). The most recent estimator is proposed in (Destrempes, Porée, and Cloutier 2013). It is referred by the authors as « XU estimator » because it uses two log-moments of the intensity, otherwise known as the U and X statistics, in order to estimate α and an algorithmic parameter γ:

$$\gamma = \frac{\varepsilon^2}{2\sigma^2} \tag{4.5}$$

Validation on simulations of low-density media has showed that the estimator it is more efficient than the other state of the art methods. For the work described in this chapter, the XU estimator was used in application on media of both low and high density.

4.2 THE XU ESTIMATOR

As described in (Destrempes, Porée, and Cloutier 2013), the XU estimator determines the values of the α and γ parameters by taking as input the mean value of the signal intensity, μ, and the values of two log-moments of the intensity, U and X:

$$U = E[logI] - logE[I] \tag{4.6}$$

$$X = E[IlogI] / E[I] - E[logI] \tag{4.7}$$

For the set of data used in the next sections (obtained from cell pellet biophantoms), the measured mean intensity, U and X statistics are presented in Figure 4.2.

What needs to be solved is the following nonlinear system of equations:

$$E[I] = \bar{I}, U_{HK} = U, X_{HK} = X \tag{4.8}$$

where U and X are the measured values of the U and X statistics, respectively, and U_{HK} and X_{HK} the analytical expressions derived for the Homodyned-K distribution as a function of α and γ :

$$\begin{aligned} U_{HK}(\gamma,\alpha) = -\gamma_E - \log(\gamma+\alpha) + \Psi(\alpha) - \gamma^{\alpha}\frac{\Gamma(-\alpha)}{\alpha\Gamma(\alpha)}{}_1F_2(\alpha;1+\alpha,1+\alpha;\gamma) \\ +\gamma\frac{\Gamma(\alpha-1)}{\Gamma(\alpha)}{}_2F_3(1,1;2,2,2-\alpha;\gamma) \end{aligned} \tag{4.9}$$

$$X_{HK}(\gamma,\alpha)=\frac{(1+2\alpha)}{(\gamma+\alpha)}-\frac{2\gamma^{\alpha/2+1/2}}{(\gamma+\alpha)\Gamma(\alpha)}K_{\alpha+1}(2\sqrt{\gamma})+\frac{\gamma^{\alpha}}{(\gamma+\alpha)}\frac{\Gamma(-\alpha)}{\Gamma(\alpha)}{}_1F_2(\alpha;1+\alpha,1+\alpha;\gamma)$$
$$-\frac{\gamma^{\alpha+1}}{(\gamma+\alpha)}\frac{\Gamma(-1-\alpha)}{(1+\alpha)\Gamma(\alpha)}{}_1F_2(1+\alpha;2+\alpha,2+\alpha;\gamma)+\frac{\gamma}{(\gamma+\alpha)}{}_2F_3(1,1;2,2,1-\alpha;\gamma)$$
$$-\frac{\gamma}{(\gamma+\alpha)}\frac{\alpha\Gamma(-1+\alpha)}{\Gamma(\alpha)}{}_2F_3(1,1;2,2,2-\alpha;\gamma) \quad (4.10)$$

where γ_E is the Euler constant, Ψ is the digamma function, ${}_pF_q(a_1,\ldots a_p;b_1,\ldots b_q;z)$ is the generalized hypergeometric series, and K_p is the modified Bessel function of the second kind of order p. In order to avoid numerical errors, the following equivalent expressions are used for the implementation:

$$U_{HK}(\gamma,\alpha)=-\gamma_E-\log(\gamma+\alpha)+\Psi(\alpha)+\frac{\pi}{\sin(\pi\alpha)}\frac{\gamma^{\alpha}{}_1F_2(\alpha;1+\alpha,1+\alpha;\gamma)}{\alpha\Gamma(\alpha)\Gamma(\alpha+1)}$$
$$+\frac{\gamma}{\alpha-1}{}_2F_3(1,1;2,2,2-\alpha;\gamma) \quad (4.11)$$

for $\alpha>1$. If $\alpha<1$, the last term is replaced by $-\frac{\pi}{\sin(\pi(1-\alpha))}\frac{\gamma}{\Gamma(\alpha)\Gamma(2-\alpha)}{}_2F_3(1,1;2,2,2-\alpha;\gamma)$.

$$X_{HK}(\gamma,\alpha)=\frac{(1+2\alpha)}{(\gamma+\alpha)}-\frac{2\gamma^{\alpha/2+1/2}}{(\gamma+\alpha)\Gamma(\alpha)}K_{\alpha+1}(2\sqrt{\gamma})+\frac{\gamma^{\alpha}}{(\gamma+\alpha)}\times\{\frac{\Gamma(-\alpha)}{\Gamma(\alpha)}{}_2F_3(1,1;2,2,1-\alpha;\gamma)$$
$$-\frac{\pi}{\sin(\pi\alpha)}\frac{\gamma^{\alpha-1}{}_1F_2(\alpha;1+\alpha,1+\alpha;\gamma)}{\Gamma(\alpha)\Gamma(1+\alpha)}+\frac{\pi}{\sin(\pi(\gamma+\alpha))}\frac{\gamma^{\alpha}{}_1F_2(1+\alpha;2+\alpha,2+\alpha;\gamma)}{(1+\alpha)\Gamma(\alpha)\Gamma(2+\alpha)}$$
$$-\frac{\alpha}{(\alpha-1)}{}_2F_3(1,1;2,2,2-\alpha;\gamma)\} \quad (4.12)$$

for $\alpha>1$. If $\alpha<1$, the last term is replaced by $\frac{\pi}{\sin(\pi(1-\alpha))}\frac{\alpha}{\Gamma(\alpha)\Gamma(2-\alpha)}{}_2F_3(1,1;2,2,2-\alpha;\gamma)$.

Both the expressions (4.11) and (4.12) can be computed directly if α is not an integer. If α is an integer, the expressions are computed by interpolation of the values calculated for the value pairs (γ, α -10^{-7}) and (γ, α +10^{-7}).

For our MATLAB implementation, accelerating the algorithm was a necessity. Developing and simplifying the hypergeometric series that intervene in the expressions of X_{HK} and U_{HK} leads to considerable improvements. The hypergeometric series are implemented as:

$$ {}_2F_3(1,1;2,2,1-\alpha;\gamma)=\sum_{k=0}^{\infty}\frac{1}{(k+1)!(k+1)}\frac{1}{(1-\alpha)(2-\alpha)...(\mathrm{k}-\alpha)}\gamma^k \tag{4.13} $$

$$ {}_2F_3(1,1;2,2,2-\alpha;\gamma)=\sum_{k=0}^{\infty}\frac{1}{(k+1)!(k+1)}\frac{1}{(2-\alpha)(3-\alpha)...(\mathrm{k}+1-\alpha)}\gamma^k \tag{4.14} $$

$$ {}_1F_2(1+\alpha;2+\alpha,2+\alpha;\gamma)=\sum_{k=0}^{\infty}\frac{1+\alpha}{(2+\alpha)(3+\alpha)...(K+1+\alpha)^2}\frac{\gamma^k}{k!} \tag{4.15} $$

$$ {}_1F_2(\alpha;1+\alpha,1+\alpha;\gamma)=\sum_{k=0}^{\infty}\frac{\alpha}{(1+\alpha)(2+\alpha)...(1+\alpha)^2}\frac{\gamma^k}{k!} \tag{4.16} $$

Furthermore, because of practical considerations, the maximum value of α is limited and the problem becomes:

$$ (\varepsilon,\sigma,\alpha)=\arg\min\left|\mathrm{U}_{HK}-U\right|,\text{ with }\mu=\bar{\mathrm{I}},X_{HK}=X,\alpha\le\alpha_{\max} \tag{4.17} $$

In the initial study, $\alpha_{\max}$ was set to 80. In some of our experiments this value was changed, since we dealt with high concentrations and wished to allow a larger possible interval of values.

The fully developed speckle regime is defined by values of the X-statistics that are inferior to 1, while the partially developed speckle corresponds to values of the X-statistics that are superior to 1. Depending on this, the initial value of the parameter α is chosen. When $X\le 1$, $\alpha_0=\alpha_{\max}$. When $X>1$, $\alpha_0=1/(\mathrm{X}-1)$ or $\alpha_0=\alpha_{\max}$, the chosen value being the minimum of the two. Since both log-moments are monotonous functions (U as a function of α, X as a function of γ), this property is used in a iterative search which allows the estimation of the final values of the parameters α and γ. The main loop is an iteration on α, as long as $\mathrm{U}_{HK}>U$, and then a refinement of this result by dichotomy. This includes an iteration on γ, as long as $X_{HK}>X$, the final result being also obtained by dichotomy.

In order to obtain the values of the parameters, ε and σ, the following relations are used :

$$ \varepsilon^2=\mu\gamma/(\gamma+\alpha),\sigma^2=\mu/(2(\gamma+\alpha)) \tag{4.18} $$

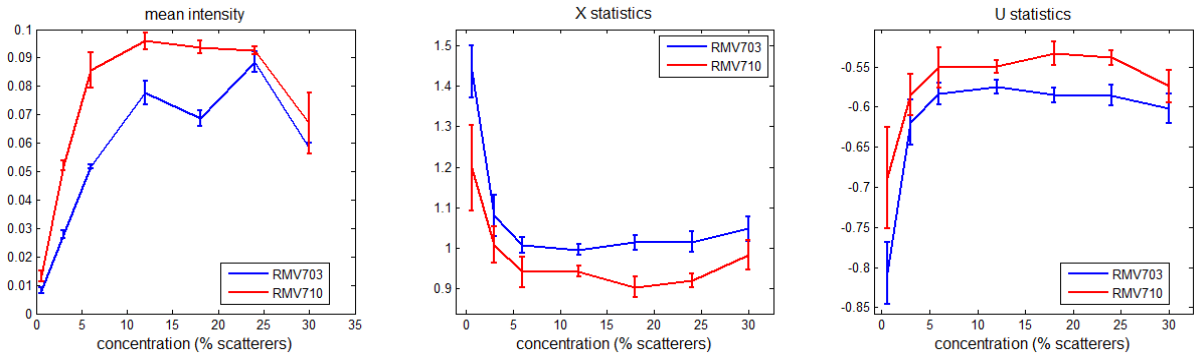

Figure 4.2 Mean intensity, X statistics and U statistics of the data extracted from the biophantoms

4.3 MODIFIED PROTOCOL: ATTENUATION COMPENSATION AND SIGNAL RECONSTRUCTION

The data that has been used for this chapter concerns mostly dense media, and results from imaging at high frequencies (>20 MHz). The simulations do not include attenuation, since it does not make the object of the study. For the acquisitions, this is impossible, and because of the high frequency equipment that has been used, the effects of the attenuation are no longer negligible, and therefore need to be compensated.

The measurement of the attenuation coefficient is done using a standard substitution method. For the first measure, a transducer is used to acquire the signal reflected by a plane, (preferably) metal surface after propagation through a reference medium with known attenuation α_{ref} (usually filtered/demineralized water). For the second measure, the settings are maintained unchanged, with the exception of the propagation medium, which is replaced by the medium with unknown attenuation (Figure 4.3). The spectrum of the first measured signal is the reference spectrum S_{ref}, and the one of the second signal gives the attenuated spectrum S_{meas}. The distance from transducer to reflector, D, is known, so the frequency-dependent attenuation coefficient is then computed as:

$$\alpha_{att}(f) = \alpha_{ref} + \frac{20}{2D}\log_{10}\left(\frac{S_{ref}(f)}{S_{meas}(f)}\right) \tag{4.19}$$

Assuming that the attenuation coefficient α_{att} (expressed in Np/(MHz*mm)) has a linear dependence on the frequency ($\alpha_{\text{att}} = \alpha_0 \cdot f$), the frequency-independent value α_0 is obtained by a linear regression of the measured values α_{att} to the interval of frequencies in the bandwidth.

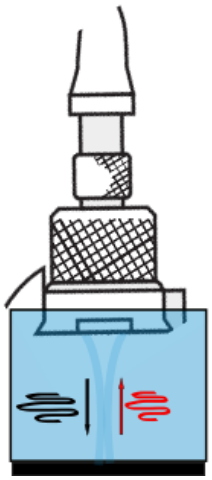

Figure 4.3 Attenuation measurement setup (blue: propagation medium, black: emitted signal, red: received attenuated signal)

Each RF line from the ROI is selected and processed for compensation. Point-compensation is applied to the power spectrum for each depth *d* and each frequency *f* in the passband (measured at -20 dB), with the measured attenuation coefficient α_0:

$$S_{comp}(d, f) = S_{raw}(d, f)\mathrm{e}^{4\alpha_{att} fd} \tag{4.20}$$

The compensated power spectrum is then used for the inversion. The phase information is conserved from the initial signal, so it is assumed that phase shifts do not occur. For a better precision, multiple non-overlapping windows are used; therefore the depth *d* will correspond to the center of each window. Examples are given in Figures 4.4 (1 window) and 4.5 (10 windows). When using 10 windows, the compensation (the difference signal) increases gradually with depth.

It should be noted that the attenuation of the cell pellet biophantoms is quite small, so that compensation will not greatly increase the signal amplitudes. For the case of the Orgasol phantoms, the difference is visible, as it can be seen in the two examples from the cited figures.

Using the Nakagami distribution exclusively for statistical modelling of ultrasound has proven to be very limited for dense media. The Homodyned-K distribution, on the other hand, shows promise with the possibility of determining statistical estimates related to the scatterer density even for Rayleigh (fully developed) speckle. The two have been compared previously, for example in (Mamou et al. 2011), for media creating different types of speckle. We have further tested the two models in simulations and different media that generate mostly fully developed speckle. The first study is applied on cell pellet biophantoms mimicking densely packed cells in tumors, a set of data previously used for another study concerning the structure factor published in (Franceschini et al. 2014). The results are compared in terms of discriminant power and precision.

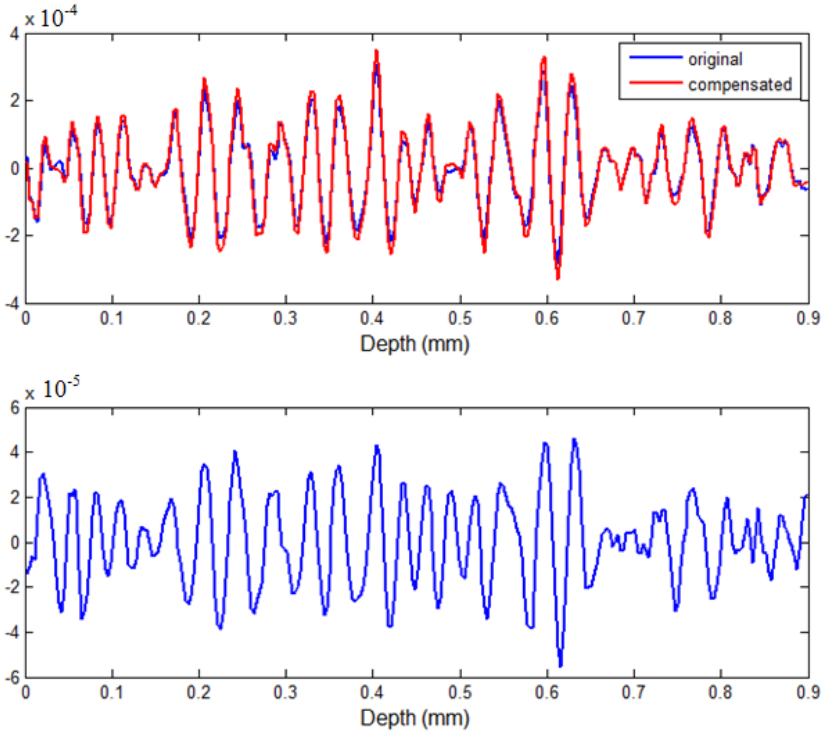

Figure 4.4 RF line compensated for attenuation in the 10-31 MHz bandwidth (α_{att}=0.07 dB/mm) using 1 window: (above) original and compensated signals (below) the difference.

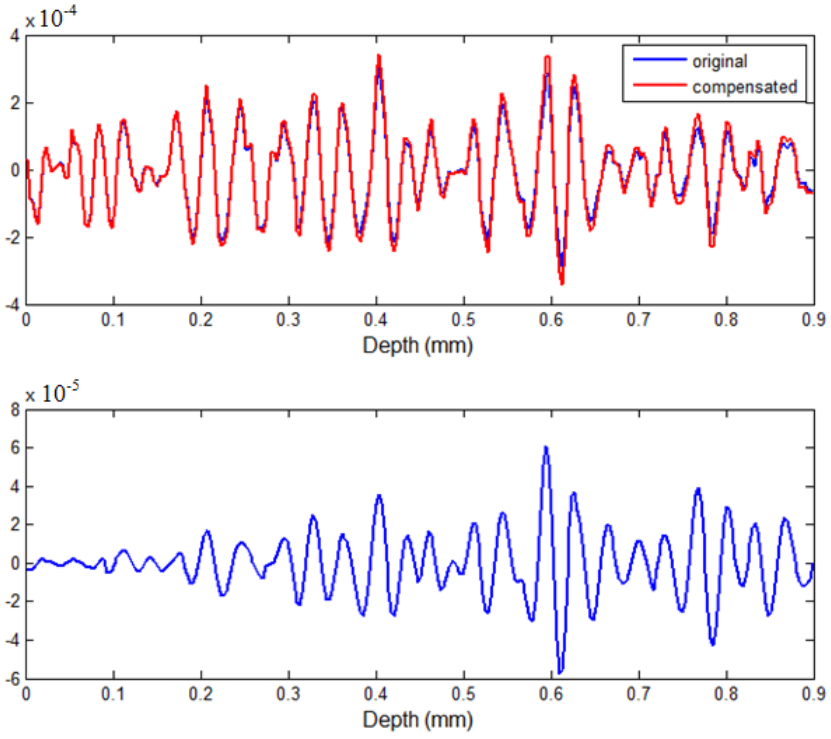

Figure 4.5 RF line compensated for attenuation in the 10-31 MHz bandwidth (α_{att}=0.07 dB/mm) using 10 windows (above) original and compensated signals (below) the difference

4.4 COMPARATIVE STUDY USING THE NAKAGAMI AND HOMODYNED-K DISTRIBUTIONS

4.4.1 Experimental Data and Equipment

The backscattered signals from biophantoms were obtained from the experiments described in section III of Franceschini et al. (2014), which are briefly summarized here. Experimental data were acquired from concentrated cell pellet biophantoms that consisted of identical human leukemia K562 cells embedded in a plasma-thrombin supportive background with various whole cell concentrations ranging from 0.006 to 0.3 (0.6% to 30%):0.006, 0.03, 0.06, 0.12, 0.18, 0.24 and 0.30 . The mean whole cell size is 6.34 ± 0.94 μm. US measurements were acquired using a Vevo 770 high frequency ultrasound system (VisualSonics Inc., Toronto, Canada). Two single-element spherically-focused transducers (i.e., RMV710 and RMV703) were used to acquire RF data from each biophantom. The RMV710 and the RMV703 transducers have center frequencies of 25 and 35 MHz, focuses at 15 and 10 mm and f-numbers of 2.1 and 2.5, respectively. For each phantom, acquisitions were performed at six different locations separated by 0.6 mm. Examples of the envelopes resulted from acquisitions using both probes are shown in Figures 4.11 and 4.12.

4.4.2 Signal Processing

Each ROI of size 0.75 mm (depth, centered at the focal point) x 0.5-1.0 mm (width) was preprocessed prior to the estimation of the envelope parameters (Figure 4.6). First, RF data were compensated for attenuation effects. The measured attenuation coefficients α_{att} for the cell pellet concentrations of 0.06, 0.12, 0.18, 0.24, and 0.30 are 0.0098, 0.0184, 0.0215, 0.0202, and 0.0280 dB MHz^{-1} mm^{-1}, respectively (see section III.C in Franceschini et al. (2014)). Point attenuation correction (Oelze and O'Brien (2002)) was applied to the power spectrum of each RF echo line, according to eq (1.30). The attenuation of the intervening medium (water) was ignored. The compensated RF signals were then filtered in the 10-32 MHz bandwidth for the RMV 710 and 18-42 MHz bandwidth for the RMV 703 transducer. The filtered signals were envelope-detected and parameter estimation was performed as described in section 2.

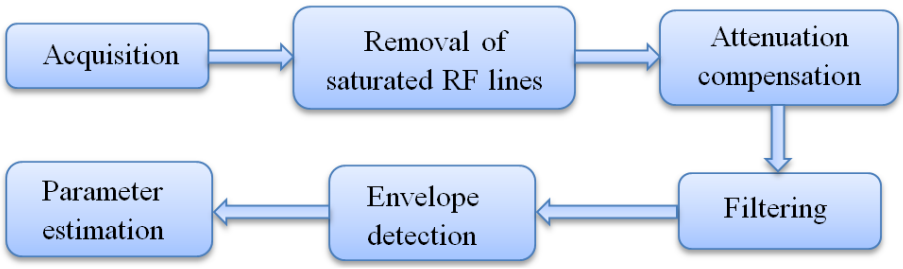

Figure 4.6 Schematic of the signal processing chain applied on the biophantom data

The resulting parameters are presented and discussed step by step as a function of concentration, and then as a function of the scatterer concentration per resolution cell. The resolution cell (Figure 4.7) was considered to be an ellipsoid with diameters equal to the system resolution in each of the three dimensions. The respective resolutions are considered as the FWHM (Full Width at Half Maximum) of the main lobe of the PSF envelope in each direction (Chapter 3, Section 4). Figure 4.10 offers an illustration of the axial resolution limit with the chosen convention. Thus, the estimated resolution cell volumes are 0.00071 mm^3 for the RMV 710, and 0.00031 mm^3 for the RMV 703.

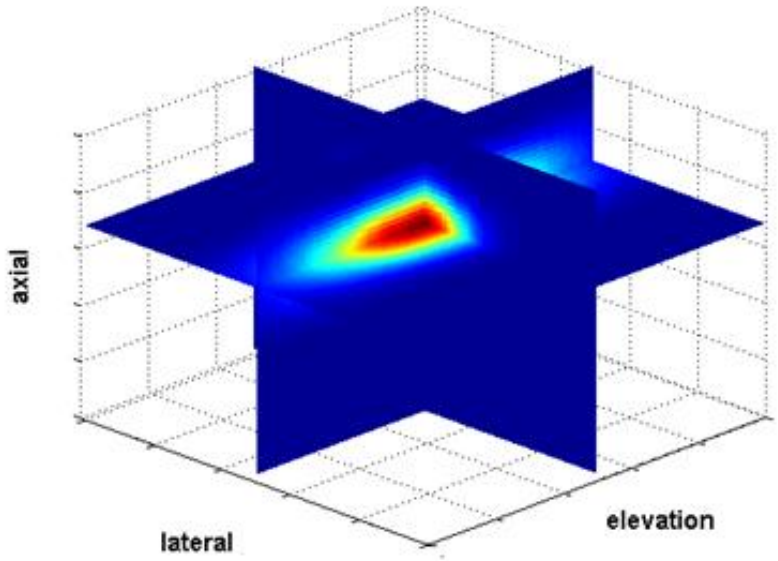

Figure 4.7 3D Resolution cell model, equivalent to ae system PSF (Field II simulation)

4.4.3 Analysis and Results

The estimated parameters for the Nakagami distribution are presented in Figure 4.11. As the theory predicts, the values of the parameter *m* increase as a function of scatterer concentration. However, *m* saturates very rapidly around 1 (corresponding to a Rayleigh distribution) and does not discriminate between biophantoms when the density is at least 6%. We can also observe that there is nearly no difference between the data acquired with the two probes, so the fully developed speckle regime is reached very fast. The scale parameter (or mean intensity) measures the backscattered echo and also increases with concentration, before decreasing for the very high concentrations (25% and 30%). For these very high concentration values, and especially at the higher frequencies (the RMV 703 probe), the effect of the attenuation is so strong that the energy conveyed by the frequencies at the higher end of the bandwidth is entirely absorbed, generating a decrease in the level of backscattered energy. Another phenomenon that is also non-negligible at

high concentrations is the increasing destructive interference due to particle agglomeration, which the models do not take into account.

On the other hand, the Homodyned-K α parameter continues to increase, but the estimation has a lower precision (Fig. 4.13). Large variability for dense media corresponding to high values of α can be explained by the Cramer Rao bound (Chapter 3 of (Kay 1993)), which stipulates that the variance of a non-biased estimator for a parameter α of the distribution is at least equal to the inverse Fischer information $I(\alpha)$ available for that parameter:

$$I(\alpha) = -E\frac{\partial^2 \ln p(x;\alpha)}{\partial \alpha^2} \tag{4.21}$$

where $p(x;\alpha)$ is the likelihood function for α. The expression of the Fischer information is difficult to develop analytically, but numerical simulations show a dependence on $1/\alpha^2$ (Figure 4.9). Therefore, the estimation variance increases an increasing value of α.

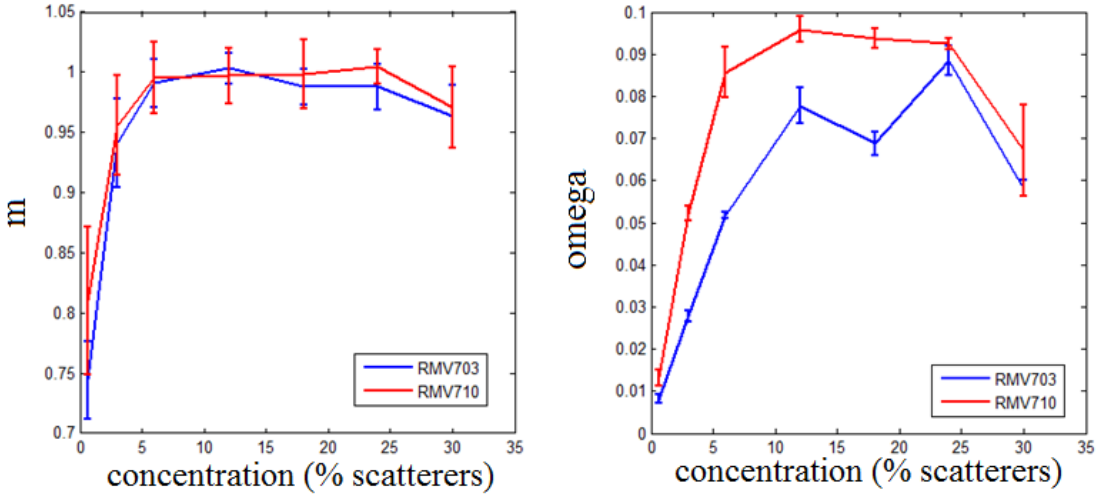

Figure 4.8 Nakagami parameters estimated from the cell pellet biophantoms

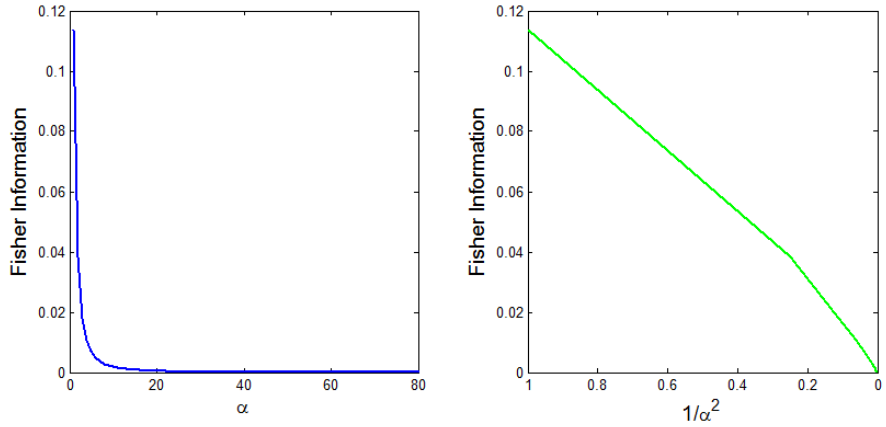

Figure 4.9 Fisher information for the parameter α (Numerical simulation)

As to the parameters that describe the distribution scale, or the power parameters, we represent the diffuse power $2\sigma^2\alpha$ and coherent power ε^2. The coherent component power increases with concentration and then appears to be constant for concentrations superior to 12%. The diffuse power follows a trend that is very similar to the one of the total power, and also constitutes the dominant component of the total power.

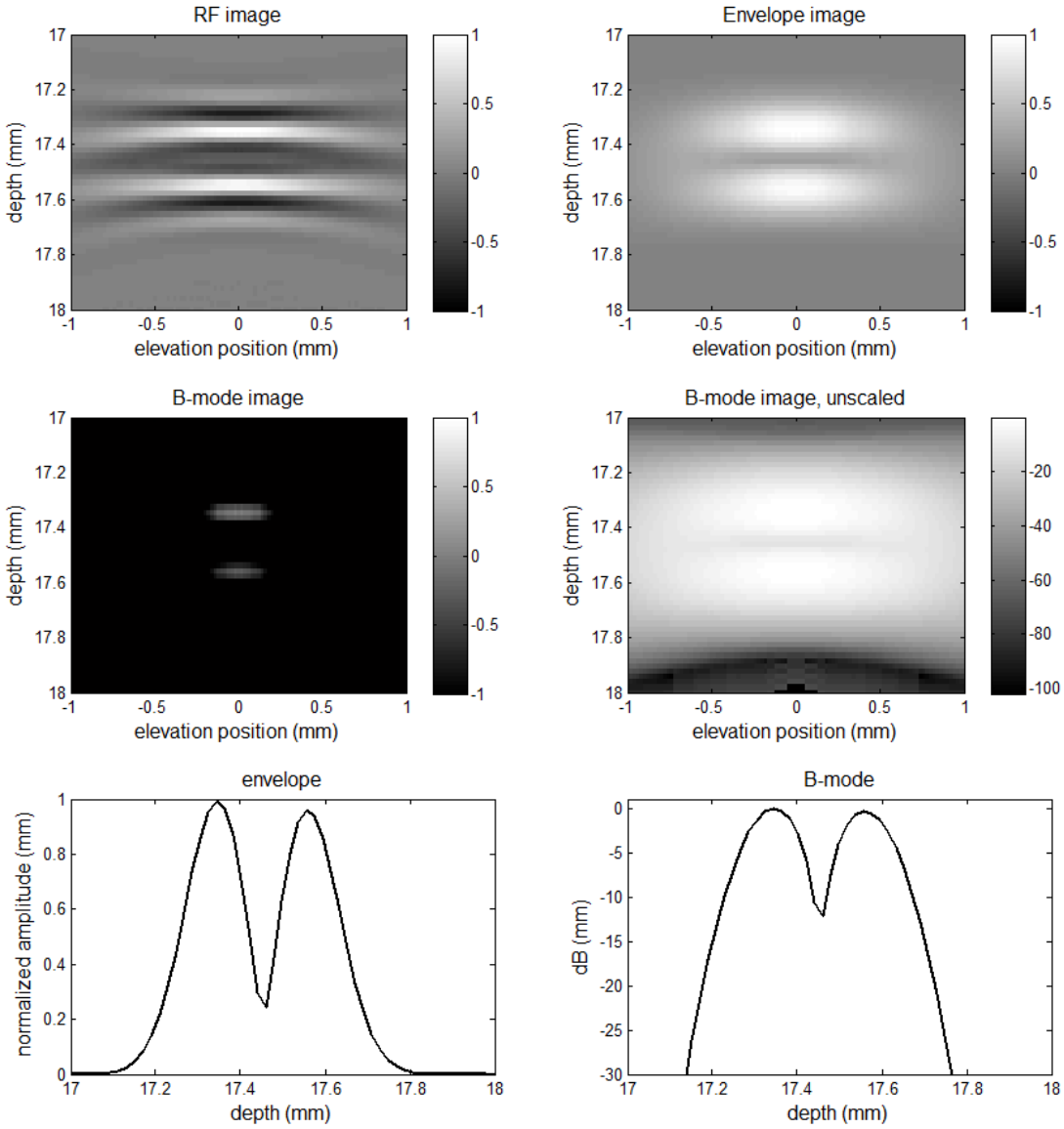

Figure 4.10 Axial resolution limit in the case of the chosen convention, for the RMV 703 probe. The two targets are placed at a distance equal to the axial (depth) resolution.

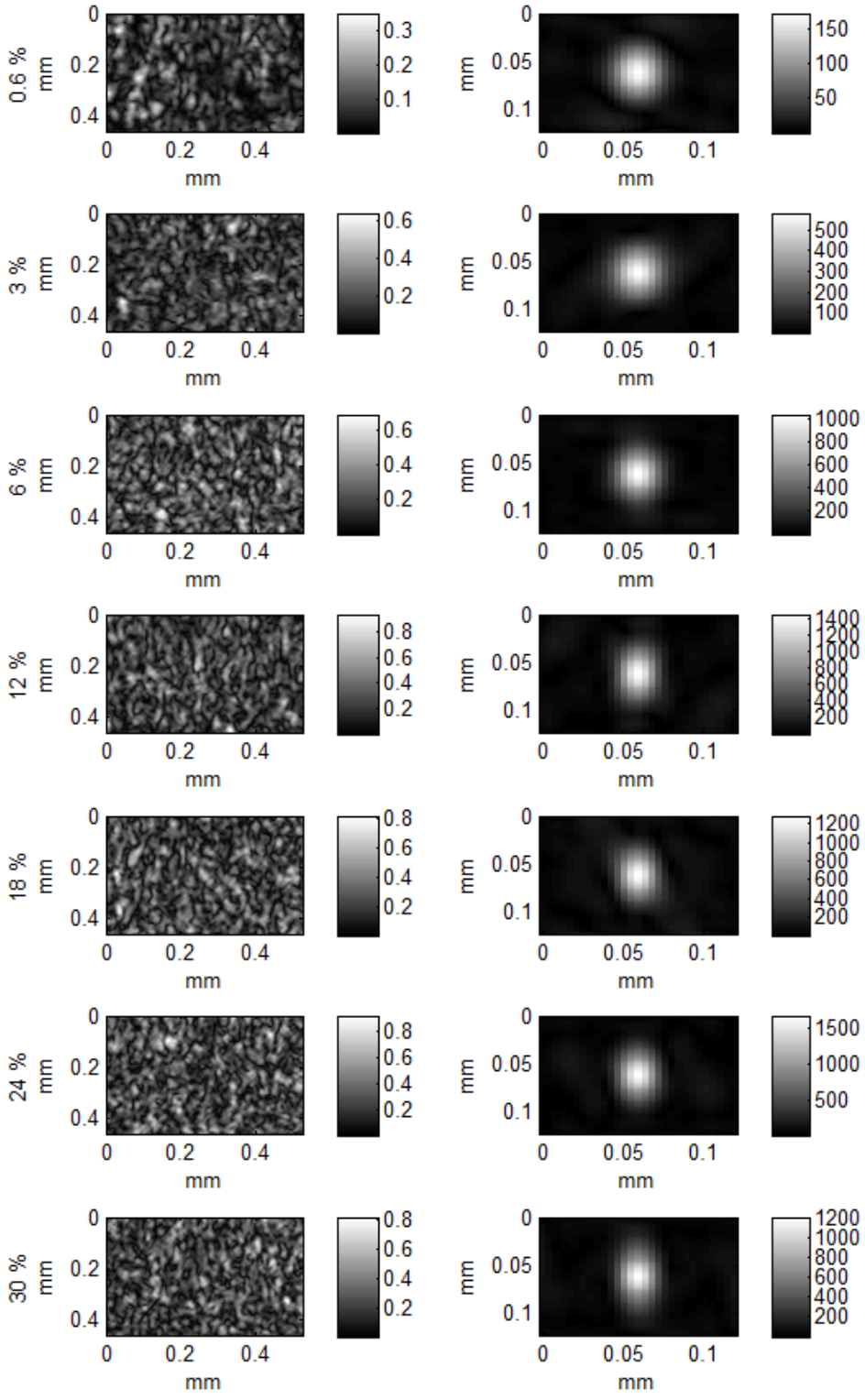

Figure 4.11 (left) Extracts of non-processed envelope images of all the biophantoms (right) corresponding speckle size approximated by the autocorrelation cell (RMV 703 probe).

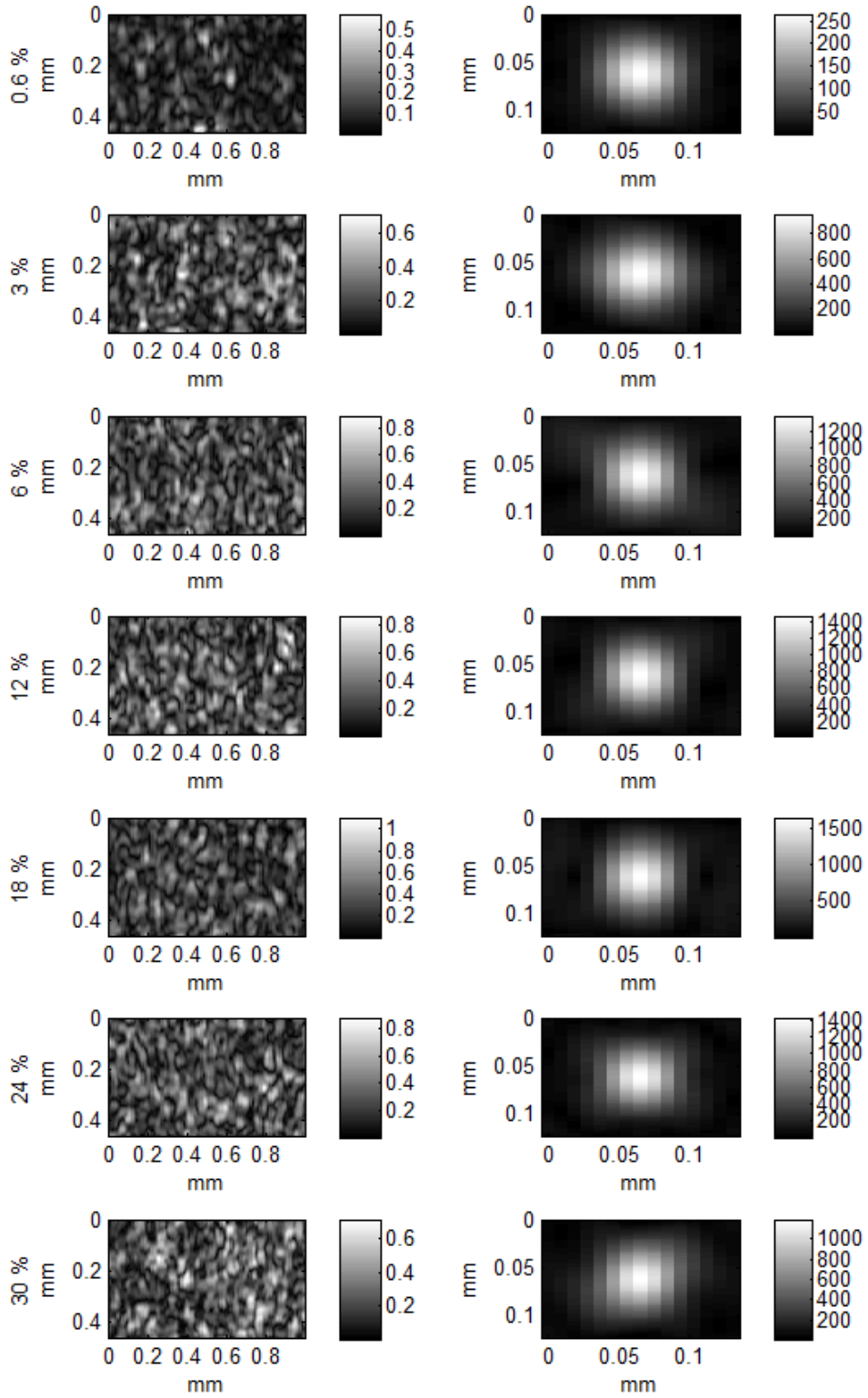

Figure 4.12 (left) Extracts of non-processed envelope images of all the biophantoms (right) corresponding speckle size approximated by the autocorrelation cell (RMV 710 probe).

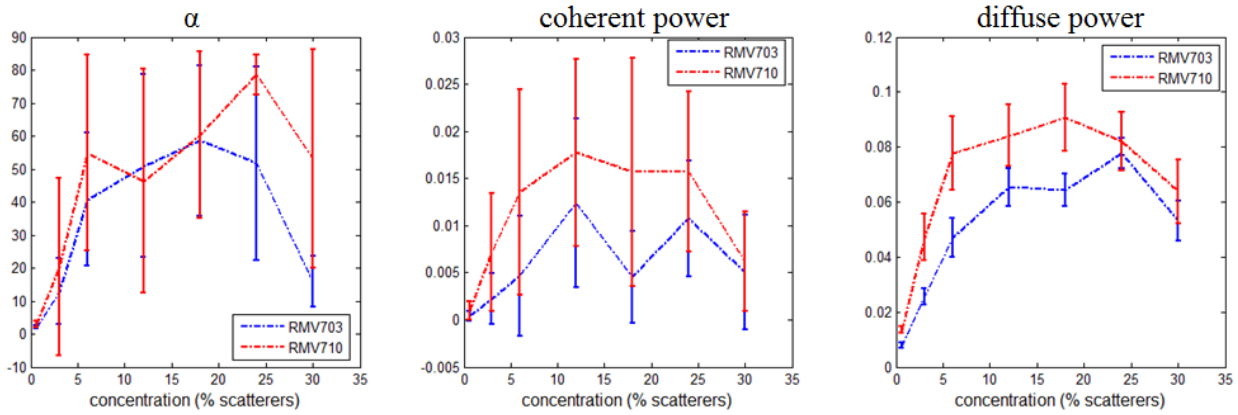

Figure 4.13 Estimated Homodyned-K parameters for the cell pellet biophantoms as a function of scatterer density

Figures 4.14 and 4.15 illustrate the evolutions of all the parameters as a function of scatterer density per resolution cell. This is relevant especially for the shape parameters. Saturation for the m parameter indeed appears around 10 scatterers/resolution cell, while α does continue to increase to a limit that varies for the two probes, suggesting that imaging system (or frequency) specific phenomena may occur. For fully developed speckle, even as α increases, its estimation seems unreliable for the amount of data that has been taken into consideration.

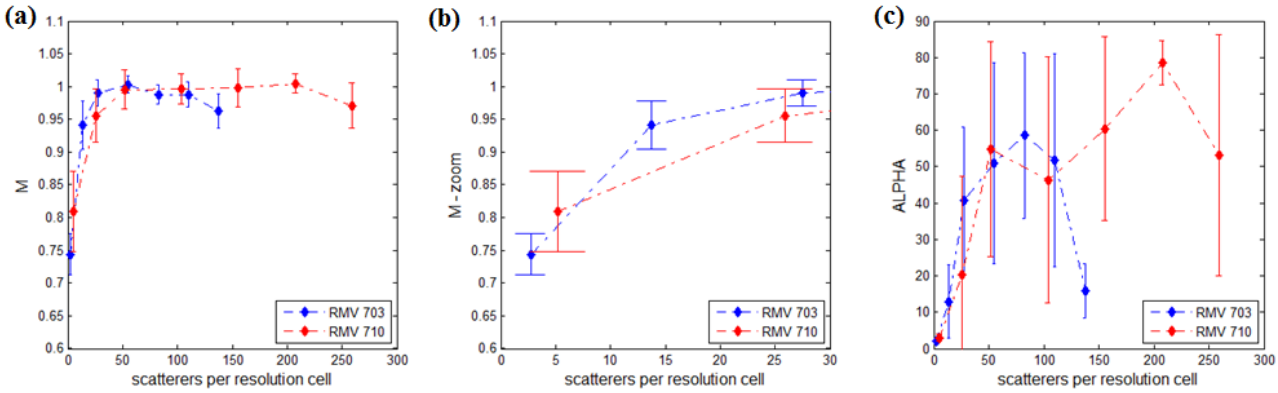

Figure 4.14 Estimated shape parameters for the two models as a function of the number of scatterers per resolution cell (a) Nakagami parameter m (b) Nakagami parameter m – zoom on low concentrations (c) Homodyned-K parameter α

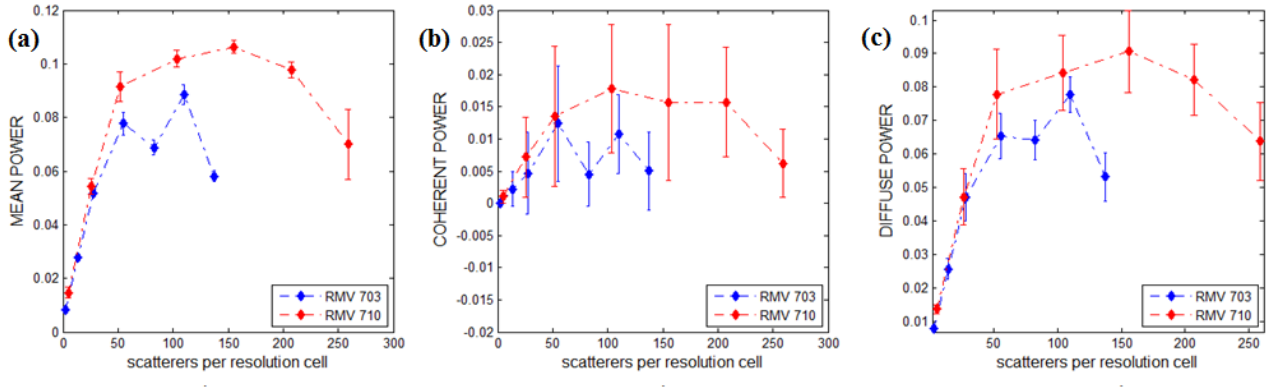

Figure 4.15 Signal power as a function of the number of scatterers per resolution cell, computed using the estimated scale parameters for the two models (a) mean power (Nakagami parameter Ω) (b) coherent power (using Homodyned-K parameters: ε^2) (c) diffuse power (using Homodyned-K parameters: $2\sigma^2\alpha$)

4.4.4 Conclusion and Perspectives

Following this analysis and our previous experiments, the use of the Nakagami distribution seems limited to partially developed speckle, whereas using the Homodyned-K (HK) distribution can offer supplementary information when dealing with fully developed speckle. We consider that fully developed speckle is generated by "concentrated media" - in this study, starting from a volume concentration of only 6% scatterers, equivalent to approx. 10 scatterers per resolution cell at working frequencies of 25-30 MHz.

For this reason, it could prove valuable for precise tissue characterization of tumors or blood. However, the estimation results are highly variable for fully developed speckle, as also stated for the HK estimator presented and used in (Hruska and Oelze 2009). This can be explained partly by the fact that the data histograms for high concentrations are very similar between each other (Figure 4.16).

A more elaborate validation is required in order to assess the conditions in which these results are reliable.

A combined characterization and validation of the XU estimator is performed on simulated ultrasound images and phantoms where scatterer concentrations are precisely controlled. The purpose is to attempt to establish a so-called "confidence interval" (in scatterers per resolution cell) for the use of the Homodyned-K distribution.

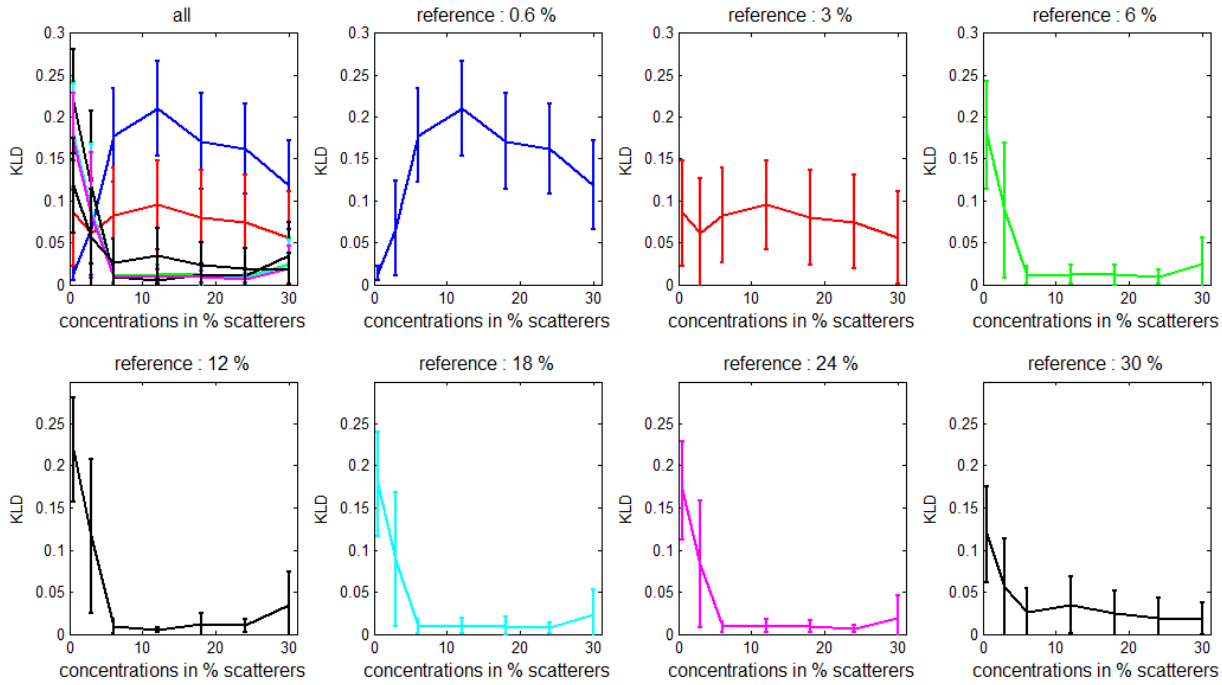

Figure 4.16 Mean values and standard deviations of the Kullback-Leibler divergence between the envelope histograms for the seven analyzed concentrations, by taking each of them as reference.

4.5 THE EFFECT OF THE SAMPLE SIZE AND SAMPLE CORRELATION ON THE HOMODYNED-K PARAMETER ESTIMATION USING THE XU ESTIMATOR

Previous tests have shown that the Homodyned-K parameters can offer some information on fully developed speckle, but the estimates show high variability. Based on estimator theory, this can be improved by selecting a large number on uncorrelated independent identically distributed (i.i.d.) samples in a ROI. In order to assign numerical values to these quantities, we conduct an analysis on simulated i.i.d. samples from Homodyned-K distributions with different sets of parameters. The parameter α is the main interest, therefore it is the one that varies in simulation. Estimations are conducted on the simulated data, and the biases and variances are extracted. These results are the n compared with a set of simulated ultrasound images, and of experimental data obtained from Orgasol particle phantoms and cell pellet biophantoms.

4.5.1 Estimations on Simulated Independent, Identically Distributed Homodyned-K Samples

The main parameter that we focus on is α, whose estimation also influences the estimation of the other two parameters of the distribution (eq 4.18).

The first step is to conclude whether the estimator is consistent for a range of values of α which have been shown to occur in practical situations. A consistent estimator for a parameter θ is an estimator that converges to the real value of θ for a number of samples that is sufficiently large ([Lehman Casella 1983 – Definition 8.1]).

For the test, we divide the values of α into two intervals: 1-20 (typical values corresponding to low-density media) and 30-80 (high density media, here we limit α to 80, for reasons explained in (Destrempes, Porée, and Cloutier 2013)).

The simulations of the i.i.d. samples are conducted according to the following law:

$$x_i = \sqrt{\left(\varepsilon + X\sigma\sqrt{z/\alpha}\right)^2 + \left(\varepsilon + Y\sigma\sqrt{z/\alpha}\right)^2} \tag{4.22}$$

where x_i is each i.i.d. HK sample, X and y are i.i.d. samples of the unit Gaussian distribution and z is a sample of the gamma distribution with shape parameter α and scale parameter 1. This can be deducted from the compound form of the HK distribution (eq. 1.22).

The secondary purpose of the test is to assess the variance of the estimates, also as a function of the number of samples. We know that the Fischer information ([Lehman Casella 1983 5.10 – pg. 115]) available for the parameter α of the Homodyned-K distribution decreases with the square of α (Figure 4.12), therefore we expect very large variations for large values of α.

For "small" values of α, the mean values and standard deviations are represented in Figure 4.17. Tables 4-1 to 4-4 contain these values, as well as the biases and SNRs (computed and the ratio of the mean and standard deviation). For "large" values of α, the analog representations are in Figure 4.18 and tables 4-5 and 4-6. We remind that the XU estimator estimates the values of the clustering parameter α and of the algorithmic parameter γ. The bias γ of affects the estimation of ε more than that of σ (eq 1.18). This can explain the larger bias of ε, compared to that of σ. Increasing the sample size visibly reduces both the bias and the variance of the estimates.

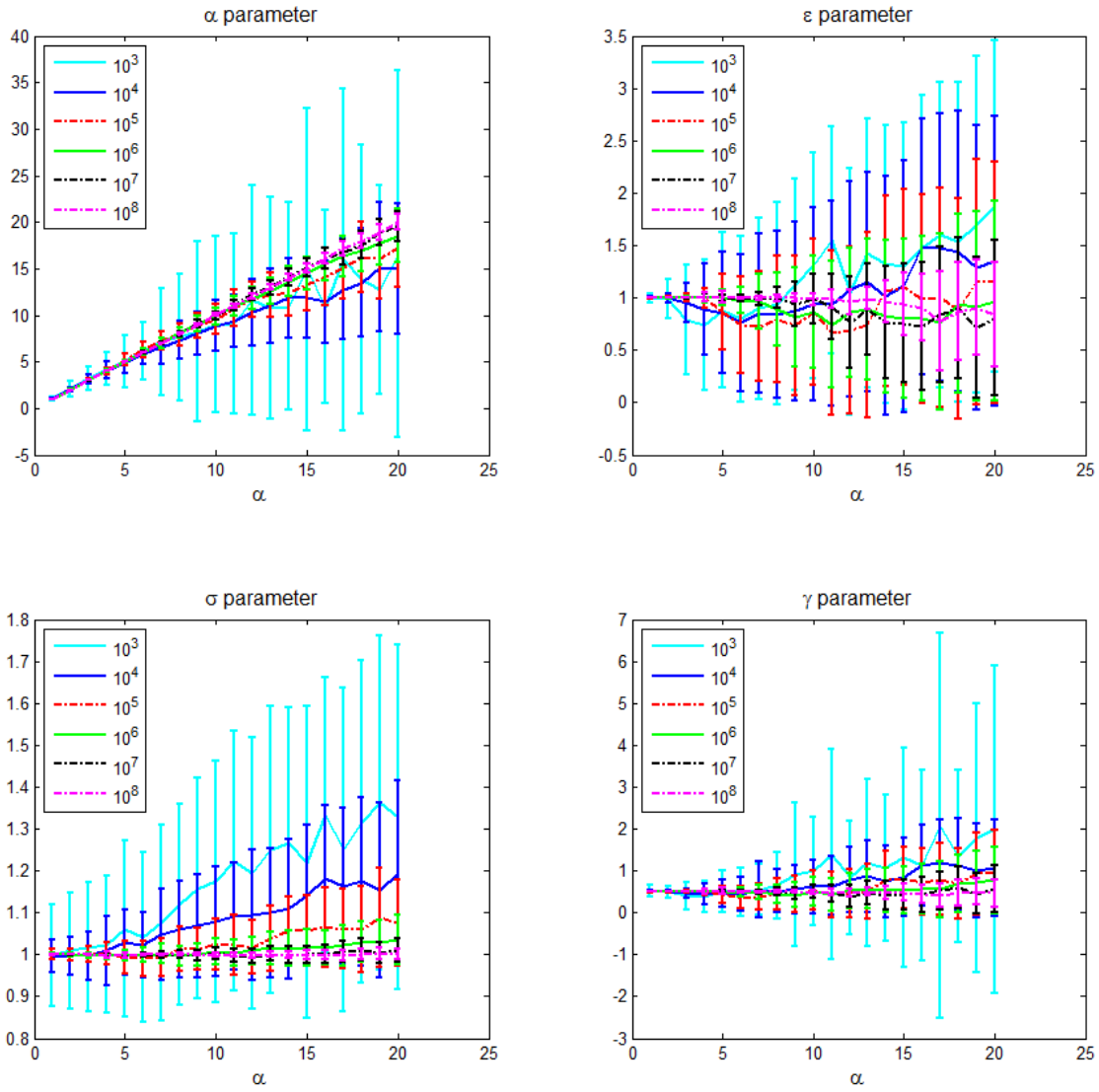

Figure 4.17 Estimation results for the parameters α, ε, σ and γ as a function of α and the number of i.i.d. samples (α from 1 to 20, ε=1, σ=1, number of realizations for each value of α: 100)

Nb of samples/ Alpha	1	2	3	4	5	6	7	8	9	10
10^3	1.04/ 0.04	2.11/ 0.11	3.21/ 0.21	4.24/ 0.24	5.06/ 0.06	6.18/ 0.18	7.16/ 0.16	7.62/ -0.38	8.31/ -0.69	9/ -1
10^4	1.01/ 0.01	2.03/ 0.03	3.09/ 0.09	4.06/ 0.06	4.82/ -0.18	5.88/ -0.12	6.51/ -0.49	7.32/ -0.68	8.07/ -0.93	8.83/ -1.17
10^5	1/ 0	2/ 0	3/ 0	3.98/ -0.02	5.18/ 0.18	6.3/ 0.3	7.28/ 0	7.9/ 0.11	8.89/ -0.11	9.57/ -0.43
10^6	1/ 0	2/ 0	3.01/ -0.01	4.01/ -0.01	5.01/ -0.01	6.05/ 0.05	7/ 0	8.11/ 0.11	9.1/ 0.1	9.89/ -0.11
10^7	1/ 0	2/ 0	3/ 0	4/ 0	5.01/ 0.01	6.02/ 0.02	7.02/ 0.02	8/ 0	9.09/ 0.09	9.94/ -0.06
10^8	1/ 0	2/ 0	3/ 0	4/ 0	5/ 0	6.01/ 0.01	7/ 0	8.01/ 0.01	8.99/ -0.01	10.03/ 0.03

Table 4-1 Mean values / biases of the α estimates obtained from simulated independent, identically-distributed samples as a function of the sample number (α from 1 to 10)

Nb of samples/ Alpha	11	12	13	14	15	16	17	18	19	20
10^3	9.05/ -1.95	11.56/ -0.44	10.79/ -2.21	10.98/ -3.02	14.93/ -0.07	10.93/ -5.07	15.91/ -1.09	13.82/ -4.18	12.72/ -6.28	16.59/ -3.41
10^4	9.4/ -1.6	10.29/ -1.71	10.99/ -2.01	11.84/ -2.16	11.84/ -3.16	11.45/ -4.55	12.79/ -4.21	13.49/ -4.51	15.19/ -3.81	14.99/ -5.01
10^5	10.74/ -0.26	11.73/ -0.27	12.2/ -0.8	12.41/ -1.59	13.29/ -1.71	14.13/ -1.87	15.11/ -1.89	16.23/ -1.77	16.07/ -2.93	17.22/ -2.78
10^6	11.02/ 0.02	11.78/ -0.22	12.58/ -0.42	13.61/ -0.42	14.53/ -0.47	15.47/ -0.57	16.32/ -0.68	16.88/ -1.12	17.81/ -1.19	18.54/ -1.46
10^7	11.07/ 0.07	12.25/ 0.25	12.97/ -0.03	14.12/ 0.12	15.09/ 0.09	16.05/ 0.05	16.74/ -0.26	17.55/ -0.45	18.94/ -0.06	19.57/ -0.43
10^8	11.03/ 0.03	12.07/ 0.07	12.99/ -0.01	14.04/ 0.04	15.02/ 0.02	16.08/ -0.08	17.18/ 0.18	17.99/ -0.01	18.93/ -0.07	20.01/ 0.01

Table 4-2 Mean values / biases of the α estimates obtained from simulated independent, identically-distributed samples as a function of the sample number (α from 11 to 20)

Nb of samples/ Alpha	1	2	3	4	5	6	7	8	9	10
10^3	0.22/ 4.71	0.82/ 2.58	1.23/ 2.6	1.76/ 2.41	2.78/ 1.82	3.08/ 2	5.73/ 1.25	6.75/ 1.13	9.67/ 0.86	9.44/ 0.95
10^4	0.07/ 14.91	0.2/ 10.2	0.47/ 6.5	0.92/ 4.4	1.08/ 4.45	1.21/ 4.87	1.75/ 3.73	2.04/ 3.6	2.29/ 3.52	2.74/ 3.23
10^5	0.02/ 46.6	0.06/ 34.57	0.14/ 21.97	0.29/ 13.65	0.64/ 8.06	0.79/ 7.93	0.97/ 7.48	1.19/ 6.65	1.28/ 6.92	1.57/ 6.08
10^6	0.01/ 150	0.02/ 98.8	0.05/ 60.5	0.1/ 39	0.16 30.4	0.33/ 18.2	0.53/ 13.2	0.61/ 13.3	0.8/ 11.4	0.95/ 10.35
10^7	0/ 229.27	0.01/ 304.19	0.02/ 187	0.02/ 184	0.04/ 112	0.1/ 61.19	0.15/ 46.36	0.26/ 31.13	0.4/ 22.93	0.45/ 21.91
10^8	0/ 220.8	0/ 1339	0.01/ 523	0/ 1244	0/ 1379	0.03/ 193	0.05/ 155	0.07/ 107	0.09/ 97.8	0.14/ 69.8

Table 4-3 Standard deviations / SNRs of the α estimates obtained from simulated independent, identically-distributed samples as a function of the sample number (α from 1 to 10)

Nb of samples/ Alpha	11	12	13	14	15	16	17	18	19	20
10^3	9.69/ 0.93	12.34/ 0.94	11.89/ 0.91	11.15/ 0.98	17.32/ 0.86	10.35/ 1.06	18.39/ 0.87	14.46/ 0.96	11.25/ 1.13	19.68/ 0.84
10^4	2.84/ 3.32	3.59/ 2.87	3.98/ 2.76	4.27/ 2.78	4.33/ 2.74	4,4/ 2.6	5,44/ 2.35	5,81/ 2.32	6,96/ 2.18	7/ 2.14
10^5	1,94/ 5.5	1,9/ 6.18	2,36/ 5.18	2,5/ 4.96	2,76/ 4.82	3,14/ 4.5	3,38/ 4.47	3,73/ 7.65	4,28/ 3.75	4,16/ 4.14
10^6	1,07/ 10.26	1,18/ 9.95	1.43/ 8.82	1.63/ 8.35	1.74/ 8.35	1.8/ 8.62	2.16/ 7.55	2.21/ 7.65	2.48/ 7.18	2.83/ 6.54
10^7	0.57/ 19.5	0.69/ 17.77	0.78/ 16.65	0.91/ 15.51	0.99/ 15.25	1.14/ 14.13	1.3/ 12.87	1.43/ 12.25	1.39/ 13.64	1.61/ 12.18
10^8	0.21/ 52.6	0.270/ 45	0.28/ 46.2	0.39/ 36	0.52/ 28.8	0.56/ 28.57	0.75/ 22.82	0.79/ 22.88	0.81/ 23.25	0.85/ 23.56

Table 4-4 Standard deviations / SNRs of the α estimates obtained from simulated independent, identically-distributed samples as a function of the sample number (α from 11 to 20)

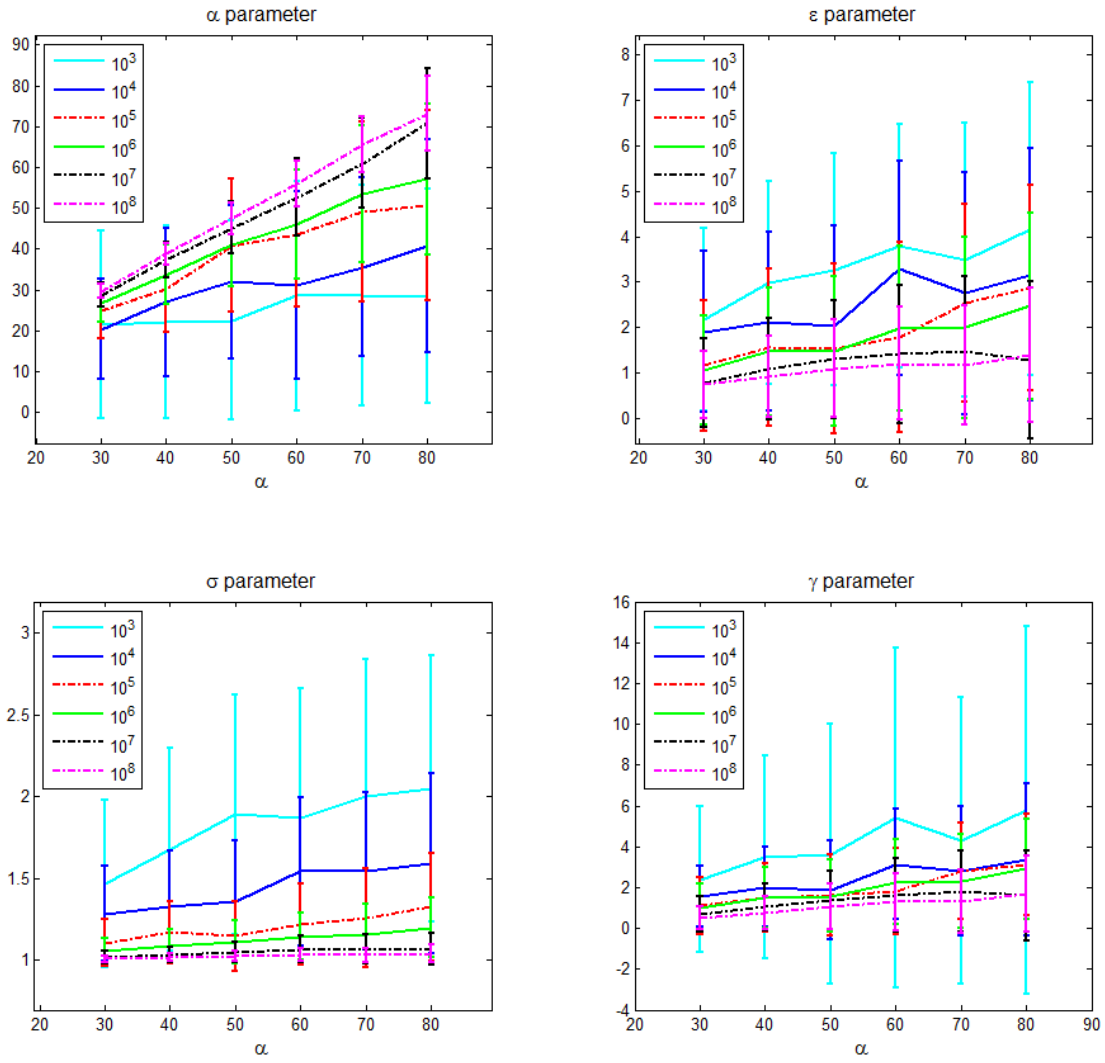

Figure 4.18 Estimation results for the parameters α, ε, σ and γ as a function of α and the number of i.i.d. samples (α from 30 to 80 in increments of 10, ε=1, σ=1, number of realizations for each value of α: 100)

Nb of samples/ Alpha	30	40	50	60	70	80
10^3	22.6/-8.4	22.13/-17.87	22.59/-27.41	28.54/-31.46	28.66/-41.34	28.38/-51.62
10^4	20.3/-9.7	27/-13	33/-17	31/-29	35.5/-34.5	40.8/-39.2
10^5	25/-5	30/-10	40.8/-9.2	43.7/-16.3	49.1/-20.9	50/-30
10^6	26.8/-3.2	33.7/-6.3	41.1/-8.9	46.2/-13.8	53.5/-16.5	57.1/-22.9
10^7	28.8/-1.2	37.3/-2.7	45.2/-4.8	52.7/-13.3	61.1/-8.9	70.8/-9.2
10^8	29.7/-0.3	38.8/-1.2	47.5/-2.5	56/-4	65.6/-4.4	73.2/-6.8

4-5 Mean values / biases of the α estimates obtained from simulated independent, identically-distributed samples as a function of the sample number (α from 30 to 80)

Nb of samples/ Alpha	30	40	50	60	70	80
10^3	23.01/0.94	23.62 /0.94	24.44/0.92	28.07/1.02	27.14/1.06	26.22/1.08
10^4	12.2/1.6	18.2/1.5	18.7/1.7	23/1.3	22/1.6	25.1.6
10^5	6.7/3.7	10.7/2.8	16.3/2.5	17.7/2.4	22.1/2.2	23.2/2.2
10^6	4.7/5.7	7.2/4.6	10.2/4	13.3/3.5	16.6/3.2	18.5/3
10^7	3/9.6	4/8.6	6.3/7.2	9.4/5.6	11.1/5.4	13.6/5.2
10^8	1.6/18.3	2.6/15	4/11.8	5.6/10	6.9/9.5	9/8

Table 4-6 Standard deviations/SNRs of the α estimates obtained from simulated independent, identically-distributed samples as a function of the sample number (α from 30 to 80)

By analyzing the previous tables and figures, or the alternative representations of the bias, relative and absolute bias in Figures 4.19 and 4.20, we can conclude that the estimator is unbiased, as the bias tends to 0 for very large values of the sample number.

For the smallest samples size, 1000, and alpha values ranging from 1 to 20, the relative bias varies greatly and randomly between 1 and 20. For the next sample size, 10000, its mean value is -0.12, which means a 12% underestimation. With increasing sample size, the mean relative biases are: -0.045, -0.017, -0.0005 and 0.0014. The absolute relative bias has a monotonic decrease: 0.12, 0.057, 0.02, 0.0068, 0.002, so it would be preferable to use it as a metric.

For alpha ranging from 30 to 80, the values of the absolute relative bias are, respectively: 0.5, 0.41, 0.25, 0.2, 0.09, and 0.05. While a 5% underestimation (all here were underestimates) would be almost perfect, it is difficult to imagine a situation where we could have access to 10^8 independent samples in practice. In practice, more feasible values are in the range of 1000-10000. With relative biases reaching 50% for alpha values larger than 30, it is obvious that the estimates would be unreliable for tissue characterization in these conditions. A feasible strategy would be to join the number of samples obtained from multiple acquisitions (for example multiple zones of a medium), under the assumption oh homogeneity of the scatterer density of the medium.

Regarding the number of realizations (or repetitions) of the same distribution needed to compute a stable mean value and variance, we conclude that 100 are sufficient, because an increase starting from this value leads neither to a reduction of the bias, nor of the variance (Figure 4.21).

An interesting observation is that the bias is negative for almost every case (and always for the range of "large" values, between 30 and 80). Therefore, underestimations are expected for a small number of samples. We will use this observation in the last part of the study, by increasing the number of samples in order to minimize this negative bias.

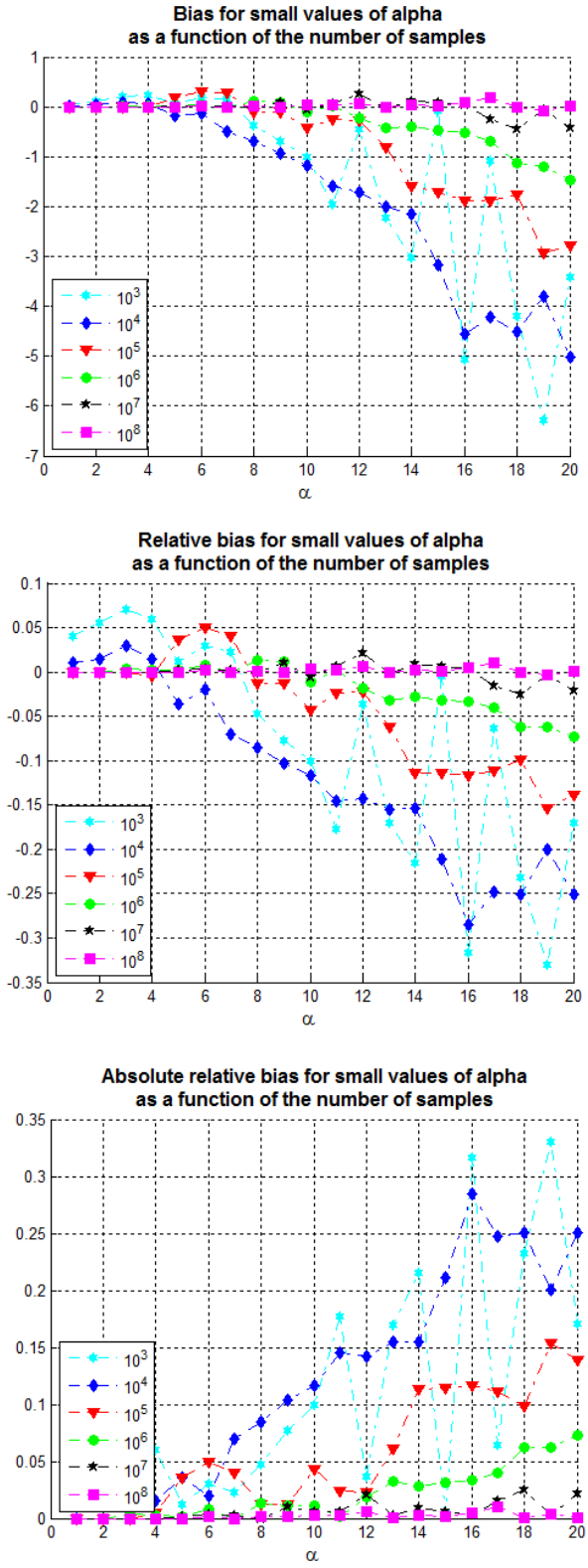

Figure 4.19 Bias, relative bias and absolute relative bias for values of α ranging from 1 to 20

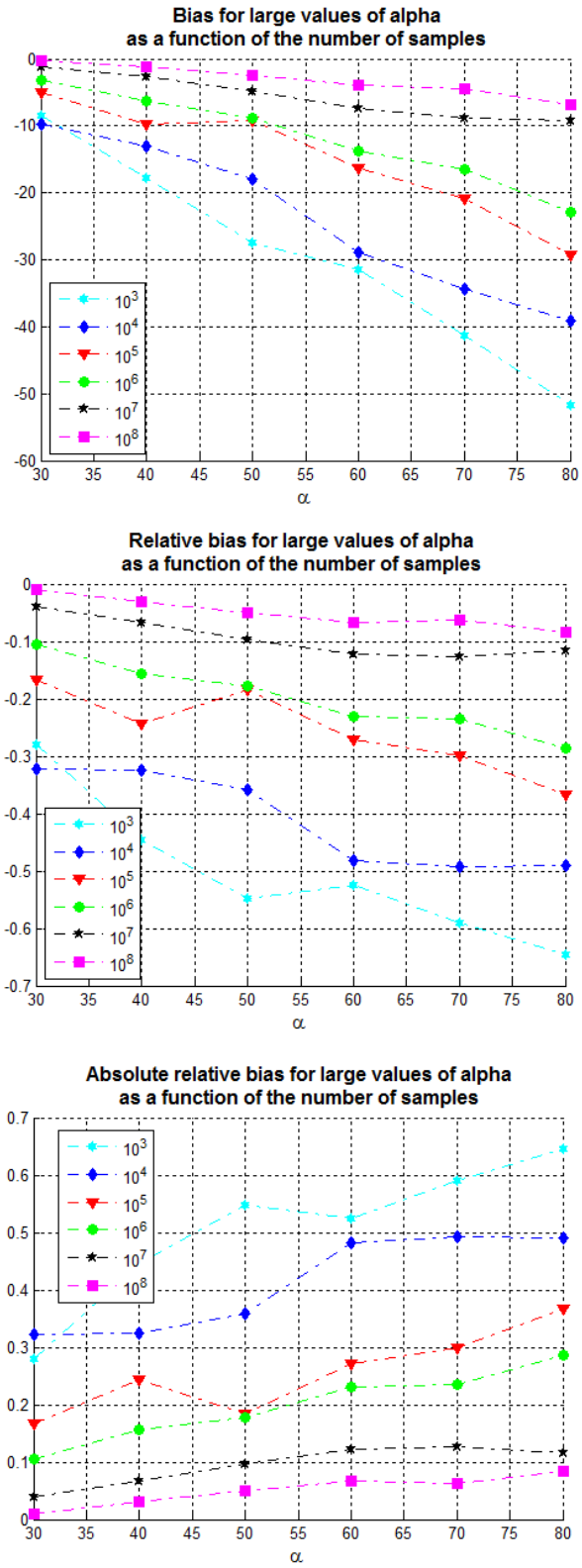

Figure 4.20 Bias, relative bias and absolute relative bias for values of α ranging from 30 to 80

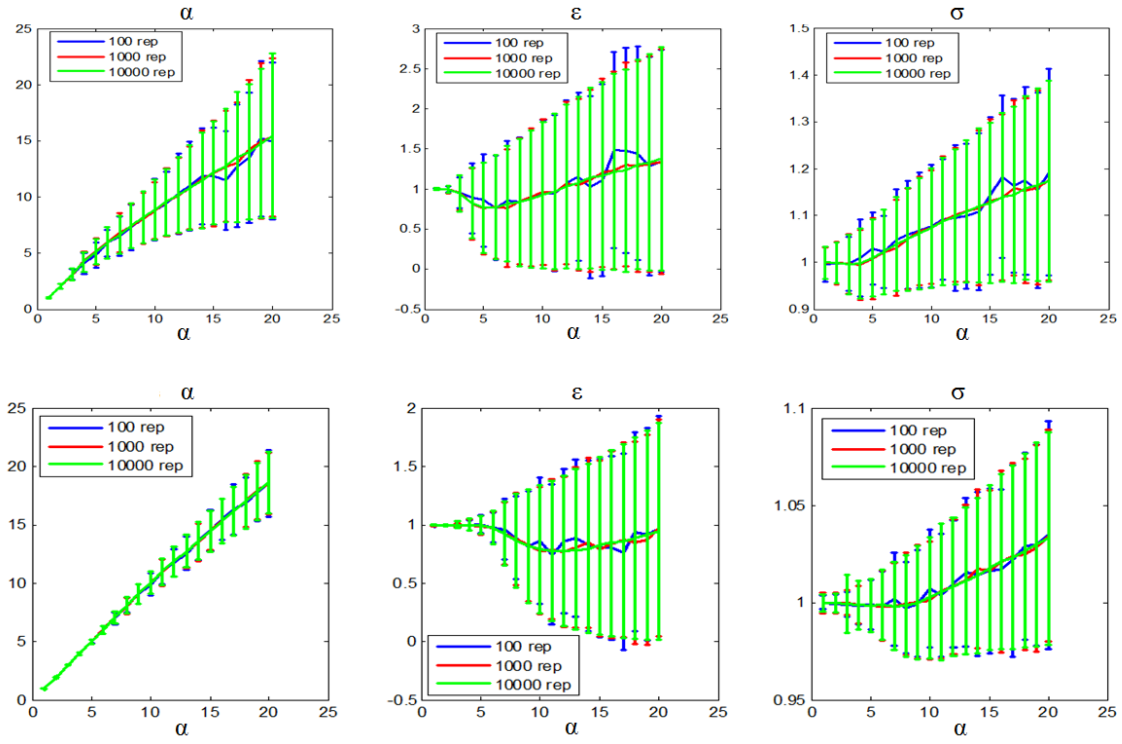

Figure 4.21 Estimation results as a function of the number of repetitions (from 100 to 10 000), considering 10^4 samples (above) and 10^6 samples (below)

4.5.2 The Role of Sample Correlation on the Variance of the Estimates

The results presented so far on the variance of the estimators for the parameters of the Homodyned-K distribution assume that the samples are uncorrelated. When the samples are correlated, the variance of the estimates will be larger than is indicated by the same number of samples for an uncorrelated case. Consequently, more samples are required in the correlated case than the uncorrelated case to achieve the same variance on the estimators. We can see this from the following discussion for the estimate of the mean (Redding 1999).

Let $X = (x_i,\ldots,x_n)$ denote the vector of random variables that correspond to the random sample (in lexicographic order if the sample is taken from a random field). Next, let C denote the covariance matrix. Furthermore, let us assume that the sample is from a stationary spatial process, i.e. the correlation between two random variables x_i and x_j is dependent on only the spatial displacement between i and j. If the spatial process of the sample X is one-dimensional, C is a symmetric Toeplitz matrix because:

$$[C]_{ij} = \sigma^2 \rho_x\left(|i-j|\right) \tag{4.23}$$

where $\rho_x(s)$ is the correlation at lag s and σ^2 is the variance of each x_j. When the spatial process of X is two-dimensional of size p x q (i.e. , n = pq), then C is symmetric block Toeplitz with Toeplitz blocks, i.e. :

$$[C]_{ij,kl} = \sigma^2 \rho_x\left(|i-k|,|j-l|\right) \tag{4.24}$$

where the paired indices ij and kl denote lexicographic order and i, k = 1,... ,p and j, I = 1,... , q. Then the variance on the estimate $\hat{\mu}$ of the mean μ is given by:

$$var\left(\hat{\mu}\right) = \frac{\sigma^2}{n} \sum_{s=-n+1}^{n-1} \left(1 - \frac{|s|}{n}\right) \rho_x\left(s\right) \tag{4.25}$$

in the case of a one-dimensional spatial process, and

$$var\left(\hat{\mu}\right) = \frac{\sigma^2}{n} \sum_{s=-q+1}^{q-1} \sum_{r=-p+1}^{p-1} \left(1 - \frac{|r||s|}{n}\right) \rho_x\left(r,s\right) \tag{4.26}$$

in the case of a two-dimensional spatial process. Therefore, the variance of the estimates depends directly on the degree of correlation between the samples. In order to be able to compare the previous results to the ones obtained on ultrasound signals, we should have an equal number of independent samples for each realization (or observation, or simply set of points in the ROI). In the case of ultrasound images, correlation is induced both in the axial and lateral direction, by oversampling and by the width of scanning ultrasound beam, respectively. In conclusion, in most cases downsampling should be applied in both directions (axial and lateral) prior to statistical analysis.

4.5.3 Simulations of Ultrasound Images

For the validation of the previously discussed point, namely the need to have uncorrelated samples prior to parameter estimation, a series of simulations have been conducted using CREANUIS. Six scatterer concentrations of particles with a diameter of 13 μ are considered: 1%, 5%, 10%, 15%, 20% and 25%. The positions of the scatterer centers are generated randomly from a uniform distribution, and the particle diameter is taken into account by imposing an exclusion distance (equal to the diameter) between the centers. Ten 3D particle distributions have been simulated for each concentration, which are being imaged in 10 volumes equal to 20 wavelengths in the axial dimension, 50 wavelengths in the lateral direction (equivalent to 90 RF lines with the given pitch) and 10 wavelengths in the elevation direction. Ten slices are being imaged for each of the volumes, resulting in 100 images for each of the concentrations. The exploration frequency

has been set at 30 MHz, with the relative bandwidth of 60% of this frequency, for a probe with 64 active elements, an element pitch of 68μm, kerf of 4 μm and height of 2.5 mm. The configuration results in a resolution cell of approximately 0.0004 mm^3. The computed equivalent scatterer concentrations per resolution cell are 3.5, 17, 34, 51, 68, and 85.

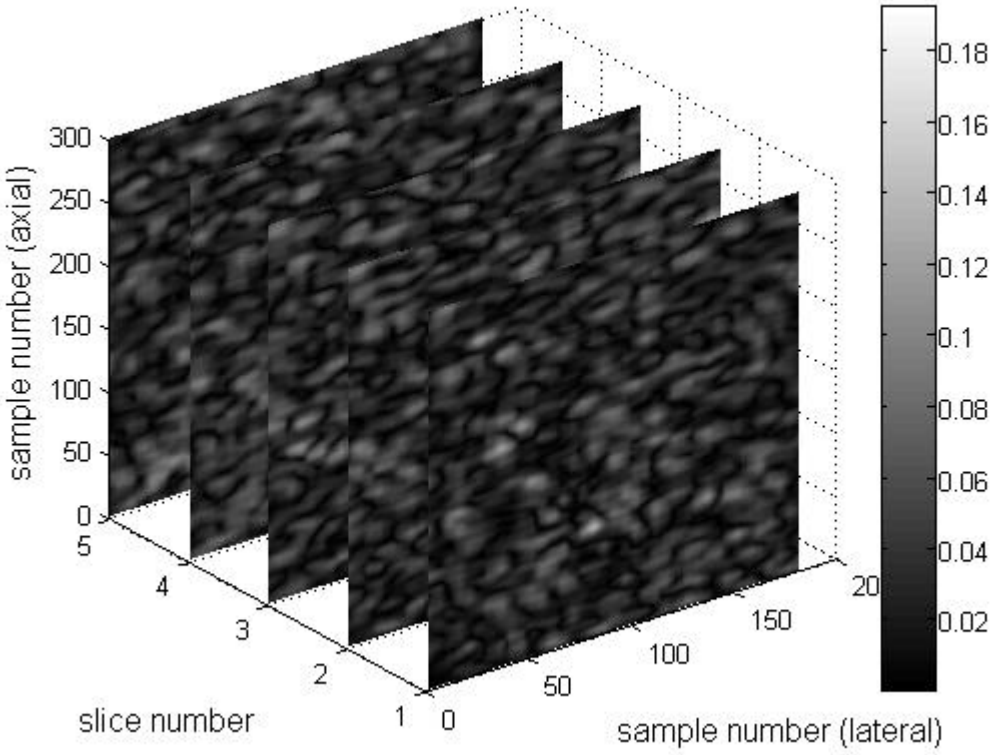

Figure 4.22 Consecutive slices (linear interpolation by a factor of 5 in the lateral direction) of a simulated volume with 1% scatterers

Envelope images corresponding to the lowest and highest scatterer densities are shown in Figures 4.22 and 4.23. For visual purposes, these images have been interpolated. The analysis is conducted on data sampled at 240 MHz and with a sparse spacing between lines (equivalent to the probe pitch). The results

The degree of correlation was assessed using the Pearson correlation coefficient:

$$\rho_{X,Y} = \frac{E[(\mathrm{X}-\mu_X)(\mathrm{Y}-\mu_Y)]}{\sigma_X \sigma_Y} \tag{4.27}$$

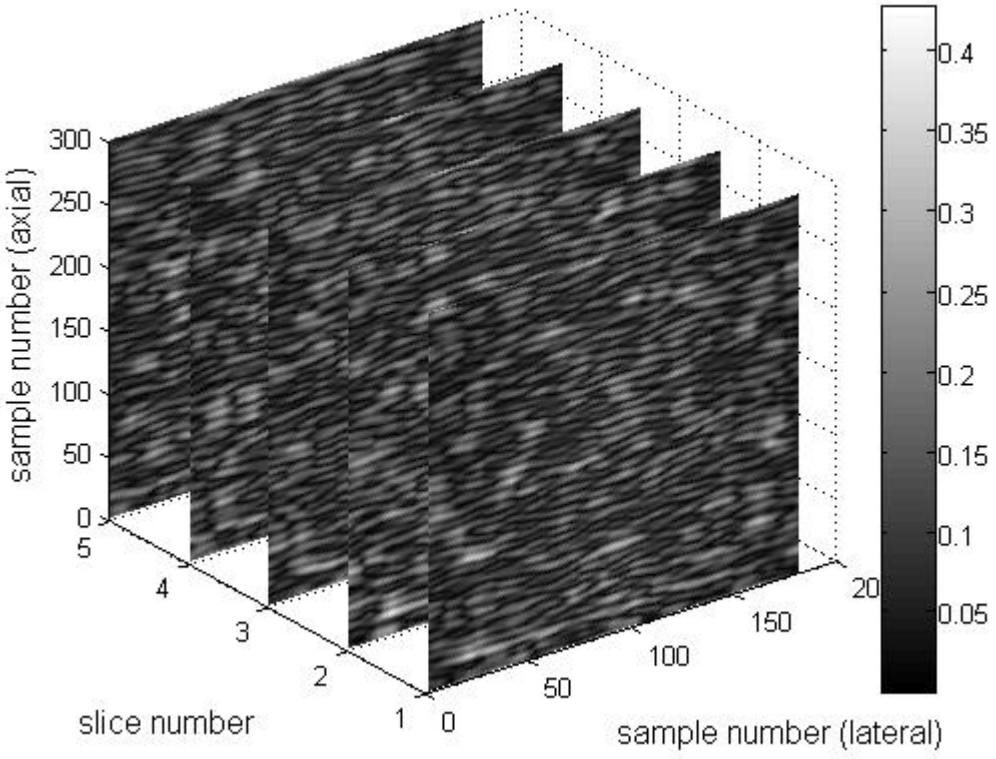

Figure 4.23 Consecutive slices (linear interpolation by a factor of 5 in the lateral direction) of a simulated volume with 25% scatterers

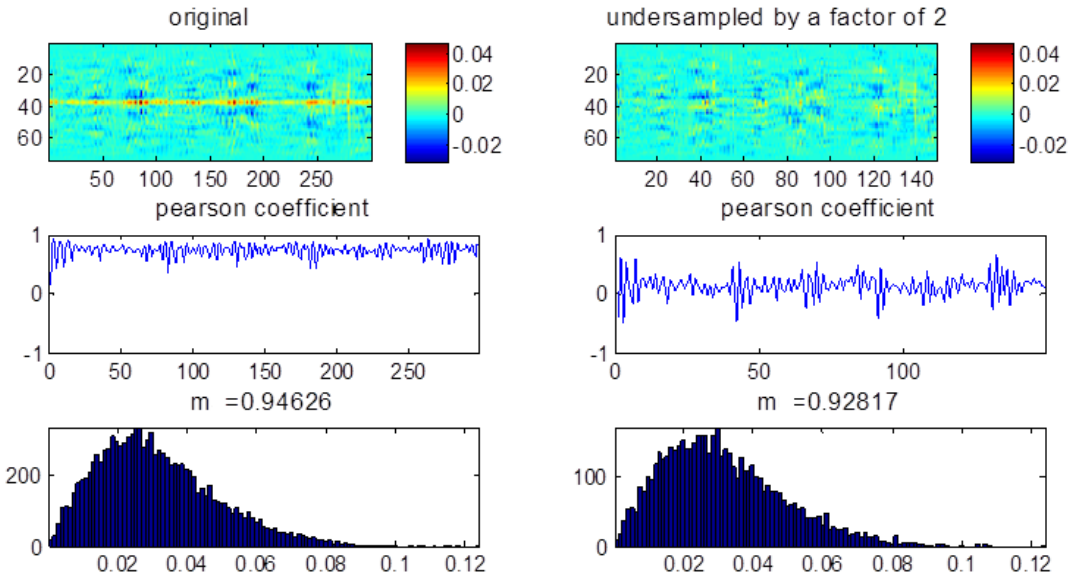

Figure 4.24 Correlation between adjacent samples for simulated images (axial direction): example from simulation. Up: correlation computed between adjacent lines. Center: Pearson coefficients. Down: Nakagami fit and parameter m

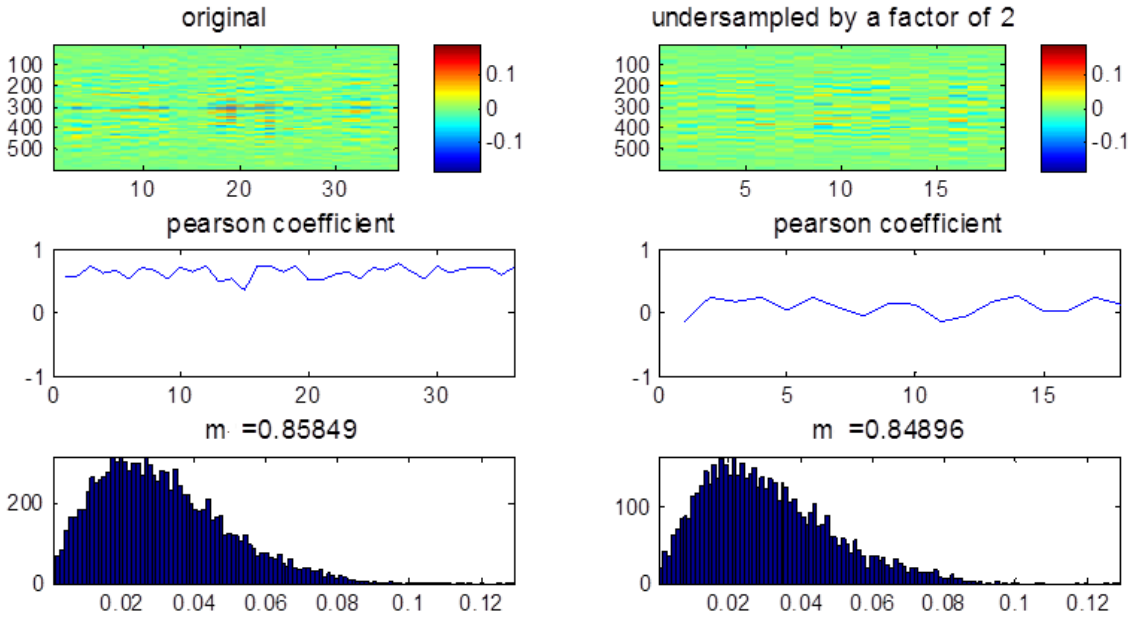

Figure 4.25 Correlation between adjacent samples for simulated images (lateral direction): example from simulation. Up: correlation computed between adjacent lines. Center: Pearson coefficients. Down: Nakagami fit and parameter m

Here, X and Y are the data vectors corresponding to adjacent lines, of means μ_X and μ_Y and standard deviations σ_X and σ_Y. The Pearson coefficient is computed for all the adjacent lines in the image (Figures 4.24 and 4.25) and its mean value is used to decide when the degree of correlation is acceptable ($\rho_{X,Y}$ <0.1).

The original image contains 11100 samples (300 x 37). A downsampling by a factor of 2 in each direction will sufficiently decorrelate the samples, reducing their number to 2775. The chosen depth is equivalent to 20 wavelengths (corresponding to the central frequency). So, when reducing the number of points in the axial direction, we use 7.5 points / wavelength.

Sample decorrelation by downsampling does not change the shape of the data histogram and therefore does not alter the statistical estimates. This operation is not a necessary pre-processing step, but it can reduce the computation time and it is useful for assessing the number of effectively non-correlated samples taken into account for the analysis.

The results of the parameter estimation on 100 ROIs containing 2775 uncorrelated samples, 10 ROIs of 27750 uncorrelated samples and 1 ROI of 277500 uncorrelated samples (in the last two cases, the larger ROIs are obtained by joining the initial ones) are shown in Figure 4.26. The maximum value of α was increased to 200, because of the likelihood of finding higher values in fully developed speckle. The estimated mean values of α did indeed increase as a function of the sample number, which according to section 3.5.1 means that the estimate is more accurate (less biased).

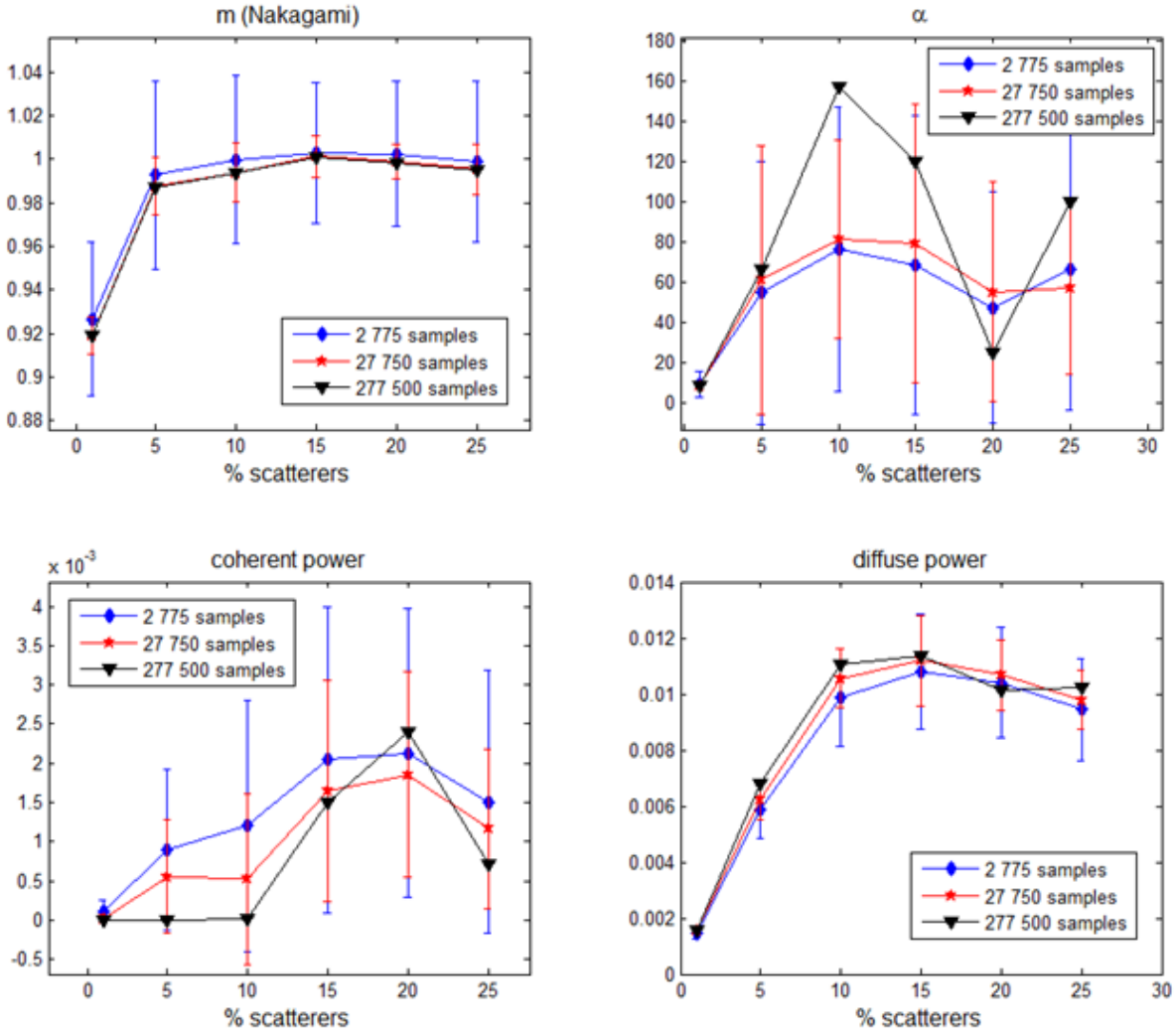

Figure 4.26 Estimates of α, the diffuse power and coherent power obtained from the simulated images, as a function of scatterer concentration and sample number

4.5.4 Phantoms of Orgasol Particles

Suspensions of polyamide Orgasol particles (diameter=10 μm), similar to those prepared for the tests conducted in Chapter 2, were prepared and analyzed using a single-element Panametrics ultrasonic transducer centered at 22 MHz. Twelve particle concentrations ranging from 0.5% to 25% were considered.

The data was compensated for attenuation and filtered in the 10-44 MHz frequency bandwidth. There is however a loss of information for frequencies above 40 MHz (measured at -20 dB), who are completely attenuated by the high density solutions (Figure 4.27). The strong effect of the attenuation at these high working frequencies restricts the depth of the ROI, which in its turn reduces the number of available samples. Therefore, a depth equal to 4.5 wavelengths was

selected (100 samples at 250 MHz). If the amplitudes within the ROI decrease with depth as a function of phenomena such as attenuation, the shape of the data histogram will change as a cause of the low-to-medium level amplitudes at in the attenuated zone, and will look like the histogram produced by a medium with a much lower density. This will affect the parameter estimation. For example, the Nakagami parameter that tends to a constant value of 1 for fully developed speckle will decrease.

Because of the relatively large bandwidth of the transducer (out of which the second harmonic has been filtered out), the correlation between axial samples is not very high and a downsampling by a factor of 3 decorrelates them (figure 4.28). The samples are laterally decorrelated and no downsampling is needed. Out of 3000 RF lines, testing was done of groups of 300, 600 and the entire 3000, leading to an equivalent number of decorrelated samples per realization of almost 10.000, 20.000 and 100.000, respectively.

The maximum value of α was set to 200, since we were dealing with fully developed speckle at high concentrations, where the occurrence of high values for α is plausible.

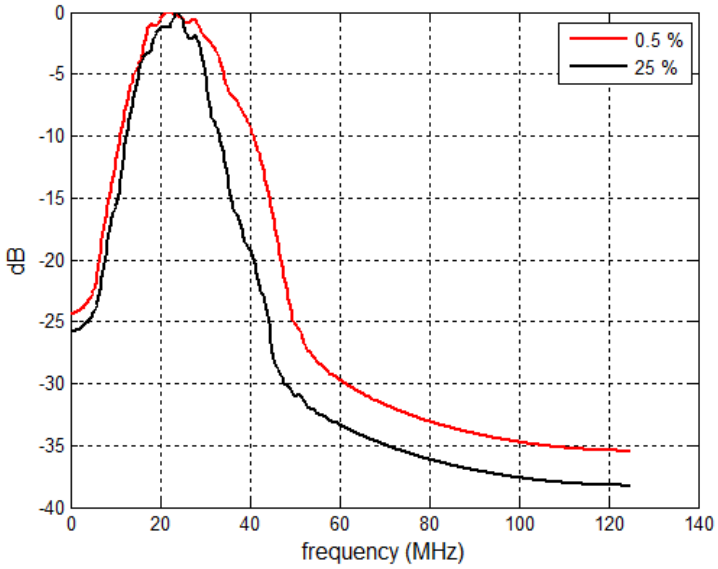

Figure 4.27 Frequency spectrums backscattered from the 0.5 % Orgasol phantom and the 25 % Orgasol phantom

The results for each case are presented in Figure 4.29. The estimated mean values of α increase monotonously as a function of scatterer concentration (until 10%), and also as a function of the sample number, which suggest a decrease of the bias (according to the conclusion of section 3.5.1).

The polyamide powder's density is very close to that of water (1.03 g/cm^3), therefore making it easy to fabricate the suspensions which served as phantoms. However, the propagation speed of sound in polyamide is 2750 m/s, very different from the speed of sound in water (approx. 1480 m/s depending on the temperature), which means that the particles have twice the acoustic

impedance of the water. This also leads to considerably higher attenuation coefficients than those of the biophantoms (for example for a density of 12% cells, the measured attenuation is 0.0184 dB Mhz^{-1} mm^{-1}, whereas for a 12% Orgasol solution it is 0.043 dB Mhz^{-1} mm^{-1}). Moreover, at high particle concentrations, the high amount of destructive wave interference determines a decrease in the backscattered power. The effect might change the speckle structure enough as to explain the decreasing values of the Nakagami shape parameter m and of the HK scatterer clustering parameter α at high concentrations.

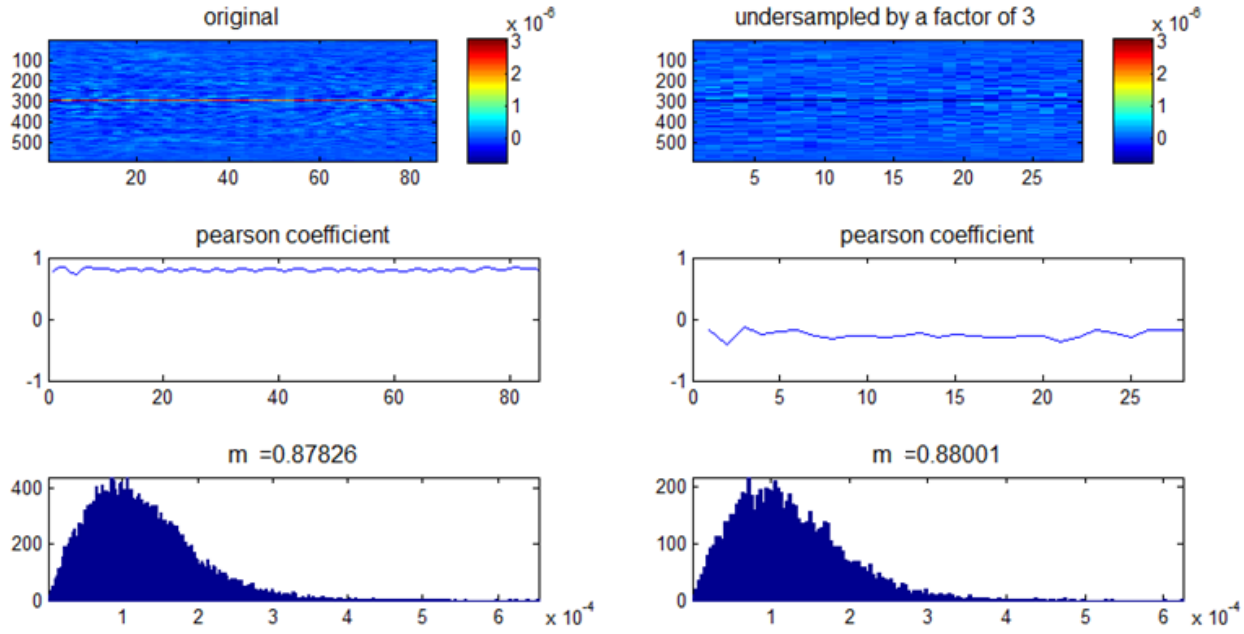

Figure 4.28 Correlation between adjacent samples for images of Orgasol phantoms (axial direction): example from simulation. Up: correlation computed between adjacent lines. Center: Pearson coefficients. Down: Nakagami fit and parameter m

4.5.5 Cell Pellet Biophantoms

The data used in the previous section for the comparative tests (Nakagami vs the Homodyned-K) is analyzed here using different sized ROIs. Within a ROI having a depth equal to 14 wavelengths (considered for the acquisitions with the 35 MHz probe), equivalent to 500 samples at a sampling rate of 500 MHz, the correlation between adjacent "axial" lines (made from points positioned at the same depth) was maximal (Figure 4.30). After a down sampling by a factor of 4, the mean correlation coefficient drops to values close to 0. One must only be careful to not sample below the Nyquist rate. Regarding the "lateral" samples (RF lines), the correlation coefficient was also maximal but a downsampling by a factor of 5 sufficed in order to bring it close to 0 (Figure 4.31). This would mean that our initial total sample size is reduced at least 20 times in order to obtain decorrelated samples. For example, we take an image composed of 93 000 samples (500 x 188), acquired with the 35 MHz probe at a sampling rate of 500 MHz,

corresponding to a medium with 10 % scatterers. After a downsampling by a factor of 4 in the axial direction and 5 in the lateral direction the samples can be considered "decorrelated". This only leaves approximately 4650 samples (out of which 125 in the axial direction, equivalent to about 8.3 points / wavelength).

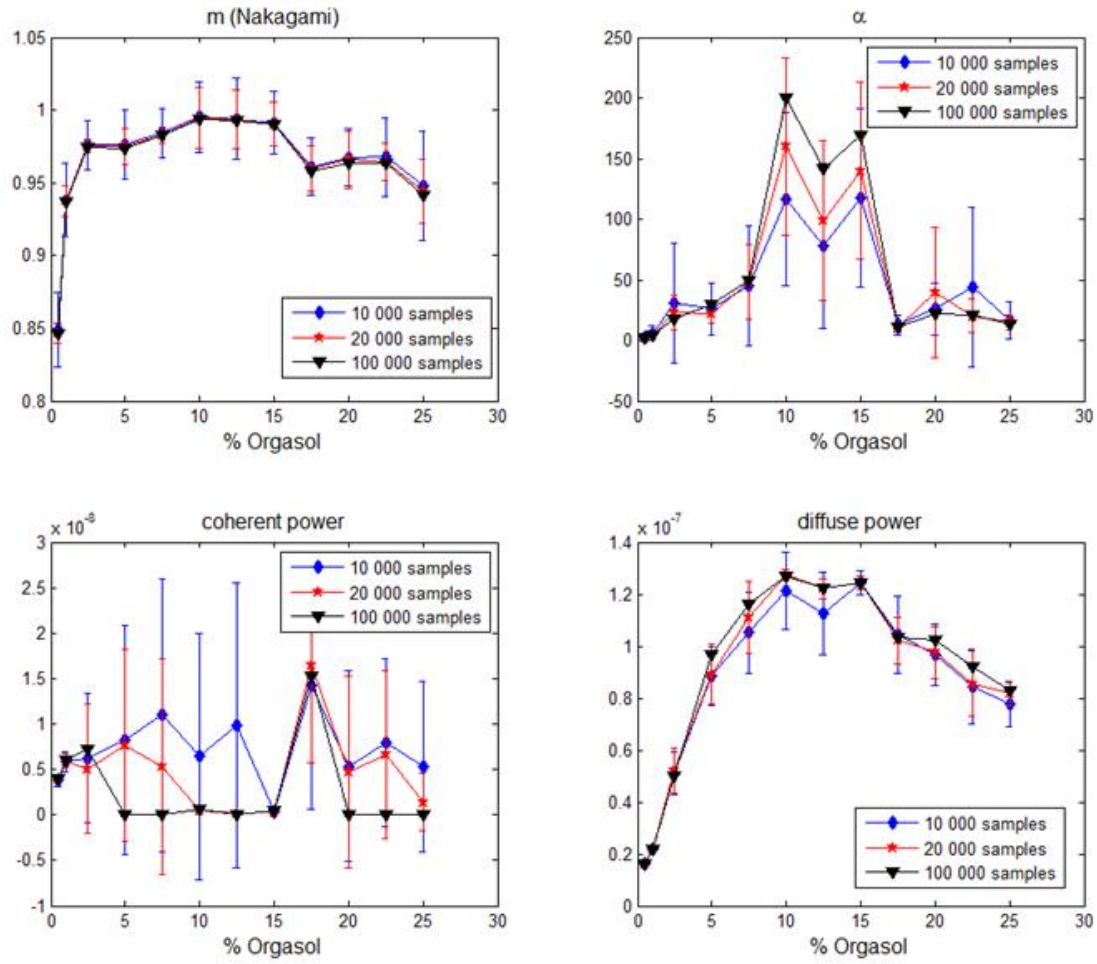

Figure 4.29 Estimation results for the Orgasol phantoms as a function of effective scatterer density and number of samples. Nakagami parameter m for comparison.

The estimations are done with an imposed maximum value of α of 200, on the same ROIs of 4650 decorrelated samples, then by joining 19 successive (but highly correlated) frames of the first ROIs, and finally by joining the acquisitions taken at each of the 6 locations in the biophantoms (Figures 4.32 and 4.33). α increases as expected as a function of the sample number, but just up to a concentration of 12%, before falling because of reason partially discussed.

4.5.6 Conclusion

Three sets of data (simulated images, acquisitions on Orgasol phantoms and on cell pellet biophantoms) have been used for Homodyned-K parameter estimation, with emphasis on the

scatterer clustering parameter α and with the purpose of assessing the possibility of obtaining reliable low-bias estimates in fully developed speckle conditions.

For the tested data, it would seem that the Homodyned-K clustering parameter α increases monotonically as a function of scatterer density until close to a volume density of 10-15%. Beyond this value, the evolution is erratic. We attribute this to the numerical limitations of the method.

Concerning the actual expected values of the parameter α for certain densities, the obtained values varied for the three sets of data. The range of densities was comparable (between 0.5% - 25 % scatterer concentration), but the concentrations of scatterers per resolution cell fell in different ranges: between 3 and 85 for the simulated images (30 MHz, particle diameter: 13 μ), between 4 and 220 for the Orgasol phantoms (22 MHz, particle diameter: 10 μ), and between 3 and 250 (considering acquisitions at two different frequencies, 25 MHz and 35 MHz) for the biophantoms (particle diameter: 13 μ). If we refer to section 3.5.1 for the expected biases when using the number of sample that were available, it can be considered that the actual values of α for the respective densities were not precisely obtained. The estimates do not follow a specific pattern as a function of scatterer density per resolution cell from one data set to another; therefore we suppose that they might depend on other imaging system-related factors or physical phenomena which need to be studied. However, we observed that the estimates increase monotonically for concentrations lower than 10% in all cases. This could be subject to future research aimed at determining if estimates can be associated with a particular "low" scatterer concentration of less than 10 %.

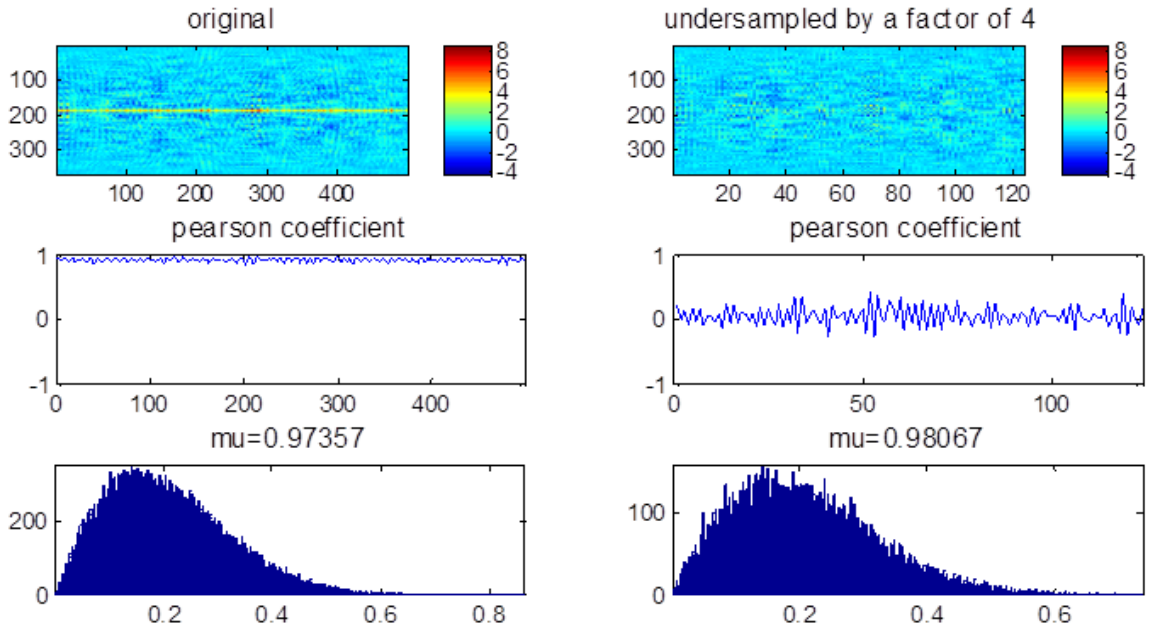

Figure 4.30 Correlation between adjacent samples for images of biophantoms (axial direction): example from simulation. Up: correlation computed between adjacent lines. Center: Pearson coefficients. Down: Nakagami fit and parameter m

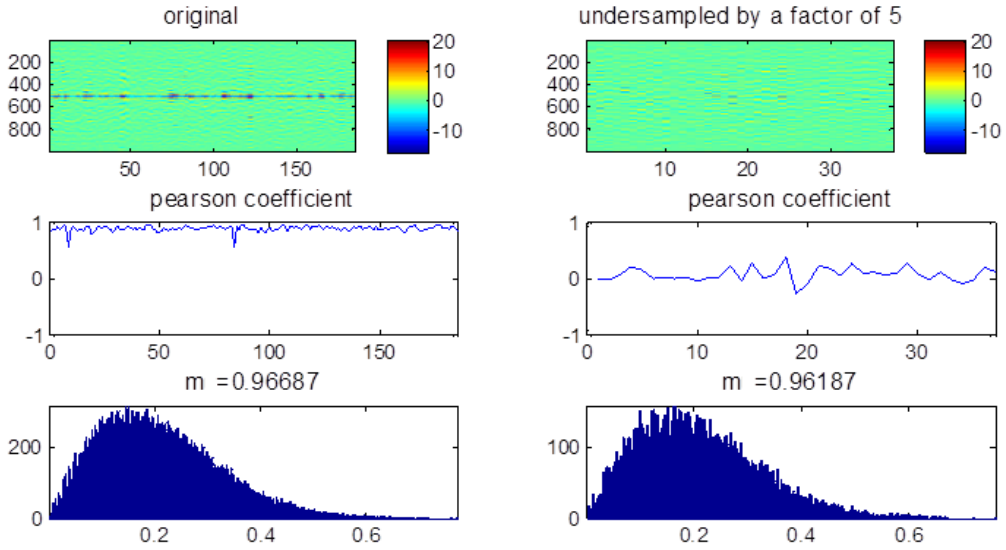

Figure 4.31 Correlation between adjacent samples for images of biophantoms (lateral direction): example from simulation. Up: correlation computed between adjacent lines. Center: Pearson coefficients. Down: Nakagami fit and parameter m

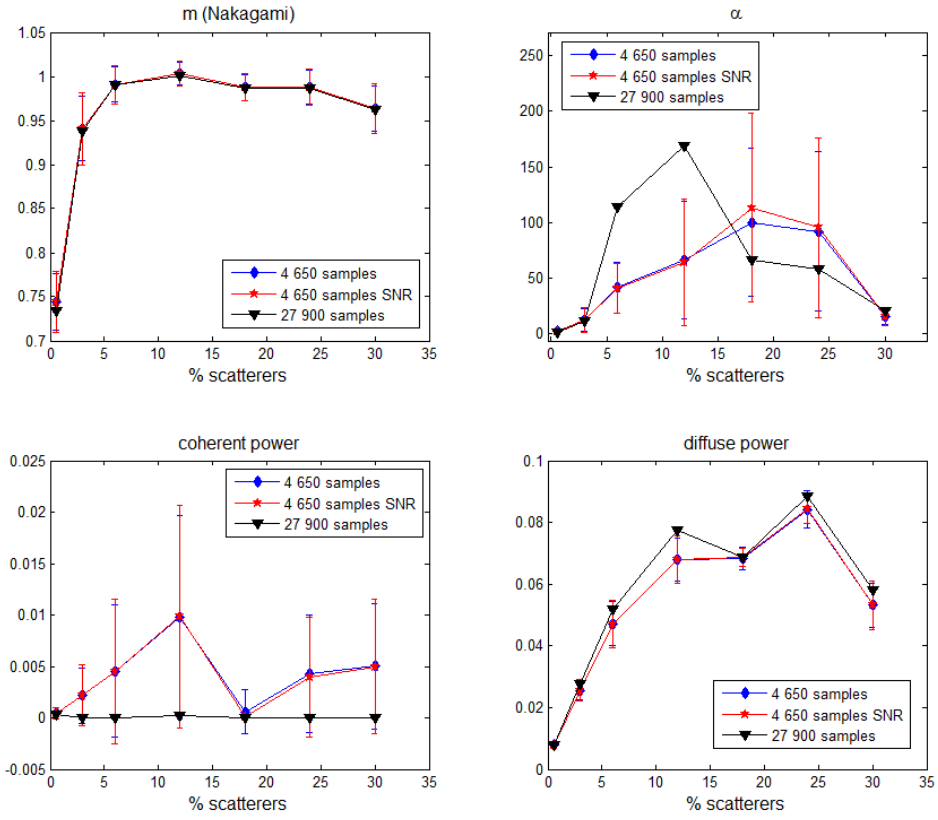

Figure 4.32 Estimation results for the biophantoms imaged with the RMV 703 probe (35 MHz) as a function of effective scatterer density and number of samples. Nakagami parameter m for comparison.

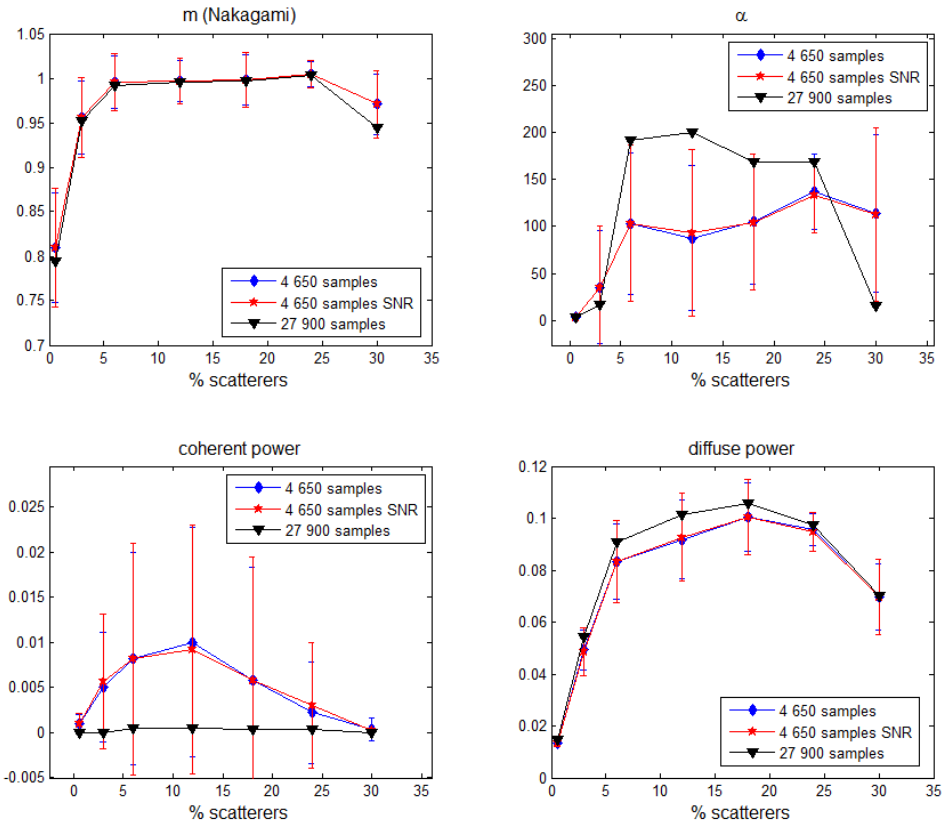

Figure 4.33 Estimation results for the biophantoms imaged with the RMV 710 probe (25 MHz) as a function of effective scatterer density and number of samples. Nakagami parameter m for comparison.

Regarding the suggested sample number, we always need to acquire a maximum possible amount of data, but an upper limit is not defined since the max α is not defined. According to our results, supposing that we have a symmetric spectrum, and we consider the wavelength corresponding to the central frequency, it would suffice to choose a number of 7-8 points per wavelength in the axial direction in order to have weakly correlated samples. While the length of the focal area depends on the transducer geometry, the choice of a depth of at least 10 wavelengths is preferable. This implies approx. 80 axial samples, which leaves the necessity of joining 125 decorrelated RF lines in order to be in the second case of section 3.5.1 (10.000 samples), which is not difficult to attain in practice. In any case, the values presented in section 3.5.1 would serve as guidelines for different situations. A "perfect experiment" is difficult to define, since the number of necessary samples is unpractical even for numerical simulation.

5 DECONVOLUTION AS A PREPROCESSING STEP

When considering the ultrasound signal in the more classical context of image processing, a problem that is just as classical arises: degradation by the imaging system. The main effect here is the blur induced by convolution with the point spread function (PSF) characteristic to the imaging system. A PSF maps a point from the real medium into the image, and therefore is the image of that point. The PSF often has the shape of a 'spot' carrying the characteristics of the imaging system. In the case of ultrasound, this is conditioned by the shape of the scanning beam, which in turn is conditioned by the scanning frequency, beam focus, and transducer geometry. When imaging a multitude of points, the corresponding spots will overlap and create a blurred image of the original medium. Additionally, constructive and destructive interference of the ultrasound waves used in imaging will create a granular texture called speckle, that determines the characteristic aspect of ultrasound images. Since speckle is a form of distortion, it is generally viewed as a negative effect and, since it is also a form of multiplicative noise, filtering it out is particularly difficult. On the other hand, speckle can also carry useful information on the microstructure of the underlying medium, which can be exploited by statistics, the main focus of this thesis. For this reason, studying the statistics of deconvolved speckle might be conflicting.

Deconvolution of ultrasound images is performed for the general purpose of improving the visual aspect of the log-compressed B-mode image, in terms of resolution and contrast. The progress of deconvolution techniques in ultrasound is briefly resumed in the following section. A particular method was designed specifically for the RF image prior to envelope detection, with the purpose of being used for tissue characterization. This is a delicate problem, however, because the theoretical conditions for applying statistical models do not necessarily hold. As it was shown before and as we also conclude, a classification using statistical estimates is possible, but the statistical parameters which are characteristic for the scatterer number density this will not necessarily be a measure of this scatterer density any more. The deconvolved image may produce histograms that can be modelled by the same distributions as speckle, but it does not mean that it is a true speckle pattern.

5.1 DECONVOLUTION METHODS USED FOR RESOLUTION IMPROVEMENT

Ultrasound images can be described using the classical convolution model between the tissue reflectivity function x and the point spread function P (considering also an additive noise n, for

example electrical noise):

$$y = P * x + n \tag{5.1}$$

or, in matrix form (H being the system matrix):

$$y = Hx + n \tag{5.2}$$

This is applied under the assumption that the interaction between the tissue reflectors (or scatterers) and ultrasound is linear, which is accurate in the case of weak scattering. Even if this is not always the case in biological tissues, the convolution model is considered as a sufficiently good approximation in most works (Michailovich and Tannenbaum 2007). The deconvolution is seen as the opposite operation, where the unknown reflectivity function x is to be determined, as only the resulting image y is known. Depending on the deconvolution method, the mathematical expression of the problem varies. This depends on the information available on the PSF (if it is known or needs to be estimated) and on different assumptions that are made for the PSF and the additive noise. When the deconvolution problem is accompanied by the problem of PSF estimation, and the two are performed simultaneously, the deconvolution is called "blind". If the PSF is partially known but the initial guess is refined during the deconvolution, then we are dealing with "semi-blind" deconvolution.

As mentioned, the PSF estimation is in itself an important problem, and some of the early estimation strategies presented in (Jensen 1991) employs an inverse ARMA (auto-regressive moving average) filter, combined with an estimation of the noise covariance using the pulse autocorrelation function. A method using higher-order statistics is used in (Abeyratne, Petropulu, and Reid 1995), and a maximum a posteriori (MAP) conjoint estimation of the PSF and of tissue reflectivity is proposed in (Kaaresen and Bolviken 1999). In the rest of the literature, the prevalent PSF estimation methods are based cepstrum-based and variations on homomorphic filtering (Taxt 1995). The principle of homomorphic filtering is that the information on the system PSF is contained in the low-frequency part of the complex cepstrum of the signal. For a 1D signal, the complex cepstrum is computed as the inverse Fourier transform of the logarithm of the Fourier spectrum:

$$c = \mathcal{F}^{-1}(\log\{|\mathcal{F}(\mathrm{P}*\mathrm{x})|\}) \tag{5.3}$$

Applying a low-pass filter on c will yield the cepstrum of the PSF, which can be then reconstructed in the temporal domain. The decomposition of the cepstrum can be also done using a wavelet basis, as it is presented in (Michailovich and Adam 2005). Research has also been done on the phase unwrapping problem, of which we cite (Taxt and Frolova 1999) who introduce a Bayesian cost functional with the purpose of phase smoothing.

The PSF is also is spatially variant, mostly with depth as the ultrasound beam diverges. For

this reason, if deconvolution is performed on an entire image, the respective image needs to be divided into multiple segments, as a function of depth, where for each segment the PSF can be considered as spatially-invariant. The problem is therefore sub-divided in a number of sub-problems which can be solved with a method of choice. Of course, this issue is avoidable when using a multifocal imaging system, and is in any case less likely to be encountered when studying statistics, since we are interested in the focal zone where the shape of the PSF is constant.

Regarding the most common approaches applied to ultrasound images, predictive deconvolution based on ARMA models was attempted in (Jensen 1991). Wiener filtering has been used extensively, together with homomorphic filtering for PSF estimation, in (Taxt and Frolova 1999) and (Taxt and Strand 2001), (Michailovich and Adam 2005) and other works of the respective teams. Deconvolution by homomorphic filtering is applicable, as showed in (Jiřík and Taxt 2006). As mentioned above, (Kaaresen and Bolviken 1999) use MAP in order to estimate both the PSF and the reflectivity in a blind deconvolution method. In (Michailovich and Tannenbaum 2007), a 2D parametric inverse filter with MAP regularization is implemented, with interesting results improving the detectability of anatomical structures in ultrasound images (Figure 5.1). In (Ng, Prager, and Kingsbury 2007), a Bayesian MAP estimation is integrated into an expectation-maximization (EM) framework, together with a gaussian-mixture model for the reflectivity and denoising by wavelet shrinkage. The norm employed in the MAP expression is usually the L^2norm (Tikhonov regularization) or the L^1norm, depending on the considered prior for the tissue reflectivity (Gaussian or Laplacian distribution). In (Alessandrini et al. 2011) a deconvolution method aimed specifically at tissue characterization is developed. The idea resembles that of the previously cited method, but here the tissue reflectivity prior is considered to be a Generalized Gaussian Distribution (GGD), and regularization is performed using the corresponding L^pnorm, where p is the GGD shape parameter. This method has been used in our tests. ADMM (Alternating Direction Method of Multipliers) approaches are tested in (Morin 2013), leading to improvements in the resolution and especially the contrast of ultrasound images (Figure 5.2).

Despite advancements in image restoration, ultrasound image deconvolution is an ill-posed problem, and the result will not conduct to the real solution, although it has been shown to be close for the case of sparse reflectivity functions. For tissues where this holds, deconvolution can lead to interesting results. But for dense tissues such as tumors and blood, we might find ourselves removing not only blur but actual useful information. In these cases « resolution improvement » (and the implied apparent gain in bandwidth) does not always mean a gain in information, as sub-resolvable structures are not separated, but rather just the reduction of the blur and an improved contrast. An additional nuisance is produced by the Gibbs ringing artefacts (when passing through the frequency domain in order to perform an inversion) and noise amplification (typically when using filters that have a non-negligible amplification outside of the signal bandwidth, or when iterative algorithms introduce high-frequency noise with repeated convolutions). These factors introduce noise in the histogram, thus altering the reliability of statistical estimates.

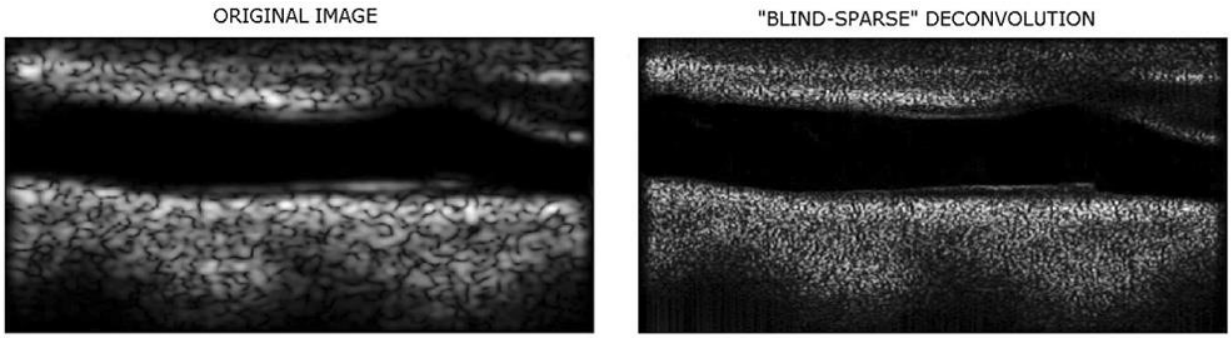

Figure 5.1 Fragment of the ultrasound image of a carotid artery (left) and corresponding deconvolved image using the inverse filtering method presented in (Michailovich and Tannenbaum 2007) **(right). Image extracted from the publication.**

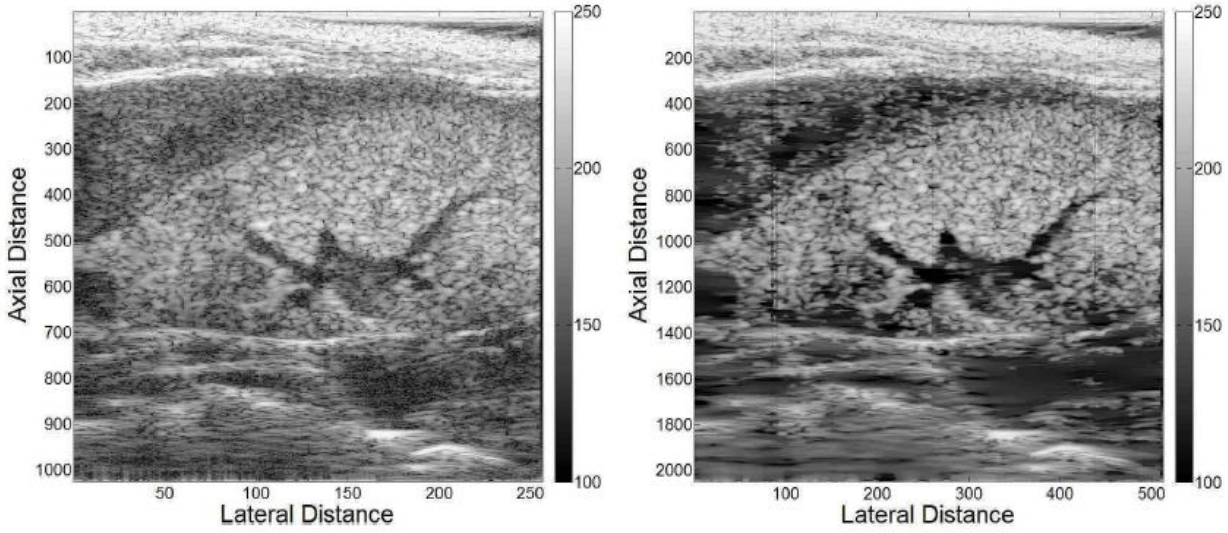

Figure 5.2 Fragment of the ultrasound image of a mouse kidney (left) and corresponding deconvolved image using the non-blind ADMM method presented in (Morin 2013) (right). Image extracted from the thesis manuscript.

5.2 DECONVOLUTION FOR TISSUE CHARACTERIZATION

5.2.1 Presentation of the Method

In (Alessandrini et al. 2011), a deconvolution framework special for tissue characterization is developed and applied on Orgasol phantoms, with promising results. The method is briefly described here and then applied for the following tests.

First of all, the method is non-blind, and therefore prior knowledge of the system PSF is necessary. For the simulated images in which the used PSF is accessible, it is preferred to use it. In all other cases, the PSF is estimated via homomorphic filtering.

The deconvolution problem is tackled as a Maximum a Posteriori (MAP) estimate, and the actual implementation is done in an Expectation Maximization (EM) framework. The tissue reflectivity prior is considered to be a Generalized Gaussian Distribution (GGD) described by a shape and scale parameter, of which the scale parameter will also be updated after each maximization step, in order to improve the prior knowledge on the reflectivity for the next iteration. The general MAP expression is:

$$X = \arg\max_{x}[\mathrm{P}(\mathrm{y}\,|\,\mathrm{x},\sigma_n)\,\mathrm{P}(\mathrm{x})] \tag{5.4}$$

where $\mathrm{P}(\mathrm{y}\,|\,\mathrm{x},\sigma_n)$ is the probability of the observation y conditioned by the knowledge of the prior x and the noise with standard deviation σ_n (or the likelihood of y when x and σ_n are known), and $\mathrm{P}(\mathrm{x})$ is the prior probability. Logarithm is typically applied in order to simplify the calculations, so that the previous equation becomes:

$$X = \arg\max_{x}[\ln(\mathrm{P}(\mathrm{y}\,|\,\mathrm{x},\sigma_n)) + \ln(\mathrm{P}(\mathrm{x}))] \tag{5.5}$$

Supposing that the noise is Gaussian, replacing it with $\mathrm{y}-\mathrm{Hx}$ (eq 2) and discarding constant in the expression of the Gaussian distribution, we obtain:

$$X = \arg\min_{x}\left[\frac{1}{2\sigma_n{}^2}\left\|\mathrm{y}-\mathrm{Hx}\right\|^2 - \ln(\mathrm{P}(\mathrm{x}))\right] \tag{5.6}$$

If the GGD prior is assumed, the log-posterior to be minimized becomes:

$$L = -\frac{1}{2\sigma_n{}^2}\left\|\mathrm{y}-\mathrm{Hx}\right\|_2^2 - \lambda\left\|x\right\|_\xi^\xi \tag{5.7}$$

where λ is a regularization constant, ξ is the shape parameter of the GGD and $\left\|x\right\|_\xi$ is the l^p norm. Since the solution of the minimization of (5.7) is not analytically tractable, it is solved using EM, with the following steps (including a preconditioner $\left[D_k\right]_{ii} = \lambda\xi \Big/ \left|x_i^k\right|^{2-\xi}$ for the l^p norm regularization):

$$E-STEP: Q(\mathrm{x}, \mathrm{x}_k) = -\frac{\|\mathrm{y}-\mathrm{Hx}\|_2^2}{2\sigma_n^{\,2}} - \frac{1}{2} x^T D_k x$$
$$M-STEP: \mathrm{x}_{k+1} = \arg\max_x \left\{ Q(\mathrm{x}, \mathrm{x}_k) \right\} = \left(\sigma_n^2 D_k + H^T H \right)^{-1} H^T y \tag{5.8}$$

As mentioned before, the parameter ξ is estimated from the sequence x_{k+1} after each M step by maximum likelihood (Chapter 2). Since the adopted method assures convergence, the stopping condition is:

$$\left| L(\mathrm{x}_{k+1}, \xi_k) - L(\mathrm{x}_k, \xi_k) \right| / L(\mathrm{x}_k, \xi_k) < \tau \tag{5.9}$$

Additionally, a method of decomposing and inverting the matrix that appears in the M-step is necessary. For this purpose, a 2D Conjugate Gradients (CG) method is implemented, and a Jacobi preconditioner is applied to the matrix that needs to be inverted in order to improve its conditioning number and thus the convergence rate of the CG algorithm. Also, for practical considerations, the algorithm is applied on the IQ-demodulated signal instead of the RF signal.

5.2.2 Target Separation

In order to observe the basic effects of the deconvolution algorithm, it is first applied on a simple point target under different configurations (PSF, number of iterations). The images are simulated using CREANUIS, so that the original PSF used for image formation is available. The simulated probe has 64 active elements, an element pitch of 68 μm, kerf of 4 μm and height of 2.5 mm. After only one iteration of the algorithm (Figure 5.3), the deblurring effect becomes visible, and so do the characteristic ringing artefacts due to passing through the Fourier domain. The number of iterations of the CG algorithm also plays a strong role in the result, and a very large number of iterations that would lead to a globally better result will also induce artefacts (Figure 5.4), much like a large number of iterations of the deconvolution algorithm itself. Since the main interest of applying deconvolution for tissue characterization is to remove as much of the blur as possible in order to better separate the individual reflectors, it is preferred to maximize the number of iterations. By design and principle, the algorithm converges when the tolerance is reached, therefore the number of iterations from one case to another varies. However, the number of iterations in the main algorithm depends on the result of the CG algorithm, which in its turn generates more artefacts as it reaches its stopping condition (Figures 5.4 and 5.5). Figures 5.3 to 5.5 show the gradual improvement (narrowing) of the axial and lateral profiles (especially the axial profile), but also the artefacts that appear. Because of the numerical algorithms, the final amplitude level seems quite random.

The role of the PSF in deconvolution is of course very important. Small differences in the PSFs used for deconvolution can lead to different results. For example, the estimated PSF in

Figure 5.6 is almost identical to the real PSF, but the artefacts resulting from the deconvolution are more obvious than those in the image deconvolved using the real PSF (Figure 5.5).

The impact of the artefacts on the statistics of different images will be studied in the following section.

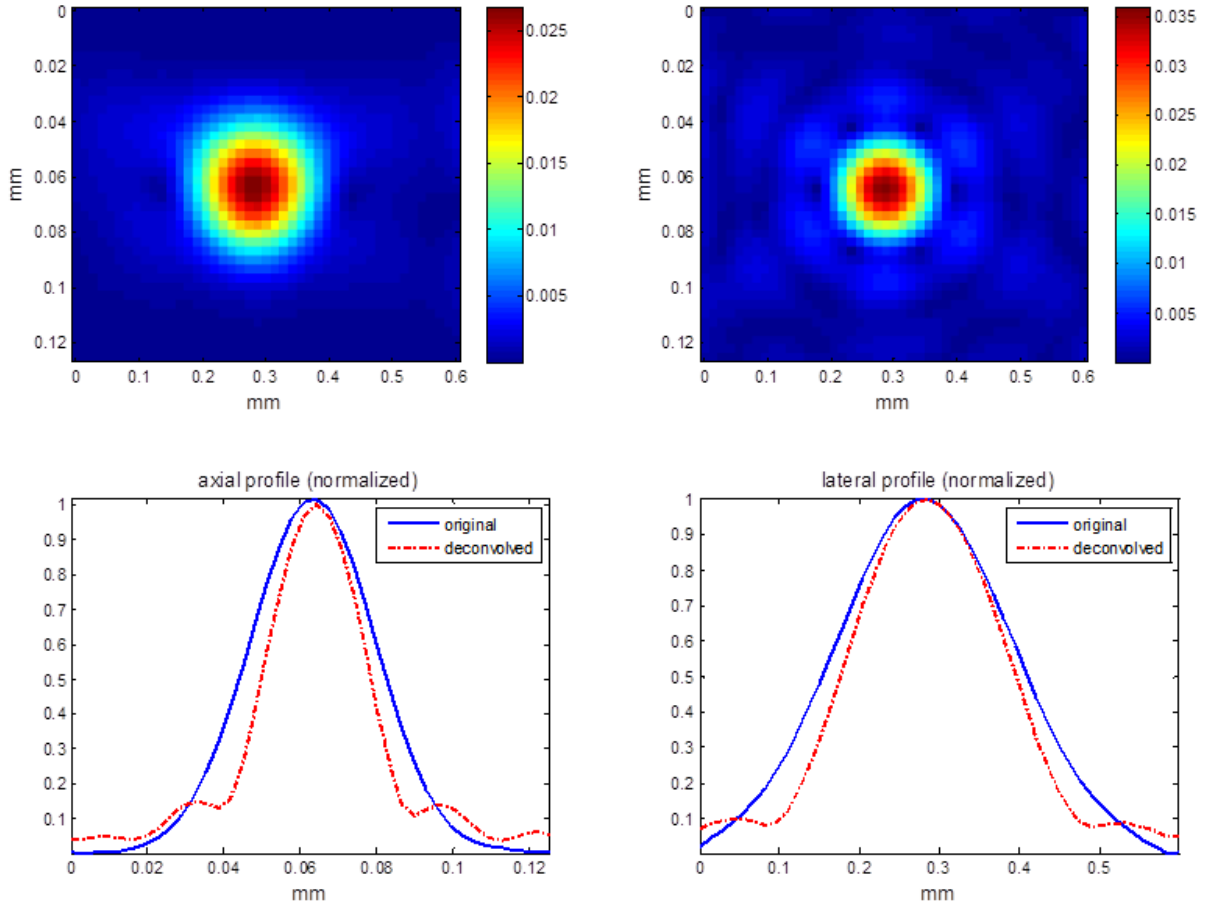

Figure 5.3 Simulated image of a point target (above, left) and the same image after 1 iteration of the deconvolution algorithm and 10 CG iterations (above, right). Axial and lateral normalized profiles of the central lines in the two directions (below)

The effect of the actual target separation in the axial dimension is shown in Figure 5.7. For targets that are placed just below the resolution limit, in this case 0.02 mm, an elongated PSF is visible on the ultrasound image but the individual targets are not separated. After deconvolution, the two are clearly visible, even if they are surrounded by artefacts. Separation is also possible for targets placed at 0.01 mm, but not at 0.005 mm. Therefore, targets can be effectively separated in the axial direction if they are sufficiently far apart that their individual images overlap only partially, otherwise if they overlap completely they will be seen as a single target even after deconvolution. Efficiency is lower in the lateral direction. For example, for two targets separated laterally by 0.12 mm, the deconvolution produced an artefact whose amplitude is more elevated than the one of the actual target (Figure 5.8; black circle : real target, red circle : artefact).

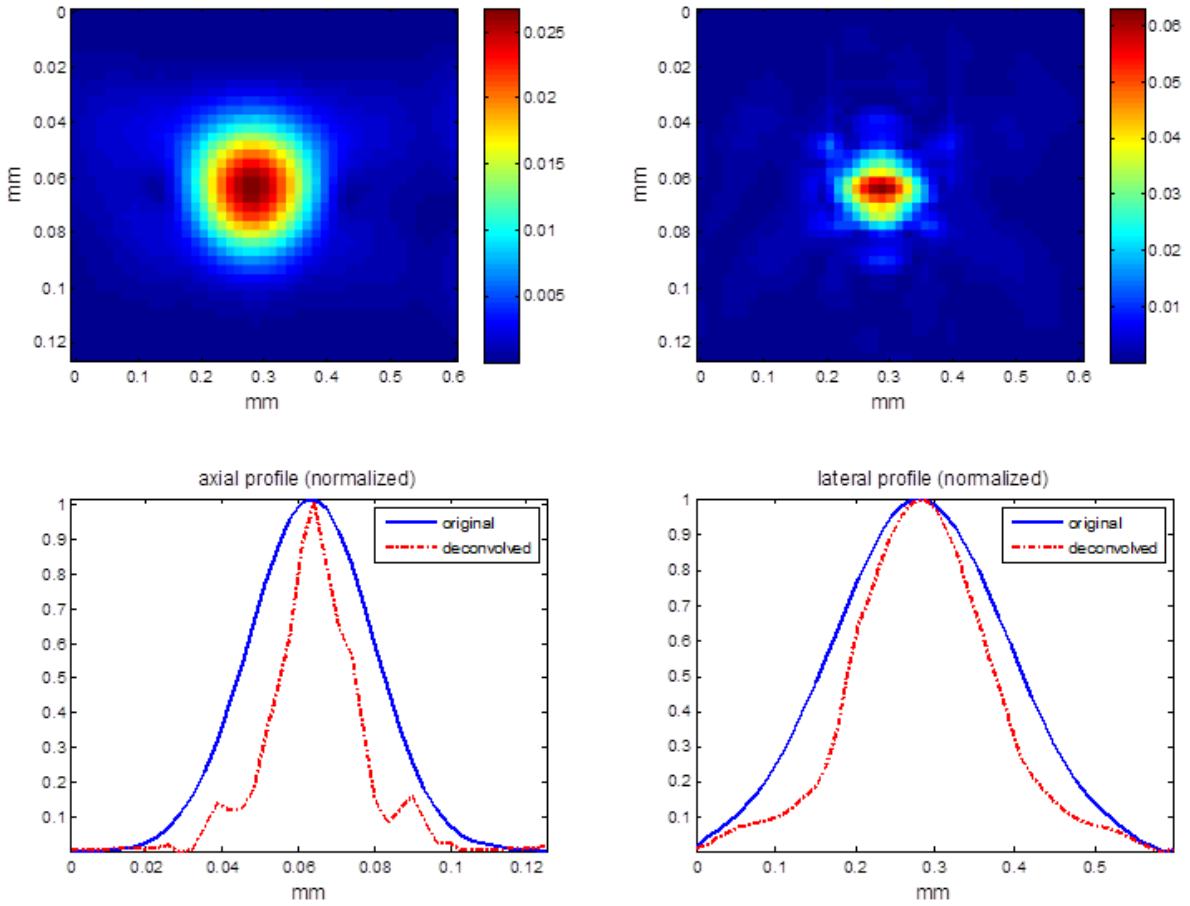

Figure 5.4 Simulated image of a point target (above, left) and the same image after 1 iteration of the deconvolution algorithm and convergence of the CG (above, right). Axial and lateral normalized profiles of the central lines in the two directions (below)

5.2.3 Effect on a Distribution of Scatterers

The effect of the deconvolution process on the overall image histogram is observed. Ideally, the deconvolution would remove the blur around the scatterers and produce the initial scatterer distribution (also called reflectivity of the medium). In practice, the scatterers are not always perfectly separated, and artefacts are introduced in the image. In order to observe the influence of this effect on the image histograms, two simple point scatterer distributions are simulated, imaged in the same configuration as the targets from the previous section, and then deconvolved.

The first distribution is relatively sparse and is composed of 100 scatterers with equal amplitudes. The corresponding RF ultrasound image, deconvolved image and original scatterer distribution (reflectivity) are shown in Figure 5.9. The histograms of the original RF image, reflectivity and deconvolved image are also presented for comparison. The result of the deconvolution algorithm indeed resembles a discrete distribution of scatterers, but some of the scatterer amplitudes are negative. Indeed, some of the scatterers are recovered, but others are not

and "false scatterers" also appear in the deconvolved image. The variable amplitudes in the deconvolved image are visible on the histogram, by comparison with the original binary image. It is difficult to separate the deconvolved reflectors and artefacts; heir amplitude levels are not differentiable (sometimes a deconvolved reflector has low amplitude, while artefacts can have high amplitudes). Globally, for this case, the number of non-zero normalized amplitudes in the deconvolved image and the number of original reflectors are very similar.

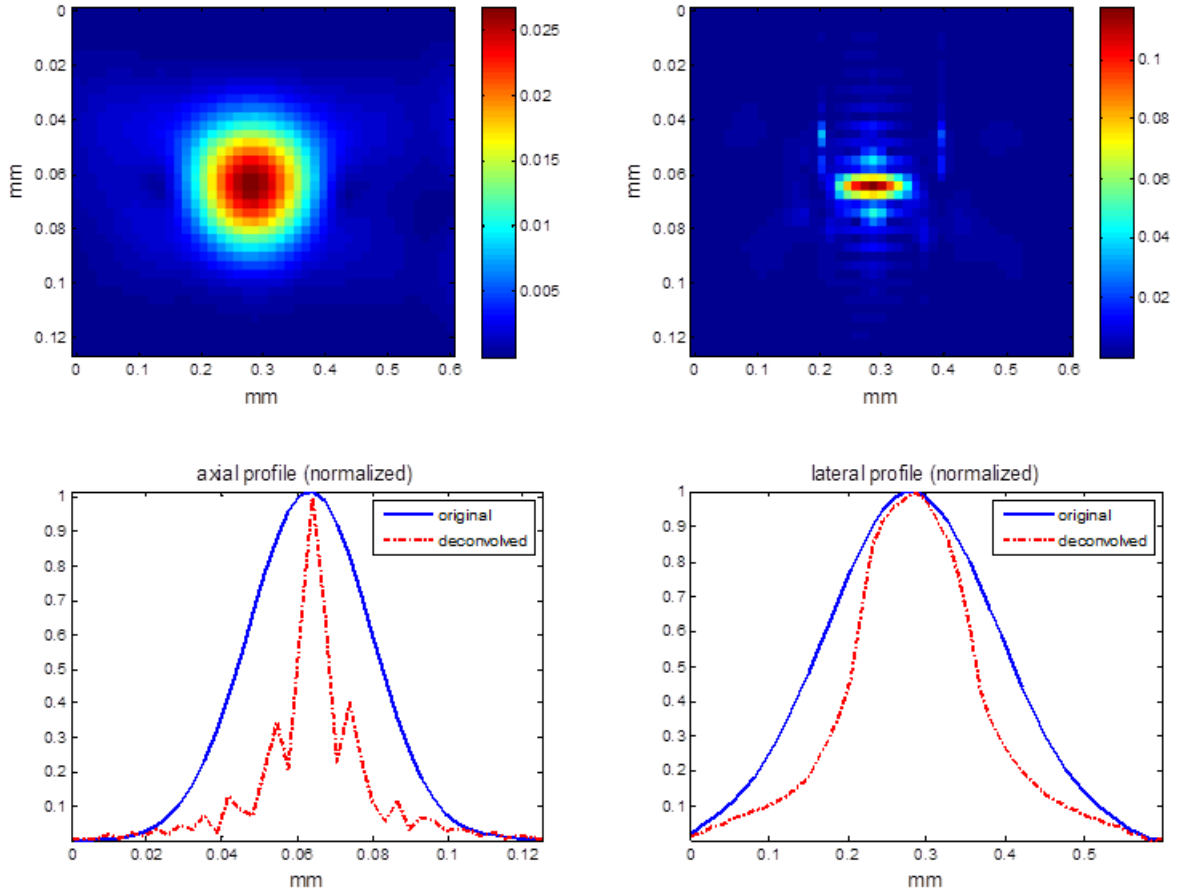

Figure 5.5 Simulated image of a point target (above, left) and the same image after convergence of the deconvolution algorithm and CG (above, right). Axial and lateral normalized profiles of the central lines in the two directions (below).

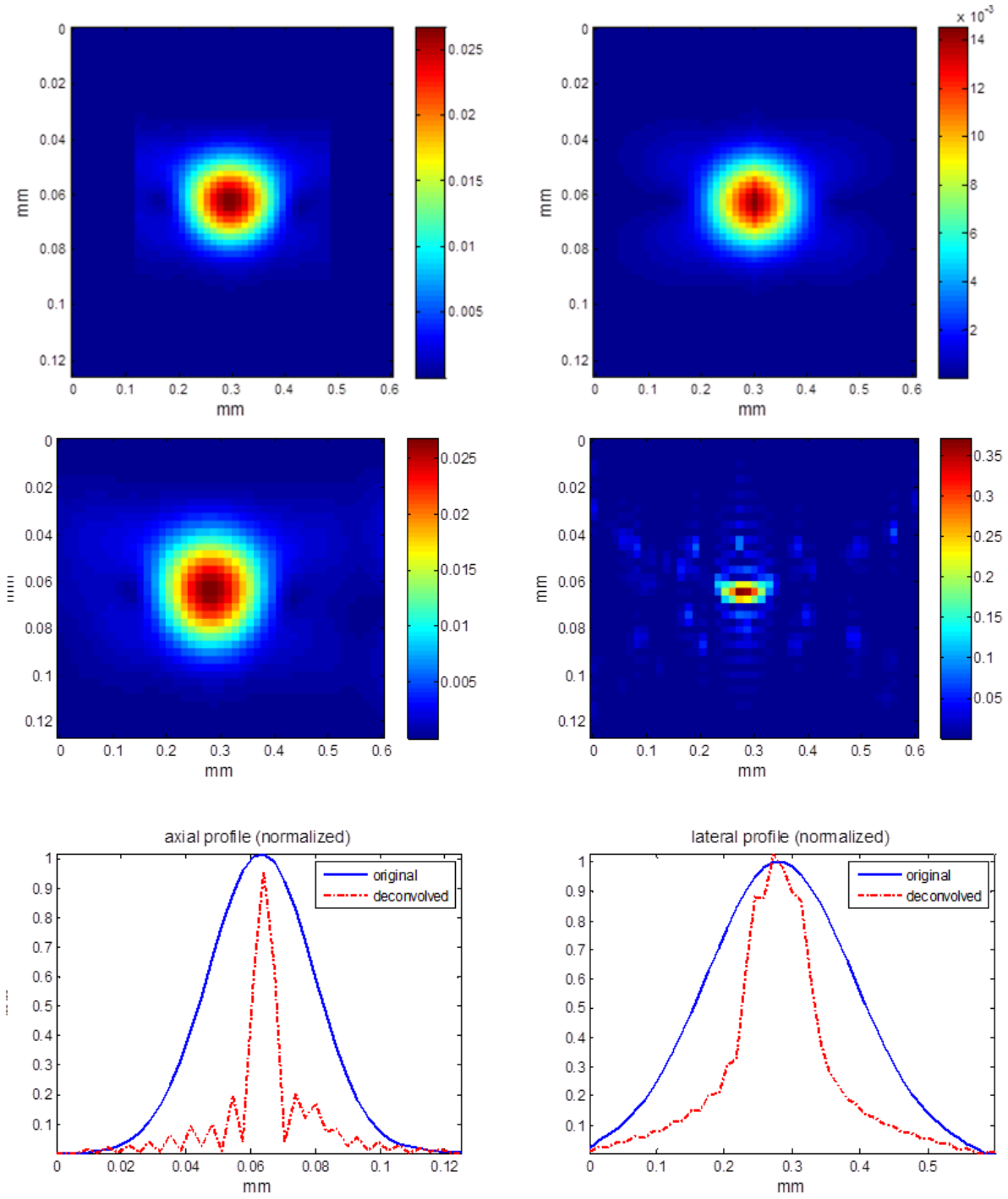

Figure 5.6 Simulated, zero-padded PSF (above row, left) and PSF estimated by homomorphic filtering of the original image (above row, right). Corresponding deconvolution results using the estimated PSF (below rows).

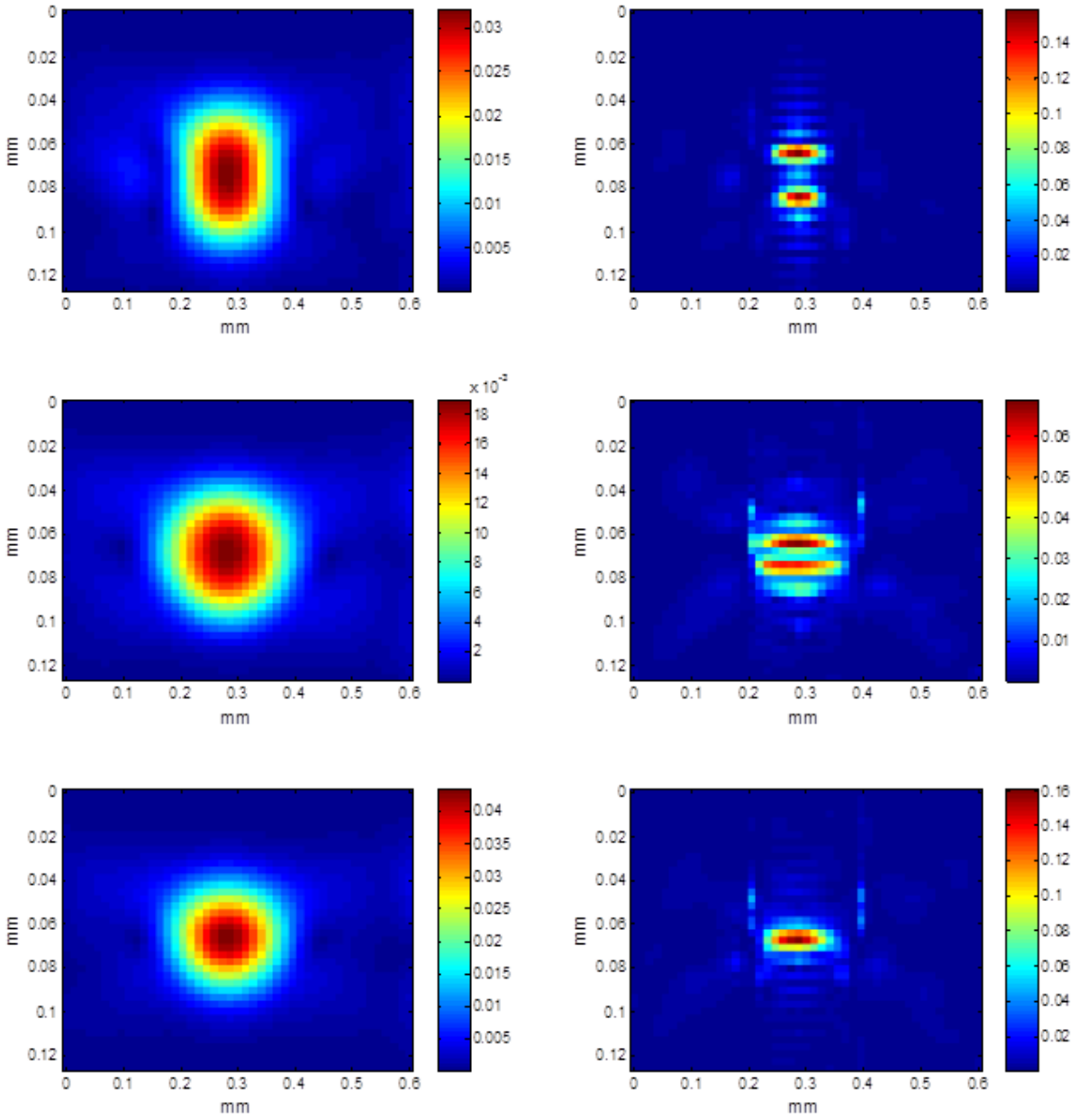

Figure 5.7 Simulated images of 2 point targets separated axially by 0.02 mm, 0.01 mm and 0.005 mm, respectively (left column) and Corresponding deconvolved images (right column).

The second distribution is chosen as less sparse, with 500 scatterers with equal amplitudes. The corresponding images and histograms are displayed in Figure 5.10. Even if the simulated medium is much denser, the resulting deconvolved image is as sparse as the previous one, and most of the initial reflectors are not recovered. The computed Generalized Gaussian shape parameters of the amplitude distributions in both images are 1.68 and 2.03, respectively, meaning that the first image is of partially developed speckle, and the second image of fully developed

speckle. The two images are just examples of realizations for the two scatterer densities, showing that the deconvolution result may not show differences in the scatterer densities of the imaged medium.

The purpose of this section and the previous one was to show that the imperfect results of the deconvolution method can be a strong barrier against the discrimination between two very different scatterer densities. The deconvolution is indeed very efficient for blur removal, but it often "over-deconvolves" and fails to detect many of the original scatterers in the medium. For this reason, when applied on test data, the method will often provide inconsistent results.

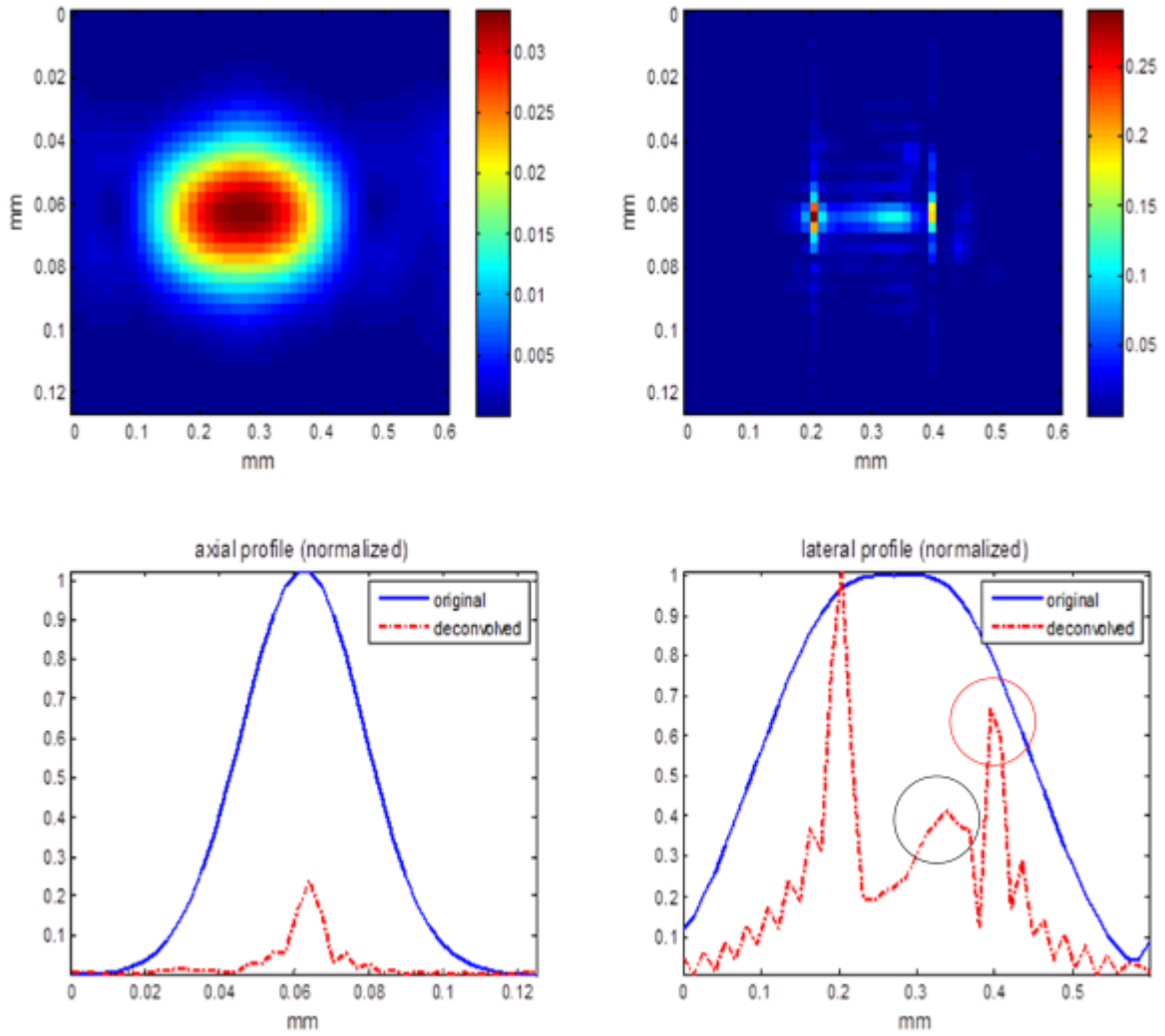

Figure 5.8 Simulated image of 2 point targets separated laterally by 0.12 mm (above left) and the same image deconvolved (above right). Axial and lateral normalized profiles of the central lines in the two directions (below). Black circle: real target, red circle: artefact.

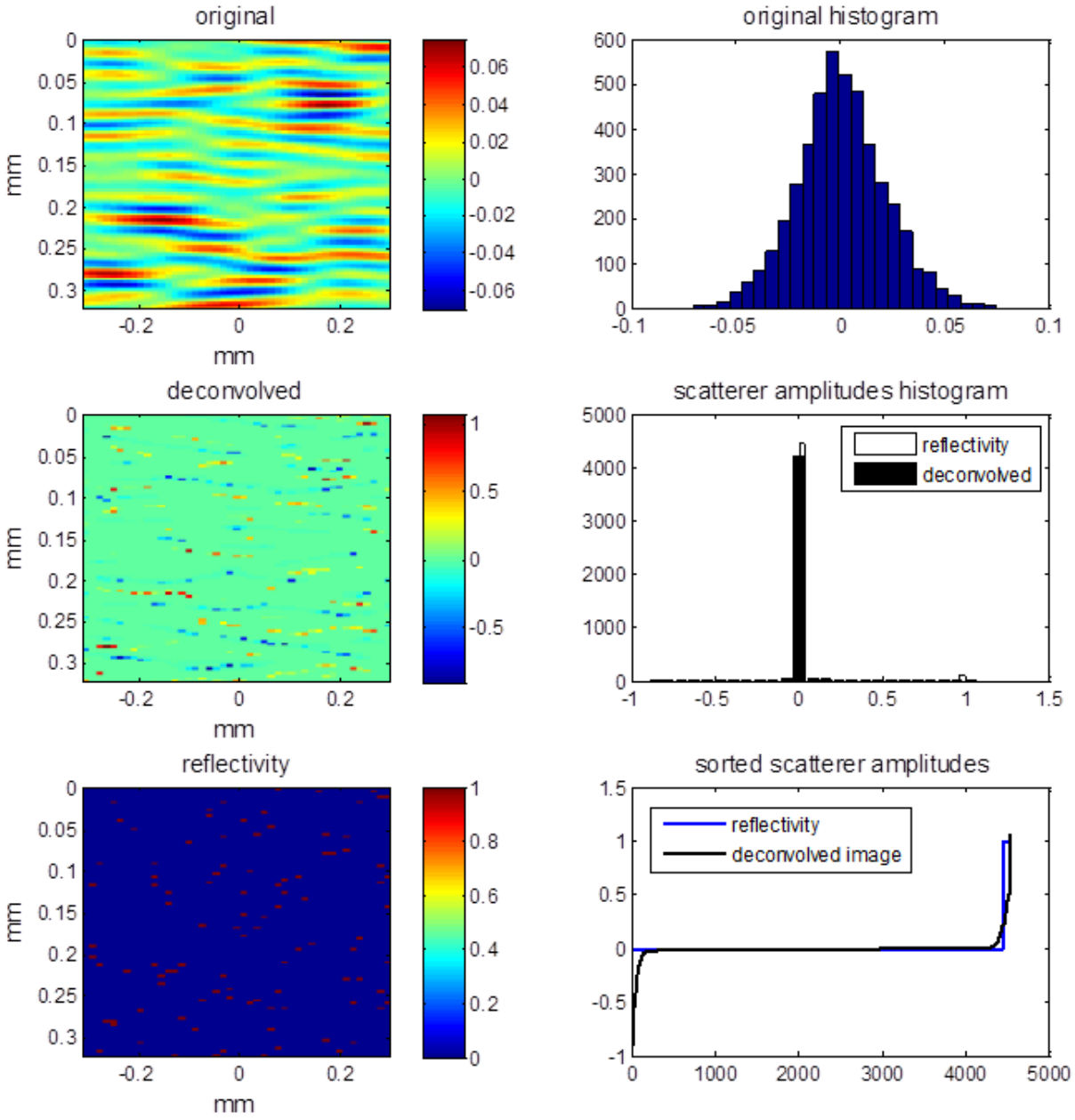

Figure 5.9 Simulated image of a distribution of 100 scatterers with equal amplitudes and random positions and its histogram (top row); deconvolution result (center left); original reflectivity (below left); compared histograms of the original and deconvolved scatterer amplitudes (center right); compared sorted scatterer amplitudes (below right)

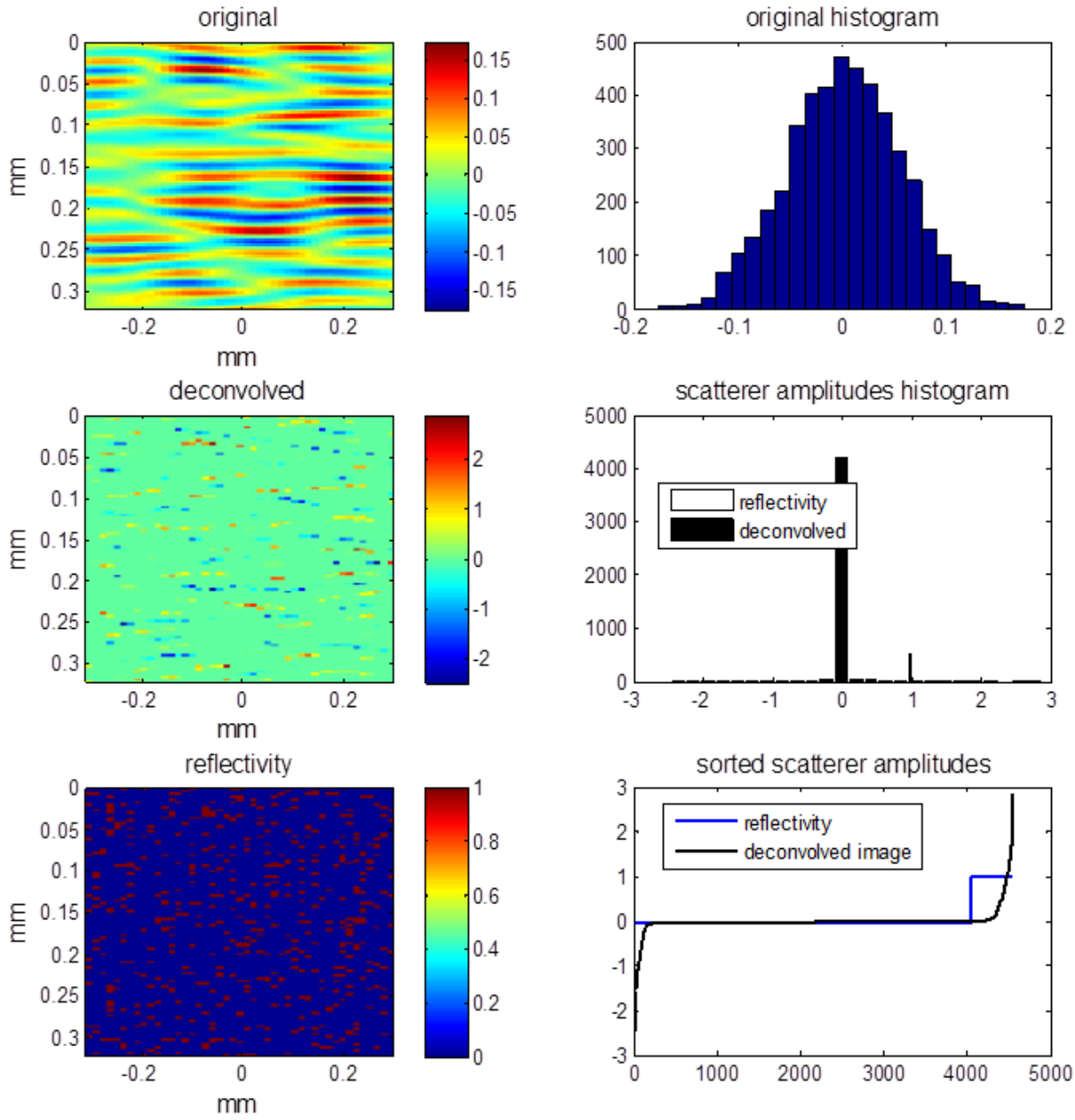

Figure 5.10 Simulated image of a distribution of 500 scatterers with equal amplitudes and random positions and its histogram (top row); deconvolution result (center left); original reflectivity (below left); compared histograms of the original and deconvolved scatterer amplitudes (center right); compared sorted scatterer amplitudes (below right)

5.2.4 Application on Simulated Data and Cell Pellet Biophantom Data

Deconvolution is applied on simulated data. CREANUIS was used to simulate a probe with 64 active elements, an element pitch of 68 µm, kerf of 4 µm and height of 2.5 mm, emitting a short pulse centered at 30 MHz and with a total bandwidth of 18 MHz at -6dB. The data consists of simulated phantoms with variable scatterer concentrations: 1%, 5%, 10%, 15%, 20% and 25%. The positions of the scatterer centers are generated randomly from independent uniform distributions, and the particle diameter is taken into account by imposing an exclusion distance (equal to the diameter) between the centers. Ten phantoms are simulated for each concentration. The size of one phantom is equal to 20 wavelengths in the axial dimension, 50 wavelengths in the lateral direction (equivalent to 90 RF lines with the given pitch) and 10 wavelengths in the elevation direction. Ten slices are being imaged for each of the volumes, resulting in 100 images for each of the concentrations. The data was analyzed in Chapter 3 using Nakagami and Homodyned-K estimates. Here, the purpose is to test if the deconvolution brings any improvements.

It can be seen in Figure 5.11 that the statistical estimates of the non-deconvolved images are more discriminating for the different concentrations than the estimates of the deconvolved images, especially the shape parameters m and α.

For the last part, deconvolution is applied on the biophantom data collected for the analysis in Chapter 3, in the idea or improving its discriminating properties (Figure 5.12). The values of the diffuse and coherent power follow trends very similar to those present in the originals, but the shape parameters do not show a more stable, monotonous evolution as a function of the scatterer density.

5.3 CONCLUSION

Various methods for the deconvolution of ultrasound signals have been developed in the previous three decades. Most of these methods target the improvement of the visual aspect of the ultrasound image, with the purpose of a clearer detectability of anatomical structures by the medical staff. For tissue characterization applications, the interest is similar, to remove the noise and blur effect in the image in order to see the image structures more clearly, but at a smaller scale: individual scatterers. A method was designed specifically for this purpose (Alessandrini et al. 2011), using a MAP framework with a Generalized Gaussian prior on the tissue reflectivity (the ensemble of scatterers). Interesting results were obtained on Orgasol biophantoms, showing potential for further research. After further testing of the method (partially in the works reported in this chapter), it is clear that the imperfections of the result do not allow the estimation of a reliable tissue reflectivity, especially in the case of dense media. Therefore, it is not helpful when studying the statistics of the deconvolved speckle / tissue reflectivity.

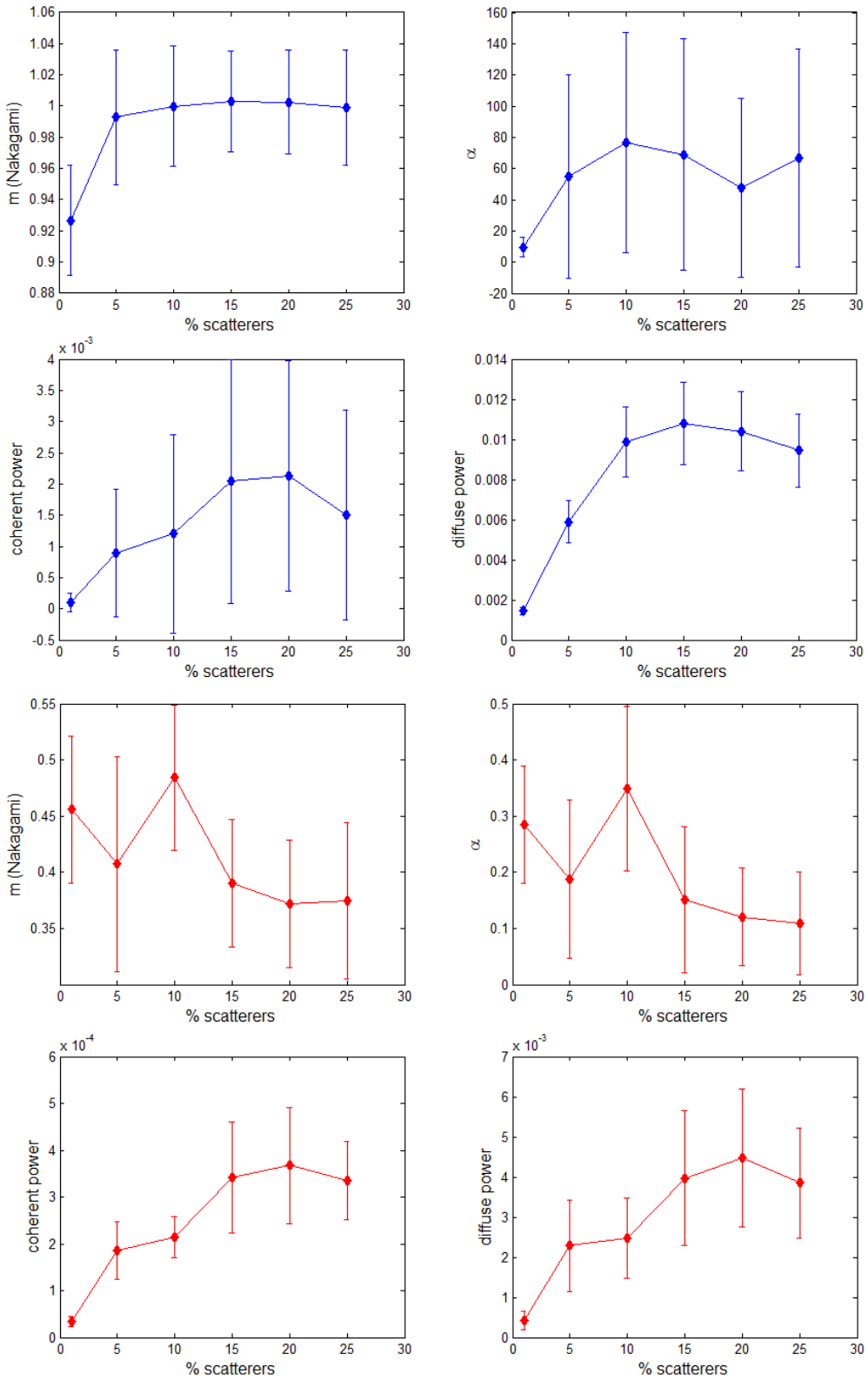

Figure 5.11 Statistical estimates obtained from simulated data, using the Nakagami and Homodyned-K distributions: from original ultrasound images (top rows, in blue) and from the deconvolved images (bottom rows, in red)

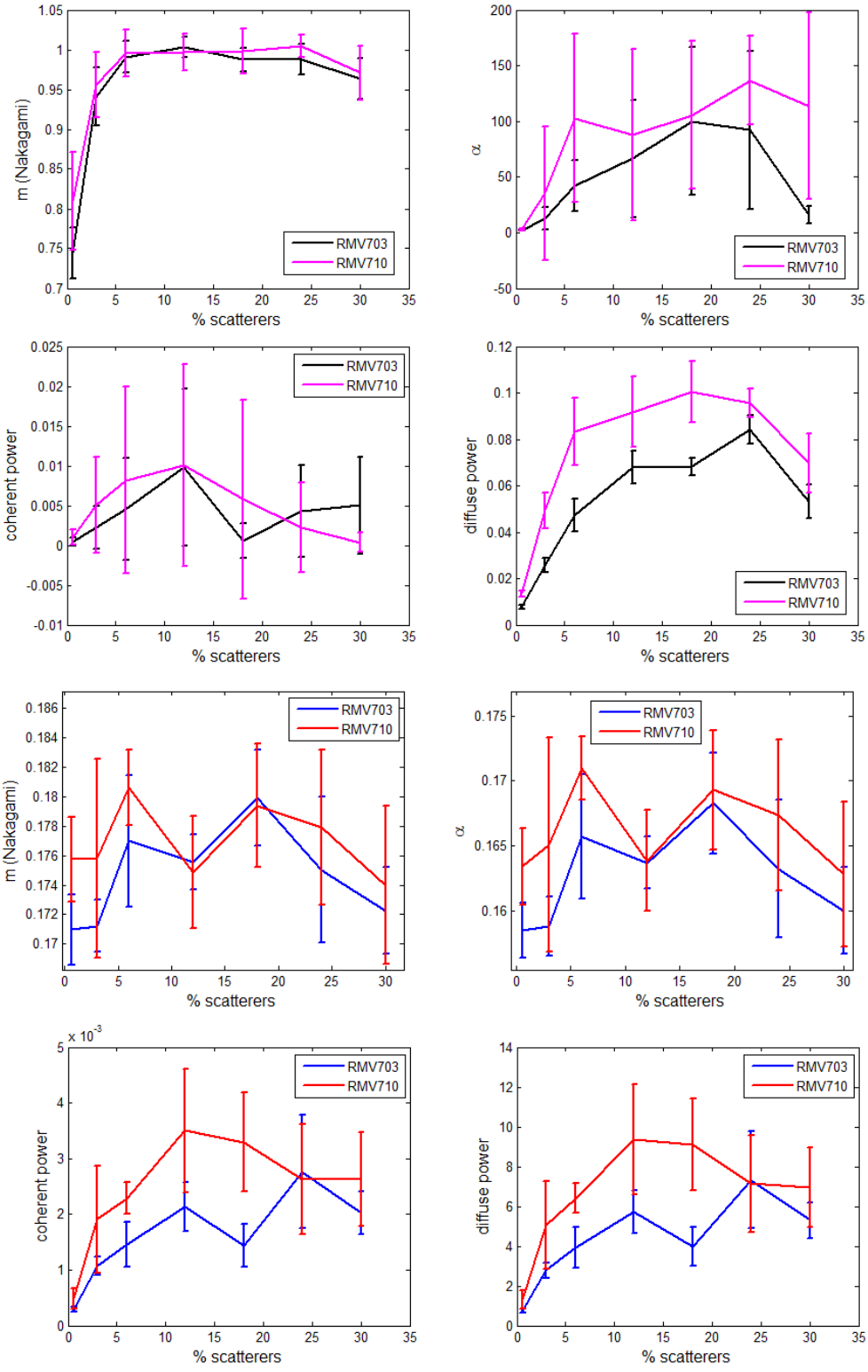

Figure 5.12 Statistical estimates obtained from deconvolved biophantom data, using the Nakagami and Homodyned-K distributions: from original ultrasound images (top rows, in black and magenta) and from the deconvolved images (bottom rows, in blue and red)

6 GLOBAL CONCLUSIONS AND PERSPECTIVES

The purpose of this thesis is to bring a contribution to ultrasound tissue characterization (Quantitative Ultrasound) using statistical modeling of ultrasound speckle. What determines the speckle pattern is the concentration of scatterers in the medium, together with the properties of the imaging system (determined mostly by the scanning frequencies). We study the possibility of quantifying the scatterer concentration by using three statistical models (distributions): the Generalized Gaussian distribution (GGD) for the RF signal, and the Nakagami and Homodyned-K distributions for the RF signal envelope.

In the first part, studies were conducted simultaneously on the Generalized Gaussian distribution and the Nakagami distribution, using the same data (simulated and experimental). The two distributions share a number of similarities. Each one is characterized by a pair of parameters: a shape parameter directly connected to the concentration of scatterers per resolution cell, and a scale parameter related to the backscattered energy (sensible to the scatterer concentration, but also to other scatterer characteristics). Moreover, their estimated shape parameters show similar, almost identical evolutions as a function of scatterer concentration per resolution cell. The values saturate for fully developed speckle (equivalent to concentrations higher than approximatively 10 scatterers per resolution cell) at around 2 for the GGD, and at around 1 for the Nakagami distribution. The dependence on the number of scatterers per resolution cell can be modelled by an exponential function. The shape parameter values obtained from simulations conducted at different frequencies fitted this model very well. However, experimental data obtained from Orgasol particle phantoms with different imaging systems did not fit a model with the same parameters, as the estimates appeared to saturate for a much lower scatterer number per resolution cell. We attribute this difference to a number of possible factors: inaccuracies in the approximation of the resolution cell size or the fabrication of the phantoms, a large variability of the scatterer size distribution, an insufficient amount of data for a reliable fit, or the presence of a diffuse background (produced by scattering structures other than the Orgasol particles) in the acquired images. Conducting a set of experiments on calibrated phantoms where the speckle pattern is influenced exclusively by the particles may produce different results. Acquisitions should be conducted with high-frequency transducers rather than with medical echograph probes, thus increasing the interval of equivalent scatterers per resolution cell in the non-saturation zone (<10) that is obtainable with a set of phantoms of different effective concentrations (Figure 3.7). This way, phantoms with relatively high effective scatterer concentrations can be used instead of the diluted ones which are harder to fabricate.

The Nakagami distribution was also used to fit simulated images of media with different nonlinearities. The shape parameters estimated on the fundamental images showed no difference from one media to another, but those computed in the same regions of the harmonic images were able to discriminate between different nonlinearities. However, a test of experimental data has yet to be conducted, in order to show if the discriminant power of the Nakagami shape parameter is

reliable. The fact of not having a method to build phantoms with a specific nonlinearity coefficient will pose a problem if we want a quantitative result.

In the second part, the Homodyned-K distribution was used to model the amplitudes on the echo envelope. This more complex model is described by three parameters, out of which α, the scatterer clustering parameter (somewhat analogous to the Nakagami shape parameter) depends on the scatterer concentration per resolution cell but is not limited to a maximal value for fully developed speckle. Simulations and experiments have shown that the estimated mean values of α do indeed increase as a function of scatterer concentration per resolution cell, even for fully developed speckle, at least up to a certain limit. In experiments, this limit is encountered for an effective scatterer concentration of around 10% at 30 MHz, but is yet to be determined with precision. The main difficulty is the high estimation bias at high concentrations, which depends directly on the number of decorrelated samples that are used for the estimation. Reduction of the bias and the search of a "reliability limit" of the parameter α by using large amounts of data is the subject of an on-going study.

A deconvolution technique for the ultrasound RF signal was also tested in order to assess its capacity of enhancing the contrast between statistical estimates obtained for different concentrations. Ideally, the deconvolution would lead to a better differentiation of the scattering structures present in the medium. Unfortunately, the resulting images do not estimate a distribution of scatterers, especially for very dense media. The statistical parameters estimated on these images sometimes increase the ambiguity between the different concentrations. Therefore we conclude that the strategy is not helpful when studying the statistics of the deconvolved speckle / tissue reflectivity.

Regarding the more distant goal of our research, we are hoping that once a framework for the reliable use of the statistical parameters (mainly α of the Homodyned-k distribution) is established, this parameter will be used as a feature in the classification of media with different concentrations. Statistical and spectral Quantitative Ultrasound estimates can be used together in order to increase their discriminant power in situations where one type of estimates are not able to clearly differentiate the media that they describe. The use of the α parameter may facilitate the application of these techniques in low-frequency imaging of the profound structures of the human body, where the low resolutions result in speckle that is fully developed even for low effective scatterer concentrations. The use of CMUT probes is an interesting perspective because of the resolution enhancement that they offer at relatively low frequencies.

7 RÉSUMÉ ÉTENDU EN FRANÇAIS

I INTRODUCTION

Une catégorie spécifique de pathologies, principalement des tumeurs bénignes et malignes, produisent des changements histologiques dans la structure du tissu affecté: la taille, la concentration et l'organisation des cellules. Du point de vue de la cytologie, des modifications de la structure des cellules sont également rencontrées. Typiquement, le diagnostic de ces lésions est effectué grâce à une biopsie réalisée à l'aide d'une aiguille, par endoscopie, laparoscopie ou même laparotomie, ici classés du moins invasif au plus invasif. L'échantillon de tissu extrait est ensuite analysé par les pathologistes afin de fournir un résultat exact, puisque la structure de la plupart de ces tissus pathologiques est bien connue.

Il serait évidemment utile pour les patients qui souffrent de ces pathologies de pouvoir bénéficier d'une technique de diagnostic non invasive qui offrirait la même fiabilité. L'imagerie par ultrasons permet l'exploration du corps humain sans le risque des effets ionisants. Cependant, les résolutions relativement faibles (lors de l'exécution d'un examen sur les structures profondes) et le faible rapport signal sur bruit (à cause du speckle ultrasonore caractéristique) sont des inconvénients non négligeables. Les tumeurs peuvent être détectées dans la majorité des cas, au cours d'un examen échographique classique, mais la nature de la tumeur est en général impossible à déterminer. Par conséquent, d'autres techniques sont utilisées pour obtenir une description plus précise de la pathologie. Ces méthodes sont regroupées sous le nom de caractérisation des tissus par ultrasons (aussi appelée Quantitative Ultrasound - QUS). QUS est en développement depuis les années 1980 et utilise l'analyse spectrale et l'analyse statistique appliquées sur le signal ultrasonore RF non-compressé ou son enveloppe pour estimer des paramètres qui peuvent être associés à des propriétés physiques des tissus telles que la taille, la concentration ou l'organisation des diffuseurs.

Les estimations QUS sont souvent dépendantes du système d'imagerie. Il est préférable d'effectuer l'analyse à des fréquences élevées, qui permettent de disposer d'une bande passante plus élevée et d'une résolution supérieure. A cause de la petite taille des réflecteurs (les diamètres des plus petites cellules ne mesurent que quelques microns), les basses fréquences n'offrent pas un niveau de détail suffisant. Le choix de la gamme de fréquence dépend de l'application, à cause du compromis profondeur-résolution caractéristique aux ultrasons. Une option intéressante pour augmenter la bande passante à des fréquences relativement basses est offerte par les transducteurs cMUT (capacitive Micromachined Ultrasonic Transducers), une technologie relativement nouvelle par rapport aux transducteurs piézoélectriques utilisés dans l'échographie clinique (fabriqués en Titano-Zirconate de Plomb, ou 'PZT').

Notre recherche est axée sur les statistiques du speckle ultrasonore. Sur la base de la théorie de la marche aléatoire, les amplitudes du speckle ultrasonore peuvent être modélisées par un nombre de distributions statistiques. Les paramètres qui définissent les distributions dépendent du nombre de diffuseurs dans le milieu et de l'énergie rétrodiffusée. L'estimation des paramètres dépend du modèle, des méthodes d'estimation, et de la quantité des données disponibles. Afin d'évaluer cela, les tests doivent être menés sur des milieux de différentes densités de diffuseurs. L'image RF peut être déconvoluée avant l'analyse statistique en tentant de récupérer la distribution de diffuseurs (réflectivité) originale du tissu. Les estimations statistiques peuvent être calculées sur l'image fondamentale ou harmonique. Après avoir défini des estimations fiables, celles-ci peuvent être utilisées comme caractéristiques pour la classification.

Le travail décrit dans cette thèse est consacré à la poursuite de l'exploitation des statistiques du speckle, appliqués sur le signal radiofréquence (RF) et son enveloppe (avec l'accent sur les distributions de Nakagami et K-Homodyne) acquis dans des milieux monodisperses homogènes. L'applicabilité de ces différents modèles statistiques et leur pouvoir discriminant est évalué. Dans les applications médicales, cela correspond à se concentrer sur une partie homogène d'un organe pour évaluer la densité des diffuseurs monodisperses qui le composent. Un changement de la densité de diffuseurs, et souvent un changement simultané de leur taille peut être un indicateur de la présence et / ou la progression de certaines pathologies (par exemple la fibrose hépatique). Travailler avec des statistiques peut être difficile et imprécis, en particulier lorsque l'on tente de caractériser des milieux très denses où la structure du speckle (nommé dans ce cas speckle pleinement développé) montre très peu d'écarts entre les différentes concentrations. Les paramètres de certains modèles sont limités à distinguer entre des densités qui engendrent du speckle partiellement développé (par exemple la distribution de Nakagami), tandis que d'autres n'ont pas cette limite (la distribution K-Homodyne).

Cette introduction est suivie d'un chapitre qui résume l'histoire et les méthodes utilisées pour la caractérisation des tissus, ainsi que la description des modèles statistiques utilisés dans ce but au cours des années. Le troisième chapitre se concentre sur l'analyse en utilisant les distributions Gaussienne Généralisée et Nakagami, mettant l'accent sur les effets des paramètres d'imagerie sur l'image fondamentale et harmonique. Le quatrième chapitre comprend une étude qui évalue les conditions nécessaires pour que la distribution K-Homodyned délivre des estimations fiables. Le cinquième chapitre reprend les résultats obtenus lors de l'application d'une technique de déconvolution comme une étape de traitement préalable à l'analyse statistique.

2 ETAT DE L'ART

La caractérisation ultrasonore des tissus mous se développe depuis plusieurs décennies. A partir des concepts les plus anciens datant des années '70 et jusqu'aux applications cliniques actuelles, une multitude de méthodes qualitatives et quantitatives ont été développées dans le but

d'extraire des informations sur la microstructure des tissus (l'ensemble des structures de diffusion de dimension inférieure à la longueur d'onde, appelées simplement diffuseurs ou réflecteurs) à partir des signaux ultrasonores. Certains exploitent le spectre des fréquences du signal rétrodiffusé, tandis que d'autres se concentrent sur la structure spatiale et les propriétés statistiques du speckle ultrasonore générée par la diffusion dans le tissu. Cette section présente un bref historique de la caractérisation ultrasonore des tissus.

Il est à noter que les diffuseurs qui font l'objet de caractérisation ultrasonore des tissus ne sont pas précisément identifiés. Considérant les bases de la physique des ultrasons, la réflexion se produit à la limite de deux zones avec un fort contraste d'impédance. Bien qu'il ait été supposé que celles-ci seraient les noyaux des cellules, certaines études sur des biofantômes (Franceschini et al. 2014) et du sang (Franceschini, Yu et Cloutier 2008b) ont conclu que les diffuseurs sont probablement les cellules entières. Bien sûr que dans un tissu complexe contenant différentes cellules ayant différentes propriétés acoustiques, de grands réflecteurs spéculaires, ou des agrégats, le problème devient plus compliqué.

Les méthodes de caractérisation des tissus se classifient dans deux grands groupes : les méthodes spectrales et les méthodes statistiques. Les méthodes spectrales visent l'analyse du spectre du signal rétrodiffusé par le milieu,, ce qui ramène au calcul du coefficient de rétrodiffusion et son intégration dans des modèles paramétriques qui permettent l'estimations des propriétés des réflecteurs, par exemple leur concentration et leur taille. Le coefficient de rétrodiffusion est défini comme l'intensité moyenne du signal rétrodiffusé par stéradian par unité de volume, normalisée par l'intensité incidente moyenne, selon (Ghoshal et al. 2013). De l'autre côté, les méthodes statistiques analysent la distribution des amplitudes du speckle ultrasonore, en utilisant comme modèle des distributions statistiques, dont les paramètres sont liés à la concentration de réflecteurs et la puissance rétrodiffusée par leur ensemble.

2.1 METHODES SPECTRALES

Historiquement, les premières idées sur l'exploitation du spectre ultrasonore pour retirer de l'information spécifique pour le milieu imagé appartiennent à (Holasek et al. 1975), qui sortent des images paramétriques du milieu basées sur la réponse du tissu à l'excitation ultrasonore en trois bandes de fréquence différentes. Leurs travaux ont inspiré d'autres équipes de recherche qui ont pu faire des mesures spectrales et donc quantifier leurs résultats. En (Lizzi et al. 1983) et (Lizzi et al. 1986), on retrouve la description théorique et expérimentale du nouveau domaine de la caractérisation des tissus ou Quantitative Ultrasound – QUS). L'influence de la microstructure du milieu se traduit par la fonction d'autocorrélation spatiale de l'impédance relative entre les réflecteurs et le milieu qui les entoure. Les caractéristiques du tissu sont associées aux quantités mesurables par ultrasons (e.g. la pente spectrale ou fréquence centrale du spectre). (M. F. Insana et al. 1989) offrent une caractérisation de la diffusion des ultrasons et les résultats de l'application

de trois modèles de diffusion (sphère fluide, Gauss et Faran) qui seront utilisés ultérieurement souvent dans le domaine. Une des conclusions de l'étude est la supériorité du modèle de Faran pour les tissus biologiques grâce au fait qu'il prenne en considération les ondes de cisaillement présentes dans le collagène. Une potentielle application très intéressante du QUS pour la thérapie ciblée du cancer est le suivi de l'apoptose : (Czarnota et al. 1999), (Kolios et al. 2002). (Chen et al. 1998) introduisent dans l'analyse spectrale le facteur de forme, défini comme la section de rétrodiffusion d'un diffuseur de taille finie. La méthode de référence pour la mesure du coefficient de rétrodiffusion est décrite dans (F. Insana and Hall 1990) : une technique de substitution en utilisant un transducteur à large bande, faiblement focalisé, analyse l'échantillon placé à proximité du rayon de courbure du transducteur. Le spectre mesuré est comparé à celui d'un milieu de référence, et des mesures de coefficient d'atténuation sont incluses. Les estimations des propriétés des diffuseurs sont obtenues en comparant la valeur mesurée avec la théorie. Les résultats des techniques basées sur le coefficient de rétrodiffusion peuvent discriminer entre fibroadénomes et carcinomes : (Oelze et al. 2004), (Oelze and O'Brien 2006), (Oelze and Zachary 2006). Les différents facteurs de forme ont été testés sur les tumeurs du rat (Hafez et al. 2009) et sur le sang (Franceschini, Yu, and Cloutier 2008a), (Franceschini, Yu, and Cloutier 2008b). Le modèle du facteur de structure (Structure Factor Model – SFM) a été utilisé dans beaucoup d'études : (Yu and Cloutier 2007), (Saha, Franceschini, and Cloutier 2011) , (Franceschini, Metzger, and Cloutier 2011), (Franceschini et al. 2014), (Han et al. 2015). Actuellement, c'est le modèle qui offre les meilleurs résultats en pratique, grâce à sa capacité de modéliser la décroissance de la puissance rétrodiffusée causée par la corrélation spatiale entre les particules à haute concentration.

2.2 METHODES STATISTIQUES

Les méthodes statistiques sont basées sur la modélisation du speckle ultrasonore en utilisant la marche aléatoire, ce qui permet de dériver des modèles de distributions statistiques pour les amplitudes du speckle. L'hypothèse générale est que le signal rétrodiffusé par un certain nombre de diffuseurs non-résolus contenus dans le volume d'une cellule de résolution peut être exprimée comme une somme de phaseurs aléatoires où l'effet de chaque diffuseur est pris en compte comme une déviation de l'onde incidente le long d'une direction aléatoire. Le signal résultant est une somme des phaseurs avec des amplitudes aléatoires x_k, des déphasages θ_k et une fréquence angulaire ω_0:

$$X = Xe^{jq} = \sum_{i=0}^{N-1} x_i e^{j\theta_i} \quad (1)$$

Les déphasages θ_i sont uniformément distribués dans l'intervalle $[-\pi, \pi]$, donc l'information intéressante reste celle donnée par les amplitudes. Alors, les modèles sont développés principalement pour l'enveloppe du signal radiofréquence (RF). Les modèles pour le signal RF

sont moins répandus.

Si le nombre des diffuseurs est suffisamment important (en pratique autour de 10 : (Rao, Mehra, and Zhu 1990), (Thijssen 2003)), les amplitudes de l'écho suivent une distribution normale et les amplitudes des phaseurs complexes (l'enveloppe de l'écho) suivent une distribution de Rayleigh (Burckhardt 1978), (Wagner et al. 1983) d'écart-type σ:

$$p_X(X) = \frac{X}{\sigma^2} e^{-\frac{X^2}{2\sigma^2}} \tag{2}$$

Si la présence d'une composante d'amplitude constante *s* (correspondant à la partie cohérente du signal rétrodiffusé) est prise en compte dans la somme de phaseurs, alors les amplitudes d'enveloppes suivent la distribution de Rice (Tuthill, Sperry, and Parker 1988) :

$$p_X(X) = \frac{X}{\sigma^2} e^{-\frac{X^2+s^2}{2\sigma^2}} I_0\left(\frac{sX}{\sigma^2}\right) \tag{3}$$

d'écart-type σ, où I_0 est la fonction de Bessel modifiée de première espèce et d'ordre zéro.

Si l'on suppose que le nombre d'étapes dans la marche aléatoire suit une loi binomiale négative(Jakeman 1980), la famille des distributions K est utilisé. La K-distribution (P M Shankar 1995) avec un facteur de forme γ et un facteur d'échelle b où $K_{\gamma-1}(\cdot)$ est la fonction de Bessel modifiée de deuxième espèce et d'ordre γ-1:

$$p_A(X) = \frac{2b}{\Gamma(\gamma)} \left(\frac{bX}{2}\right)^{\gamma} K_{\gamma-1}(bX) \tag{4}$$

est utilisée pour modéliser les milieux à faible densité de diffuseurs, tandis que la K-Homodyne (Dutt and Greenleaf 1994) :

$$p_A(\mathrm{A}) = \mathrm{A}\int_0^{\infty} xJ_0(\varepsilon x)J_0(\mathrm{A}x)\left(1+\frac{x^2\sigma^2}{2}\right)^2 dx \tag{5}$$

couvre toutes les configurations, et est donc le modèle le plus général. Le paramètre α est lié à la densité de diffuseurs dans le milieu, ε est la composante cohérente (puissance cohérente: ε^2), et σ est une composante de la puissance diffuse $2\sigma^2\alpha$.

Un modèle simple souvent considéré comme une approximation de la distribution K-Homodyne est la distribution de Nakagami : très utilisée dans la caractérisation des tissus (P. M. Shankar 2001),(Tsui et al. 2008) grâce à la robustesse et simplicité d'estimation de ses paramètres m (forme) et σ (échelle):

$$p_X(\mathrm{X}) = \frac{2m^m}{\Gamma(m)\Omega^m} x^{2m-1} \exp\left(-\frac{m}{\Omega}x^2\right) \quad (6)$$

La différence principale entre les deux est que la valeur du paramètre de forme de Nakagami, lié à la densité de diffuseurs, sature à 1 pour les concentrations élevées (au-delà de 10 diffuseurs/cellule de résolution, qui génèrent du speckle « pleinement développé »), alors que la valeur du paramètre analogue α de la distribution K-Homodyne ne sature pas. Cependant, la précision d'estimation de ce paramètre diminue. Pour cette raison, la plupart des études (par exemple (Hruska and Oelze 2009), (Mamou et al. 2011),(Trop et al. 2014)) analysent les milieux moins dense (qui génèrent du speckle partiellement développé), pour lesquels il est possible de montrer des résultats fiables en utilisant un nombre relativement faible d'échantillons.

Concernant le signal RF, il peut être modélisé à l'aide de la distribution normale, la distribution K_{RF} (Bernard, D'Hooge, and Friboulet 2006) ou la distribution Gaussienne Généralisée (Bernard et al. 2007) avec un paramètre de forme ξ et un paramètre d'échelle b:

$$g_X(\mathrm{X}) = \frac{\xi}{2b\Gamma(\frac{1}{\xi})} e^{-(\frac{|X|}{b})^{\xi}} \quad (7)$$

Ce type de modélisation est une alternative à la modélisation de l'enveloppe, utile surtout pour l'intégration dans des applications ou on travaille avec le signal RF (déconvolution, segmentation).

Cette thèse a comme objectif la caractérisation des tissus, donc on recherche un modèle fiable pour les données issues des milieux denses, ainsi que peu denses, qui permettrait de discriminer ces milieux. Les distributions Nakagami et K-Homodyne sont employées pour l'enveloppe, et la Gaussienne Généralisée (GGD) pour le signal RF.

3 CARACTERISATION STATISTIQUE DE L'ECHO RETRODIFFUSE EN UTILISANT LA DISTRIBUTION GAUSSIENNE GENERALISEE ET LA DISTRIBUTION DE NAKAGAMI

On propose d'évaluer la densité de diffuseurs dans le milieu à l'aide de la distribution Gaussienne Généralisée (appliquée sur le signal RF) et la distribution de Nakagami (appliquée sur l'enveloppe du signal RF). Le procédé d'évaluation est composé par les éléments suivants :

Sélection de la région d'intérêt: La théorie de la modélisation statistique du speckle suppose qu'un certain nombre de diffuseurs sont présents dans la cellule de résolution imagée. Par conséquent, afin de respecter cette hypothèse et obtenir des estimations statistiques qui peuvent être interprétées comme des mesures de la concentration de diffuseurs, la taille de la cellule de résolution à l'intérieur de la région d'intérêt (ROI) analysée devrait avoir une taille constante. Idéalement, la taille doit également être minimale. Ceci est valable dans la zone focale du transducteur. Puisqu'on travaille avec des statistiques, il est avantageux de choisir le nombre maximum d'échantillons disponibles dans ces conditions, afin d'obtenir des estimations non biaisées. On utilise des ROI 2D.

Le traitement du signal: Pour chaque expérience, l'analyse statistique est réalisée sur les ROI de même taille. L'analyse porte essentiellement sur l'image fondamentale, qui offre le meilleur rapport signal sur bruit (SNR), en filtrant les harmoniques et le bruit. Le système d'acquisition est généralement calibré afin d'éviter d'avoir des signaux (lignes RF) saturés, mais ceci est vérifié en post-acquisition et les signaux saturés sont supprimés. Les amplitudes de l'image RF résultante sont mises en correspondance avec une distribution Gaussienne Généralisée (GGD). Son enveloppe est calculée comme étant la valeur absolue de la transformée de Hilbert de cette image RF et puis la distribution de ses amplitudes est associée à une distribution de Nakagami.

Ajustement (correspondance) statistique: Cela signifie essentiellement l'association à un modèle dont les paramètres sont estimés. Ici, l'estimation se fait en intégrant les expressions du maximum de vraisemblance dans des itérations de Newton-Rhapson. Selon (Bernard et al., 2007), cette méthode est la plus efficace pour la GGD. Elle offre également le biais minimum pour la distribution de Nakagami.

3.1 STATISTIQUES DU SPECKLE EN FONCTION DE LA RESOLUTION DU SYSTEME D'IMAGERIE

Les paramètres de forme de ces deux distributions dépendent du nombre de diffuseurs par cellule de résolution. La résolution axiale, respectivement latérale sont égales à:

$$r_{ax} = \frac{c}{2 * BW} \tag{8}$$

$$r_{lat} = \lambda \frac{D_f}{D_{ap}} \tag{9}$$

Des expériences ont été menées sur des données issues des simulations et des acquisitions sur des fantômes.

Simulations 2D: Des milieux avec cinq concentrations différentes de diffuseurs (entre 10 et 1000 par mm^2) ont été simulés. Six sondes linéaires ont également été simulées pour l'exploration (Tableau 1). La taille de la cellule de résolution et la densité équivalente de diffuseurs par cellule de résolution ont été calculées (Tableau 2). La forme des diffuseurs n'est pas prise en compte, ils sont considérés comme diffuseurs à forme ponctuelle. La taille de la ROI a été choisie en fonction de la longueur d'onde, comprenant 10 longueurs d'onde dans la direction axiale (profondeur) et 20 longueurs d'onde dans la dimension latérale.

Fantômes : Des suspensions avec des différentes concentrations de particules d'Orgasol (particules fines en polyamide) ont été préparées pour étudier l'évolution des paramètres de la GGD et de Nakagami. Le diamètre des particules (entre 5-20 µ) a été adaptée à la résolution du système d'imagerie, pour chaque cas (pour que le diamètre de la particule soit petit par rapport à la longueur d'onde). Les suspensions ont été imagées en utilisant :

- Vevo 770 + transducteur RMV 704 (VisualSonics), F_c = 30 MHz
- Ula-Op + LA533 sonde linéaire PZT (MsD Lab, Florence, Italy), F_c= 8 MHz
- Sonix MDP + L14-5W/60 sonde linéaire PZT (Ultrasonix), F_c = 7 MHz
- Sonix MDP + sonde linéaire CMUT (Vermon, Tours, France), F_c = 4 MHz

où F_c est la fréquence de résonance de chaque probe.

Fc (MHz)	λ (µm)	Pitch (µm)	Kerf (µm)	Hauteur (mm)	Focus (mm)
5	308	428	25.00	4.00	17.5
10	154	214	12.5	2.00	15.5
15	102	141	8.33	1.33	12.5
20	77	107	6.35	1.00	10.0
25	61	85	5.00	0.72	8.0
30	51	68	4.00	0.62	6.0

Tableau 1 Caractéristiques des sondes simulées

Les résultats montrent une dépendance entre les paramètres de forme des deux distributions et la concentration de réflecteurs dans le milieu. On observe aussi la saturation (ξ=2, m=1) qui apparait à partir d'une certaine concentration, qui est de plus en plus basse quand on monte en fréquence. Les paramètres de forme dépendent donc de la fréquence d'imagerie. Ils dépendent également de la largeur de bande du transducteur ou de la sonde, et de la profondeur d'exploration dans le cas d'un transducteur focalisé. Tous ces facteurs influencent la résolution du système, ce qui revient à dire que les paramètres de forme dépendent plutôt de la concentration de diffuseurs par cellule de résolution. La saturation correspond à du speckle nommé « pleinement développé », qui se forme à partir d'une concentration d'environ 10 diffuseurs par cellule de résolution. De l'autre côté, les paramètres d'échelle dépendent du niveau

d'énergie rétrodiffusée (le paramètre Ω de Nakagami est effectivement équivalent à la puissance moyenne du signal) et ne sont donc pas des indicateurs de la structure du milieu.

Fc (MHz) / Densité de réflecteurs (nb part/mm^2)	10	50	100	500	1000	Surface de la cellule de résolution (mm^2)
5	1.800	9.00	18.00	90.00	180.0	0.1800
10	0.450	2.25	4.50	22.50	45.0	0.0450
15	0.200	1.00	2.00	10.00	20.0	0.0200
20	0.110	0.55	1.10	5.50	11.0	0.0110
25	0.075	0.37	0.75	3.75	7.5	0.0075
30	0.050	0.25	0.50	2.50	5.0	0.0050

Tableau 2 Nombre de diffuseurs par cellule de résolution

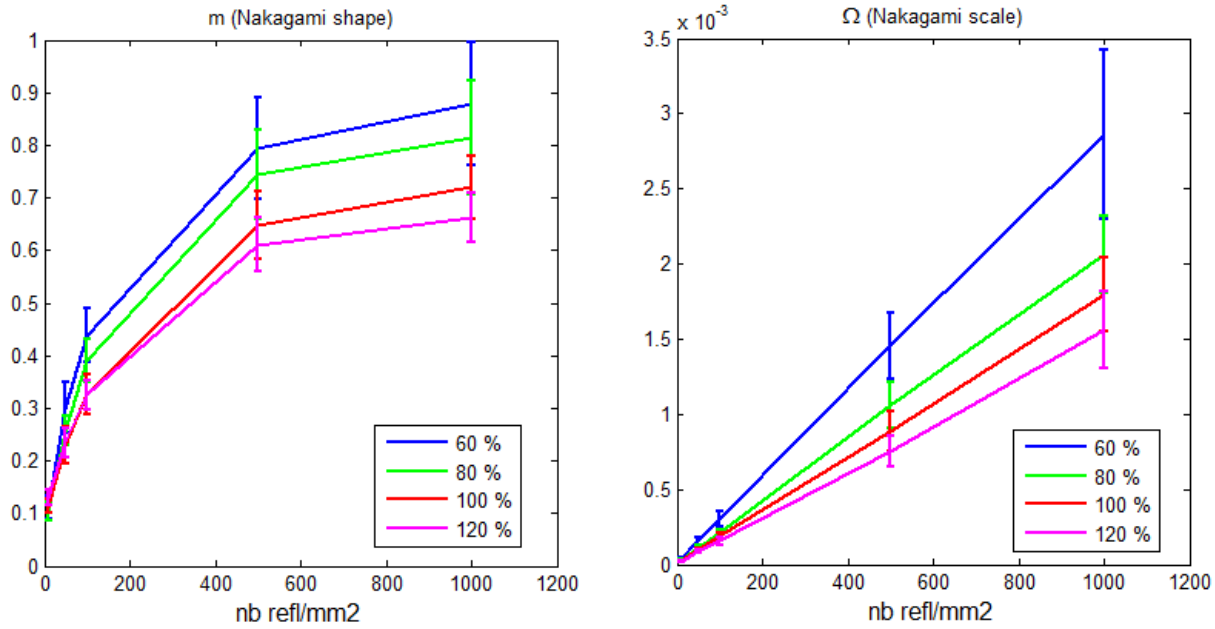

Figure 1 Paramètres de Nakagami en fonction de la largeur de bande de la sonde (exprimée en fonction de % de la fréquence centrale). Résultats en simulations à 30 MHz.

L'évolution des paramètres de forme en fonction de la densité de réflecteurs par cellule de résolution peut être modélisée par :

$$f(x) = a_1 * (1 - a_2 * e^{(-a_3 * x)}) \quad (10)$$

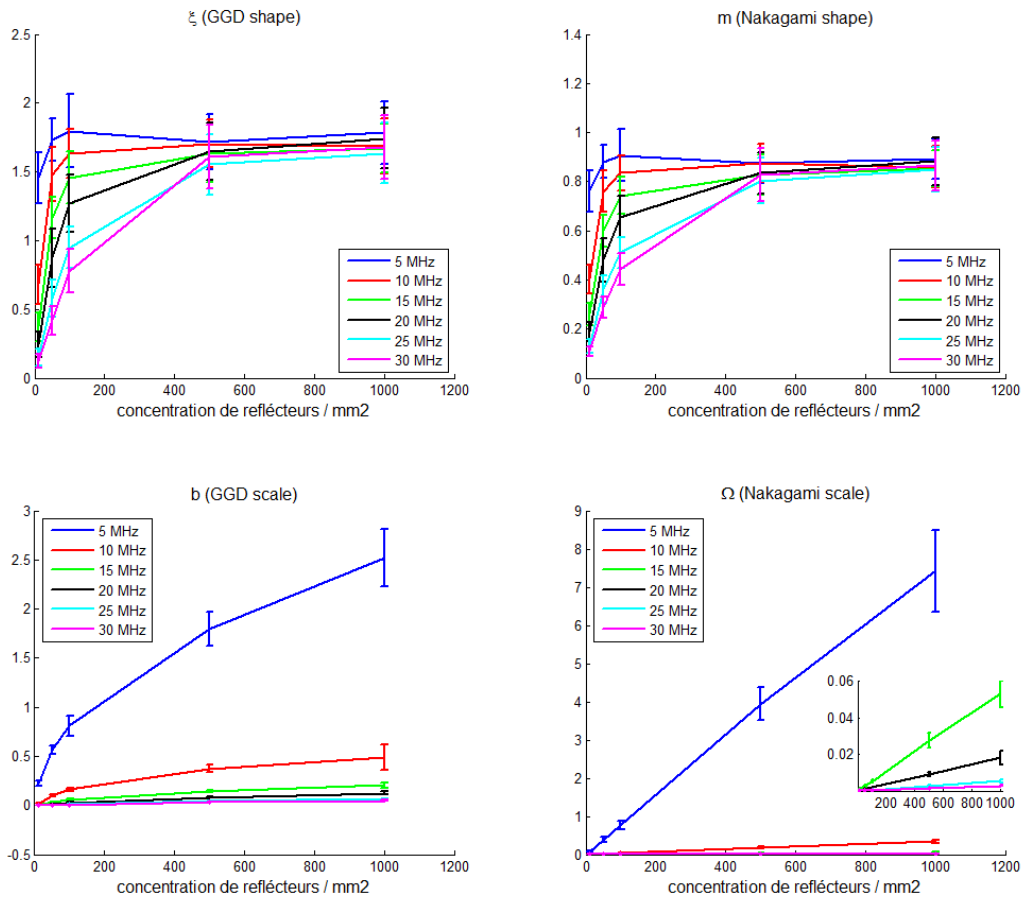

Figure 2 Résultats des estimations statistiques en fonction de la fréquence d'exploration et densité de diffuseurs par mm^2. Résultats obtenus sur des images simulées.

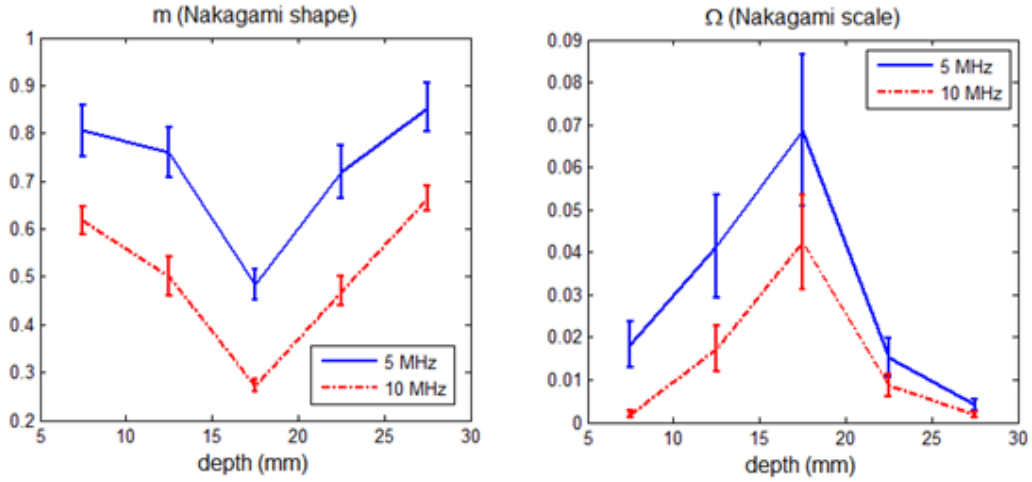

Figure 3 Paramètres de Nakagami en fonction de la profondeur d'exploration. Simulations du même milieu simulé avec 2 probes à 5 MHz, respectivement 10 MHz.

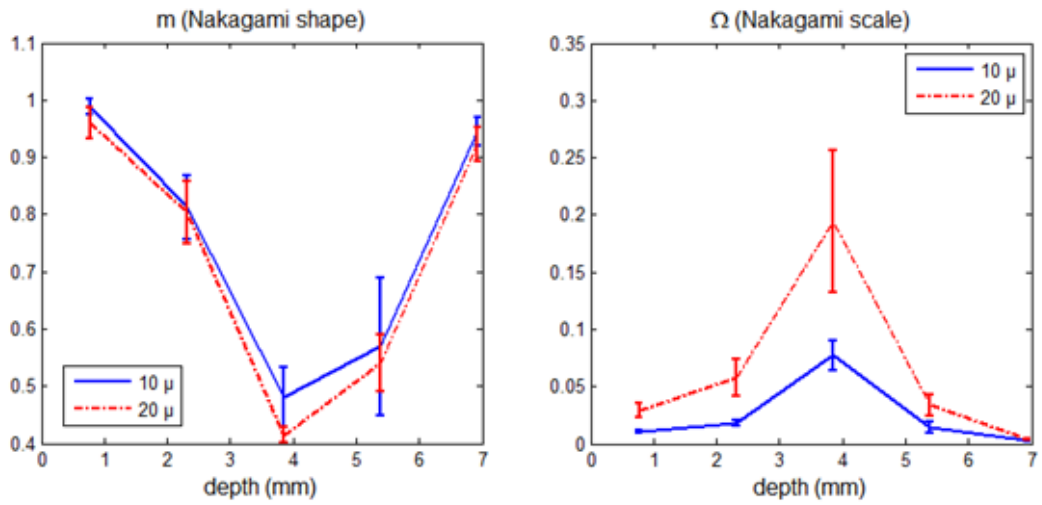

Figure 4 Paramètres de Nakagami en fonction de la profondeur d'exploration. Expériences à 30 MHz avec des particules d'Orgasol, diamètres de 10µ respectivement 20µ.

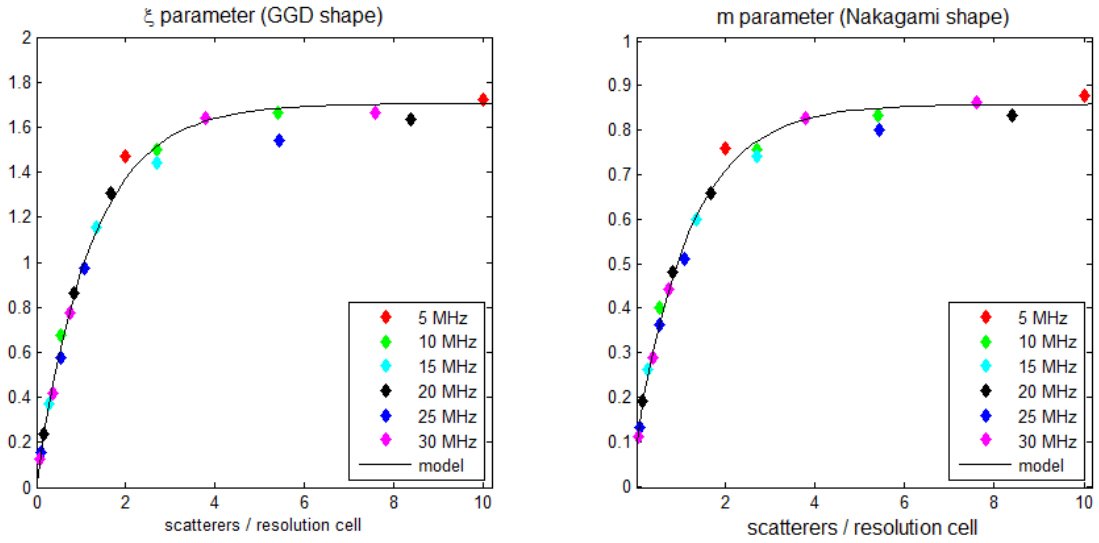

Figure 5 Evolution des paramètres de forme des deux distributions en fonction de la densité de particules par cellule de résolution, en simulation. Paramètres du modèle: (gauche) a_1=0.98, a2=0.81, a_3=1.70; (droite) a_1=0.90 ,a_2=0.82, a_3=0.85

Conclusions globales de l'étude : les paramètres de forme des deux distributions qui ont été utilisées pour la modélisation suivent bien la concentration des diffuseurs par cellule de résolution, ce qui permet de modéliser leur évolution en fonction de cette concentration à l'aide d'une simple modèle exponentiel. Ce modèle est très précis en simulation ; par contre, en combinant les données de fantômes obtenues avec plusieurs sondes et en utilisant la même convention pour la cellule de résolution, on a des difficultés à retrouver la même dépendance

globale, où à justifier complètement cette disparité. On suppose que parmi les sources d'erreur se trouvent l'approximation de la cellule de résolution, la variabilité de la taille des diffuseurs, le besoin d'une quantité plus élevée de données où, dans le cas des réflecteurs comme la polyamide qui a une impédance acoustiques bien différente de celle de l'eau, la présence des réflexions multiples qui ne sont pas prises en compte par les modèles statistiques.

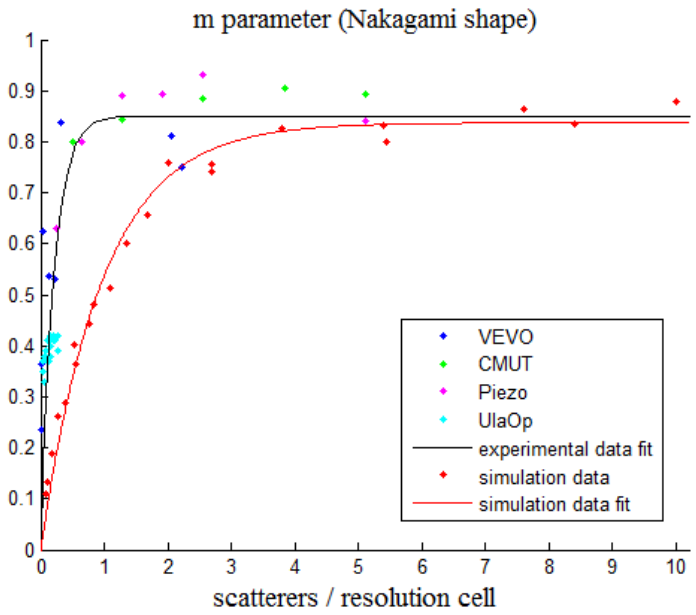

Figure 6 Evolution du paramètre m de Nakagami en fonction de la densité de particules par cellule de résolution, pour les données simulées et expérimentales. Paramètres du modèle (courbe expérimentale): a1=0.87, a2=0.55, a3=2.57

3.2 UTILISATION DES PARAMETRES STATISTIQUES COMME MESURE DE LA NONLINEARITE DU MILIEU

La propagation des ondes ultrasonores est intrinsèquement non linéaire, en raison de l'existence d'une phase de pression positive et une phase de pression négative. La conséquence immédiate d'une augmentation de la pression locale correspond à une augmentation de la température et par la suite de la vitesse de propagation (célérité) de l'onde. Par conséquent, la propagation du front de pression positive est plus rapide que celle du front de pression négative, ce qui conduit à une distorsion de la forme d'onde. Notamment dans le cas des échographes modernes qui émettent des ondes à haute pression (de l'ordre du MPa), la pression acoustique dans le tissu sera très élevée par rapport à celle du tissu au repos, générant ainsi une onde acoustique fortement non linéaire. D'un point de vue spectral, le phénomène génère des harmoniques. La vitesse de propagation des fronts d'onde positif (c^+) et négatif (c^-) dépende du paramètre de nonlinéarité β :

$$c^{\pm} = c_0 \pm \beta \frac{p}{\rho_0 c_0} \quad (11)$$

Ce paramètre est intéressant pour le domaine médical parce qu'il est spécifique pour chaque tissu. Les méthodes d'estimation utilisant des méthodes basées sur la théorie des ondes à amplitude finie sont très répandues pour les mesures de tels milieux. On teste la possibilité d'utiliser les paramètres des modèles statistiques appliqués sur l'image harmonique pour retrouver le paramètre de nonlinéarité du milieu. Les tests sont conduits sur des images simulées à l'aide de CREANUIS. La sonde simulée transmet à une fréquence de 10 MHz, est focalisée à 20 mm et présente les mesures suivantes : un Pitch de 214 µm, un Kerf de 12,5 µm, et une hauteur de 2 mm. La région d'intérêt (ROI) a une profondeur de 4,3 mm centré à la profondeur focale. Les lignes de RF sont échantillonnées à 80 MHz et espacées à une distance égale à la Pitch. La ROI et le milieu ambiant ont des coefficients de non-linéarité β différents : 3.5 constant pour le milieu ambient, et entre 3.5 et 50 dans la ROI. Diffuseurs avec des densités variables (2-30 diffuseurs par cellule de résolution) sont placés uniquement dans la ROI. Pour chaque concentration et chaque coefficient β, 50 images des diffuseurs placés aléatoirement sont été simulées. Chaque image simulée a été filtré dans la bande fondamentale et dans la bande du second harmonique, en utilisant un filtre Butterworth d'ordre 3.

Les paramètres estimés sur les images non-filtrés ou filtrés autour de la fréquence fondamentale ne montrent pas de différences entre les courbes correspondant aux paramètres de nonlinéarité différents, le seul facteur discriminant étant la concentration. Par contre, les images filtrées autour de la seconde harmonique ont des statistiques bien différentes. La raison est le phénomène d'augmentation de l'amplitude de l'onde harmonique en fonction de la profondeur, plus prononcé dans les milieux à forte nonlinéarité. Ce phénomène génère des inhomogénéités au niveau de la distribution des amplitudes dans l'image (Figure 7 - dans le cas d'une forte nonlinéarité, l'histogramme contient un plus grand nombre de basses amplitudes, ce qui correspond à une valeur basse du paramètre de forme).

Des simulations ont montré que les paramètres statistiques de Nakagami peuvent être utilisés comme une mesure de la non-linéarité, si elles sont calculées sur l'image harmonique. Bien sûr, certaines valeurs du β choisies pour la simulation sont très élevées par rapport à celles typiques rencontrées dans les tissus. L'étude évalue la capacité discriminante théorique des estimations statistiques. Si une application réelle est souhaitée pour les tissus, une étude plus complète sur une grande quantité de données serait nécessaire pour évaluer l'exactitude. Ne pas avoir une méthode pour construire des fantômes avec un coefficient de non-linéarité spécifique pourrait être un obstacle. L'utilisation des estimations statistiques comme une méthode de caractérisation complémentaire pourrait s'avérer aussi intéressant, et pourrait fournir un soutien pour une meilleure classification si les estimations sont considérées comme caractéristiques des milieux respectifs.

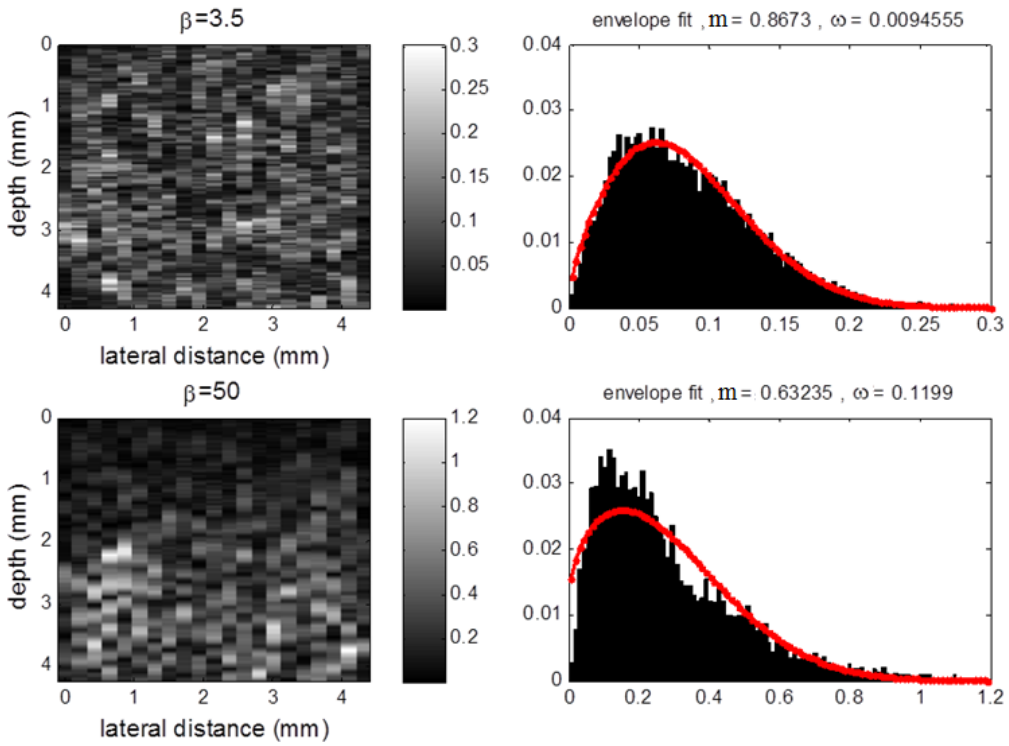

Figure 7 Exemples d'images harmoniques simulées et leurs ajustement statistique, pour une concentration de 14 diffuseurs/cellule de résolution, et paramètres β égaux à to 3.5 (en haut) et 50 (en bas)

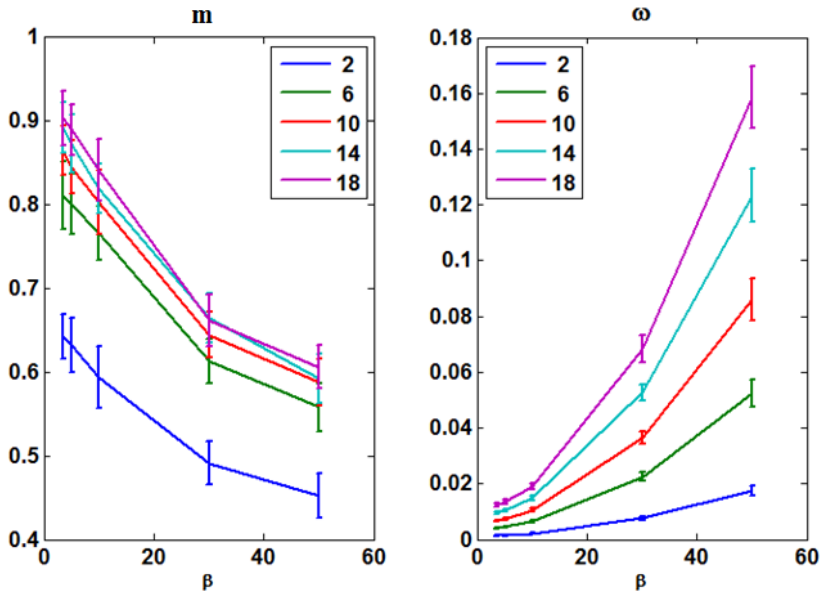

Figure 8 Estimations des paramètres de forme (m) et échelle (ω) de Nakagami pour les images harmoniques en fonction de β. Le nombre de diffuseurs par cellule de résolution est donné dans la légende.

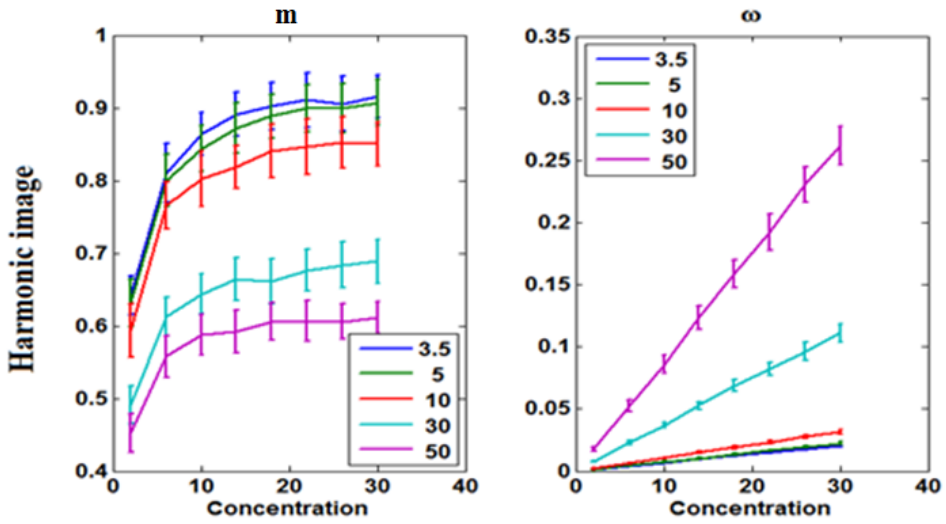

Figure 9 Estimations des paramètres de forme (m) et échelle (ω) de Nakagami pour les images harmoniques en fonction du nombre de diffuseurs par cellule de résolution. Le coefficient β est donné dans la légende.

4 CARACTERISATION STATISTIQUE DE L'ECHO RETRODIFFUSE EN UTILISANT LA DISTRIBUTION K-HOMODYNE

La distribution K-Homodyne est la distribution statistique la plus complète et polyvalente utilisée pour modéliser l'enveloppe du speckle ultrasonore produit par des milieux de faible densité (moins de 10 diffuseurs / cellule de résolution) et les milieux de haute densité (plus de 10 diffuseurs / cellule de résolution), tout en tenant compte de la présence d'une composante cohérente d'amplitude constante. On rappelle l'expression de la densité de probabilité de la distribution K-Homodyne:

$$p_A(\mathrm{A}) = \mathrm{A}\int_0^\infty x J_0(\varepsilon x) J_0(\mathrm{A}\,x)\left(1+\frac{x^2\sigma^2}{2}\right)^{-\alpha} dx \qquad (12)$$

Pour l'estimation des paramètres, on utilisera l'algorithme décrit en (Destrempes, Porée, and Cloutier 2013). Selon les auteurs, les trois paramètres de la distribution qui ont une signifiacation physique sont : l'intensité moyenne μ, le paramètre « de forme » décrivant l'agglomération des diffuseurs α, et le paramètre de structure κ (le rapport entre la puissance cohérente ε^2 et la puissance diffuse $2\sigma^2\alpha$). L'algorithme se sert des valeurs de μ, et des statistiques U et X calculées sur les échantillons de l'intensité I:

$$U = E[\log I] - \log E[I] \qquad (13)$$

$$X = E\left[IlogI\right] / E\left[I\right] - E\left[logI\right] \tag{14}$$

Ainsi, l'estimation peut être formulée comme le problème de minimisation :

$$E[I] = \bar{\mathrm{I}}, \mathrm{U}_{HK} = U, X_{HK} = X \tag{15}$$

L'algorithme vise l'estimation de α et d'un paramètre algorithmique γ :

$$\gamma = \frac{\varepsilon^2}{2\sigma^2} \tag{16}$$

L'estimation se fait à partir d'une initialisation de α comme le minimum entre $\alpha_0 = 1/(\mathrm{X}-1)$ et un $\alpha_{\max}$ imposé pour optimiser le processus. L'estimation des paramètres α et γ se fait consécutivement par dichotomie, en utilisant la propriété de monotonie des statistiques U et X. Ultérieurement, ε et σ sont estimés à partir de :

$$\varepsilon^2 = \mu\gamma / (\gamma + \alpha), \sigma^2 = \mu / (2(\gamma + \alpha)) \tag{17}$$

4.1 ETUDE SUR DES BIOFANTÔMES

Une étude est conduite pour estimer le pouvoir discriminant des paramètres de la K-Homodyne dans les milieux denses, sur des données provenue des biofantômes. Les signaux rétrodiffusés de biofantômes ont été obtenues à partir des expériences décrites dans la section III de Franceschini et al. (2014), qui sont brièvement résumées ici. Les données expérimentales ont été acquises à partir de biofantômes concentrées composées de cellules identiques de leucémie K562 noyées dans un fond de soutien en plasma-thrombine avec différentes concentrations de cellules entières allant de 0,006 à 0,3 (de 0,6% à 30%): 0,006; 0,03; 0,06; 0,12; 0,18; 0,24 et 0,30.

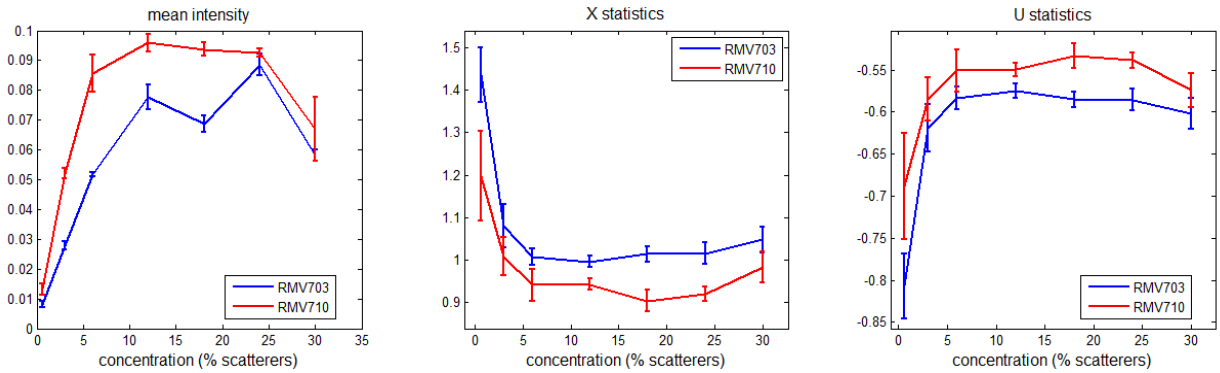

Figure 10 Intensité moyenne, valeurs des statistiques X et U pour les données provenant de biofantômes

La taille moyenne d'une cellule est 6,34 ± 0,94 µm. Les mesures ont été faites en utilisant un système haute fréquence Vevo 770 (VisualSonics Inc., Toronto, Canada). Deux transducteurs monoélément sphériques (RMV710 et RMV703) ont été utilisés pour acquérir des données RF de chaque biofantôme. Le RMV710 et le RMV703 ont des fréquences centrales des 25 et 35 MHz, sont focalisés à 15 et 10 mm et ont un f-number de 2,1 et 2,5, respectivement. Pour chaque fantôme, les acquisitions ont été réalisées à six endroits différents séparés par 0,6 mm.

Chaque ROI de taille de 0,75 mm (profondeur, centrée au point focal) x 0,5-1,0 mm (largeur) a été prétraité avant l'estimation des paramètres statistiques. Premièrement, les données RF sont compensées pour les effets d'atténuation. Les coefficients d'atténuation α_{att} mesurées pour les concentrations de 0,06, 0,12, 0,18, 0,24, et 0,30 sont 0,0098, 0,0184, 0,0215, 0,0202 et 0,0280 dB MHz-1 mm-1, respectivement (voir la section III.C dans Franceschini et al., (2014)).

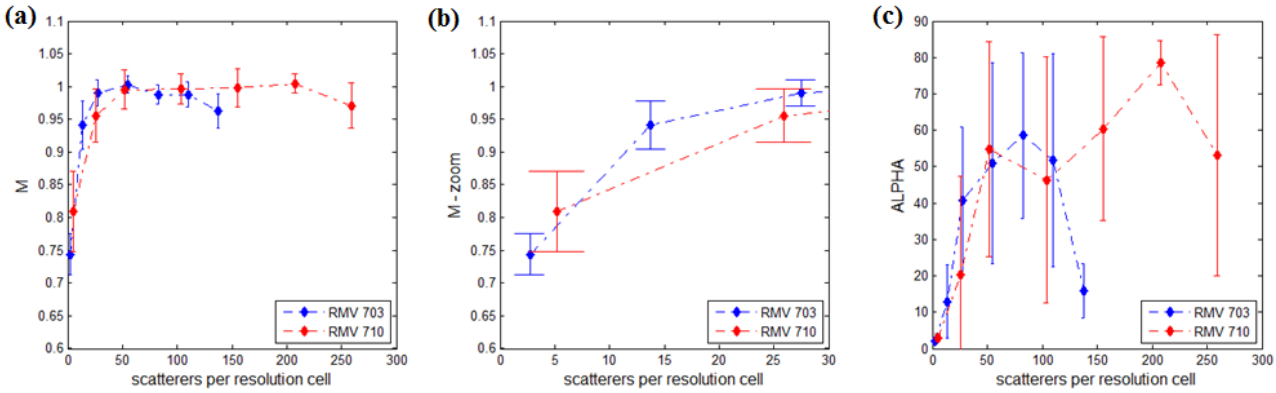

Figure 11 Paramètres de forme des deux distributions en fonction du nombre de diffuseurs par cellule de résolution (a) Paramètre m de Nakagami (b) Paramètre m de Nakagami –concentrations basses (c) Paramètre α de la K-Homodyne

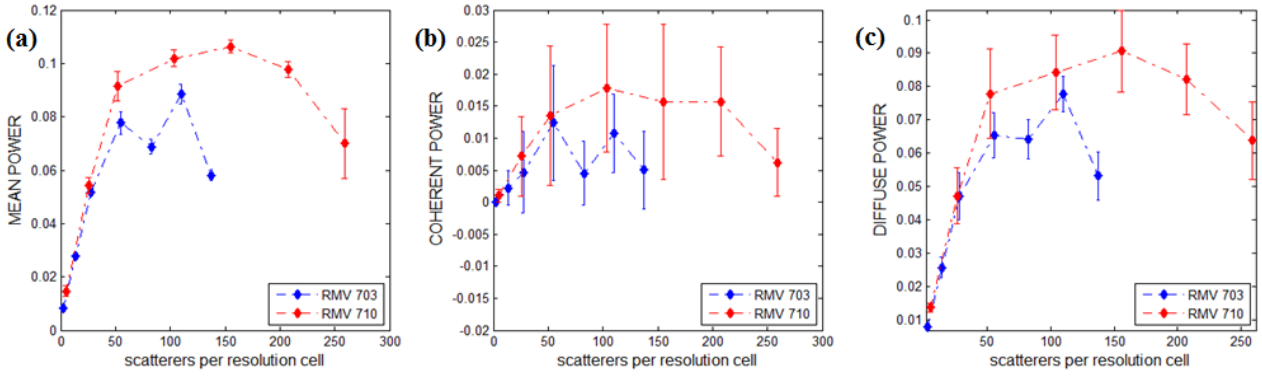

Figure 12 Puissance rétrodiffusée en fonction du nombre de diffuseurs par cellule de résolution, estimée à l'aide des paramètres d'échelle des deux distributions (a) puissance moyenne (paramètre Ω de Nakagami) (b) puissance cohérente ε^2 (c) puissance diffuse $2\sigma^2\alpha$

L'atténuation a été compensée selon (Oelze et O'Brien (2002)) pour chaque ligne RF. L'atténuation du milieu intermédiaire (l'eau) a été ignorée. Les signaux RF compensés ont ensuite été filtrés dans la bande 10-32 MHz pour le RMV 710 et 18-42 MHz pour le RMV 703. Après le calcul des enveloppes, l'estimation de paramètre se fait avec l'algorithme de (Destrempes, Porée, and Cloutier 2013). La cellule de résolution a été considérée comme un ellipsoïde dont le diamètre est égal à la résolution du système dans chacune des trois dimensions.

Comme la théorie le prédit, les valeurs du paramètre m augmentent en fonction de la concentration de diffuseurs. Cependant, m sature très rapidement autour de 1 (correspondant à une distribution de Rayleigh) et ne discrimine pas entre les concentrations lorsque la densité est d'au moins 6%. Nous pouvons également observer qu'il n'y a presque pas de différence entre les données acquises avec les deux sondes, vu qu'on a du speckle pleinement développé. Le paramètre d'échelle (ou intensité moyenne) mesure l'écho rétrodiffusé augmente également avec la concentration, avant de diminuer pour les concentrations très élevées (25% et 30%). Pour ces valeurs très élevées de concentration, et surtout aux fréquences plus élevées (sonde RMV 703), l'effet de l'atténuation est si fort que l'énergie véhiculée par les fréquences à la fin de la bande passante est entièrement absorbée, générant une diminution du niveau d'énergie rétrodiffusée. Un autre phénomène qui est également non négligeable à des concentrations élevées est l'interférence destructive croissante due à l'agglomération des particules, que les modèles ne prennent pas en compte.

D'autre part, le paramètre α continue à augmenter, mais l'estimation a une précision plus faible. La grande variabilité pour les milieux denses correspondant à des valeurs élevées de α peut être expliquée par la borne de Cramer Rao (chapitre 3 (Kay, 1993)), qui stipule que la variance d'un estimateur non-biaisé est au moins égale à l'inverse de l'information de Fisher $I(\alpha)$:

$$I(\alpha) = -E\frac{\partial^2 \ln p(x;\alpha)}{\partial \alpha^2} \qquad (18)$$

ou $p(x;\alpha)$ est la function de vraisemblance pour α. Pour la distribution K-Homodyne, l'information de Fischer est compliqué à développer sous forme analytique, mais les simulations numériques montrent qu'elle dépend de $1/\alpha^2$. Donc, la variance de l'estimation va augmenter en fonction de la vraie valeur de α.

Quant aux paramètres qui décrivent l'échelle de la distribution, la puissance de la composante cohérente augmente avec la concentration et semble être constante pour des concentrations supérieures à 12%. La puissance diffuse suit une tendance qui est très similaire à celle de la puissance totale, et constitue également l'élément dominant de la puissance totale.

4.2 EFFET DU NOMBRE D'ECHANTILLONS ET DE LEUR CORRELATION SUR L'ESTIMATION DES PARAMETRES

Simulations des échantillons indépendants identiquement distribués (i.i.d.)

En utilisant la formule :

$$x_i = \sqrt{\left(\varepsilon + X\sigma\sqrt{z/\alpha}\right)^2 + \left(\varepsilon + Y\sigma\sqrt{z/\alpha}\right)^2} \tag{19}$$

on simule des échantillons i.i.d. d'une distribution K-Homodyne de paramètres $(\alpha, \varepsilon, \sigma)$ à partir des échantillons X and Y des distributions normales unitaires, et des échantillons z d'une distribution gamma avec un paramètre de forme α et un paramètre d'échelle 1. Les simulations sont conduites avec des valeurs de α imposées (2 intervalles qui correspondent à des valeurs typiques pour 2 catégories de concentrations : entre 1-20 avec un pas de 1 et entre 30 et 80 avec un pas de 10) et des valeurs de ε et σ constantes (ε=σ=1). Le nombre d'échantillons pour chaque trinôme de valeurs (α,1,1) varie entre 10^3 et 10^8, et le nombre de réalisations est fixé à 100.

Les valeurs du biais et de la variance augmentent avec la valeur de α, mais décroissent quand le nombre d'échantillons augmente. Le biais est globalement négatif mais tend vers 0 quand on augmente le nombre d'échantillons, ce qui signifie que α est sous-estimé et on s'attend que la valeur de cette estimation monte avec un nombre croissant d'échantillons. On applique cette observation dans la section suivante, ou on fait des estimations sur des images ultrasonores simulées et issus des biofantômes étudiés précédemment.

Un autre point important est le fait que la corrélation des échantillons adjacents, induite par le sur-échantillonnage (axial ou latéral) augmente la variance de l'estimation globale, alors on a l'intérêt de décorréler les échantillons avant l'estimation, pour pouvoir comparer les résultats avec ceux obtenus précédemment.

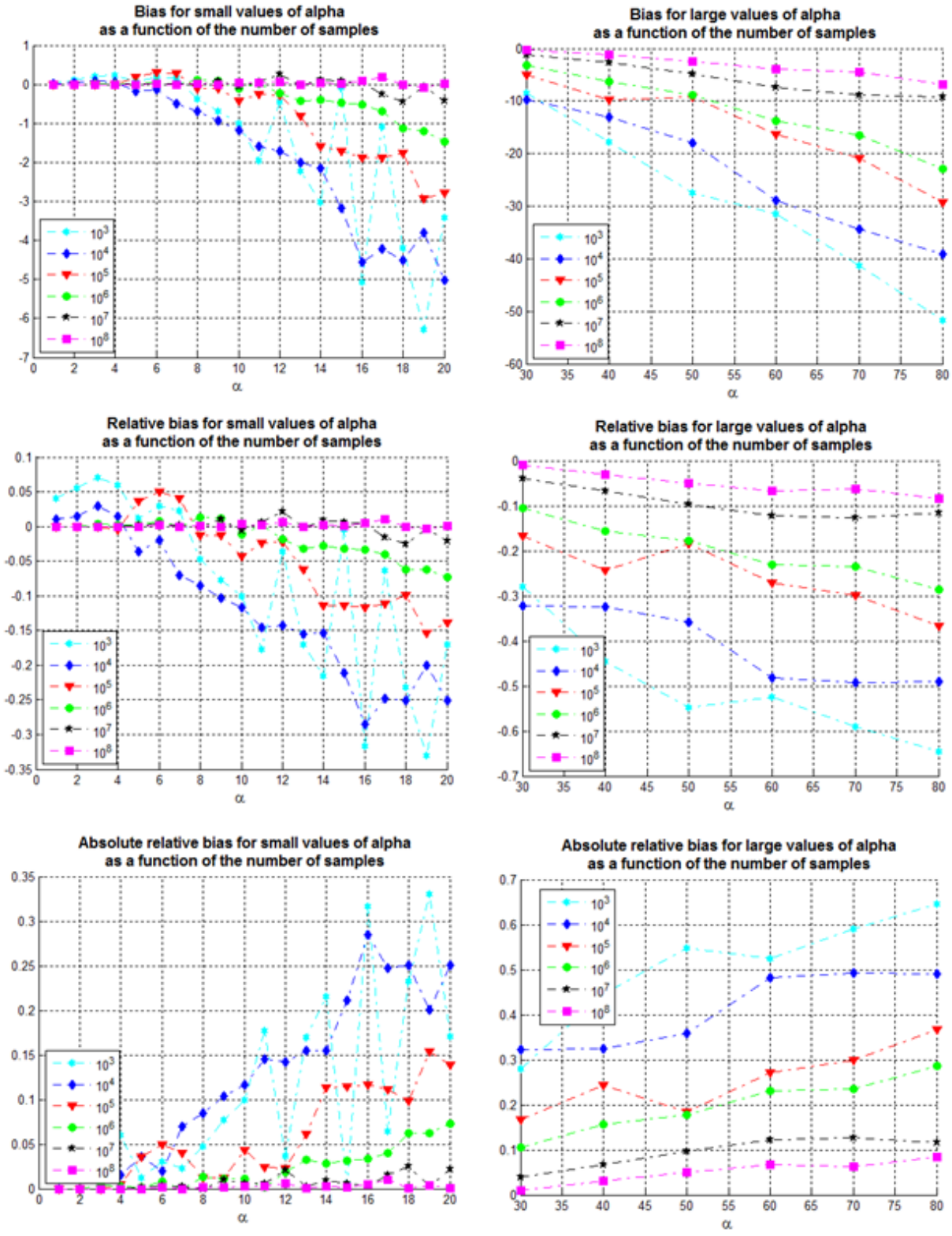

s

Figure 13 Biais, biais relatif et biais relatif absolu pour les estimations de α dans le cas des deux gammes de α réel : 'petit' (1-20) et 'grand' (30-80)

Simulations d'images ultrasonores: Six concentrations de diffuseurs avec un diamètre de 13 µ sont considérés: 1%, 5%, 10%, 15%, 20% et 25%. Les positions des centres de diffuseurs sont générées de façon aléatoire à partir d'une distribution uniforme, et le diamètre des particules est pris en compte en imposant une distance d'exclusion (égale au diamètre) entre les centres. Dix distributions de particules 3D ont été simulées pour chaque concentration, équivalentes à 10 volumes égaux de 20 longueurs d'onde dans la dimension axiale, 50 longueurs d'onde dans la direction latérale et 10 longueurs d'onde dans la direction azimutale. Dix tranches sont imagées pour chacun des volumes, résultant en100 images pour chacune des concentrations. La fréquence d'exploration a été fixée à 30 MHz, avec la bande passante relative de 60% de cette fréquence, pour une sonde avec 64 éléments actifs, un pas d'élément de 68 µm, entaille de 4 µm et une hauteur de 2,5 mm. La configuration donne une cellule de résolution de l'ordre de 0.0004 mm^3. Les concentrations de diffuseurs équivalentes calculées par cellule de résolution sont de 3,5, 17, 34, 51, 68, et 85. Les estimations sont faites sur des zones (ROI) de tailles différentes, et le résultat est représenté en fonction du nombre d'échantillons non-corrélés dans l'image.

Biofantômes : Les même que précédemment.

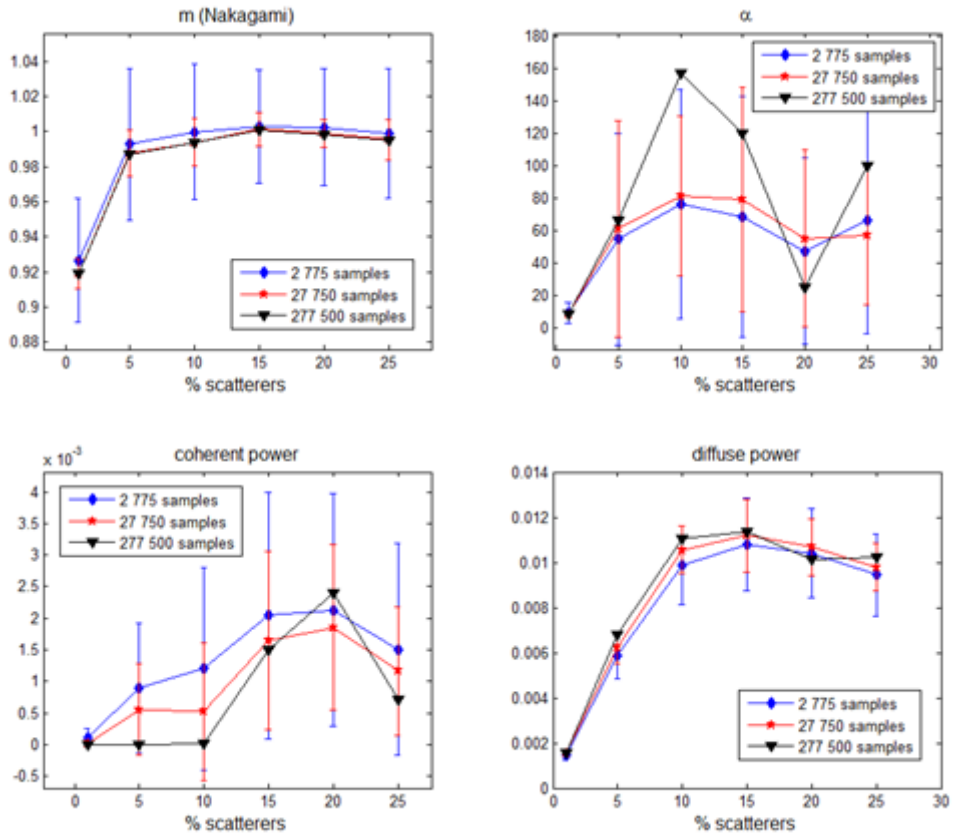

Figure 14 Valeurs estimées pour α, la puissance diffuse et puissance cohérente obtenues à partir des images simulées, en fonction de la concentration de diffuseurs et nombre d'échantillons non-corrélés

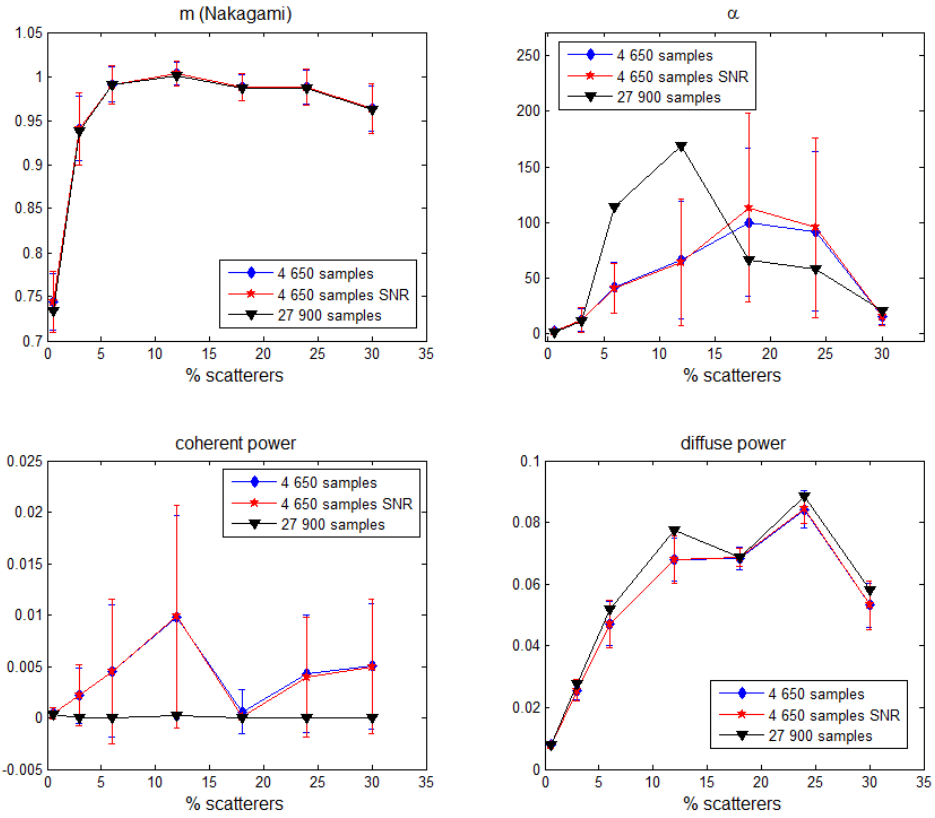

Figure 15 Valeurs estimées pour α, la puissance diffuse et puissance cohérente obtenues à partir des données acquises sur les biofantômes avec la sonde RMV 703, en fonction de la concentration de diffuseurs et nombre d'échantillons non-corrélés

Pour les données testées, le paramètre α de la K-Homodyne augmente de façon monotone en fonction de la densité de diffuseurs jusqu'à 'une densité volumique comprise entre 10 et15%. Au-delà de cette valeur, l'évolution ne tient plus compte de la concentration, et on suppose que c'est à cause des limitations numériques de l'algorithme. En ce qui concerne les valeurs réelles du paramètre α, si on se réfère à l'étude précédente pour les biais attendus lors de l'utilisation du nombre d'échantillons qui étaient disponibles, il peut être considéré que les valeurs réelles de α pour les densités respectives n'ont pas été obtenues avec précision. Les estimations ne suivent pas un modèle spécifique en fonction de la densité de diffuseur par cellule de résolution d'un jeu des données à un autre; donc nous supposons qu'ils pourraient dépendre d'autres facteurs liés au système d'imagerie ou de phénomènes physiques qui doivent être étudiés. Cependant, nous avons observé que les estimations augmentent de façon monotone pour des concentrations inférieures à 10% dans tous les cas. Cela pourrait faire l'objet de futurs travaux de recherche visant à déterminer si les estimations peuvent être associées à une "faible" concentration particulière de diffuseur de moins de 10%.

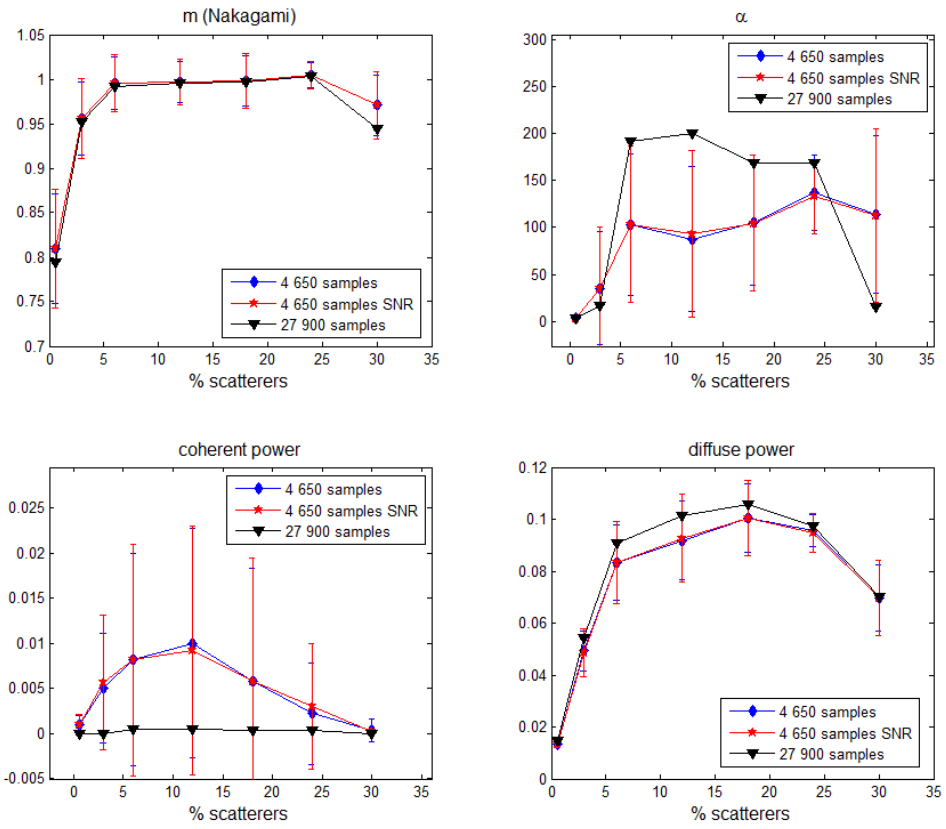

Figure 16 Valeurs estimées pour α, la puissance diffuse et puissance cohérente obtenues à partir des données acquises sur les biofantômes avec la sonde RMV 710, en fonction de la concentration de diffuseurs et du nombre d'échantillons non-corrélés

5 APPORT DE LA DECONVOLUTION POUR LA CARACTERISATION DES TISSUS

Si on pense à l'imagerie ultrasonore dans le cadre plus classique de traitement de l'image, un problème aussi classique apparaît: la dégradation par le système d'imagerie. L'effet principal est ici le flou induit par convolution avec l'image d'un point, la Point Spread Function (PSF) caractéristique pour le système d'imagerie. La déconvolution dans l'imagerie médicale ultrasonore tente à enlever cet effet de flou, améliorer la résolution et le contraste de l'image, pour mieux mettre en évidence certaines structures anatomiques d'intérêt. Pour la caractérisation des tissus, l'intérêt est de récupérer la distribution originale des diffuseurs dans le milieu.

Les méthodes les plus répandues dans la littérature utilisent le filtrage inverse (Taxt and Frolova 1999), le filtrage homomorphique (Jiřík and Taxt 2006), et les cadres statistiques du type Maximum A Posteriori (MAP) - (Michailovich and Tannenbaum 2007). Une méthode qui intègre

le MAP dans un schéma itératif de type Expectation Maximization (EM) a été développée en (Alessandrini et al. 2011) spécialement pour être appliquée dans la caractérisation des tissus. L'apport souhaité de la déconvolution dans notre contexte est d'améliorer le pouvoir discriminant des paramètres statistiques. La réflectivité de tissu est considérée comme suivant une distribution gaussienne généralisée (GGD), dont le paramètre d'échelle est également mis à jour après chaque étape de maximisation, afin d'améliorer la connaissance préalable de la réflectivité pour la prochaine itération. Le MAP s'exprime comme :

$$X = \arg\max_{x}[\mathrm{P}(\mathrm{y}\,|\,\mathrm{x},\sigma_n)\,\mathrm{P}(\mathrm{x})] \tag{20}$$

où $\mathrm{P}(\mathrm{y}\,|\,\mathrm{x},\sigma_n)$ est la probabilité de y conditionnée par x (ou la vraisemblance de y quand x et σ_n sont connus), et $\mathrm{P}(\mathrm{x})$ est la probabilité à priori de x. En appliquant le logarithme, remplaçant la vraisemblance qui dépend des propriétés statistiques du bruit et supposant l'a priori de type GGD spour $\mathrm{P}(\mathrm{x})$, la fonction à minimiser devient :

$$L = -\frac{1}{2\sigma_n^{\,2}}\left\|\mathrm{y}-\mathrm{Hx}\right\|_2^2 - \lambda\left\|x\right\|_\xi^\xi \tag{21}$$

ou λ est une constante de régularisation, ξ est le paramètre de forme de la GGD, $\left\|x\right\|_\xi$ est la norme l^p, et H est la matrice du système . La solution est cherchée à l'aide de l'algorithme EM:

$$\begin{aligned} &E-STEP: Q(\mathrm{x},\mathrm{x}_k) = -\frac{\left\|\mathrm{y}-\mathrm{Hx}\right\|_2^2}{2\sigma_n^{\,2}} - \frac{1}{2}x^T D_k x \\ &M-STEP: \mathrm{x}_{k+1} = \arg\max_{x}\left\{Q(\mathrm{x},\mathrm{x}_k)\right\} = \left(\sigma_n^2 D_k + H^T H\right)^{-1} H^T y \end{aligned} \tag{22}$$

ou $\left[D_k\right]_{ii} = \lambda\xi \Big/ \left|x_i^k\right|^{2-\xi}$ est un préconditionneur pour la régularisation utilisant la norme l^p. L'exécution s'arrête quand le seuil τ est atteint:

$$\left|L(\mathrm{x}_{k+1},\xi_k) - L(\mathrm{x}_k,\xi_k)\right| / L(\mathrm{x}_k,\xi_k) < \tau \tag{23}$$

L'application de cet algorithme peut effectivement mener à une réduction sensible du flou dans l'image. Par contre, la convergence des algorithmes implique qu'ils atteignent une solution très éparse, ce qui peut conduire à des résultats erronés. La présence des artéfacts numériques (comme le phénomène de Gibbs généré par des passages par le domaine fréquentiel) est un autre désavantage. Globalement, le résultat manque de la fiabilité. Les figures 16 et 17 montrent les résultats de l'estimation des paramètres statistiques après l'application de l'algorithme de déconvolution sur les données utilisées dans la dernière section du Chapitre 4. Visiblement, l'amélioration souhaitée n'est pas atteinte, en termes de pouvoir de séparation (l'évolution des paramètres de forme en fonction de la concentration n'est même plus monotone) où réduction de

la variance. On a donc conclut que cette technique ne va pas servir pour la caractérisation statistique des tissus.

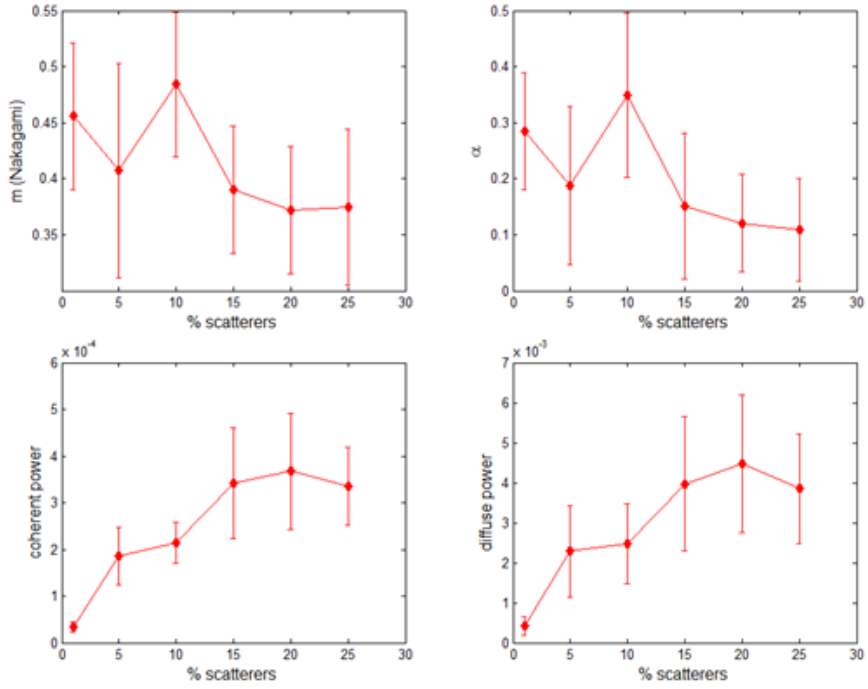

Figure 16 Estimations obtenues après déconvolution : simulation

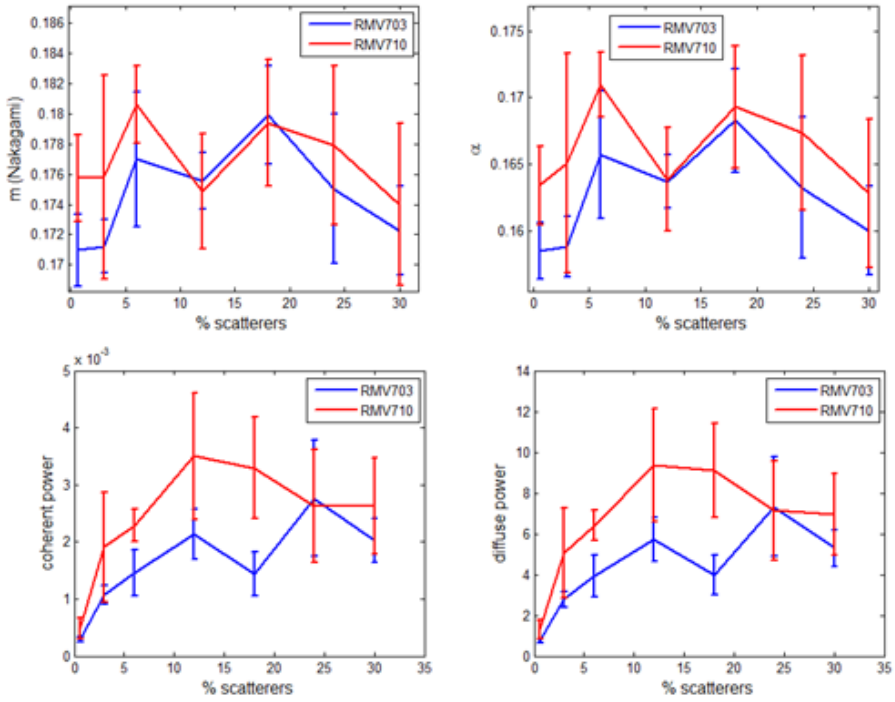

Figure 17 Estimations obtenues après déconvolution : biofantômes

6 CONCLUSIONS GENERALES ET PERSPECTIVES

L'objectif de cette thèse est d'apporter une contribution à la caractérisation des tissus par ultrasons, en utilisant la modélisation statistique du speckle ultrasonore. La structure du speckle est déterminée par la concentration de diffuseurs dans le milieu, ainsi que les propriétés du système d'imagerie (principalement déterminées par les fréquences de balayage). Nous étudions la possibilité de quantifier la concentration de diffuseurs en utilisant trois modèles statistiques (distributions): la distribution Gaussienne Généralisée (GGD) pour le signal RF, et les distributions Nakagami et K-Homodyne pour l'enveloppe du signal RF.

Dans la première partie, des études ont été menées simultanément sur la distribution Gaussienne Généralisée et la distribution de Nakagami, en utilisant les mêmes données (simulées et expérimentales). Les deux distributions partagent un certain nombre de similarités. Chacune d'elles est caractérisée par une paire de paramètres: un paramètre de forme directement relié à la concentration de diffuseurs par cellule de résolution, et un paramètre d'échelle en rapport avec l'énergie rétrodiffusée (sensible à la concentration de diffuseurs, mais aussi aux autres caractéristiques des diffuseurs). En outre, leurs paramètres de forme estimés montrent des évolutions similaires, presque identiques en fonction de la concentration de diffuseurs par cellule de résolution. Les valeurs saturent pour un speckle pleinement développé (équivalent à des concentrations supérieures à environ 10 diffuseurs par cellule de résolution) à environ 2 pour la GGD, et à environ 1 pour la distribution de Nakagami. La dépendance entre ces paramètres de forme et le nombre de diffuseurs par cellule de résolution peut être modélisée par une fonction exponentielle. Les valeurs du paramètre de forme obtenues à partir des simulations effectuées à des fréquences différentes s'ajuste très bien sur ce modèle. Toutefois, les données expérimentales obtenues avec différents systèmes d'imagerie à partir des fantômes de particules d'Orgasol ne suivent pas une courbe avec les mêmes paramètres, et la saturation apparaît pour un nombre de diffuseurs par cellule de résolution beaucoup plus faible. Nous attribuons cette différence à un certain nombre de facteurs possibles: imprécision dans l'approximation de la taille de la cellule de résolution ou dans la fabrication des fantômes, une grande variabilité de la distribution des tailles des diffuseurs, une quantité insuffisante de données pour un ajustement fiable, ou la présence d'un fond diffus (produit par la diffusion des structures autres que les particules Orgasol) dans les images acquises. La réalisation d'une série d'expériences sur des fantômes calibrées où le speckle est influencé exclusivement par les particules pourrait produire des résultats différents. Les acquisitions devraient être menées avec des transducteurs haute fréquence plutôt qu'avec des sondes d'échographes, augmentant ainsi l'intervalle de diffuseurs équivalents par cellule de résolution dans la zone de non-saturation (<10) que l'on peut obtenir avec un ensemble de fantômes de concentrations volumiques différentes (Figure 3.7). De cette façon, des fantômes avec des concentrations volumiques de particules relativement élevées peut être utilisées à la place des fantômes dilués plus difficile à fabriquer.

La distribution de Nakagami a également été utilisée pour analyser des images simulées de

milieux avec différentes non-linéarités. Les paramètres de forme estimés sur les images fondamentales ne montrent aucune différence d'un milieu à l'autre, mais celles calculées dans les mêmes régions des images harmoniques étaient capables de distinguer entre les différentes non-linéarités. Toutefois, un test sur des données expérimentales n'a pas encore été mené, afin de montrer si le pouvoir discriminant du paramètre de forme de Nakagami est fiable. Le fait de ne pas avoir une méthode pour construire des fantômes avec un coefficient de nonlinéarité spécifique va poser un problème si on souhaite avoir un résultat quantitatif.

Dans la deuxième partie, la distribution K-Homodyne a été utilisée pour modéliser les amplitudes de l'enveloppe. Ce modèle plus complexe est défini par trois paramètres, dont α, le paramètre de regroupement des diffuseurs (quasiment analogue au paramètre de forme de Nakagami) dépend de la concentration de diffuseur par cellule de résolution, mais n'est pas limité à une valeur maximale pour le speckle pleinement développé. Des simulations et des expériences ont montré que les valeurs moyennes de α augmentent en effet en fonction de la concentration de diffuseur par cellule de résolution, même pour un speckle pleinement développé, au moins jusqu'à une certaine limite. Dans les expériences, cette limite est rencontrée pour une concentration volumique de diffuseurs d'environ 10% à 30 MHz, mais doit encore être déterminée avec précision. La difficulté principale est posée par le grand biais d'estimation à des concentrations élevées, qui dépend directement du nombre d'échantillons décorrélés utilisés pour l'estimation. La réduction du biais et la recherche d'une "limite de la fiabilité" du paramètre α en utilisant de grandes quantités de données fait l'objet d'une étude en cours.

Une technique de déconvolution pour le signal RF a également été testée afin d'évaluer sa capacité d'améliorer le contraste entre les estimations statistiques obtenues pour différentes concentrations. Idéalement, la déconvolution conduirait à une meilleure différenciation des diffuseurs présents dans le milieu. Malheureusement, les images qui en résultent n'approximent pas correctement la distribution de diffuseurs, en particulier pour les milieux très denses. Les paramètres statistiques estimés sur ces images augmentent dans certains cas l'ambiguïté entre les différentes concentrations. Nous concluons donc que la stratégie n'est pas utile lorsque l'on étudie les statistiques du speckle / de la réflectivité du milieu.

En ce qui concerne l'objectif plus lointain de notre recherche, nous espérons qu'une fois avoir établi un cadre pour l'utilisation fiable des paramètres statistiques (principalement α de la distribution K-Homodyne), ce paramètre sera utilisé en tant que caractéristique dans la classification des milieux avec différentes concentrations. Les estimations statistiques et spectrales peuvent être utilisées ensemble pour augmenter leur pouvoir discriminant dans les situations où un seul type d'estimation ne différencie pas clairement les milieux. L'utilisation du paramètre α peut faciliter l'application de ces techniques à l'imagerie basse fréquence des structures profondes du corps humain, où les basses résolutions entraînent du speckle pleinement développé, même pour des concentrations volumiques faibles. L'utilisation des sondes CMUT est une perspective intéressante grâce à l'amélioration de la résolution qu'elles offrent à des fréquences relativement basses.

PERSONAL BIBLIOGRAPHY

- **A. Cristea, C. Cachard, A. Bernard, T. Lefort, O. Basset**: "Influence des Paramètres de la Sonde Pour la Caractérisation Ultrasonore des Tissus par une Approche Statistique", Congrès Français d'Acoustique, 2014

- **A. Cristea, E. Franceschini, F. Lin, J. Mamou, C. Cachard, O. Basset**: "Quantitative Characterization of Concentrated Cell Pellet Biophantoms using Statistical Models for the Ultrasound Echo Envelope", Physics Procedia Vol .70 – Proceedings of The International Congress on Ultrasonics, 2015 : 1091-1095

- **F. Lin, A. Cristea, C. Cachard, O. Basset**: "Tissue Characterization of Ultrasound Harmonic Signals using Nakagami Statistics", Physics Procedia Vol .70 – Proceedings of The International Congress on Ultrasonics, 2015 : 1065-1068

- **F. Lin, A. Cristea, C. Cachard, O. Basset :** "Ultrasound Tissue Characterization: Comparison of Statistical Results using Fundamental and Harmonic Signals", 20th International Symposium on Nonlinear Acoustics, 2015

BIBLIOGRAPHY

Abeyratne, Udantha R., A.P. Petropulu, and John M Reid. 1995. "Higher Order Spectra Based Deconvolution of Utrasound Images" 42 (6): 1064–75.

Alessandrini, Martino, Simona Maggio, Jonathan Porée, Luca De Marchi, Nicolo Speciale, Emilie Franceschini, Olivier Bernard, and Olivier Basset. 2011. "A Restoration Framework for Ultrasonic Tissue Characterization." *IEEE Transactions on Ultrasonics, Ferroelectrics, and Frequency Control* 58 (11): 2344–60.

Banihashemi, Behzad, Roxana Vlad, Branislav Debeljevic, Anoja Giles, Michael C. Kolios, and Gregory J. Czarnota. 2008. "Ultrasound Imaging of Apoptosis in Tumor Response: Novel Preclinical Monitoring of Photodynamic Therapy Effects." *Cancer Research* 68 (20): 8590–96. doi:10.1158/0008-5472.CAN-08-0006.

Bernard, Olivier, Jan D'hooge, and Denis Friboulet. 2006. "Segmentation Of Echocardiographic Images Based On Statistical Modelling Of The Radio-Frequency Signal." *EUSIPCO*.

Bernard, Olivier, Jan D'Hooge, and Denis Friboulet. 2006. "Statistics of the Radio-Frequency Signal Based on K Distribution with Application to Echocardiography." *IEEE Transactions on Ultrasonics, Ferroelectrics, and Frequency Control* 53 (9): 1689–94. doi:10.1109/TUFFC.2006.1678198.

Bernard, Olivier, B. Touil, J D'hooge, and D Friboulet. 2007. "Statistical Modeling of the Radio-Frequency Signal for Partially and Fully Developed Speckle Based on a Generalized Gaussian Model with Application to Echocardiography." *IEEE Transactions on Ultrasonics, Ferroelectrics, and Frequency Control* 54 (10): 2189–94.

Bigelow, Timothy, and William D O'Brien. 2004. "Scatterer Size Estimation in Pulse-Echo Ultrasound Using Focused Sources: Theoretical Approximations and Simulation Analysis." *The Journal of the Acoustical Society of America* 116 (1): 578–93. doi:10.1121/1.1757452.

Blacknell, D, and R J A Tough. 2001. "Parameter Estimation for the K-Distribution Based on [z Log(z)]." *Radar, Sonar and Navigation, IEE Proceedings* - 148 (6): 309–12. doi:10.1049/ip-rsn:20010720.

Bouman, C, and K Sauer. 1993. "A Generalized Gaussian Image Model for Edge-Preserving MAP Estimation." *Image Processing, IEEE Transactions on* 2 (3): 296–310. doi:10.1109/83.236536.

Bui, Thanh Minh, Alan Coron, Jonathan Mamou, Saegusa-Beecroft Emi, Yamaguchi Tadashi, Yanagihara Eugene, Machi Junji, Bridal Lori, and Ernest J. Feleppa. 2014. "Modeling the

Envelope Statistics of Three-Dimensional High-Frequency Ultrasound Echo Signals from Dissected Human Lymph Nodes." *Japanese Journal of Applied Physics* 53 (7S): 157–62. doi:10.1037/a0030561.Striving.

Burckhardt, C. B. 1978. "Speckle in Ultrasound B-Mode Scans." *IEEE Transactions on Sonics and Ultrasonics* 25 (1): 1–6. doi:10.1109/T-SU.1978.30978.

Chen, Jiang-Feng, James A. Zagzebski, Fang Dong, and Ernest L. Madsen. 1998. "Estimating the Spatial Autocorrelation Function for Ultrasound Scatterers in Isotropic Media." *Medical Physics* 25 (5): 648. doi:10.1118/1.598247.

Coleman, D.J., and F. L. Lizzi. 1983. "Computerized Ultrasonic Tissue Characterization of Ocular Tumors." *Amer. J. Ophthalmology* 96: 165–75.

Coleman, D.J., F.L. Lizzi, R.H. Silverman, L. Helson, J.H. Torpey, and M.J. Rondeau. 1985. "A Model for Acoustic Characterization of Intraocular Tumors." *Investigative Ophthalmology &Visual Science* 26: 545–50.

Czarnota, G J, M C Kolios, J Abraham, M Portnoy, F P Ottensmeyer, J W Hunt, and M D Sherar. 1999. "Ultrasound Imaging of Apoptosis: High-Resolution Non-Invasive Monitoring of Programmed Cell Death in Vitro, in Situ and in Vivo." *British Journal of Cancer* 81 (3): 520–27. doi:10.1038/sj.bjc.6690724.

Dantas, Ricardo G., Eduardo T. Costa, and Sidney Leeman. 2005. "Ultrasound Speckle and Equivalent Scatterers." *Ultrasonics* 43 (6): 405–20. doi:10.1016/j.ultras.2004.11.003.

Destrempes, F., Jean Meunier, Marie-France Giroux, Gilles Soulez, and Guy Cloutier. 2009. "Segmentation in Ultrasonic B-Mode Images of Healthy Carotid Arteries Using Mixtures of Nakagami Distributions and Stochastic Optimization." *IEEE Medical Imaging* 28 (2).

Destrempes, F., Jonathan Porée, and Guy Cloutier. 2013. "Estimation Method of the Homodyned K-Distribution Based on the Mean Intensity and Two Log-Moments." *SIAM Journal of Imaging Sciences* 6 (3): 1499–1530.

Dutt, V, and J F Greenleaf. 1994. "Ultrasound Echo Envelope Analysis Using a Homodyned K Distribution Signal Model." *Ultrasonic Imaging*. doi:10.1177/016173469401600404.

Dutt, V., and J.F. Greenleaf. 1995. "K Distribution Model of Ultrasound Speckle: Fractional Order SNRsand Log Compression Variance." *1995 IEEE Ultrasonics Symposium. Proceedings. An International Symposium* 2: 1375–78. doi:10.1109/ULTSYM.1995.495812.

Eltoft, T. 2006. "Modeling the Amplitude Statistics of Ultrasonic Images." *IEEE Medical Imaging* 25 (2): 229–40.

Fang, Jui, and Po-Hsiang Tsui. 2015. "Evaluation of Thrombolysis by Using Ultrasonic Imaging: An in Vitro Study." *Scientific Reports* 5. Nature Publishing Group: 11669.

doi:10.1038/srep11669.

Franceschini, E., R. Gu, F Tourniaire, S Roffino, E Lamy, and J-F Landrier. 2014. “Structure Factor Model for Understanding the Measured Backscatter Coefficients from Concentrated Cell Pellet Biophantoms.” *JASA* 135.

Franceschini, E., and R Guillermin. 2012. “Experimental Assessement of Four Ultrasound Scattering Models for Characterizing Concentrated Tissue-Mimicking Phantoms.” *JASA* 132 (6): 3735–47.

Franceschini, E., B. Metzger, and Guy Cloutier. 2011. “Forward Problem Study of an Effective Medium Model for Ultrasound Blood Characterization.” *IEEE Transactions on Ultrasonics, Ferroelectrics, and Frequency Control* 58 (12): 2668–79.

Franceschini, E., Francois T. H. Yu, and Guy Cloutier. 2008a. “Simultaneous Estimation of Attenuation and Structure Parameters of Aggregated Red Blood Ccell from Backscatter Measurements.” *JASA* 123 (4).

Franceschini, E., François T. H. Yu, and Guy Cloutier. 2008b. “Ultrasound Characterization of Aggregated Red Blood Cells: Towards in Vivo Application.” *Research Network GDR 2501, France*.

Ghoshal, Goutam, Jonathan Mamou, and Michael L. Oelze. 2013. “State of the Art Methods for Estimating Backscatter Coefficients.” In *Quantitative Ultrasound in Soft Tissues*, 3–19.

Goodman, J. W. 1976. “Some Fundamental Properties of Speckle.” *Journal of the Optical Society of America* 66 (11): 1145. doi:10.1364/JOSA.66.001145.

Hafez, Zachary T., Lauren A. Wirtzfeld, Andrew Battles, Rita J. Miller, Sandhya Sarwate, Michael L. Oelze, Timothy J. Hall, and William D. O’Brien. 2009. “Estimating Scatterer Properties in Rat Fibroadenomas Using Various Mathematical Form Factors.” *Proceedings - IEEE Ultrasonics Symposium*, 294–96. doi:10.1109/ULTSYM.2009.5441787.

Han, Aiguo, Student Member, William D O Brien, and Life Fellow. 2015. “Structure Function for High-Concentration Biophantoms of Polydisperse Scatterer Sizes” 62 (2).

Ho, Ming Chih, Jen Jen Lin, Yu Chen Shu, Chiung Nien Chen, King Jen Chang, Chien Cheng Chang, and Po Hsiang Tsui. 2012. “Using Ultrasound Nakagami Imaging to Assess Liver Fibrosis in Rats.” *Ultrasonics* 52 (2). Elsevier B.V.: 215–22. doi:10.1016/j.ultras.2011.08.005.

Holasek, E, E W Purnell, and A Sokollu. 1975. “A Method for Spectra-Color B-Scan Ultrasonography,” no. 55: 175–78.

Hruska, David P., and Michael L. Oelze. 2009. “Improved Parameter Estimates Based on the Homodyned K Distribution.” *IEEE Transactions on Ultrasonics, Ferroelectrics, and*

Frequency Control 56 (11): 2471–81. doi:10.1109/TUFFC.2009.1334.

Insana, F, and J Hall. 1990. "Parametric Ultrasound Imaging from Backscatter Coefficient Measurements: Image Formation and Interpretation." *Ultrasonic Imaging* 267: 245–67.

Insana, M F, R F Wagner, D G Brown, and T J Hall. 1989. "Describing Small-Scale Structure in Random Media Using Pulse-Echo Ultrasound." *The Journal of the Acoustical Society of America* 87 (1): 179–92. doi:10.1121/1.399283.

Jakeman, E. 1980. "On the Statistics of K-Distributed Noise." *Journal of Physics A* 13: 31–48.

Jakeman, E, and P N Pusey. 1976. "A Model for Non-Rayleigh Sea Echo." *Antennas and Propagation, IEEE Transactions on* 24 (6): 806–14. doi:10.1109/TAP.1976.1141451.

Jakeman, E, and R J A Tough. 1987. "Generalized K Distribution: A Statistical Model for Weak Scattering." *J. Opt. Soc. Am. A* 4 (9). OSA: 1764–72. doi:10.1364/JOSAA.4.001764.

Jensen, J A. 1991. "Estimation of Pulses in Ultrasound B-Scan Images." *Medical Imaging, IEEE Transactions on* 10 (2): 164–72. doi:10.1109/42.79474.

Jensen, J Arendt, Dk- Lyngby, Published Medical, Biological Engineering, and Information Technology. 1996. "Field : A Program for Simulating Ultrasound Systems." *Medical & Biological Engineering* 34 (Supplement 1, Part 1): 351–53.

Jirijk, Radovan, Torfinn Taxt, and Jiri Jan. 2004. "Ultrasound Attenuation Imaging." *Journal of Electrical Engineering* 55 (7-8): 180–87.

Jiřík, Radovan, and Torfinn Taxt. 2006. "High-Resolution Ultrasonic Imaging Using Fast Two-Dimensional Homomorphic Filtering." *IEEE Transactions on Ultrasonics, Ferroelectrics, and Frequency Control* 53 (8): 1440–48. doi:10.1109/TUFFC.2006.1665101.

Kaaresen, Kjetil F., and Erik Bolviken. 1999. "Blind Deconvolution of Ultrasonic Traces Accounting for Pulse Variance." *IEEE Transactions on Ultrasonics, Ferroelectrics, and Frequency Control* 46 (3): 564–73. doi:10.1109/58.764843.

Kanzler, Steven G, and Michael L Oelze. 2008. "Improved Scatterer Size Estimation Using Backscatter Coefficient Measurements with Coded Excitation and Pulse Compression." *The Journal of the Acoustical Society of America* 123 (6): 4599–4607. doi:10.1121/1.2908293.

Kay, Steven M. 1993. "Fundamentals of Statistical Signal Processing." *Englewood Cliffs NJ Prentice Hall* Volume I.: 513.

Kolios, Michael, M.J. Czarnota, M. Lee, J.W. Hunt, and M.D. Shrerar. 2002. "Ultrasonic Spectral Parameter Characterization of Apoptosis." *Ultrasound in Medicine and Biology* 28 (5): 589–97.

Lavarello, Roberto J., and Michael L. Oelze. 2010. "Assessment of the Effects of Scatterer Size

Distributions on Effective Scatterer Diameter Estimates." *Proceedings - IEEE Ultrasonics Symposium*, 732–35. doi:10.1109/ULTSYM.2010.5935475.

Lavarello, Roberto J., Michael L. Oelze, Michael Berggren, Steven Johnson, Marko Orescanin, and Rebecca Yapp. 2009. "Implementation of Scatterer Size Imaging on an Ultrasonic Breast Tomography Scanner." *Proceedings - IEEE Ultrasonics Symposium*, 305–8. doi:10.1109/ULTSYM.2009.5442021.

Law, W.K., L.a. Frizzell, and F. Dunn. 1985. "Determination of the Nonlinearity Parameter B/A of Biological Media." *Ultrasound in Medicine & Biology* 11 (2): 307–18. doi:10.1016/0301-5629(85)90130-9.

Liao, Yin-Yin, Chia-Hui Li, Po-Hsiang Tsui, Chien-Cheng Chang, Wen-Hung Kuo, King-Jen Chang, and Chih-Kuang Yeh. 2012. "Strain-Compounding Technique with Ultrasound Nakagami Imaging for Distinguishing between Benign and Malignant Breast Tumors." *Medical Physics* 39 (5): 2325. doi:10.1118/1.3700167.

Liebgott, Hervé. 2005. "Synthèse de Réponse Impulsionelle En Imagerie Ultrasonore Pour L'estimation Vectorielle Du Déplacement." INSA de Lyon. doi:10.1007/s13398-014-0173-7.2.

Lizzi, FL, M Greenebaum, EJ Feleppa, M Elbaum, and DJ Coleman. 1983. "Theoretical Framework for Spectrum Analysis in Ultrasonic Tissue Characterization." *JASA* 73 (4): 1366–73.

Lizzi, M Ostromogilsky, E J Feleppa, M C Rorke, and M M Yaremko. 1986. "Relationship of Ultrasonic Spectral Parameters to Features of Tissue Microstructure." *IEEE Transactions on Ultrasonics, Ferroelectrics, and Frequency Control* 33 (3): 319–29. doi:10.1109/T-UFFC.1987.26950.

Mallat, S G. 1989. "A Theory for Multiresolution Signal Decomposition: The Wavelet Representation." *Pattern Analysis and Machine Intelligence, IEEE Transactions on* 11 (7): 674–93. doi:10.1109/34.192463.

Mamou, Jonathan, Alain Coron, Michael L. Oelze, Emi Saegusa-Beecroft, Masaki Hata, Paul Lee, Junji Machi, Eugene Yanagihara, Pascal Laugier, and Ernest J. Feleppa. 2011. "Three-Dimensional High-Frequency Backscatter and Envelope Quantification of Cancerous Human Lymph Nodes." *Ultrasound in Medicine and Biology* 37 (3): 345–57. doi:10.1016/j.ultrasmedbio.2010.11.020.

Mamou, Jonathan, Michael L Oelze, William D O'Brien, and James F Zachary. 2008. "Extended Three-Dimensional Impedance Map Methods for Identifying Ultrasonic Scattering Sites." *The Journal of the Acoustical Society of America* 123 (2): 1195–1208. doi:10.1121/1.2822658.

Mamou, Jonathan, Michael L Oelze, and James F Zachary. 2005. "Identifying Ultrasonic Scattering Sites from Three-Dimensional Impedance Maps." *Society* 117 (January): 413–23. doi:10.1121/1.1810191.

Michailovich, Oleg, and D Adam. 2005. "A Novel Approach to the 2-D Blind Deconvolution Problem in Medical Ultrasound." *Medical Imaging, IEEE Transactions on* 24 (1): 86–104. doi:10.1109/TMI.2004.838326.

Michailovich, Oleg, and Allen Tannenbaum. 2007. "Blind Deconvolution of Medical Ultrasound Images: A Parametric Inverse Filtering Approach." *IEEE Image Processing* 16 (12): 3005–19.

Morin, Renaud. 2013. "Amélioration de La Résolution En Imagerie Ultrasonore." Université de Toulouse.

Moser, G, J Zerubia, and S B Serpico. 2006. "SAR Amplitude Probability Density Function Estimation Based on a Generalized Gaussian Model." *Image Processing, IEEE Transactions on* 15 (6): 1429–42. doi:10.1109/TIP.2006.871124.

Moulin, Pierre, and Juan Liu. 1998. "Analysis of Multiresolution Image Denoising Schemes Using Generalized-Gaussian Priors." In *Time-Frequency and Time-Scale Analysis, 1998. Proceedings of the IEEE-SP International Symposium on*, 633–36.

Muir, T G, and E. L. Carstensen. 1980. "Prediction of Nonlinear Acoustic Effects at Biomedical Frequencies and Intensities." *Ultrasound in Medicine and Biology* 6 (4): 345–57.

Namburete, Ana I.L., Bahbibi Rahmatullah, and J Alison Noble. 2013. "Nakagami-Based AdaBoost Learning Framework for Detection of Anatomical Landmarks in 2D Fetal Neurosonograms." *Annals of the BMVA*, no. 2.

Ng, James, Richard Prager, and Nick Kingsbury. 2007. "Wavelet Restoration of Medical Pulse-Echo Ultrasound Images in an EM Framework." *IEEE Transactions on Ultrasonics, Ferroelectrics, and Frequency Control* 54 (3): 550–67.

O'Donnel, M, and JG Miller. 1981. "Quantitative Broadband Ultrasonic Backscatter: An Approach to Nondestructive Evaluation in Acoustically Inhomogeneous Materials." *Journal of Applied Physics* 52 (2): 1056–65.

Oelze, Michael, W.D. O'Brien, and J.F. Zachary. 2007. "Quantitative Ultrasound Assessment of Breast Cancer Using a Multiparameter Approach." *2007 IEEE Ultrasonics Symposium Proceedings*, 981–84. doi:10.1109/ULTSYM.2007.250.

Oelze, Michael, and Wiliam O'Brien. 2006. "Application of Three Scattering Models to Characterization of Solid Tumors in Mice." *Ultrasonic Imaging* 28: 83–96.

Oelze, Michael, William O'Brien, James Blue, and James Zachary. 2004. "Differentiation and

Characterization of Rat Mammary Fibroadenomas and 4T1 Mouse Carcinomas Using Quantitative Ultrasound Imaging." *IEEE Medical Imaging* 23 (6): 764–71.

Oelze, Michael, and Williams O'Brien. 2002. "Frequency-Dependent Attenuation-Compensation Functions for Ultrasonic Signals Backscattered from Random Media." *The Journal of the Acoustical Society of America* 111 (5 Pt 1): 2308–19. doi:10.1121/1.1612491.

Oelze, Michael, and James F Zachary. 2006. "Examination of Cancer in Mouse Models Using High-Frequency Quantitative Ultrasound." *Ultrasound in Medicine & Biology* 32 (11): 1639–48. doi:10.1016/j.ultrasmedbio.2006.05.006.

Oelze, Michael, James F Zachary, and William O'Brien. 2002a. "Parametric Imaging of Rat Mammary Tumors In Vivo for the Purposes of Tissue Characterization." *Journal of Ultrasound in Medicine*, 1201–10.

Oelze, Michael, James Zachary, and William O'Brien. 2002b. "Characterization of Tissue Microstructure Using Ultrasonic Backscatter : Theory and Technique for Optimization Using a Gaussian Form Factor." *JASA* 112 (3): 1202–11.

Oosterveld, B J, J M Thijssen, P C Hartman, R L Romijn, and G J Rosenbusch. 1991. "Ultrasound Attenuation and Texture Analysis of Diffuse Liver Disease: Methods and Preliminary Results." *Physics in Medicine and Biology* 36 (8): 1039–64. doi:10.1088/0031-9155/36/8/002.

Powers, Jeff, and Frederick Kremkau. 2011. "Medical Ultrasound Systems." *Interface Focus* 1 (4). Royal Society: 477–89.

Rao, N., S. Mehra, and H. Zhu. 1990. "Ultrasound Speckle Statistics Variations with Imaging SystemsImpulse Response." *IEEE Symposium on Ultrasonics*, 1435–40. doi:10.1109/ULTSYM.1990.171602.

Redding, Nicholas J. 1999. *Estimating the Parameters of the K Distribution in the Intensity Domain*. Salisbury, Australia.

Saha, Ratan K., E. Franceschini, and G Cloutier. 2011. "Assessment of Accuracy of the Structure-Factor-Size-Estimator Method in Determining Red Blood Cell Aggregate Size from Ultrasound Spectral Backscatter Coefficient." *JASA* 129 (4): 2269–77.

Sannachi, Lakshmanan, Hadi Tadayyon, Ali Sadeghi-Naini, Michael L Oelze, and Gregory J Czarnota. 2014. "Noninvasive Evaluation of Locally-Advanced Breast Cancer Response to Neoadjuvant Chemotherapy Using Quantitative Ultrasonic Backscatter Parameters." *39th International Symposium on Ultrasonic Imaging and Tissue Characterization (UITC)* 20 (1). Elsevier B.V.: 224–36. doi:10.1016/j.media.2014.11.009.

Shankar, P M. 1995. "A Model for Ultrasonic Scattering from Tissues Based on the K

Distribution." *Physics in Medicine and Biology* 40 (10): 1633–49. doi:10.1088/0031-9155/40/10/006.

———. 2000. "A General Statistical Model for Ultrasonic Backscattering from Tissues." *IEEE Transactions on Ultrasonics, Ferroelectrics, and Frequency Control* 47 (3): 727–36.

Shankar, P M, C W Piccoli, J M Reid, F Forsberg, and B B Goldberg. 2005. "Application of the Compound Probability Density Function for Characterization of Breast Masses in Ultrasound B Scans." *Physics in Medicine and Biology* 50 (10): 2241. http://stacks.iop.org/0031-9155/50/i=10/a=004.

Shankar, P M, J M Reid, H Ortega, C W Piccoli, and B B Goldberg. 1993. "Use of Non-Rayleigh Statistics for the Identification of Tumors in Ultrasonic B-Scans of the Breast." *Medical Imaging, IEEE Transactions on* 12 (4): 687–92. doi:10.1109/42.251119.

Shankar, P. M. 2001. "Ultrasonic Tissue Characterization Using a Generalized Nakagami Model." *IEEE Transactions on Ultrasonics, Ferroelectrics, and Frequency Control* 48 (6): 1716–20. doi:10.1109/58.971725.

Shankar, P.M., V.A. Dumane, J Reid, V Genis, F Forsberg, C Piccoli, and B Goldberg. 2001. "Classification of Ultrasonic B-Mode Images of Breast Masses Using Nakagami Distribution." *IEEE Transactions on Ultrasonics, Ferroelectrics, and Frequency Control* 48 (2).

Shankar P.M., Vishruta A Dumane, Thomas George, Catherine W Piccoli, John M Reid, Flemming Forsberg, and Barry B Goldberg. 2003. "Classification of Breast Masses in Ultrasonic B Scans Using Nakagami and K Distributions." *Physics in Medicine and Biology* 48: 2229–40.

Taxt, T. 1995. "Restoration of Medical Ultrasound Images Using Two-Dimensional Homomorphic Deconvolution" 42 (4): 543–54.

Taxt, T, and G V Frolova. 1999. "Noise Robust One-Dimensional Blind Deconvolution of Medical Ultrasound Images." *IEEE Transactions on Ultrasonics, Ferroelectrics, and Frequency Control* 46 (2): 291–99. doi:10.1109/58.753017.

Taxt, T, and Jarle Strand. 2001. "Two-Dimensional Noise-Robust Blind Deconvolution of Ultrasound Images." *IEEE Transactions on Ultrasonics, Ferroelectrics, and Frequency Control* 48 (4): 861–67. doi:10.1109/58.935701.

Teisseire, Maxime, Aiguo Han, Rami Abuhabsah, James P Blue, Sandhya Sarwate, and William D O'Brien. 2010. "Ultrasonic Backscatter Coefficient Quantitative Estimates from Chinese Hamster Ovary Cell Pellet Biophantoms." *The Journal of the Acoustical Society of America* 128 (5): 3175–80. doi:10.1121/1.3655879.

Thijssen, J M. 2003. "Ultrasonic Speckle Formation, Analysis and Processing Applied to Tissue Characterization." *Pattern Recognition Letters* 24: 659–75.

Topp, Karen, James Zachary, and William O'Brien. 2001. "Quantifying B-Mode Images of In Vivo Rat Mammary Tumors by the Frequency Dependence of Backscatter." *Journal of Ultrasound in Medicine* 20: 605–12.

Trop, I, F Destrempes, M El Khoury, A Robidoux, L Gaboury, L Allard, B Chayer, and G Cloutier. 2014. "The Added Value of Statistical Modeling of Backscatter Properties in the Management of Breast Lesions at US." *Radiology* 275 (3): 666–74.

Tsui, Po-Hsiang, Cheng-Wei Hsu, Ming-Chih Ho, Yung-Sheng Chen, Jen-Jen Lin, Chien-Cheng Chang, and Chin-Chou Chu. 2010. "Three-Dimensional Ultrasonic Nakagami Imaging for Tissue Characterization." *Physics in Medicine and Biology* 55 (19): 5849–66. doi:10.1088/0031-9155/55/19/015.

Tsui, Po-Hsiang, Chih-Chung Huang, and Shyh-Hau Wang. 2006. "Use of Nakagami Distribution and Logarithmic Compression in Ultrasonic Tissue Characterization." *Journal of Medical and Biological Engineering* 26 (2): 69–73.

Tsui, Po-Hsiang, Yung Liang Wan, Yu Ting Chien, Chia Chun Yeh, and Chiao Yin Wang. 2013. "Dependency of Ultrasonic Nakagami Images on the Mechanical Properties of Scattering Medium." *Journal of Medical and Biological Engineering* 33 (1): 95–102. doi:10.5405/jmbe.1101.

Tsui, Po-Hsiang, Yung-Liang Wan, Dar-In Tai, and Yu-Chen Shu. 2015. "Effects of Estimators on Ultrasound Nakagami Imaging in Visualizing the Change in the Backscattered Statistics from a Rayleigh Distribution to a Pre-Rayleigh Distribution." *Ultrasound in Medicine & Biology*, no. Holfman 1960: 1–12. doi:10.1016/j.ultrasmedbio.2015.04.003.

Tsui, Po-Hsiang, and Shyh Hau Wang. 2004. "The Effect of Transducer Characteristics on the Estimation of Nakagami Paramater as a Function of Scatterer Concentration." *Ultrasound in Medicine and Biology* 30 (10): 1345–53. doi:10.1016/j.ultrasmedbio.2004.08.009.

Tsui, Po-Hsiang, Chih-Kuang Yeh, Chien-Cheng Chang, and Yin-Yin Liao. 2008. "Classification of Breast Masses by Ultrasonic Nakagami Imaging: A Feasibility Study." *Physics in Medicine and Biology* 53 (21): 6027–44. doi:10.1088/0031-9155/53/21/009.

Tsui, Po-Hsiang, Chih-Kuang Yes, and Chien-Cheng Yang. 2008. "Noise Effect on the Performance of Nakagami Image in Ultrasound Tissue Characterization." *Journal of Medical and Biological Engineering* 28 (4).

Tuthill, T.A., R.H. Sperry, and K J Parker. 1988. "Deviations from Rayleigh Statistics in Ultrasonic Speckle." *Ultrasonic Imaging* 10: 81–89.

Van Wijk, M. C., and J. M. Thijssen. 2002. "Performance Testing of Medical Ultrasound Equipment: Fundamental vs. Harmonic Mode." *Ultrasonics* 40 (1-8): 585–91. doi:10.1016/S0041-624X(02)00177-4.

Varray, François, Olivier Basset, Piero Tortoli, and Christian Cachard. 2013. "CREANUIS: A Non-Linear Radiofrequency Ultrasound Image Simulator." *Ultrasound in Medicine and Biology* 39 (10): 1915–24. doi:10.1016/j.ultrasmedbio.2013.04.005.

Wagner, RF, SW Slith, J M Sandrik, and H Lopez. 1983. "Statistics of Speckle in Ultrasound B-Scans." *IEEE Sonics and Ultrasonics* 30 (3): 156–63.

Wells, P N T. 1999. "Ultrasonic Imaging of the Human Body." *Reports on Progress in Physics* 62 (5): 671. http://stacks.iop.org/0034-4885/62/i=5/a=201.

Yu, François T. H., and Guy Cloutier. 2007. "Experimental Ultrasound Characterization of Red Blood Cell Aggregation Using the Structure Factor Size Estimator." *JASA* 122: 645–56.